Development of Highly Efficient Multimetallic Alloy Catalysts for Alkane Dehydrogenation

(アルカン脱水素に有効な多元素合金触媒の開発)

中谷　勇希

Yuki Nakaya

Graduate School of Chemical Sciences and Engineering

Hokkaido University

2023

Contents

Abbreviations 4

Chapter 1. General Introduction 5

1.1. The Status of Alkane Dehydrogenation 6

1.2. Fundamental Aspects of Catalyst Design 6

1.2.1. Reaction Mechanism 6

1.2.2. Geometric Effect 7

1.2.3. Electronic Effect 8

1.3. Strategy for PDH 8

1.3.1. Isolated Pt Sites for PDH 8

1.3.2. Pt–Cu Single-Atom Alloy 9

1.3.3. PtZn Intermetallic Compound 10

1.3.4. Surface Decoration of PtGa Intermetallic Compound 11

1.3.5. High-Entropy Intermetallics 12

1.4. Fundamental of Intermetallic Compounds 12

1.4.1. Intermetallic Compounds 12

1.4.2. Pseudo-Binary Alloys 13

1.4.3. High-Entropy Intermetallics 13

1.4.4. Surface Modification of Intermetallic Compounds 13

1.5. Aim of This Thesis 14

1.6. Concluding Remarks 15

References 16

Chapter 2. Platinum–Iron–Zinc Pseudo-Binary Alloy as a Highly Efficient Catalyst for Methylcyclohexane Dehydrogenation 19

2.1. Introduction 20

2.2. Experimental 21

2.2.1. Catalyst Preparation 21

2.2.2. Catalytic Reactions 22

2.2.3. Characterization 22

2.2.4. Computational Details 24
2.3. Results 25
2.3.1. Bimetallic System 25
2.3.2. Trimetallic System 27
2.3.3. Mechanic Study 36
2.4. Discussion 40
References 41
Chapter 3. Single-Atom Pt in Surface-Modified Intermetallics as a Stable and Selective Catalyst for Propane Dehydrogenation 43
3.1. Introduction 44
3.2. Experimental 45
3.2.1. Catalyst Preparation 45
3.2.2. Catalytic Reactions 46
3.2.3. Characterization 47
3.2.4. Computational Details 48
3.3. Results 48
3.3.1. Characterization of PtGa–Pb/SiO_2 48
3.3.2. Catalytic Performance in PDH 52
3.3.3. DFT Calculations 59
3.4. Discussion 60
References 67
Chapter 4. Electronic Modification of Single-Atom Pt in Surface-Modified Intermetallics for Propane Dehydrogenation 70
4.1. Introduction 71
4.2. Experimental 73
4.2.1. Catalyst Preparation 73
4.2.2. Catalytic Reactions 74
4.2.3. Characterization 74
4.2.4. Computational Details 76
4.3. Results 77
4.3.1. Characterization of PtGa–Ca/SiO_2 77

4.3.2. Characterization of PtGa–Ca–Pb/SiO_2 79
4.3.3. DFT Calculations 82
4.3.4. Catalytic Performance in PDH 83
4.4. Discussion 82
References 91
Chapter 5. Single-Atom Pt in High-Entropy Intermetallics as an Ultrastable Catalyst for Propane Dehydrogenation 95
5.1. Introduction 96
5.2. Experimental 97
5.2.1. Catalyst Preparation 97
5.2.2. Catalytic Reactions 99
5.2.3. Characterization 100
5.2.4. Computational Details 102
5.3. Results 103
5.3.1. Characterization of (PtCoCu)(GeGaSn)/Ca–SiO_2 103
5.3.2. Catalytic Performance in PDH 113
5.3.3. DFT Calculations 121
5.4. Discussion 150
References 151
Chapter 6. General Conclusions 154
Acknowledgement 157

Abbreviations

CN	coordination number
DFT	density functional theory
DOS	density of states
EDX	energy-dispersive X-ray
EXAFS	Extended X-ray absorption fine structure
FT-IR	Fourier-transform infrared
HAADF-STEM	high-angle annular dark-field scanning transmission electron microscopy
HEA	high-entropy alloy
HEI	high-entropy intermetallic
ICP-AES	inductively coupled plasma atomic emission spectroscopy
IMCs	intermetallic compounds
JASRI	Japan Synchrotron Radiation Research Institute
MCH	methylcyclohexane dehydrogenation
PDH	propane dehydrogenation
SAA	single-atom alloy
SAC	single-atom catalyst
TCD	thermal conductivity detector
TOF	turnover frequency
TPD	Temperature-programmed desorption
TPO	Temperature-programmed oxidation
TPR	Temperature-programmed reduction
TPSR	Temperature-programmed surface reaction
XAFS	X-ray absorption fine structure
XANES	X-ray absorption near edge structure
XPS	X-ray photoelectron spectroscopy
XRD	X-ray diffraction

Chapter 1

General Introduction

1. General Introduction

1.1. The Status of Alkane Dehydrogenation

The dehydrogenation of alkanes to alkenes is an important molecular transformation in various application such as in hydrogen production/carriage,[1,2] petroleum industry,[3] and polymer synthesis.[1,2] For instance, the dehydrogenation of cycloalkanes to aromatics, (*e.g.*, benzene, toluene, and naphthalene) is an emerging topic and a promising platform for the hydrogen production/carriage application because of the high hydrogen content, low toxicity, and/or availability in existing petroleum infrastructure.[1,2] Compared to other systems (*e.g.*, benzene and naphthalene), the dehydrogenation of methylcyclohexane (MCH) into toluene has been extensively studied due to its better advantages. In contrast to cycloalkanes, light olefins, including ethylene, propylene, and butene, are important raw materials in industry for the production of a wide variety of chemicals.[3,5–11] However, the supply of light olefins from conventional processes cannot compensate the growing global demand due to the advent of shale gas resources. Consequently, the alternative processes, including on-purpose alkane dehydrogenation, methanol-to-olefins, and Fischer–Tropsch-to-olefins, have been intensively studied to meet this demand.[3,5–11] Among these alternative processes, alkane dehydrogenation has been regarded as the most promising owing to its high light olefin selectivity and abundance of alkanes in shale gas. In particular, intense research efforts have been focused on the development of efficient propane dehydrogenation (PDH) catalysts.

Because of its high ability in C–H scission and relatively low ability in C–C cleavage, Pt is the most effective element in the dehydrogenation of alkanes.[1–3,5–11] However, the high endothermicity of alkane dehydrogenation requires high operating temperatures to attain high olefin yield. Because of the high reaction temperatures, even the Pt-based catalysts often suffer from catalyst degradation due to coke accumulation and/or nanoparticle sintering. Therefore, the catalysts must be regenerated, which increases the overall cost of alkane dehydrogenation processes. If the highly stable catalysts were developed, it would significantly benefit the future applications. Thus, an innovative catalyst with a long lifetime and a high selectivity for alkenes must be developed to solve these issues and for future applications.

1.2. Fundamental of Catalyst Design

1.2.1. Reaction Mechanism.

The mechanism of PDH is illustrated in Figure 1a. First, propane weakly physisorbs on the Pt sites with adsorption energy of typically −0.4 ~ −0.2 eV.[12,13] Propylene is formed by the first and second C–H scissions of physisorbed propane on Pt sites (E_1 and E_2 are their activation barriers, respectively). These reactions (propane to propylene) are largely unaffected by the geometric and electronic features of Pt.[14] The as-produced propylene is chemisorbed on the Pt site with adsorption energy ranging −0.4 ~ −1.0 eV.[12,13] However, the chemisorbed propylene (di-σ or π adsorption mode) can be further activated to make C_3H_5 (third C–H scission), followed by deep dehydrogenations, cracking, and finally coke production. Thus, the difference in activation energies ($\Delta E = E_3 - E_d$) between propylene desorption (E_d) and the third C–H scission (E_3) is a key determinant for propylene selectivity and catalyst stability. Notably, the ΔE value is highly dependent on the geometric and

electronic states of Pt.[3,5–10] As a result, modifying the characteristics of Pt *via* the addition of second metals and/or supports has been widely used as a standard catalyst design approach to date.

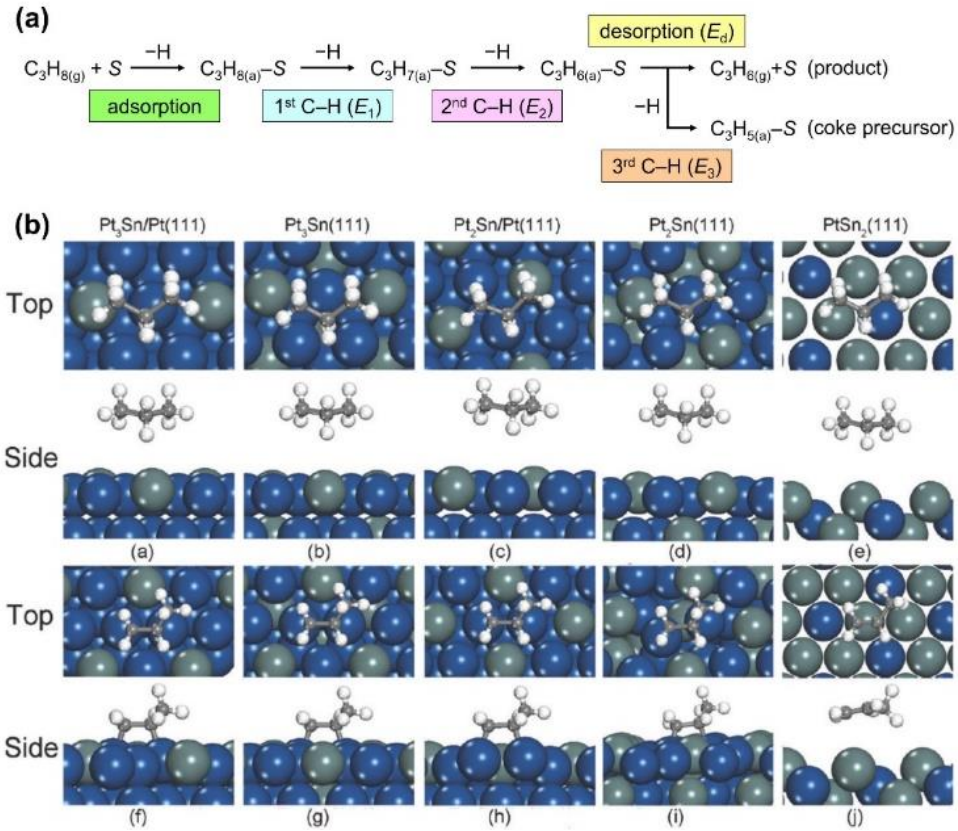

Figure 1. (a) Reaction mechanism of propane dehydrogenation. *S* represents the surface Pt sites. (b) Top and side views of propane (a-e) and propylene (f to j) adsorption configurations on the Pt-Sn alloyed surfaces. (b) was reproduced with permission from ref.[15] Copyright 2012 American Chemical Society.

1.2.2. Geometric Effect.

Pt ensembles (multiple-fold active sites) strongly adsorbs propylene in a di-σ adsorption mode, facilitating further C–H scissions and resulting in low propylene selectivity and coke production.[13,16,17] To increase selectivity and stability, large Pt ensembles can be diluted by alloying with less active metals such as Cu, Zn, Ga, In, and Sn. This is because the binding strength of propylene to Pt is weakened by alloying.[3,5–10] With an increase in the second metal fraction to Pt, the adsorption mode may change from di-σ (strong) to π (weak) (Figure 1b), thereby suppressing the side reactions that result in coke formation.[15,18] Additionally, the extent to which coke forms is determined by the crystal planes[13,19–21] and the coordination number (*CN*) of Pt.[19] In general, a Pt atom with a lower coordination number is more reactive and adsorptive, and hence more prone to causing the undesired side reactions.

1.2.3. Electronic Effect.

Due the fact that the electronic features of Pt contribute to the desorption of propylene,[22–25] the electronic effect is another important factor. The electronic effect has been interpreted in two ways: (1) in terms of Pt's electron density and (2) in terms of the location of the of *d*-band center. (1) Increased Pt electron density causes electronic repulsion with electron-rich propylene, promoting propylene desorption.[22–24] (2) The downshifting the Pt *d*-band center reduces the binding energy between propylene and Pt, facilitating the desorption of propylene.[13,15,26–28] When Pt ensembles remain on the surface, however, the side reactions can continue to decrease selectivity. Thus, the electronic modification should be provided as a supplementary effect on selectivity, whereas one should preferentially modify the surface geometry to sufficiently dilute Pt–Pt ensembles.

1.3. Strategy for PDH

1.3.1. Isolated Pt Sites for PDH

On the basis of foregoing, the optimal structure of Pt for selective light alkane dehydrogenation may be an entirely isolated Pt atom. Single-atom catalysts (SACs), in which active metal atoms are entirely isolated from the support, are experiencing a gold rush in catalysis due to their superior catalytic performance and high degree of atom utilization.[29–34] Notably, the single-atoms are strongly attached *via* electron transfer from metal to support, resulting in electron-deficient metal atoms with no metal ensembles.[35] Due to the absence of neighboring Pt, it is envisaged that single-atom Pt (Pt_1) will serve as a potential active site for PDH catalysis. Zhou *et al*. investigated the size dependence of Pt and discovered that positively charged Pt_1 is more active than clusters or nanoparticles.[36] However, with Pt_1 in the catalyst, aggregated Pt was found. It is noted that a small fraction of clusters and nanoparticles within SACs may largely contribute to the overall catalyst activity. Corma *et al*. also investigated the size dependency of the activity of Pt_1 and discovered that it is less active than clusters and nanoparticles.[37] Additionally, the single-atom Pt agglomerates into clusters under reaction conditions, resulting in an increase in catalytic activity. Zhou *et al*. recently tweaked the oxidation states of Pt SACs using a variety of supports and discovered a volcano-type curve between the electronic properties of SACs and catalytic activity.[25]

For Pt SAC catalysts, the trends in selectivity and catalyst life are contrary to what was expected from the isolation strategy. Chen *et al*. demonstrated that the propylene selectivity decreased upon downsizing to a particle size in the range of 1–9 nm, and 1 nm nanoparticle exhibited a 52% propylene selectivity at 520°C.[38] Moreover, Datye *et al*. discovered that Pt_1 sites strongly anchored on CeO_2 support ($Pt_1@CeO_2$) yield only byproduct CH_4 and CO_2 with no evidence of dehydrogenation selectivity at 680°C.[39] Density functional theory (DFT) studies revealed that positively charged Pt_1 significantly adsorbs propylene in the di-σ adsorption mode, and propylene is amenable to subsequent reactions. Additionally, Pt acts as a selective catalyst in the metallic state.[3,16] Thus, it is desirable to construct a metallic Pt_1, which is coordinated with other metals, and is capable of selectively catalyzing PDH process.

In this perspective, the solitary Pt site (Pt_1), which is atomically dispersed on the surface of host alloys in the metallic form, is an ideal active center. Three efficient PDH systems catalyzed by metallic Pt_1 sites

implanted in (1) single-atom alloys (SAAs),[16,40] (2) intermetallic compounds,[41] (3) surface-decorated intermetallic compounds,[17,24] and high-entropy intermetallics (HEIs)[42] have been reported in recent years.

1.3.2. Pt–Cu Single-Atom Alloy.

A scaling relationship, or the Sabatier principle, has been recognized as a key principle for determining alkane dehydrogenation activity and selectivity. A lower absorptivity increases product desorption (selectivity) while inhibiting reactant adsorption (activity); thus, the optimal catalyst is often a compromise. In this regard, discovering a catalyst that overcomes this impasse, is highly desirable in order to achieve both high catalytic activity and selectivity.

Single-atom alloys, which are solid-solution alloys composed of an active dopant and an inert host metal with very biased atomic ratios (typically 1 : >50),[43–46] can supply metallic Pt_1 sites.[16,40,47] Gong *et al*. recently reported on the unmatched catalytic performance of a Pt–Cu SAA catalyst in PDH,[16,40] which breaks the scaling relationship. As illustrated in Figure 2, the Pt–Cu SAA exhibited a high ΔE and a moderate C–H activation barrier for propane, implying that in contrast to conventional PtM binary alloys, high catalytic activity (turnover number)

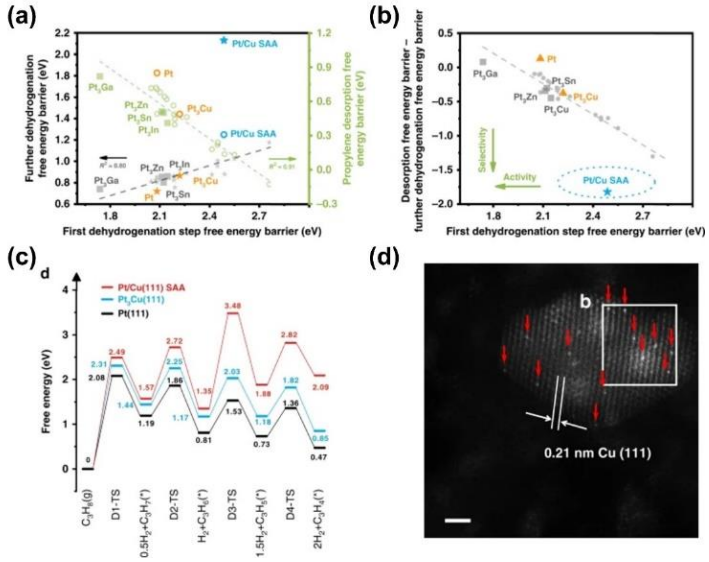

Figure 2. (a) Scaling relationship between first dehydrogenation and propylene desorption barrier/deep dehydrogenation barrier (highest barrier from di-σ propylene to C_3H_4), data for the Pt_3M alloy systems are obtained from ref.[13] (b) Screening of Pt-based bimetallic catalyst for PDH, data form the Pt_3M alloy systems are obtained from ref.[13] (c) Energy profiles of PDH over Pt/Cu SAA, $Pt_3Cu(111)$ and Pt(111). (d) High-angle annular dark-field scanning transmission electron microscopy (HAADF-STEM) images with typical region of the reduced $0.1Pt10Cu/Al_2O_3$ catalyst, showing Pt atoms individually dispersed on Cu(111). Pt atoms are highlighted by red arrows. Scale bar: 1 nm. Reproduced with permission from ref.[16] Copyright © 2018 Springer Nature.

and selectivity can be attained. To validate this theoretical prediction, they produced and characterized Pt–Cu SAA nanoparticles. According to DFT calculations, the Pt–Cu SAA catalyst exhibited high catalytic activity and stability at 520°C with ~90% propylene selectivity in the presence of co-feed H_2 (catalyst lifetime τ = 3640 h, calculated using the first-order deactivation model.[3] Theoretical and experimental results demonstrate the validity of PDH's metallic Pt_1 sites. However, due to insufficient thermal stability, this catalyst was unable to tolerant nanoparticle sintering at elevated temperatures, resulting in a rapid deactivation (τ = 5 h at 600°C), emphasizing the importance nature of host material stability.

1.3.3. PtZn Intermetallic Compound.

Metallic Pt_1 sites can operate as effective active sites in the PDH reaction. However, the alloy phase's thermal stability at elevated temperatures is crucial. Alternatives to overcome this barrier include IMCs, which have highly structured crystal structures and a largely negative formation enthalpy (ΔH_f).[16,17,24,48] While Pt_3M-type IMCs (space group: $Pm\bar{3}m$) are commonly used for PDH, they retain Pt_3 hollow sites on the most stable (111) surface, resulting in an insufficient lifetime by coke formation. As a result, intermetallic phases richer in second-metals should be used to serve Pt_1 sites on the surface of IMCs.

Gong *et al*. recently discovered that Pt_1 in the PtZn IMC (Pt:Zn = 1:1, Space group of $P4/mmm$) functions as an extremely stable active site at elevated operation temperatures (520°C–620°C) (Figure 3).[16] PtZn IMC can stabilize Pt_1 sites in $[PtZn_4]$ ensembles at the most stable (110) plane with the higher electron density of Pt due to the ligand effect of Zn (Figure 4). As a result, the PtZn IMC catalyst demonstrated a long catalyst lifetime (τ = 433 h at 600°C) with high propylene selectivity (>97%), and high resistance against nanoparticle sintering in the presence of co-fed H_2. Although PtZn IMC exhibited anti-sintering properties at high temperatures due to its high thermodynamic stability ($\Delta H_f = -65.0$ kJ mol^{-1}), Zn was liberated slightly during the reaction due to the relatively high vapor pressure of metallic Zn (boiling point: 907°C) as observed in other Zn-containing bimetallic systems.[49,50] Moreover, the PtZn IMC catalyst was rapidly deactivated when H_2 was not co-fed. Therefore, materials that have chemical and physical robustness as well as high selectivity with minimum side reactions are necessary for highly efficient PDH.

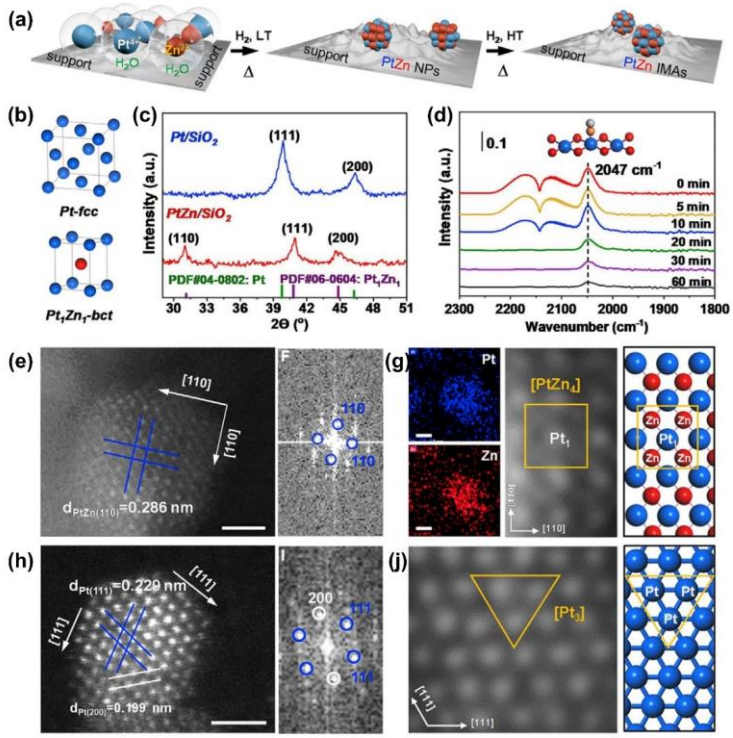

Figure 3. Formation of the Single-Atom Pt_1 sites in PtZn IMAs (a) Schematic illustration of high-temperature H_2 reduction to form ordered PtZn IMAs on SiO_2. (b) Crystal structures of Pt and PtZn IMA (Pt, blue; Zn, red). (c) X-ray diffraction (XRD) patterns of $1Pt/SiO_2$ and $1Pt1.7Zn/SiO_2$. (d) CO-DRIFTS of $0.1Pt0.17Zn/SiO_2$ IMAs. (e) AC-HAADF-STEM images of $1Pt1.7Zn/SiO_2$. The scale bar is 1 nm. (f) FFT image of the PtZn particle in (e). (g) EDS mapping images enlarged AC-HAADF-STM image of $1Pt1.7Zn/SiO_2$ and DFT simulated structure of PtZn(110) (Pt, blue; Zn, red). (The framed rectangular represents the surface $[PtZn_4]$ ensemble, wherein single-atom Pt_1 sites form) (h) AC-HAADF-STEM images of $1Pt/SiO_2$. The scale bar is 1 nm. (i) FFT image of the Pt particle in (h). (j) Enlarged AC-HAADF-STEM image of $1Pt/SiO_2$ and DFT simulated structure of Pt(111) (Pt blue). (The framed triangle represents the $[Pt_3]$ ensemble). Reproduced with permission from ref.[41] Copyright 2021 Elsevier Inc.

1.3.4. Surface Decoration of PtGa Intermetallic Compound.

Another possibility for producing stable Pt_1 is intermetallic PtGa (Pt:Ga = 1:1, space group of $P2_13$).[17] In addition to the high thermal stability ($\Delta H_f = -55.6$ kJ mol^{-1}, boiling point of Ga: 2204°C), PtGa displays a unique surface structure at the most stable (111) plane, where catalytically active Pt_1 and Pt_3 sites are present.[14] While the former is supposed to function as an ideal (selective and stable) active site, the latter may function as ensemble sites, resulting in undesired side reactions. As a result, some additional modifications are required to ensure that only the Pt_1 site functions. As a result of this anticipation, we used a "surface modification strategy" involving a third element to disable the Pt_3 sites selectively, while leaving Pt_1 intact. This was accomplished successfully by depositing a suitable amount of Pb (Pt/Pb =2) as a surface modifier, where Pb was stably deposited on the Pt_3 hollow sites without covering the Pt_1 site (PtGa–Pb). The details of this strategy will be explained in **Chapter 3**.

In addition, using PtGa–Pb and Ca as secondary modifiers, we developed a more improved catalyst based on this innovation. The double-decoration of PtGa by Pb and Ca will be introduced in **Chapter 4** in detail.

1.3.5. High-Entropy Intermetallics.

After the discovery that the decoration of PtGa effectively works in PDH, we applied the strategy of "metallic Pt_1 sites" using different materials, namely, high-entropy intermetallics. The thermally stable Pt_1 sites can also be constructed using HEIs. The combination of the ensemble (site-isolation), ordering, and mixing effects provides outstandingly stable Pt_1 sites without toxic Pb and Pt blocking. The (PtCoCu)(GeGaSn) HEI catalyst had significantly higher catalyst lives than PtGa–Ca–Pb (4146/628 h at 600°C with/without co-feed H_2, respectively), which currently hold the world records in PDH. Please refer to **Chapter 5** in detail.

1.4. Fundamental Aspects of Intermetallic Compounds

1.4.2. Intermetallic Compounds.

Although intermetallic compounds (IMCs) have been used as catalysts since 1970s, the number of publications has significantly increased since 2010.[51] Intermetallic compounds are still hot materials in the catalysis research on alloys nowadays. The major characteristics of intermetallic compounds as catalyst materials are (1) a unique electronic structure, (2) ordered atomic arrangement, (3) different atomic sizes, (4) thermodynamic stability, and (5) expandability (Figure 4). The electronic structure of the main active metal can be drastically modified (1) due to the large difference in the electronegativity and *d*-band structure of the constituent metals. The ordering and steric effects can be exerted only by intermetallic compounds for catalysis, among many kinds of alloys (2 and 3). Due to the largely negative formation enthalpy and covalent bonding character, the alloy phase is highly stable thermodynamically and kinetically (4).

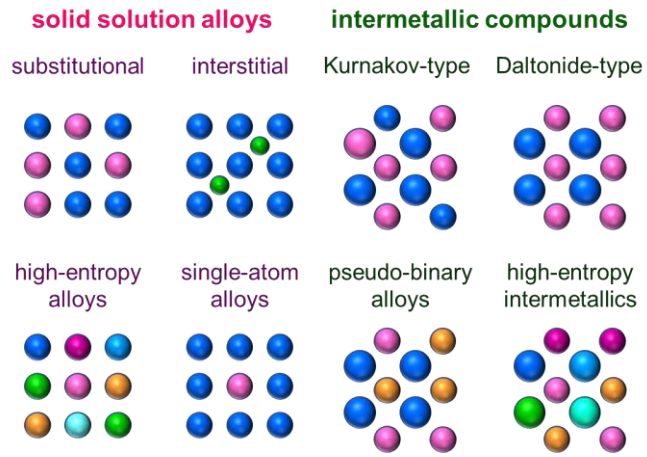

Figure 4. Schematic representation of various alloy structures.

Although the basic concepts for ligand and ensemble effects are similar to that of solid-solution alloys, there are several additional merits and considerations on catalyst design. First, intermetallic compounds generally show a greater extent of ligand and ensemble effects than solid-solution alloys due to the larger difference in electronegativity between the constituent metals and of the inertness of the counterpart metals (mostly early transition and typical metals). Generally, typical metals in intermetallic compounds are not capable of chemical adsorption of hydrogen, hydrocarbons, and carbon monooxide; therefore, the ensemble effects on these adsorbates are very strong. Besides, the ligand effect by typical metals can largely increase the electron density and lower the *d*-band center of noble metals.

1.4.3. Pseudo-Binary Alloys.

Although binary intermetallic compounds have many advantages as catalyst materials, there are also some limitations in the catalyst design, such as the lack of tunability in the composition ratio and expandability of functions. These limitations typically result in volcano-type restriction of the reaction rate and/or activity–selectivity tradeoff, thereby hampering the development of truly efficient and innovative catalytic systems. Pseudo-binary alloys are capable of breaking these limitations.[52–55] One can introduce a third element into the binary system within some composition range without changing the parent crystal structure. The catalytic performance can be optimized tuning the ligand/ensemble effects and/or remarkably enhanced introducing the multifunctional effects.

1.4.4. High-Entropy Intermetallics.

As an extension of pseudo-binary systems, binary intermetallics can be multi-metallized to the corresponding high-entropy materials, namely, high-entropy intermetallics.[42,56–64] The parent binary intermetallics must have significantly negative formation enthalpy (ΔH_f) to overcome disordering driven by mixing entroy (ΔS_{mix}). This material is very new and has only recently begun to attract attention even in the field of metallurgy.[65] The catalytic use of high-entropy intermetallics was first described in 2020, and only ten examples have been reported to date.[42,56–64] The main advantages of high-entropy intermetallics as catalyst materials are (1) site-isolation and ordering, (2) thermal stability, (3) tunability, and (4) multifunctional effect. Therefore, high-entropy intermetallics are upward compatible with pseudo-binary alloys comprising three elements.

1.4.5. Surface Modification of Intermetallic Compounds.

The surface modification of alloys is a powerful strategy for tuning surface catalysis. Ordered surface geometry of IMCs is a promising active site for selective catalysis. However, the crystal structures of IMCs are thermodynamically determined, and only limited composition ratios are allowed for IMCs, restricting the flexible control of the geometric and electronic features. To overcome this challenge, it is imperative to selectively modify the surface of IMCs without changing the bulk structures.

1.5. Aim of This Thesis

Alloying has long been used as a promising methodology to improve the catalytic performance of metallic materials. In recent years, the field of alloy catalysis has made remarkable progress with the emergence of a variety of novel alloy materials and their functions. Importantly, alloy architectures must be precisely controlled to serve the desired surface environments for the target reactions, yet challenging. Alkane dehydrogenation is an important molecular transformation in various application such as in hydrogen production/carriage,[1,2] petroleum industry,[3] and polymer synthesis.[1,2] However, due to its endothermicity, alkane dehydrogenation requires high operation temperatures to obtain sufficient alkene yield, in which severe catalyst deactivation by coking and/or sintering inevitably occurs in short periods. In this context, developing an innovative dehydrogenation catalyst that exhibits high alkene selectivity and catalyst stability even at high operation temperatures is incredibly beneficial. Although numerous efforts have been made to overcome this obstacle, only a few catalysts have been reported to function as stable catalysts. In this thesis, the study discussed below had conducted in order to establish a guideline for the catalyst design for alkane dehydrogenation, providing a better understanding of the catalytic chemistry of alloys. Specifically, in this thesis, two broad approaches have been explored using intermetallic compounds as starting materials, *i.e.*, (i) multimetallization (pseudo-binary alloys and HEIs), (ii) surface modification (geometric and electronic decorations). **Chapter 2** introduces the pseudo-binary alloys for MCH dehydrogenation. **Chapters 3 and 4** shows that the geometric and electronic decorations of intermetallic compounds for efficient PDH catalysis, respectively. **Chapter 5** demonstrates that HEIs functioned as outstandingly efficient PDH catalysts.

Chapter 2 shows that the $Pt_3(Fe_{0.75}Zn_{0.25})$ pseudo binary alloys on SiO_2 exhibited an outstanding catalytic performance in the dehydrogenation of methylcyclohexane. Catalyst design based on a pseudo-binary alloy concept was applied to develop a highly efficient catalytic system for alkane dehydrogenation. A series of Pt-based alloy catalysts supported on silica (Pt_3M/SiO_2, where M = Fe, Co, Cu, Zn, Ga, In, Sn, and Pb) were prepared and tested for the dehydrogenation of methylcyclohexane, which has been an emerging topic in the hydrogen carrier/production application. Nanoparticulate intermetallic Pt_3Fe exhibited high catalytic activity and durability. The Pt_3Fe catalyst was further modified by substituting a part of Fe with a series of metals (M = Co, Ni, Cu, Zn, Ga, In, Sn, and Pb) to form the $Pt_3(Fe_{0.75}M_{0.25})$ pseudo-binary alloy. The partial substitution of Fe with Zn to form $Pt_3(Fe_{0.75}Zn_{0.25})$ resulted in outstandingly high catalytic activity, selectivity, and durability: a 2.7-fold higher turnover frequency (TOF) than that of Pt/SiO_2 (the highest H_2 evolution rate ever reported), >99% toluene selectivity (methane concentration <500 ppm), and long-term durability with >99% MCH conversion for at least 50 h. The mechanistic study based on detailed characterization and theoretical calculations revealed that the Fe enhanced hydrogenation of CH_x species (decoking) and Zn promoted toluene desorption by both ligand and ensemble effects. The adjacency of Pt, Fe, and Zn in at the atomic level allows to construct a multifunctional active site for effective C–H activation, decoking, and toluene desorption.

As well as MCH dehydrogenation, converting propane into propylene *via* PDH is an important catalytic reaction, however, it is highly difficult to obtain a stable catalyst that works even at high reaction temperatures. **Chapter 3** shows that the surface modification of PtGa intermetallic using Pb enables to serve only isolated Pt sites as active sites for the dehydrogenation of propane. Propylene production *via* PDH requires high reaction

temperatures to obtain sufficient propylene yields, which results to prominent catalyst deactivation due to coke formation. Developing highly stable catalysts for PDH without deactivation even at high temperatures is of great interest and benefit for industry. We found that single-atom Pt included in thermally stable intermetallic PtGa works as an ultrastable and selective catalyst for PDH at high temperatures. Intermetallic PtGa displays three-hold-Pt ensembles and single Pt atoms isolated by catalytically inert Ga at the surface, the former of which can be selectively blocked and disabled by Pb deposition. The PtGa–Pb/SiO_2 catalyst exhibits 30% conversion with 99.6% propylene selectivity at 600°C for 96 h without lowering the performance. The single-atom Pt well catalyzes the first and second C–H activation, while effectively inhibits the third one, which minimizes the side reactions to coke and drastically improves the selectivity and stability.

As well as the geometric property, the electronic properties of active site contribute the catalysis. In **Chapter 4**, I further modified the PtGa–Pb/SiO_2 catalyst *via* dispersing Ca species around the nanoparticles. The double decoration of PtGa intermetallics by Pb and Ca, which synergize the geometric and electronic promotion effects on the catalyst stability, respectively. Pb is deposited on the three-fold Pt_3 sites of the PtGa nanoparticles to block them, whereas Ca, which affords an electron-enriched single-atom-like Pt_1 site, is placed around the nanoparticles. Thus, PtGa–Ca–Pb/SiO_2 exhibits an outstandingly high catalytic stability, even at 600°C (k_d = 0.00033 h^{-1}, τ = 3067 h), and almost no deactivation of the catalyst was observed for up to one month for the first time.

In **Chapter 5**, an another approach to isolate the active sites was explored, namely, high-entropy intermetallics (HEIs). Pt–Pt ensembles, which cause side reactions, are entirely diluted by the component inert metals in PtGe-type HEI. The resultant HEI: (PtCoCu)(GeGeSn)/Ca–SiO_2 exhibited an outstandingly high catalytic stability, even at 600°C (k_d^{-1} = τ = 4146 h = 173 d), and almost no deactivation of the catalyst was observed two months for the first time. Detailed experimental studies and theoretical calculations demonstrated that the combination of the site-isolation and entropy effects upon multi-metallization of PtGe drastically enhanced the desorption of propylene and the thermal stability, eventually suppressing the side reactions even at high reaction temperatures.

1.6. Concluding Remarks

In conclusion, I have successfully developed the innovative alloy catalysts that exhibited excellent catalytic performance in the dehydrogenation of methylcyclohexane and propane. The insights obtained in the thesis provide direction for the development of truly efficient catalysts for alkane dehydrogenation and other important reactions.

Reference

1 E. Gianotti, M. Taillades-Jacquin, J. Rozière and D. J. Jones, *ACS Catal.*, 2018, **8**, 4660–4680.

2 R. B. Biniwale, S. Rayalu, S. Devotta and M. Ichikawa, *Int. J. Hydrogen Energy*, 2008, **33**, 360–365.

3 J. J. H. B. Sattler, J. Ruiz-Martinez, E. Santillan-Jimenez and B. M. Weckhuysen, *Chem. Rev.*, 2014, **114**, 10613–10653.

4 J. C. Bricker, *Top. Catal.*, 2012, **55**, 1309–1314.

5 Z. P. Hu, D. Yang, Z. Wang and Z. Y. Yuan, *Chinese J. Catal.*, 2019, **40**, 1233–1254.

6 S. Chen, C. Pei, G. Sun, Z.-J. Zhao and J. Gong, *Accounts Mater. Res.*, 2020, **1**, 30–40.

7 G. Wang, X. Zhu and C. Li, *Chem. Rec.*, 2020, **20**, 604–616.

8 S. Liu, B. Zhang and G. Liu, *React. Chem. Eng.*

9 S. Chen, X. Chang, G. Sun, T. Zhang, Y. Xu, Y. Wang, C. Pei and J. Gong, *Chem. Soc. Rev.*, 2021, **50**, 3315–3354.

10 S. Furukawa, T. Komatsu and K. I. Shimizu, *J. Mater. Chem. A*, 2020, **8**, 15620–15645.

11 X. Chen, Z. Jia, F. Huang, J. Diao and H. Liu, *Chem. Commun.*, 2021, **57**, 11591–11603.

12 L. Nykänen and K. Honkala, *J. Phys. Chem. C*, 2011, **115**, 9578–9586.

13 S. Zha, G. Sun, T. Wu, J. Zhao, Z. J. Zhao and J. Gong, *Chem. Sci.*, 2018, **9**, 3925–3931.

14 Z. J. Zhao, C. C. Chiu and J. Gong, *Chem. Sci.*, 2015, **6**, 4403–4425.

15 M. L. Yang, Y. A. Zhu, X. G. Zhou, Z. J. Sui and D. Chen, *ACS Catal.*, 2012, **2**, 1247–1258.

16 G. Sun, Z. J. Zhao, R. Mu, S. Zha, L. Li, S. Chen, K. Zang, J. Luo, Z. Li, S. C. Purdy, A. J. Kropf, J. T. Miller, L. Zeng and J. Gong, *Nat. Commun.*, 2018, **9**, 4454.

17 Y. Nakaya, J. Hirayama, S. Yamazoe, K. Shimizu and S. Furukawa, *Nat. Commun.*, 2020, **11**, 2838.

18 R. J. Meyer, Q. Zhang, A. Kryczka, C. Gomez and R. Todorovic, *ACS Catal.*, 2018, **8**, 566–570.

19 M. L. Yang, Y. A. Zhu, C. Fan, Z. J. Sui, D. Chen and X. G. Zhou, *Phys. Chem. Chem. Phys.*, 2011, **13**, 3257–3267.

20 L. Nykänen and K. Honkala, *ACS Catal.*, 2013, **3**, 3026–3030.

21 M. L. Yang, J. Zhu, Y. A. Zhu, Z. J. Sui, Y. Da Yu, X. G. Zhou and D. Chen, *J. Mol. Catal. A Chem.*, 2014, **395**, 329–336.

22 F. Jiang, L. Zeng, S. Li, G. Liu, S. Wang and J. Gong, *ACS Catal.*, 2015, **5**, 438–447.

23 J. Liu, Y. Yue, H. Liu, Z. Da, C. Liu, A. Ma, J. Rong, D. Su, X. Bao and H. Zheng, *ACS Catal.*, 2017, **7**, 3349–3355.

24 Y. Nakaya, F. Xing, H. Ham, K. Shimizu and S. Furukawa, *Angew. Chem. Int. Ed.*, 2021, **60**, 19715–19719.

25 W. Zhang, H. Ma, H. Wang, J. Jiang, Z. Sui, Y.-A. Zhu, D. Chen and X. Zhou, *Catal. Sci. Technol.*, 2021, **11**, 7840–7843.

26 W. Cai, R. Mu, S. Zha, G. Sun, S. Chen, Z. J. Zhao, H. Li, H. Tian, Y. Tang, F. Tao, L. Zeng and J. Gong, *Sci. Adv.*, 2018, **4**, 1–9.

27 Z. Wu, B. C. Bukowski, Z. Li, C. Milligan, L. Zhou, T. Ma, Y. Wu, Y. Ren, F. H. Ribeiro, W. N. Delgass, J. Greeley, G. Zhang and J. T. Miller, *J. Am. Chem. Soc.*, 2018, **140**, 14870–14877.

28 B. Zhang, L. Zheng, Z. Zhai, G. Li and G. Liu, *ACS Appl. Mater. Interfaces*, 2021, **13**, 16259–16266.
29 X. Yang, A. Wang, B. Qiao and J. U. N. Li, *Acc. Chem. Res.*, 2013, **46**, 1740–1748.
30 H. Jeong, S. Shin and H. Lee, *ACS Nano*, 2020, **14**, 14355–14374.
31 S. Ji, Y. Chen, X. Wang, Z. Zhang, D. Wang and Y. Li, *Chem. Rev.*, 2020, **120**, 11900–11955.
32 B. Singh, V. Sharma, R. P. Gaikwad, P. Fornasiero, R. Zbořil and M. B. Gawande, *Small*, 2021, **17**, 1–27.
33 A. Wang, J. Li and T. Zhang, *Nat. Rev. Chem.*, 2018, **2**, 65–81.
34 M. Peng, C. Dong, R. Gao, D. Xiao, H. Liu and D. Ma, *ACS Cent. Sci.*, 2021, **7**, 262–273.
35 H. Jeong, O. Kwon, B. S. Kim, J. Bae, S. Shin, H. E. Kim, J. Kim and H. Lee, *Nat. Catal.*, 2020, **3**, 368–375.
36 W. Zhang, H. Wang, J. Jiang, Z. Sui, Y. Zhu, D. Chen and X. Zhou, *ACS Catal.*, 2020, **10**, 12932–12942.
37 L. Liu, D. M. Meira, R. Arenal, P. Concepcion, A. V. Puga and A. Corma, *ACS Catal.*, 2019, **9**, 10626–10639.
38 J. Zhu, M. L. Yang, Y. Yu, Y. A. Zhu, Z. J. Sui, X. G. Zhou, A. Holmen and D. Chen, *ACS Catal.*, 2015, **5**, 6310–6319.
39 H. Xiong, S. Lin, J. Goetze, P. Pletcher, H. Guo, L. Kovarik, K. Artyushkova, B. M. Weckhuysen and A. K. Datye, *Angew. Chem. Int. Ed.*, 2017, **56**, 8986–8991.
40 S. Sun, G. Sun, C. Pei, Z. J. Zhao and J. Gong, *J. Phys. Chem. C*, 2021, **125**, 18708–18716.
41 S. Chen, Z. Zhao, S. Chen, Z. Zhao, R. Mu, X. Chang, J. Luo, S. C. Purdy, A. J. Kropf, G. Sun, C. Pei, J. T. Miller, X. Zhou, E. Vovk, Y. Yang and J. Gong, *Chem*, 2021, **7**, 1–19.
42 Y. Nakaya, E. Hayashida, H. Asakura, S. Takakusagi, S. Yasumura, K. Shimizu and S. Furukawa, *J. Am. Chem. Soc.*, 2022, **144**, 15944–15953.
43 T. Zhang, A. G. Walsh, J. Yu and P. Zhang, *Chem. Soc. Rev.*, 2021, **50**, 569–588.
44 F. Qin and W. Chen, *Chem. Commun.*, 2021, **57**, 2710–2723.
45 R. T. Hannagan, G. Giannakakis, M. Flytzani-Stephanopoulos and E. C. H. Sykes, *Chem. Rev.*, 2020, **120**, 12044–12088.
46 G. Giannakakis, M. Flytzani-Stephanopoulos and E. C. H. Sykes, *Acc. Chem. Res.*, 2019, **52**, 237–247.
47 M. D. Marcinkowski, M. T. Darby, J. Liu, J. M. Wimble, F. R. Lucci, S. Lee, A. Michaelides, M. Flytzani-Stephanopoulos, M. Stamatakis and E. C. H. Sykes, *Nat. Chem.*, 2018, **10**, 325–332.
48 E. C. Wegener, B. C. Bukowski, D. Yang, Z. Wu, A. J. Kropf, W. N. Delgass, J. Greeley, G. Zhang and J. T. Miller, *ChemCatChem*, 2020, **12**, 1325–1333.
49 L. Xie, Y. Chai, L. Sun, W. Dai, G. Wu, N. Guan and L. Li, *J. Energy Chem.*, 2021, **57**, 92–98.
50 S. Furukawa, R. Suzuki and T. Komatsu, *ACS Catal.*, 2016, **6**, 5946–5953.
51 S. Furukawa and T. Komatsu, *ACS Catal.*, 2017, **7**, 735–765.
52 Y. Nakaya, M. Miyazaki, S. Yamazoe, K. Shimizu and S. Furukawa, *ACS Catal.*, 2020, **10**, 5163–5172.
53 S. Furukawa, R. Suzuki, T. Komatsu, J. Jeon, K. ichi Kon, T. Toyao, K. ichi Shimizu, S. Furukawa, Y. Matsunami, I. Hamada, Y. Hashimoto, Y. Sato and T. Komatsu, *ACS Catal.*, 2018, **8**, 8177–8181.

54 J. Jeon, K. ichi Kon, T. Toyao, K. ichi Shimizu, S. Furukawa, R. Suzuki, T. Komatsu, Y. Matsunami, I. Hamada, Y. Hashimoto, Y. Sato and T. Komatsu, *ACS Catal.*, 2018, **8**, 8177–8181.

55 F. Xing, Y. Nakaya, S. Yasumura, K. ichi Shimizu and S. Furukawa, *Nat. Catal.*, 2022, **5**, 55–65.

56 J. Ma, F. Xing, Y. Nakaya, K. ichi Shimizu and S. Furukawa, *Angew. Chem. Int. Ed.*, 2022, e202200889.

57 F. Xing, J. Ma, K. ichi Shimizu and S. Furukawa, *Nat. Commun.*, 2022, **13**, 5065.

58 G. Feng, F. Ning, Y. Pan, T. Chen, J. Song, Y. Wang, R. Zou, D. Su and D. Xia, *J. Am. Chem. Soc.*, 2023, **145**, 11140–11150.

59 Z. Jia, T. Yang, L. Sun, Y. Zhao, W. Li, J. Luan, F. Lyu, L. C. Zhang, J. J. Kruzic, J. J. Kai, J. C. Huang, J. Lu and C. T. Liu, *Adv. Mater.*, 2020, **32**, 2000385.

60 G. Zhu, Y. Jiang, H. Yang, H. Wang, Y. Fang, L. Wang, M. Xie, P. Qiu and W. Luo, *Adv. Mater.*, 2022, **34**, 2110128.

61 W. Chen, S. Luo, M. Sun, X. Wu, Y. Zhou, Y. Liao, M. Tang, X. Fan, B. Huang and Z. Quan, *Adv. Mater.*, 2022, **34**, 2206276.

62 D. Wang, Z. Chen, Y. Wu, Y. Huang, L. Tao, J. Chen, C. Dong, C. V. Singh and S. Wang, *SmartMat*, 2023, **4**, 1–11.

63 Y. Wang, N. Gong, H. Liu, W. Ma, K. Hippalgaonkar and Z. Liu, *Adv. Mater.*, 2023, 2302067.

64 M. Cui, C. Yang, S. Hwang, M. Yang, S. Overa, Q. Dong, Y. Yao, A. H. Brozena, D. A. Cullen, M. Chi, T. F. Blum, D. Morris, Z. Finfrock, X. Wang, P. Zhang, V. G. Goncharov, X. Guo, J. Luo, Y. Mo, F. Jiao and L. Hu, *Sci. Adv.*, 2022, **8**, eabm4322.

65 G. Firstova, A. Timoshevski, T. Kosorukova, Y. Koval, Y. Matviychuk and P. Verhovlyuk, *MATEC Web Conf.*, 2015, **33**, 0–3.

Chapter 2

Platinum–Iron–Zinc Pseudo-Binary Alloy as a Highly Efficient Catalyst for Methylcyclohexane Dehydrogenation

2.1. Introduction

The dehydrogenation of alkanes to alkenes is an important molecular transformation in various application such as in petroleum industry[1], polymer synthesis,[1,2] and hydrogen production/carriage.[3,4] Activation of the robust C–H bond, limited equilibrium conversion, and high energy consumption are the characteristic of alkane dehydrogenation, which makes efficient alkane conversion a challenging but attracting task in pure and applied chemistry.[1,5–7] The conversion of light alkanes to the corresponding alkenes (*e.g.*, ethylene,[8,9] propylene,[1,7,8,9] isobutene[10]) have been studied for a long time to achieve better production of feedstock in chemical industry. Several catalytic systems have been developed as industrial processes for this conversion.[1] However, the dehydrogenation of cycloalkanes to aromatics, (*e.g.*, benzene, toluene, and naphthalene) is an emerging topic and a promising platform for the hydrogen production/carriage application because of the high hydrogen content, low toxicity, and/or availability in existing petroleum infrastructure.[3,4] Pt-based catalysts[3,4,11,12] have been typically used as well as for the light alkane conversion[14–18] owing to the greater capability of C–H bond activation and lower affinity to C–C cleavage compared with those of other transition metals.[1,5] However, the performance of the current catalytic system should be considerably improved to save the cost of hydrogen to realize the hydrogen energy society. Ideally, the catalyst should be highly active, selective, and durable to achieve sufficiently high production rate, ultra-high purity, and long-term stable supply of hydrogen, respectively. To overcome this challenge, an innovative catalyst design for cycloalkane dehydrogenation is needed that enables considerable enhancement in catalytic activity, selectivity, and durability.

The alloying of an active metal with another metal has been employed as a conventional approach to modify the catalytic property of the main active metal. Active Pt is typically diluted with a less active or inactive second metal to inhibit undesired side reactions such as C–C cleavage for selectivity enhancement in alkane dehydrogenation, where the catalytic activity is compromised. This trade-off in the activity-selectivity relationship has long been a dilemma in catalyst design based on alloys. A game-changing technology to break this limitation is necessary to develop an active, selective, and durable catalyst for alkane dehydrogenation. Recently, we developed a catalyst design based on trimetallic alloys, *i.e.*, pseudo-binary alloys.[18] A part of the second metal constituting a bimetallic ordered alloy is substituted by a third metal without changing the parent crystal structure. For instance, the partial substitution of B in intermetallic A_mM_n with C yields $A_m(B_{1-x}C_x)_n$. This catalyst design allows the flexible modification of the metal composition ratio and the resulting catalytic performances and also provides multifunctional properties on the active site owing to the presence of three different elements.[18]

In this study, we applied this catalyst design concept, which is based on the pseudo-binary alloys, to develop a highly efficient catalytic system for cycloalkane dehydrogenation. A series of nanoparticulate Pt_3M intermetallic compounds supported on silica (Pt_3M/SiO_2, where M = Fe, Co, Ni, Cu, Zn, Ga, In, Sn, and Pb) were prepared with high phase-purities and examined their catalytic performance in MCH, which is one of the most promising hydrogen carriers. The optimized bimetallic combination was expanded to trimetallic systems along with the pseudo-binary alloy concept [$Pt_3(Fe_{1-x}M_x)/SiO_2$: M = Co, Ni, Cu, Zn, Ga, In, Sn, and Pb] to achieve further improvement in the catalytic performance. The obtained results were analyzed using several characterization techniques and DFT) calculations to clarify the role of each metal element on the great

enhancement. Herein, we report not only a highly active, selective, and durable catalyst for alkane dehydrogenation but also deep insights to construct multifunctional active sites.

2.2. Experimental

2.2.1. Catalyst Preparation.

Pt-based bimetallic catalysts were prepared by the pore-filling co-impregnation method using SiO_2 as the support (Pt_3M/SiO_2, where M = Fe, Co, Cu, Zn, Ga, In, Sn, and Pb). $Fe(NO_3)_3 \cdot 9H_2O$ (Sigma-Aldrich, 98%), $Co(NO_3)_3 \cdot 6H_2O$ (Wako, 98%), $Cu(NO_3)_2 \cdot 3H_2O$ (Sigma-Aldrich, 99%), $Zn(NO_3)_2 \cdot 6H_2O$ (Kanto, 99%), $Ga(NO_3)_3 \cdot nH_2O$ (n = 7–9) (Wako, 99.9%), $In(NO_3)_3 \cdot 8.8H_2O$ (Kanto, 99.9%, the number of coordinated water was analyzed by ICP-AES), $SnCl_2$ (Wako, 99%), and $Pb(NO_3)_2$ (Wako, 99.5%) were used as the second or third metal precursors and Pt loading was adjusted at 3 wt%. The metal precursors were precisely weighted and dissolved together in deionized water so that Pt/M or Pt/(Fe+M) atomic ratio was 3. For Pt_3M/SiO_2, the mixed aqueous solution of $Pt(NH_3)_2(NO_3)_2$ (Furuya Metal, Pt 5wt% in HNO_3 solution) and second metal was added dropwise to ground dried silica gel (CARiACT G–6, Fuji Silysia, S_{BET} = *ca.* 500 $m^2\ g^{-1}$) so that the solutions just filled the pores of the silica gel (volume of solution: 1.6 mL per gram of silica). The mixtures were sealed by a piece of plastic film and kept overnight at room temperature, followed by freeze-drying in vacuum at 0°C and further drying in an oven at 90°C overnight. The resulting powder was calcined at 400°C in dry air for 1 h and reduced under flowing H_2 (0.1 MPa, 50 mL min^{-1}) at 700–900°C for 1 h. The reduction temperature for each catalyst was as follows: 700°C for Pt_3Fe, Pt_3Cu, Pt_3In, Pt_3Sn and Pt_3Pb; 800°C for Pt_3Co; 900°C for Pt_3Ga. The reduction temperature was determined so that the second metal was completely reduced. After the reduction, the catalysts except Pt/SiO_2 were annealed under flowing H_2 (0.1 MPa, 50 mL min^{-1}) at 400°C for 2 h to enhance alloying without further sintering. Ramping rate was set to 20°C/min for each thermal treatment.

The corresponding trimetallic catalysts were also prepared using a similar method [$Pt_3(Fe_{0.75}M_{0.25})/SiO_2$, where M = Co, Ni, Cu, Zn, Ga, In, Sn, and Pb; Pt: 3 wt%]. $Co(NO_3)_3 \cdot 6H_2O$, $Ni(NO_3)_2 \cdot 6H_2O$ (Wako, 98%), $Cu(NO_3)_2 \cdot 3H_2O$, $Zn(NO_3)_2 \cdot 6H_2O$, $Ga(NO_3)_3 \cdot nH_2O$ (n = 7–9), $In(NO_3)_3 \cdot 8.8H_2O$, $SnCl_2$ and $Pb(NO_3)_2 \cdot 6H_2O$ were used as third metal precursors and the reduction under flowing H_2 was done at 700°C for 1 h. The actual metal ratios on some prepared catalysts were measured by X-ray fluorescence spectroscopy: for instance, for Pt_3Fe/SiO_2, Pt:Fe ratio was 73.2 : 26.8.

2.2.2. Catalytic Reactions.

MCH dehydrogenation was carried out in a fixed-bed continuous flow system using a Pyrex glass reactor (internal diameter: 8 mm) under an atmospheric pressure. A total of 10 mg of catalysts diluted with quartz sand (a total of 1.5 g) were charged in the reactor. Before the catalytic run, the catalyst was reduced under flowing H_2 at 300, 350, or 400°C for 30 min, followed by the He purge. The reaction was started at the same temperature by feeding a reactant gas mixture; C_7H_{14} : He = 1.55 : 23.45, a total of 25 mL min^{-1} under atmospheric pressure. The equilibrium conversion of MCH was almost 100% under these reaction conditions. For all the Pt-based catalysts, toluene selectivity was approximately 100% with negligible formation of by-product benzene and methane. The product gas was analyzed using a thermal conductivity detector (TCD) gas chromatograph (Shimadzu GC–8A with a column of Unipak S, GL Science) and flame ionization detector-gas chromatograph (Shimadzu GC–14B with a column of PoraBOND Q). For the evaluation of TOF and apparent activation energy, H_2 was co-fed in the reactant gas mixture (C_7H_{14} : H_2 : He = 1.55 : 5: 18.45, a total of 25 mL min^{-1}) to promote coke removal and suppress catalyst deactivation. TOF was calculated as an initial conversion rate of MCH (mmol/s, before deactivation, if any) per the number of exposed Pt atoms measured by CO chemisorption (mmol). Using some Pt-based catalysts, we confirmed that the addition of H_2 does not have strong influence on TOF: reaction orders of H_2 pressure on TOF were 0.25, −0.04, −0.05 and 0.07 for Pt/SiO_2, Pt_3Fe/SiO_2, Pt_3Sn/SiO_2 and Pt_3In/SiO_2, respectively. To obtain apparent activation energy, the conversion rates of MCH were measured at 280°C, 290°C, 300°C, 310°C, 320°C in a stepwise manner. Therefore, it is difficult to clarify the influence of H_2 on apparent activation energy, because the reaction rates in the absence of H_2 cannot be properly evaluated due to deactivation occurring during the change in temperature.

2.2.3. Characterization.

XRD patterns of the prepared catalysts were acquired by a MiniFlex 700+D/teX Ultra using a Cu Kα X–ray source. Synchrotron XRD measurement was performed for the best catalyst with the wavelength of 0.5 Å (25 keV) at the BL02B2 beamline of SPring-8, Japan Synchrotron Radiation Research Institute (JASRI).

HAADF-STEM was conducted using an FEI Titan G2 microscope equipped with an energy-dispersive X-ray (EDX) analyzer. For the observed nanoparticles in a TEM image, the volume averaged particle size was used.

Pt dispersion of the catalysts was estimated by CO-pulse chemisorption under a dynamic condition at room temperature. Prior to chemisorption, the as-prepared catalyst (after calcination and reduction) (50 mg) was reduced in 40 mL min^{-1} of 5% H_2/Ar (40 mL min^{-1}) at 300°C for 30 min, then cooled to room temperature under flowing He (40 mL min^{-1}) to remove chemisorbed hydrogen. A pulse of 10% CO/He was introduced into the reactor and CO passed thought the catalyst bed was quantified downstream by the TCD detector. The amount of chemisorbed CO was estimated using an assumption of 1:1 chemisorption to Pt atom. According to the literature reporting CO adsorption on Pt–Cu and Pt–Co alloys,[19] CO did not adsorb on Cu and Co sites, but exclusively adsorbed on Pt sites at room temperature. Therefore, in this study, we did not consider CO adsorption on Cu and Co.

X-ray photoelectron spectroscopy (XPS) analysis for the catalysts was carried out by using a JEOL JPS-9010MC (Mg-Kα irradiation) spectrometer. The as-prepared catalysts (after calcination and reduction) were

reduced in a Pyrex reactor under following H_2 (0.1 MPa, 20 mL min^{-1}) at 400°C for 30 min. The sample was transferred into the spectrometer in air. Prior to the measurement, the sample were sputtered by Ar^+ ion to remove the surface region oxidized by air (voltage: 500 V, rate: 20%, time: 1 s, etching depth: ca. 2.5 Å). Binding energies were calibrated with the Si 2p emission of SiO_2 as 103.9 eV.

The amount of coke deposited on spent catalysts after dehydrogenation (400°C for 150 min, catalyst: 30 mg) was quantified by temperature-programmed oxidation (TPO). A total of 25 mg of the spent catalyst was loaded into a quartz tube reactor. Before the TPO experiment, the catalyst was first heated to 150°C under flowing He (40 mL min^{-1}), kept at the same temperature for 30 min, and then cooled to room temperature. After cooling, the catalyst was heated from room temperature to 900°C with a ramping rate of 5 °C/min under flowing 50% O_2/He (40 mL min^{-1}) and kept at 900°C for 10 min. The outlet gas was analyzed by mass spectrometry.

X-ray absorption fine structure (XAFS) measurements of the catalysts were performed at BL01B1 beamline of SPring-8, JASRI. A Si(111) double-crystal was used as a monochromator. The spectra were recorded at the Pt L_{III}-, Fe K-, and Zn K-edges in transmission (for Pt) and fluorescence (for Fe and Zn) modes at room temperature. First, the catalyst was pressed into a pellet (diameter: 13 mm) and reduced under flowing H_2 at 700°C for 0.5 h. Then, the reduced sample was then transferred into an Ar glove box (O_2: < 0.1 ppm) without exposing to air and sealed in a plastic bag (Barrier Nylon) with an ISO A500-HS oxygen absorber (Fe powder). The obtained XAFS spectra were analyzed using Athena and Artemis software ver. 0.9.25 included in the Demeter package.[20] The k^3-weighted extended XAFS (EXAFS) oscillation was Fourier-transformed in the k range of 3−15 $Å^{-1}$, 3−11 $Å^{-1}$, and 3−11 $Å^{-1}$ for Pt L_{III}-, Fe K-, and Zn K-edges, respectively. Curve-fitting was performed using the back Fourier-transforms of the coordination peaks ranging between 1.5−3.5 Å, 1.0−3.0 Å, and 1.4−3.5 Å for Pt L_{III}-, Fe K-, and Zn K-edges, respectively. The back-scattering amplitude and phase shift functions were calculated by FEFF8.[21] R-factor (R^2) for curve-fitting was defined as follows: $R^2 = \Sigma_i\{k^3\chi_i^{exp}(k)-k^3\chi_i^{fit}(k)\}^2/\Sigma_i\{k^3\chi_i^{exp}(k)\}^2$.

2.2.4. Computational Details.

Periodic DFT calculations for surface reactions were performed using the CASTEP code with Vanderbilt-type ultrasoft pseudopotentials and a Perdew−Burke−Ernzerhof exchange−correlation functional based on the generalized gradient approximation. The plane-wave basis set was truncated at the kinetic energy of 370 eV. A Fermi smearing of 0.1 eV was utilized. In this study, we chose the Pt(111) and $Pt_3M(111)$ planes as the most stable surfaces. Dispersion correlations were considered using the OBS method. The reciprocal space was sampled using a k-point mesh with a spacing of 0.04 $Å^{-1}$, as generated by the Monkhorst−Pack scheme. Geometry optimizations and transition state (TS) searches were performed on supercell structures using periodic boundary conditions. The surfaces were modeled using metallic slabs with a thickness of six atomic layers with 13 Å and 10 Å of vacuum spacing for the adsorption of toluene on $Pt_3M(111)$ surfaces and the activation energy of carbon hydrogenation on $Pt_3M(111)$ surfaces, respectively. For the calculation of toluene adsorption, the unit cells were (4 × 4) for Pt(111) and (2 × 2) for $Pt_3M(111)$, (1 × 1) for $Pt_3(Fe_{0.75}Zn_{0.25})(111)$. For the calculation of carbon hydrogenation, the unit cells were (2 × 2) for Pt(111) and (1 × 1) for $Pt_3M(111)$ and $Pt_3(Fe_{0.75}Zn_{0.25})(111)$. The convergence criteria for structure optimization and energy calculation were set to the (a) self-consistent field tolerance of 1.0×10^{-6} eV per atom, (b) energy tolerance of 1.0×10^{-5} eV per atom, (c) maximum force tolerance of 0.05 eV $Å^{-1}$, and (d) maximum displacement tolerance of 1.0×10^{-3} Å.

The adsorption energy of toluene was defined as follows: $E_{ad} = E_{tol/sl} - E_{sl} - E_{tol}$, where $E_{tol/sl}$ is the energy of the slab together with toluene, E_{tol} is the total energy of free toluene, and E_{sl} is the total energy of the bare slab. In principle, adsorption of saturated hydrocarbon like MCH is of physisorption, where van der Waals interaction dominates adsorption energy. Because van der Waals interaction does not differ so much depending on surface, we did not focus on the adsorption energy of MCH.

Decoking ability was also evaluated by comparing the energy barriers of stepwise CH_x (x = 0-3) hydrogenation from an adsorbed C atom to CH_4 for each surface, where CH_x species were regarded as coke precursors. The TS search was performed using the complete linear synchronous transit/quadratic synchronous transit (LST/QST) method. An LST maximization was performed, followed by energy minimization in the directions conjugating to the reaction pathway. The approximated TS was used to perform QST maximization with conjugate gradient minimization refinements. This cycle was repeated until a stationary point was found. Convergence criteria for the TS calculations were set to root-mean-square forces on an atom tolerance of 0.10 eV $Å^{-1}$.

2.3. Results

2.3.1. Bimetallic Systems.

A series of Pt-based bimetallic intermetallic catalysts supported on silica (Pt_3M/SiO_2, where M = Fe, Co, Cu, Zn, Ga In, Sn, and Pb) were prepared by the co-impregnation method using freeze-drying. To identify the resulting bimetallic phases, Pt_3M /SiO_2 were analyzed by powder XRD. For most catalysts except Pt–Ga and Pt–Pb, 111 and 200 diffractions assignable to the desired 3:1 alloy or intermetallic phases were observed with high phase purities. Because the diffraction peaks were very broad, we could not clearly observe the 110 diffraction for most catalysts, which appears when the ordered Pt_3M ($L1_2$-type) structure is formed. However, for Pt_3Fe/SiO_2, the 110 diffraction could be observed at 32.7° when the catalyst was annealed at 900°C. Generally, ordered structures tend to convert to disordered structure at higher temperatures[22] because of the increase in entropy term ($\Delta G = \Delta H - T\Delta S$: ΔS is positive for disordering). Therefore, considering that the ordered Pt_3Fe structure was retained at 900°C, the as-prepared Pt_3Fe likely has the ordered structure. The Pt dispersions estimated by CO pulse chemisorption revealed that the Pt dispersion ranged typically from 20% to 30%. Figures 5a and b show the representative HAADF-STEM image of Pt_3Fe/SiO_2 and the size distribution of nanoparticles, respectively. There is a narrow particle size distribution of small and uniform nanoparticles. The particle sizes ranged from 1 nm to 4 nm with a volume weighted average of 2.6 nm. The elemental maps of Pt and Fe that were acquired using the EDX analysis of this field revealed that the nanoparticles consisted of Pt and Fe (Figures 5c and d).

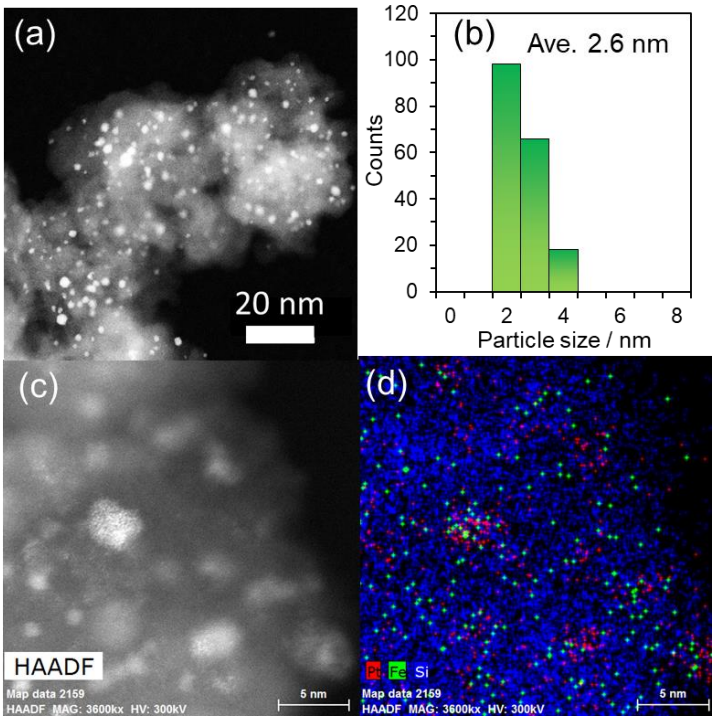

Figure 5. (a) High angle annular dark field scanning transmission electron microscopy (HAADF-STEM) image of Pt_3Fe/SiO_2 (Pt loading was 3 wt%) and (b) the size distribution of nanoparticles. (c) HAADF-STEM image of Pt_3Fe/SiO_2 (Pt loading was 3 wt%). (d) Elemental maps of the Pt + Fe overlayer obtained using EDX.

The synthesized Pt-based bimetallic catalysts were tested in MCH dehydrogenation. The reaction temperature was set to 300°C to compare both the catalytic activity and stability. Figures 6a and b show the change in MCH conversion for each catalyst. Toluene selectivity was approximately 100% for all the Pt-based catalysts with negligible formation of by-product benzene and methane. As represented by Pt/SiO_2, the activities of Pt-based catalysts were gradually decreased probably owing to coking. Conversely, some Pt_3M/SiO_2 catalysts (M = Fe, Sn, In, and Pb) exhibited good durability under MCH dehydrogenation. A similar trend was also observed in a much harsher condition at 400°C, where Pt_3Fe still showed the best durability. The TOF of durable catalysts (Pt_3M/SiO_2: M = Fe, Sn, In, Pb) catalysts was compared to that of Pt/SiO_2, as shown in Figure 6c. TOF differed considerably depending on the second metal (Pt_3Fe >> Pt_3In >> Pt_3Sn > Pt_3Pb). This trend was roughly consistent with that of apparent activation energy estimated by Arrhenius-type plot (Figure 6d: Pt_3Fe > Pt_3Sn ~ Pt_3In > Pt_3Pb). Thus, the formation of intermetallic phases drastically changed the catalytic activity and durability in MCH dehydrogenation. Note that Pt_3Fe exhibited not only the highest TOF (twice higher than that of Pt) and good durability but also the highest MCH conversion owing to the highest Pt dispersion. In the dehydrogenation of alkanes, non-noble metals typically show much lower catalytic activity than noble metals, and Pt has been extensively studied.[1] Therefore, the activities of Pt-free catalysts are expected to show very low catalytic activity.

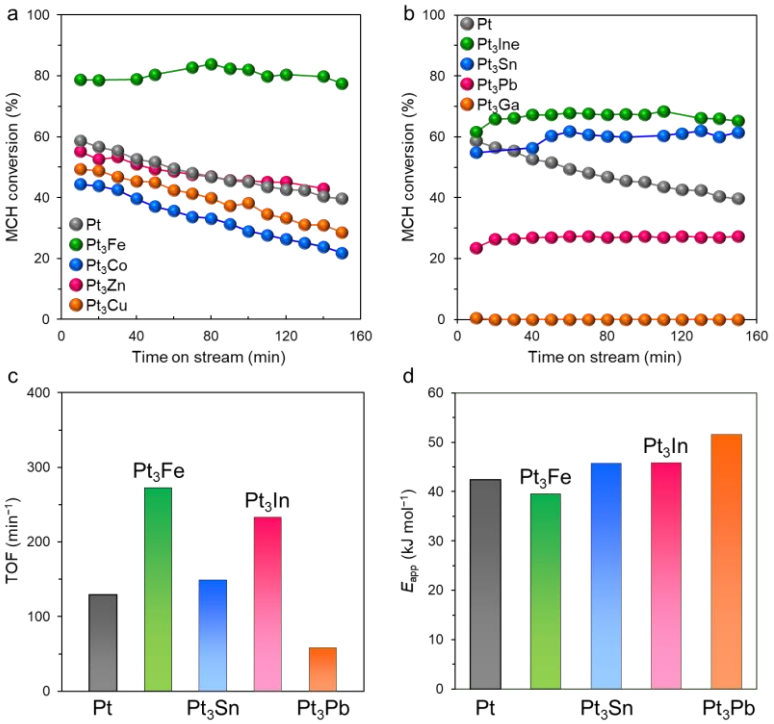

Figure 6. (a), (b) Time on stream of MCH conversion on silica-supported Pt-based catalysts at 300°C. (c) TOF on silica-supported Pt-based catalysts at 300°C. Apparent activation energies of methylcyclohexane dehydrogenation over silica-supported Pt-based catalysts obtained by Arrhenius-type plots.

2.3.2. Trimetallic Systems.

The aforementioned catalyst survey revealed that Pt_3Fe was the most suitable bimetallic combination for catalytic activity and durability for MCH dehydrogenation. However, a further improvement in the long-term stability is required for the practical use application. Therefore, we focused on a catalyst design based on a pseudo-binary alloy structure of $Pt_3(Fe_{1-x}M_x)$ using a third metal element M (Scheme 1) to make further modification in the catalytic performance. Here, the second metal Fe is partially substituted by a third metal with any Fe/M atomic ratio without changing the $L1_2$ crystal structure of the parent Pt_3Fe phase (space group: $Pm\bar{3}m$). The fundamental factors determining the catalytic performance [*e.g.*, the electronic state of Pt and geometric parameter (lattice constant)] can be tuned upon the Fe-M substitution. Moreover, an additional property can be provided by the third element M possessing a unique character, which allows to develop a multifunctional active site to achieve better performance.

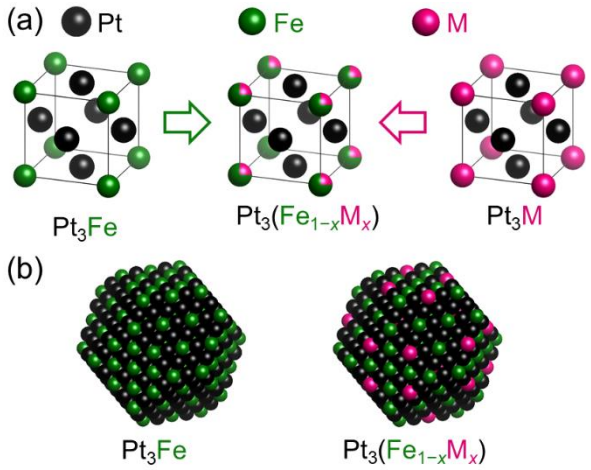

Scheme 1. (a) Catalyst design concept and the (b) cuboctahedron model for Pt_3Fe-based pseudo-binary alloys with Fe–M substitution.

A series of $Pt_3(Fe_{0.75}M_{0.25})/SiO_2$ (M = Co, Ni, Cu, Zn, Ga, In, Sn, and Pb) were prepared in a manner similar to that used to prepare the bimetallic catalysts. For each catalyst, the position of 111 diffraction was consistent with the theoretical value calculated using Vegard's law, where the lattice constant of $Pt_3(Fe_{0.75}M_{0.25})$ was assumed to be a 3:1 linear combination of those of Pt_3Fe and Pt_3M, which suggested the formation of the desired pseudo binary alloy structure. CO chemisorption revealed that Pt dispersion slightly decreased from 29% (Pt_3Fe) to typically 23~25% [$Pt_3(Fe_{0.75}M_{0.25})$]. Figures 7a and b show the HAADF-STEM image of $Pt_3(Fe_{0.75}Zn_{0.25})/SiO_2$ and the particles size distribution, respectively. The particle sizes ranged from 1 nm to 4 nm with a volume weighted average of 2.7 nm. The elemental maps of Pt, Fe, and Zn acquired using the EDX showed that the nanoparticles were consisted of Pt, Fe, and Zn atoms (Figure 7c). The HAADF-STEM images of a single nanoparticle showed lattice fringes with a spacing of 3.91 Å, which is consistent with the interplanar distance of $Pt_3(Fe_{0.75}Zn_{0.25})$(100) planes (3.88 Å). Moreover, the observed atomic arrangement closely matched the corresponding crystal structure

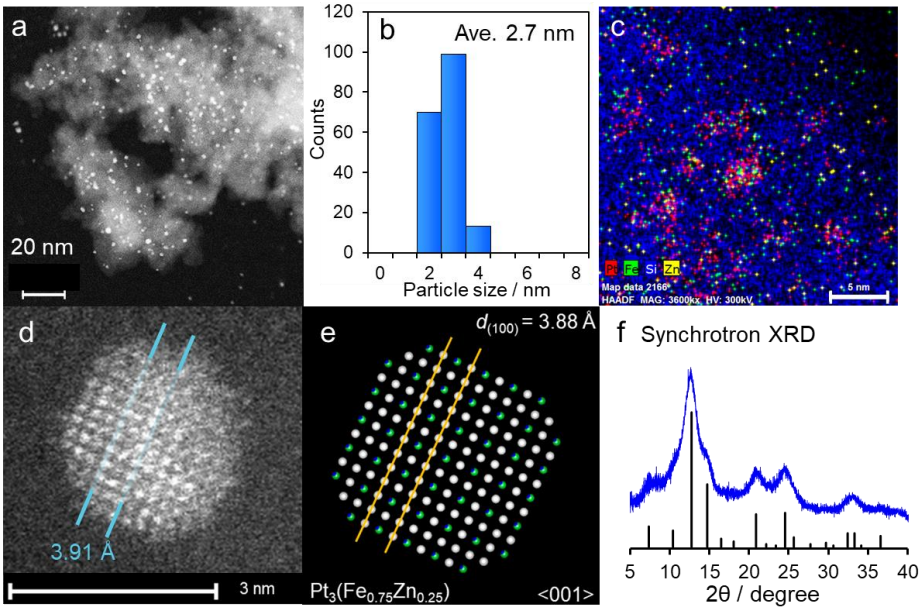

Figure 7. (a) HAADF-STEM image of $Pt_3(Fe_{0.75}Zn_{0.25})/SiO_2$ (Pt loading was 3 wt%) and the (b) size distribution of nanoparticles. (c) Elemental maps of the Pt + Fe + Zn overlayer obtained using EDX. (d) High-resolution STEM image of a single nanoparticle. (e) $Pt_3(Fe_{0.75}Zn_{0.25})$ crystal viewed along the <001> direction (white: Pt, green: Fe or Zn). (f) Background-subtracted synchrotron XRD pattern of $Pt_3(Fe_{0.75}Zn_{0.25})/SiO_2$ (Pt loading was 3 wt%). Black vertical lines indicate the simulated diffraction patterns of $Pt_3(Fe_{0.75}Zn_{0.25})$.

viewed along the [111] direction (Figures 7d and e). The large difference in Z contrast allows to distinguish dark Fe(Zn) columns and surrounding bright Pt columns, which is consistent with the atomic arrangement of the $L1_2$ crystal structure. In addition, we performed the synchrotron XRD (λ = 0.496 Å) analysis for $Pt_3(Fe_{0.75}Zn_{0.25})/SiO_2$, the diffraction pattern of which is shown in Figure 7f. The experimental pattern matched well the simulated one. Note that the superlattice diffractions were clearly observed (100 and 110 at 7.3° and 10.4°, respectively), which is a strong evidence of the formation of the $L1_2$ structure.

Besides, we performed the XAFS analysis of $Pt_3(Fe_{0.75}Zn_{0.25})/SiO_2$ and related materials to obtain the information of local structure (Figures 8 and 9 for X-ray absorption near edge structure (XANES) spectra and raw EXAFS oscillations, respectively). The Fe and Zn K-edge XANES spectra revealed that Fe and Zn in Pt_3Fe/SiO_2 and $Pt_3(Fe_{0.75}Zn_{0.25})/SiO_2$ were almost in metallic states. Table 1 summarizes the representative results of curve-fitting. Pt_3Fe/SiO_2 showed Pt–Fe and Pt–Pt scatterings at 2.67 Å (CN = 2.0) and 2.71 Å (CN = 5.9), respectively. The ratio of CN_{Pt-Pt}/CN_{Pt-Fe} was 2.9, which was consistent roughly to that of bulk intermetallic Pt_3Fe (2: CN_{Pt-Pt} = 8, CN_{Pt-Fe} = 4). A similar result was observed for $Pt_3(Fe_{0.75}Zn_{0.25})/SiO_2$: Pt–Fe(Zn) at 2.66 Å ($CN$ = 2.5) and Pt–Pt at 2.71 Å (CN = 5.8), CN_{Pt-Pt}/CN_{Pt-Fe} was 2.3. Note that, for intermetallic Pt_3Fe, Pt–Fe and Pt–Pt scatterings at the first coordination shell are distinguishable by EXAFS even though their distances are crystallographically identical. However, Pt–Fe and Pt–Zn scatterings with the same distance cannot be distinguished because the backscattering amplitude and phase shift for Fe are similar to those of Zn. Therefore, the presence of Zn that neighbors to Pt cannot be identified by Pt L_{III}-edge EXAFS, while should be considered from Zn K-edge EXAFS. For both Fe K- and Zn K-edge EXAFS, the corresponding Fe–Pt and Zn–Pt bonds

were observed for $Pt_3(Fe_{0.75}Zn_{0.25})/SiO_2$. Conversely, our attempt to assume Fe–Zn or Zn–Fe scattering did not provide good fitting. These results strongly suggest that Zn is selectively substituted at the Fe position in Pt_3Fe crystal but not with Pt. Only a small contribution of Fe–O and Zn–O was observed, probably originating from chemical interaction with SiO_2 support. Thus, the combination of XRD, HAADF-STEM-EDS, and XAFS analyses strongly supports the formation of the $Pt_3(Fe_{0.75}Zn_{0.25})$ pseudo-binary alloy structure with Fe–Zn substation in Pt_3Fe. However, considering that $CN_{Zn–Pt}$ (6.8) is smaller than $CN_{Fe–Pt}$ (7.6), Zn distribution in the nanoparticle might be slightly biased to surface region. Considering that the Pt dispersion of $Pt_3(Fe_{0.75}Zn_{0.25})$ was slightly lower than that of Pt_3Fe, not only Fe but also Pt might be replaced with a small amount of Zn at the surface region.

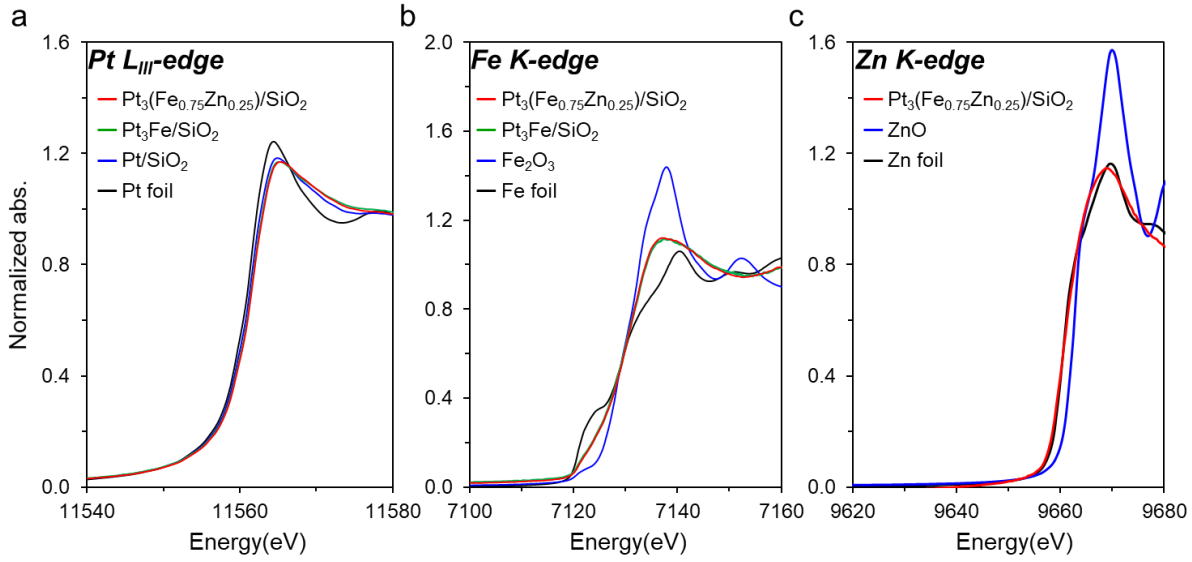

Figure 8. (a) Pt L_{III}-, (b)Fe K-, and (c) Zn K- edge XANES spectra of the catalysts and reference compounds. The features of Fe K-edge XANES of Pt_3Fe/SiO_2 and $Pt_3(Fe_{0.75}Zn_{0.25})/SiO_2$ well agreed with that of *in-situ*-reduced Pt_3Fe/C reported in literature,[23] of which Fourier transformed EXAFS shows no peak assignable to Fe–O between 1–2Å. These demonstrate that the specific XANES feature of Pt_3Fe does not originate from oxides, but probably from alloying with Pt. Similar trends have also been reported for the relevant systems of bulk Pt–Co[24] and Pt_3Ni.[25] In these papers, the increased intensity of white line ($1s \rightarrow 4p$ transition) was explained by the increase in the number of Co(Ni) 4*p* empty state of Co(Ni), which is caused alloying with Pt. Thus, it can be said that the Fe in Pt_3Fe/SiO_2 and $Pt_3(Fe_{0.75}Zn_{0.25})/SiO_2$ is mainly in the metallic state.

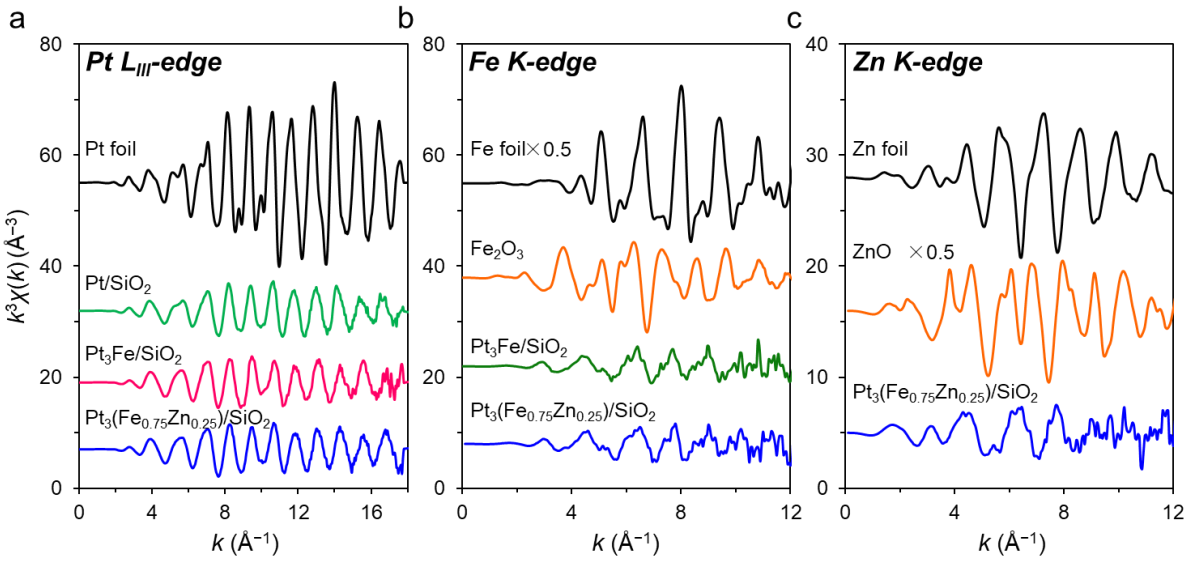

Figure 9. (a) Pt L_{III}-edge k^3-weighted raw EXAFS oscillations for Pt foil (Black), Pt/SiO_2 (Green), Pt_3Fe/SiO_2 (Magenta), and $Pt_3(Fe_{0.75}Zn_{0.25})/SiO_2$ (Blue). (b) Fe K-edge k^3-weighted raw EXAFS oscillations for Fe foil (Black), Fe_2O_3 (Orange), Pt_3Fe/SiO_2 (Green), and $Pt_3(Fe_{0.75}Zn_{0.25})/SiO_2$ (Blue). (c) Zn K-edge k^3-weighted raw EXAFS oscillations for Zn foil (Black), ZnO (Orange) and $Pt_3(Fe_{0.75}Zn_{0.25})/SiO_2$ (Blue).

Table 1. Summary of the representative EXAFS curve fitting for Pt-based catalysts.

Sample	Edge	Shell	*CN*	*R* (Å)[a]	σ^2 (Å^2)[b]	*R*-factor (R^2)[c]
Pt foil	Pt L_{III}	Pt–Pt	12.0 (fix)	2.77 ± 0.00	0.005	0.000
Pt/SiO_2	Pt L_{III}	Pt–Pt	7.1 ± 0.3	2.73 ± 0.01	0.007	0.001
Pt_3Fe/SiO_2	Pt L_{III}	Pt–Fe	2.0 ± 0.6	2.67 ± 0.02	0.014	0.003
		Pt–Pt	5.9 ± 0.5	2.71 ± 0.00	0.007	
	Fe K	Fe-O	0.8 ± 0.5	1.93 ± 0.02	0.006	0.008
		Fe–Pt	6.0 ± 1.1	2.64 ± 0.01	0.012	
$Pt_3(Fe_{0.75}Zn_{0.25})/SiO_2$	Pt L_{III}	Pt–Fe	2.5 ± 0.7	2.66 ± 0.01	0.017	0.002
		Pt–Pt	5.8 ± 0.4	2.71 ± 0.00	0.007	
	Fe K	Fe–O	0.7 ± 0.7	1.92 ± 0.04	0.006	0.015
		Fe–Pt	7.6 ± 1.9	2.65 ± 0.01	0.013	
	Zn K	Zn–O	1.1 ± 1.1	2.01 ± 0.02	0.009	0.024
		Zn–Pt	6.8 ± 1.8	2.61 ± 0.02	0.019	

[a]Distance between absorber and backscatterer atoms. [b]Correction term in the absorption edge. [c]Disorder term (EXAFS Debye–Waller factor).

The synthesized Pt_3Fe-based pseudo-binary alloy catalysts were also tested in MCH dehydrogenation at 400°C (Figures 10a and b). This reaction is typically performed at 300~350°C to obtain sufficient MCH conversion; here, we employed a relatively harsh condition to obtain the deactivation trend in a short period of time. The durability was further enhanced by the substitution of a part of Fe with M, where the Zn-substituted catalyst, $Pt_3(Fe_{0.75}Zn_{0.25})/SiO_2$, exhibited the highest durability in the trimetallic system. We also optimized the Zn content in $Pt_3(Fe_{1-x}Zn_x)/SiO_2$ (x = 0, 0.25, 0.5, 0.75, and 1), which revealed that the Zn content of 0.25 gave the highest stability and TOF (Figure 11). A further increase in the Zn content lowered the stability stepwise to the level of Pt_3Zn. Figure 12 summarizes the catalytic performance of Pt-based catalysts in MCH dehydrogenation. Pt_3Sn and Pt_3In, which are known as catalysts that are stable during alkane dehydrogenation,[26–29] showed rapid deactivation, which suggested that the reaction condition was harsh for MCH dehydrogenation. Conversely, the $Pt_3(Fe_{0.75}Zn_{0.25})/SiO_2$ catalyst showed little deactivation even at this harsh condition, highlighting the remarkably high durability. Moreover, this catalyst showed a 2.7-fold higher TOF than that of Pt/SiO_2 and retained excellent toluene selectivity (>99%). Thus, the pseudo-binary alloy system drastically changed the catalytic performance.

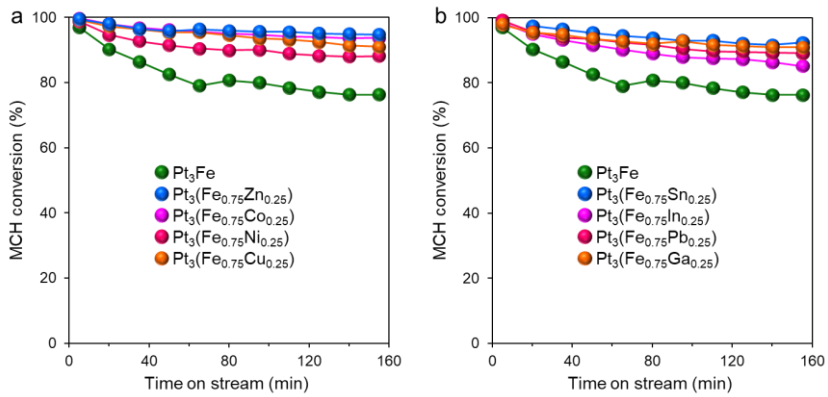

Figure 10. (a,b) Durability test for silica-supported Pt_3Fe-based pseudo binary alloy catalysts in MCH dehydrogenation at 400°C.

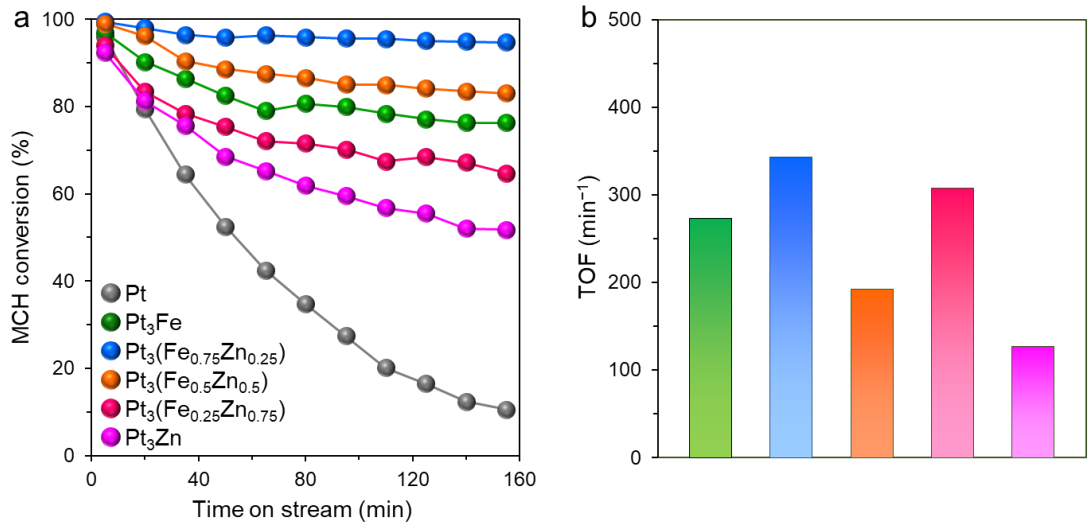

Figure 11. (a) Durability test for $Pt_3(Fe_{1-x}Zn_x)/SiO_2$ in MCH dehydrogenation at 400°C. (b) TOF of $Pt_3(Fe_{1-x}Zn_x)/SiO_2$ in MCH dehydrogenation at 300°C.

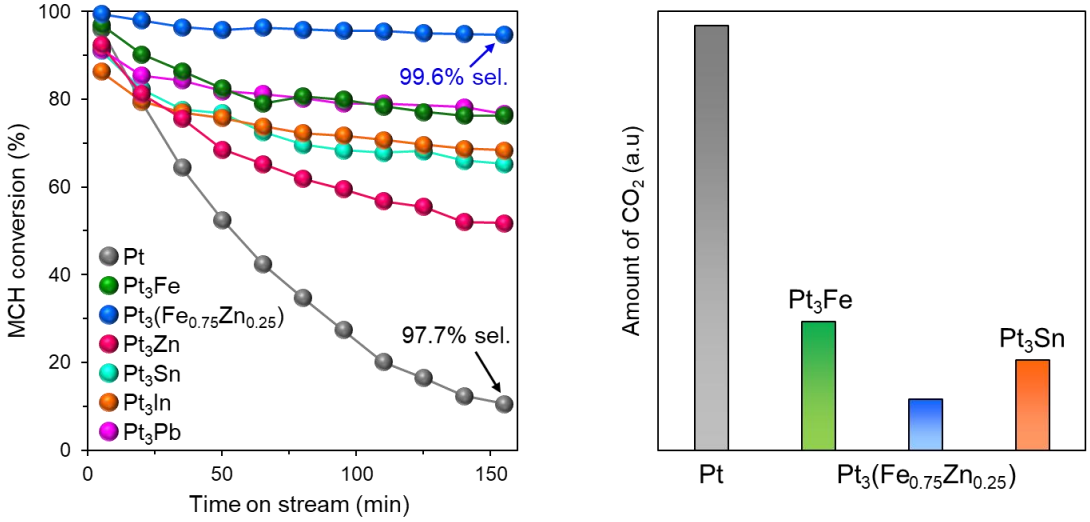

Figure 12. (a) Change in MCH conversion in durability test at 400°C and (b) TOF at 300°C.

We also performed a long-term durability test using the $Pt_3(Fe_{0.75}Zn_{0.25})/SiO_2$ catalyst with 0.25 wt% Pt loading under a standard reaction temperature (at 320°C), where the sufficiently high catalytic performance (99% MCH conversion and >99.8% toluene selectivity) was retained for longer than 2 days. We observed that lower Pt loading gave better durability for MCH dehydrogenation (the order of the long-term durability: 3 wt% < 1 wt% < 0.5 wt% < 0.25 wt% Pt). This is probably because of the size effect: the lower the loading amount is, the smaller the size is, and undesired side reactions are suppressed on smaller-sized particles, as reported in literatures.[30] However, the TOF value did not depend on Pt loading and dispersion; therefore, there is no clear size dependence on the catalytic activity. The H_2 evolution rate on 3 wt% $Pt_3(Fe_{0.75}Zn_{0.25})/SiO_2$ catalyst was 539 mmol/g_{Pt}/min at 300°C, which increased to 757 mmol/g_{Pt}/min when the reaction temperature was increased to 350°C (Figure 13). To the best of our knowledge, these rates are much higher than the highest values ever

reported for MCH dehydrogenation (see Table 2 for comparison with literature), which is likely due to the outstandingly high TOF. It should be emphasized that $Pt_3(Fe_{0.75}Zn_{0.25})/SiO_2$ also exhibited excellent selectivity to toluene (>99.9% at 350°C) with only a ppm level of methane released in the gas phase (Figure 14). This is very important for practical applications, such as in fuel cells, which typically require ultra-pure hydrogen.[31] Thus, we developed a highly active, selective, and durable catalyst for MCH dehydrogenation. We also performed TPO experiments using spent catalysts to estimate the amount of coke accumulated on the catalyst during MCH dehydrogenation. Figure 15 shows the amount of heavy coke deposited on the representative catalysts after use in MCH dehydrogenation. Monometallic Pt had a large amount of coke, which is consistent with the rapid deactivation during the catalytic run. Conversely, the coke amount was much lower for the catalysts with high durability, particularly for $Pt_3(Fe_{0.75}Zn_{0.25})/SiO_2$. Thus, the catalyst lifetime also depends on the amount of coke deposited and the Fe-containing catalysts showed high resistance to coke accumulation.

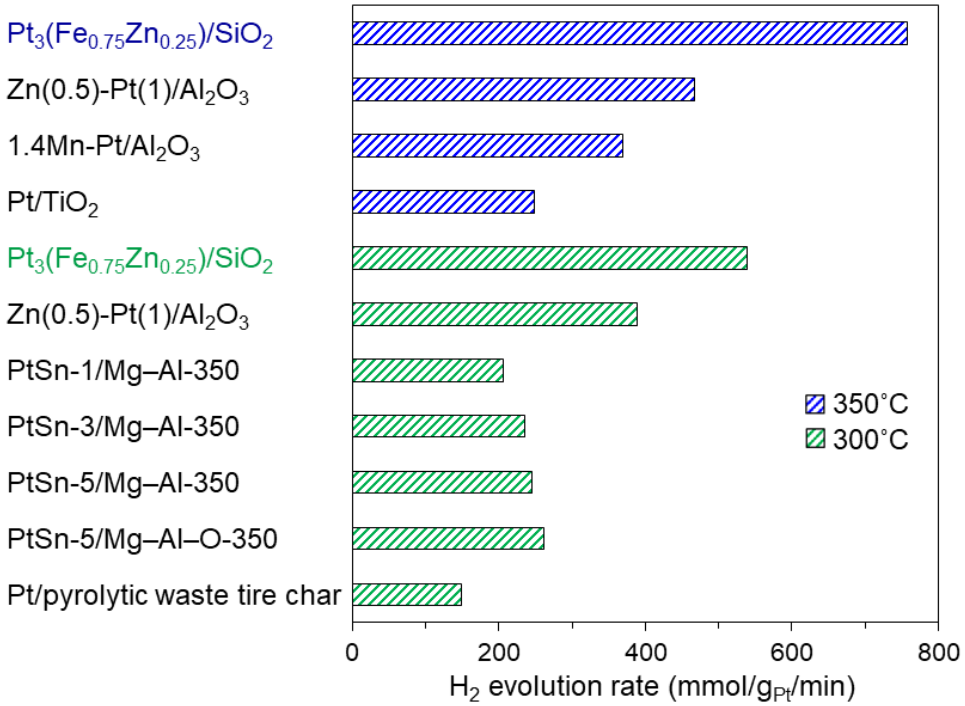

Figure 13. Comparison of H_2 evolution rates (calculated based on MCH conversion) for $Pt_3(Fe_{0.75}Zn_{0.25})/SiO_2$ and other reported Pt-based catalysts (references are listed in Table 2).

Table 2. Comparison catalytic performance in MCH dehydrogenation for $Pt_3(Fe_{0.75}Zn_{0.25})/SiO_2$ and other reported Pt-supported catalysts.

Entry	Catalyst	Pt loading (wt%)	Temp (°C)	Conv. (%)	H_2 evolution rate (mmol/g_{Pt}/min)	Ref.
1	$Pt_3(Fe_{0.75}Zn_{0.25})/SiO_2$	3	300	78.9	539	this study
2			350	71.2	757	
3	Zn(0.5)-Pt(1)/Al_2O_3	1	300	75	389	13
4			350	90	466.7	13
5	1.4Mn-Pt/Al_2O_3	1	350	89	369	14
6	Pt/TiO_2	1	350	60	249	15
7	PtSn-1/Mg–Al-350	2	300	71	205.6	16
8	PtSn-3/Mg–Al-350	2	300	81.1	234.9	16
9	PtSn-5/Mg–Al-350	2	300	84.5	244.8	16
10	PtSn-5/Mg–Al-O-350	2	300	90.5	262.1	16
11	Pt/pyrolytic waste tire char	0.4	300	95	149.3	17

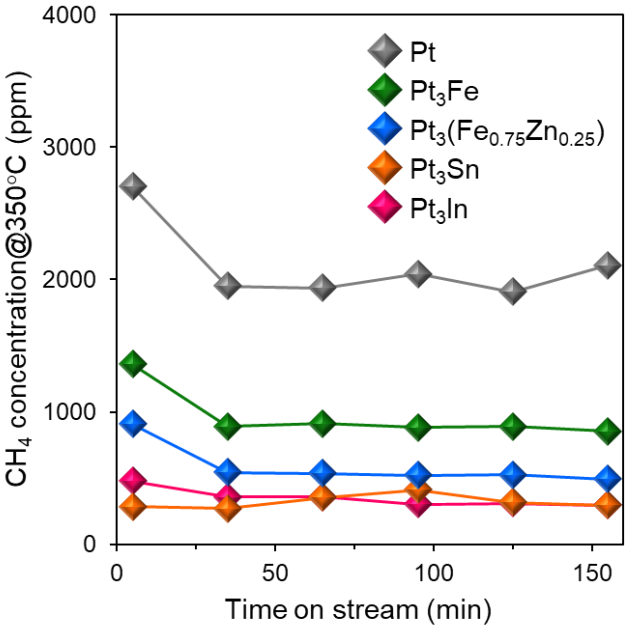

Figure 14. CH_4 concentration in the outlet gas during MCH dehydrogenation over silica-supported Pt-based catalysts at 350°C.

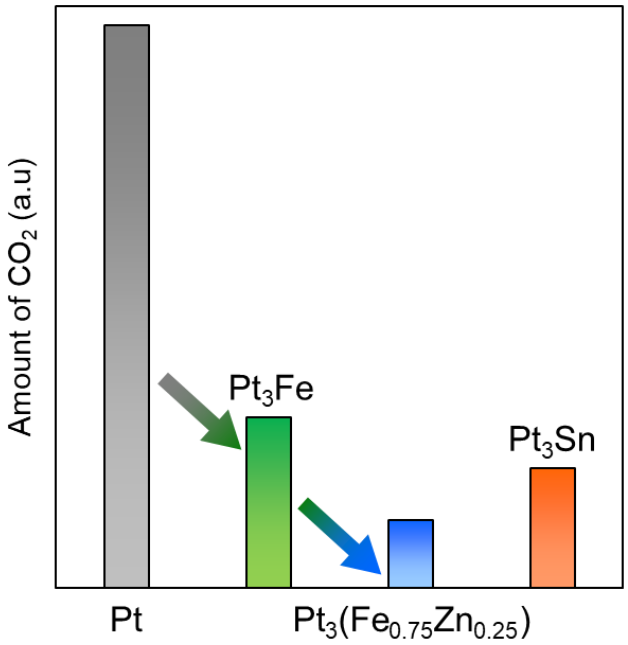

Figure 15. The relative amount of heavy coke accumulated on the catalysts (500–800°C) estimated from TPO experiment. CO_2 evolution at *ca*. 300°C and *ca*. 500°C were regarded as light (probably, product toluene) and heavy coke, respectively.

2.3.3. Mechanic study.

Next, we performed DFT calculation to understand the origin of the high catalytic performance of $Pt_3(Fe_{0.75}Zn_{0.25})/SiO_2$. First, we focused on the adsorption energy of toluene (E_{ad}) on the $Pt_3M(111)$ surface to evaluate the trend of product desorption. In general, enhanced product desorption suppresses any successive side reactions such as demethylation of toluene, which typically leads to coke formation and catalyst deactivation.[11,30,32,33,36–38] Therefore, product desorption is an important factor for improving selectivity and stability. Figure 16 shows E_{ad} for $Pt_3M(111)$ surfaces estimated by periodic DFT calculations. For the monometallic Pt(111) surface, the stable adsorption geometry of toluene was di-σ-di-π configurations on a 4-Pt-atom ensemble. However, for $Pt_3M(111)$ surfaces, the stable adsorption geometry of toluene was tri-π configuration with the center of the aromatic ring located above a hollow site, where substantially higher E_a were obtained for all Pt_3M. This likely occurs owing to the absence of the 4-Pt-atom ensemble, namely, ensemble effect.[39,40] Interestingly, the E_{ad} values considerably differed depending on the second metals (Pt_3Pb > Pt_3Sn > Pt_3In > Pt_3Zn > Pt_3Fe > Pt_3Ga > Pt_3Co), and a good linear correlation was observed between E_{ad} and the lattice constant of the Pt_3M crystal (Figure 17). This indicates that the size (steric hindrance) of the second metal M strongly contributes to the adsorption strength of toluene. Thus, toluene desorption is promoted by the formation of Pt_3M intermetallic phases. For the model of the $Pt_3(Fe_{0.75}Zn_{0.25})$ surface, we considered a $Pt_3Fe(111)$-like surface with 25% Fe→Zn (bulk + surface) and Pt→Zn (only surface) substitution and toluene adsorption on Pt_3 and Pt_2Zn hollow sites, as suggested from the results of CO chemisorption and EXAFS curve fitting mentioned above. Here, $Pt_3(Fe_{0.75}Zn_{0.25})$ showed comparable and much higher E_{ad} than Pt_3Fe, when toluene adsorbed on Pt_3 and Pt_2Zn hollow sites, respectively. This occurs because Pt ensemble was further diluted by Zn (Pt_3 → Pt_2Zn). Here the Pt_2Zn hollow site can act as an effective desorption

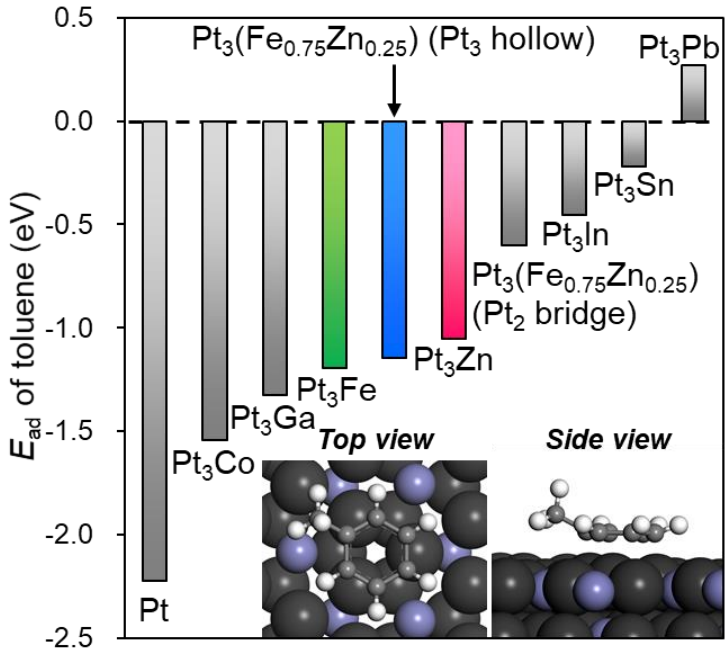

Figure 16. Adsorption energy of toluene on the $Pt_3M(111)$ surface calculated by DFT. The inset shows the optimized structure of toluene adsorbed on a Pt_3 hollow site of the $Pt_3(Fe_{0.75}Zn_{0.25})(111)$ surface (tri-π adsorption).

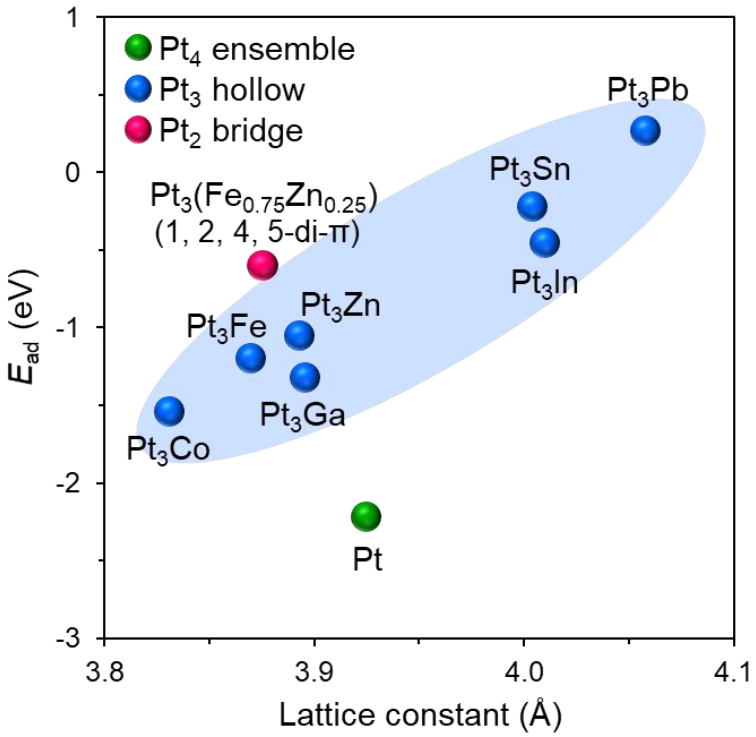

Figure 17. Adsorption energy of toluene on $Pt_3M(111)$ surface plotted against the lattice constant of Pt_3M crystals.

site of toluene, because the migration of toluene from Pt_3 to Pt_2Zn site is possible. Thus, the ensemble effect by alloying can be a major factor for determining the desorption behavior of toluene. Besides, it should be noted that the order of E_{ad} approximately agreed with that of the catalyst stability at 400°C except for Fe-containing materials: $Pt_3(Fe_{0.75}Zn_{0.25})$ >> Pt_3Fe ~ Pt_3Pb > Pt_3Sn ~ Pt_3In > Pt_3Zn > Pt_3Co > Pt > Pt_3Ga. This supports that toluene desorption is an important factor that contributes to catalyst durability. However, considering that the Fe-containing catalysts exhibited superior durability even though Pt_3Pb and Pt_3Sn gave higher E_{ad}, Fe seems to be essential for the stability of catalysis.

According to the high coke resistance of abovementioned Fe-containing catalysts, we focused on the "decoking" property, which is the capability of removing carbonaceous species by hydrogenation, as another factor that contributes to catalyst durability. Here, we considered stepwise hydrogen attack to surface carbon atom to release methane ($CH_x + H \rightarrow CH_x + 1$: $x = 0$~3) as a simple model of removing coke precursors. Figure 18 shows E_a of CH_x hydrogenation on $Pt_3M(111)$ surface. Pt_3Fe and $Pt_3(Fe_{0.75}Zn_{0.25})$ gave lower E_a than those of Pt and Pt_3Sn for each step, indicating that surface Fe is capable of enhancing the hydrogenation of coke precursors. The greater ability of Fe for decoking is consistent with the higher CH_4 concentration in the gas phase and the lower coke amount.

Finally, we discuss another role of Zn on the best catalytic performance of $Pt_3(Fe_{0.75}Zn_{0.25})/SiO_2$. The substitution of Fe with M typically improved catalytic durability and decreased Pt dispersion. Therefore, it is likely that Pt ensembles at the surface were further diluted by M as indicated by the EXAFS analysis for Zn, which enhanced toluene desorption. Therefore, Zn should have a specific character to improve the best catalytic

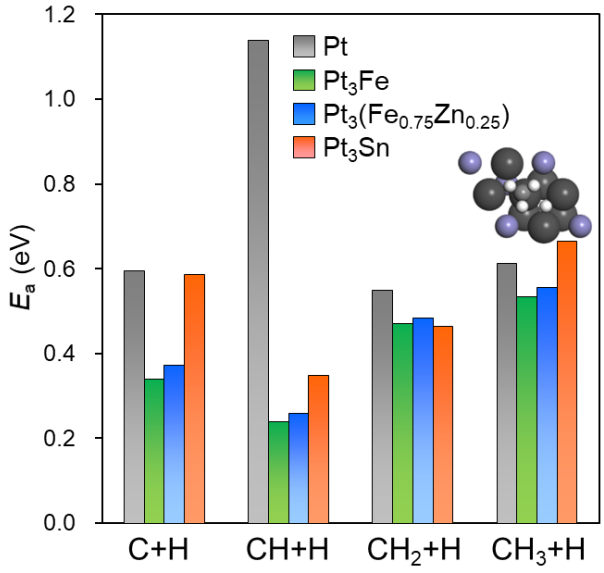

Figure 18. Activation energy of CH_x (coke precursor) hydrogenation on $Pt_3M(111)$ calculated by DFT. The inset shows the initial state of CH_3 hydrogenation ($CH_3 + H \rightarrow CH_4$) on the $Pt_3Fe(111)$ surface.

performance for Fe–M substitution. A possible interpretation is the ligand effect to modify the electronic structure of Pt. Several researchers have reported that electron-rich Pt suppressed side reactions and enhanced the catalyst durability in MCH (or hydrocarbon) dehydrogenation.[30,32,37,41] Electron-rich Pt was considered to enhance electrostatic repulsion between Pt and toluene, which accelerated toluene desorption and inhibited the subsequent side reactions such as demethylation. Therefore, we performed XPS analysis to investigate the electronic state of surface Pt (Figure 19). For Pt/SiO_2, three signals appeared at 68.9 eV, 71.6 eV, and 74.8 eV, which are assigned to $4p_{1/2}$, $4f_{5/2}$ and $4f_{7/2}$ emissions of metallic Pt, respectively.[42–45] Pt_3Fe/SiO_2 showed binding energies to be almost identical to those of Pt/SiO_2, indicating that the electronic state of surface Pt did not so change upon alloying with Fe. However, the binding energies of Pt $4f_{7/2}$ for $Pt_3(Fe_{0.75}Zn_{0.25})/SiO_2$ and Pt_3Zn/SiO_2 were lower (71.3 eV and 71.1 eV, respectively) than those for Pt/SiO_2 and other alloys, which suggests that the electron density of Pt increased upon the incorporation of Zn. Thus, alloying with Zn donates electrons to Pt (ligand effect), as reported for other Pt–Zn bimetallic systems.[32,43,46,47] This ligand effect can further enhance toluene desorption, hence improve the selectivity and catalytic durability.

On the basis of these DFT calculations, we can summarize that the origin of high selectivity and stability of Pt_3Fe intermetallic catalyst is derived from the synergetic effect of desorption and decoking. Besides, the performance is further improved by substituting a part of Fe(Pt) with Zn because of the enhanced toluene desorption by both ligand and ensemble effects. Thus, the catalyst design based on the pseudo-binary alloy structure allows to construct multifunctional active sites that mediate C–H activation (Pt), promote decoking (Fe), and accelerate toluene desorption (Fe, Zn). The weaker adsorption of toluene and lower coke amount allow to retain a larger number of active Pt sites during MCH dehydrogenation, which would explain the high catalytic activity of $Pt_3(Fe_{0.75}Zn_{0.25})$. The combination of these three elements and their promotion effects allows to develop a highly active, selective, and durable catalyst for cycloalkane dehydrogenation.

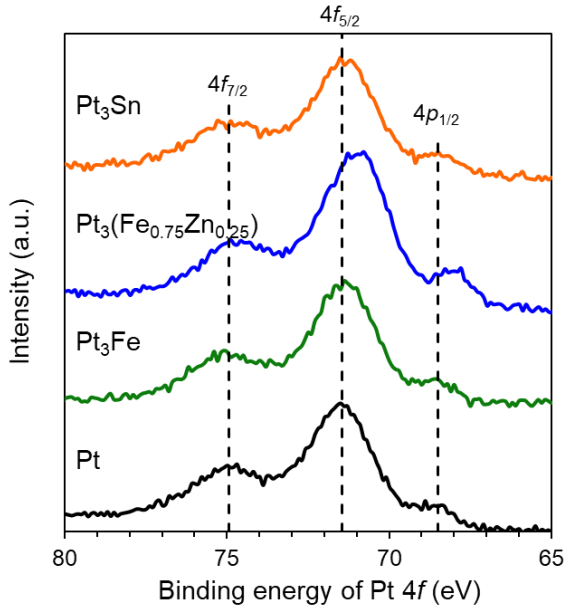

Figure 19. Pt 4*f* and 4*p* XPS spectra of silica-supported Pt-based catalysts.

2.4. Discussion

In this study, a series of Pt-based intermetallic compounds supported on silica (Pt_3M/SiO_2, where M = Fe, Co, Ni, Cu, Zn, Ga, In, Sn, and Pb) were tested as catalysts for the dehydrogenation of methylcyclohexane to toluene. Pt_3Fe/SiO_2 acts as a highly active and durable heterogeneous catalyst, and a 2.1-fold higher TOF than Pt/SiO_2 is observed. The substitution of part of Fe by Zn forms the $Pt_3(Fe_{0.75}Zn_{0.25})$ pseudo-binary alloy structure, which exhibits a three times higher TOF than that of Pt/SiO_2, excellent toluene selectivity (>99%, methane: <500 ppm), and long-term durability (>50 h). To the best of our knowledge, this catalyst exhibits the highest hydrogen evolution rate among the reported materials. The remarkably high selectivity and stability are derived from the synergy of enhanced toluene desorption and decoking capability. Fe has a unique capability to facilitate the hydrogenation of coke precursor to methane. Zn makes Pt electron-rich and further dilutes Pt_3 hollow sites, which strongly accelerates toluene desorption owing to the ligand and ensemble effects, respectively. The combination of each element, Pt (C–H activation), Fe (decoking), and Zn (toluene desorption) results in a highly active, selective, and durable catalyst for MCH dehydrogenation. Thus, the catalyst design based on the pseudo-binary alloy structure allows to construct multifunctional active sites that are highly efficient for alkane dehydrogenation. The present study provides an innovative catalytic system for alkane dehydrogenation as well as deep insights for the fine tuning of active sites and catalytic properties.

Reference

1 J. J. H. B. Sattler, J. Ruiz-Martinez, E. Santillan-Jimenez and B. M. Weckhuysen, *Chem. Rev.*, 2014, **114**, 10613–10653.

2 J. C. Bricker, *Top. Catal.*, 2012, **55**, 1309–1314.

3 E. Gianotti, M. Taillades-Jacquin, J. Rozière and D. J. Jones, *ACS Catal.*, 2018, **8**, 4660–4680.

4 R. B. Biniwale, S. Rayalu, S. Devotta and M. Ichikawa, *Int. J. Hydrogen Energy*, 2008, **33**, 360–365.

5 O. O. James, S. Mandal, N. Alele, B. Chowdhury and S. Maity, *Fuel Process. Technol.*, 2016, **149**, 239–255.

6 D. Sanfilippo and I. Miracca, *Catal. Today*, 2006, **111**, 133–139.

7 M. M. Bhasin, J. H. McCain, B. V. Vora, T. Imai and P. R. Pujadó, *Appl. Catal. A Gen.*, 2001, **221**, 397–419.

8 E. C. Wegener, Z. Wu, H. T. Tseng, J. R. Gallagher, Y. Ren, R. E. Diaz, F. H. Ribeiro and J. T. Miller, *Catal. Today*, 2018, **299**, 146–153.

9 Z. Wu, E. C. Wegener, H. T. Tseng, J. R. Gallagher, J. W. Harris, R. E. Diaz, Y. Ren, F. H. Ribeiro and J. T. Miller, *Catal. Sci. Technol.*, 2016, **6**, 6965–6976.

10 S. M. Stagg, C. A. Querini, W. E. Alvarez and D. E. Resasco, *J. Catal.*, 1997, **168**, 75–94.

11 F. Alhumaidan, D. Cresswell and A. Garforth, *Energy and Fuels*, 2011, **25**, 4217–4234.

12 Y. Okada, E. Sasaki, E. Watanabe, S. Hyodo and H. Nishijima, *Int. J. Hydrogen Energy*, 2006, **31**, 1348–1356.

13 S. Zha, G. Sun, T. Wu, J. Zhao, Z. J. Zhao and J. Gong, *Chem. Sci.*, 2018, **9**, 3925–3931.

14 J. Im and M. Choi, *ACS Catal.*, 2016, **6**, 2819–2826.

15 G. Siddiqi, P. Sun, V. Galvita and A. T. Bell, *J. Catal.*, 2010, **274**, 200–206.

16 V. J. Cybulskis, B. C. Bukowski, H. T. Tseng, J. R. Gallagher, Z. Wu, E. Wegener, A. J. Kropf, B. Ravel, F. H. Ribeiro, J. Greeley and J. T. Miller, *ACS Catal.*, 2017, **7**, 4173–4181.

17 H. N. Pham, J. J. H. B. Sattler, B. M. Weckhuysen and A. K. Datye, *ACS Catal.*, 2016, **6**, 2257–2264.

18 J. Jeon, K. Kon, T. Toyao, K. Shimizu and S. Furukawa, *Chem. Sci.*, 2019, **10**, 4148–4162.

19 T. Komatsu and A. Tamura, *J. Catal.*, 2008, **258**, 306–314.

20 B. Ravel and M. Newville, *J. Synchrotron Rad.*, 2005, **12**, 537–541.

21 A. Ankudinov and B. Ravel, *Phys. Rev. B, Condens. Matter Mater. Phys.*, 1998, **58**, 7565–7576.

22 H. Okamoto, M. E. Schlesinger and E. M. Mueller, Eds., *Alloy Phase Diagrams*, 2016, 3, 0.

23 F. J. Lai, H. L. Chou, L. S. Sarma, D. Y. Wang, Y. C. Lin, J. F. Lee, B. J. Hwang and C. C. Chen, *Nanoscale*, 2010, **2**, 573–581.

24 A. I. Figueroa, J. Bartolomé, L. M. García, F. Bartolomé, O. Bunəu, J. Stankiewicz, L. Ruiz, J. M. González-Calbet, F. Petroff, C. Deranlot, S. Pascarelli, P. Bencok, N. B. Brookes, F. Wilhelm, A. Smekhova and A. Rogalev, *Phys. Rev. B, Condens. Matter Mater. Phys.*, 2014, **90**, 1–16.

25 J. Chen, Y. M. Yiu, Z. Wang, D. Covelli, R. Sammynaiken, Y. Z. Finfrock and T. K. Sham, *J. Phys. Chem. C*, 2020, **124**, 2313–2318.

26 S. Zha, G. Sun, T. Wu, J. Zhao, Z. J. Zhao and J. Gong, *Chem. Sci.*, 2018, **9**, 3925–3931.

27 L. Nykänen and K. Honkala, *ACS Catal.*, 2013, **3**, 3026–3030.
28 L. Nykänen and K. Honkala, *J. Phys. Chem. C*, 2011, **115**, 9578–9586.
29 S. Furukawa, A. Tamura, K. Ozawa and T. Komatsu, *Appl. Catal. A Gen.*, 2014, **469**, 300–305.
30 S. Nagatake, T. Higo, S. Ogo, Y. Sugiura, R. Watanabe, C. Fukuhara and Y. Sekine, *Catal. Letters*, 2016, **146**, 54–60.
31 Y. Li, D. Li and G. Wang, *Catal. Today*, 2011, **162**, 1–48.
32 K. Mori, Y. Kanda and Y. Uemichi, 2018, **61**, 350–356.
33 A. Nakano, S. Manabe, T. Higo, H. Seki, S. Nagatake, T. Yabe, S. Ogo, T. Nagatsuka, Y. Sugiura, H. Iki and Y. Sekine, *Appl. Catal. A Gen.*, 2017, **543**, 75–81.
34 J. Yan, W. Wang, L. Miao, K. Wu, G. Chen, Y. Huang and Y. Yang, *Int. J. Hydrogen Energy*, 2018, **43**, 9343–9352.
35 C. Zhang, X. Liang and S. Liu, *Int. J. Hydrogen Energy*, 2011, **36**, 8902–8907.
36 D. S. Sethi, C. T. Chew, L. W. Jossens, E. E. Petersen, W. J. Doolittle, N. D. Skoularikis, R. W. Coughlin, K. Liu, S. C. Fung, T. C. Ho, D. S. Rumschitzki, R. Prestvik, K. Moljord, K. Grande, A. Holmen, R. W. Coughlin, K. Kawakami, A. Hasan, K. Jothlmurugesan, S. Bhatla and R. D. Srlvastava, *J. Catal.*, 1998, **36**, 581–588.
37 Y. Sugiura, T. Nagatsuka, K. Kubo, Y. Hirano, A. Nakamura, K. Miyazawa, Y. Iizuka, S. Furuta, H. Iki, T. Higo and Y. Sekine, *Chem. Lett.*, 2017, **46**, 1601–1604.
38 A. Nakano, S. Manabe, T. Higo, H. Seki, S. Nagatake, T. Yabe, S. Ogo, T. Nagatsuka, Y. Sugiura, H. Iki, Y. Sekine, A. Nakano, S. Nagatake, T. Higo, S. Ogo, H. Nakai and Y. Sekine, *Chem. Phys. Lett.*, 2018, **543**, 75–81.
39 S. Furukawa and T. Komatsu, *ACS Catal.*, 2017, **7**, 735–765.
40 S. Furukawa, Y. Matsunami, I. Hamada, Y. Hashimoto, Y. Sato and T. Komatsu, *ACS Catal.*, 2018, **8**, 8177–8181.
41 J. Yu, R. Wang, S. Ren, X. Sun, C. Chen, Q. Ge, W. Fang, J. Zhang, H. Xu and D. S. Su, *ChemCatChem*, 2012, **4**, 1376–1381.
42 J. Llorca, P. R. De Lapiscina, J. L. G. Fierro, J. Sales and N. Homs, *J. Catal.*, 1995, 156, 139–146.
43 S. Iihama, S. Furukawa and T. Komatsu, *ACS Catal.*, 2016, **6**, 742–746.
44 M. Muhler, Z. Paál and R. Schlögl, *Appl. Surf. Sci.*, 1991, **47**, 281–285.
45 N. P. Company and P. O. Box, .
46 J. A. Rodriguez and M. Kuhn, *J. Chem. Phys.*, 1995, **102**, 4279–4289.
47 J. Silvestre-Albero, A. Sepúlveda-Escribano, F. Rodríguez-Reinoso and J. A. Anderson, *J. Catal.*, 2004, **223**, 179–190.

Chapter 3

Single-Atom Pt in Surface-Modified Intermetallics as a Stable and Selective Catalyst for Propane Dehydrogenation

3.1. Introduction

Propylene is one of the most important building blocks for the production of a wide range of chemicals, such as polymers, resins, surfactants, dyes, and pharmaceuticals.[1] The supply of propylene has been reduced because of the recent shift in feedstock for steam crackers from oil-based naphtha to shale-based ethane. Catalytic PDH using Pt- or Cr_2O_3-based materials is a promising on-purpose technique to satisfy the increasing global demand of propylene production.[1–3] Owing to the endothermicity, high reaction temperatures (preferably ≥600°C) are required to obtain sufficient propylene yields. However, severe catalyst deactivation due to coke deposition and/or sintering is inevitable under such harsh conditions; therefore, the catalysts in practical use must be regenerated continuously or in short cycles. Although a number of literatures on catalytic PDH have been reported to this day, no catalyst that exhibits high catalytic activity, selectivity, and day-long stability at high temperatures (≥600°C) has been developed to the best of our knowledge.[1–5] Developing a catalyst to meet this demanding task is of a great challenge in pure and applied chemistry.

Generally, selectivity and stability in PDH are determined by the balance between whether the product propylene desorbs or undergoes undesired side reactions, such as further C–H(C) scissions and the subsequent coke formation.[6–10] For Pt-based catalysts, Pt–Pt ensembles are known to be active for over-dehydrogenation of propylene and its hydrogenolysis.[1] The isolation of Pt atoms is a promising strategy to inhibit these undesired side reactions in PDH.[11] For instance, alloying of active main metal (mostly Pt) with a certain inactive metal (mostly typical elements such as Sn) has been a conventional approach to dilute Pt–Pt ensembles and enhance propylene selectivity and stability.[1] However, it is difficult to completely isolate Pt atoms by the conventional alloying approach. Single-atom[12–15] and SAA[11,16] catalysts are also effective tools to use isolated Pt, where active metals are atomically dispersed on an oxide support and isolated by excess amount of 11 group metal like Cu, respectively. However, it is difficult to apply them to high-temperature reactions such as PDH due to its insufficient thermal stability: Pt atoms[17] or alloy nanoparticles[11,16] without spatial separation[13] are easily aggregated to form larger nanoparticles at very high temperatures.

A possible candidate to solve this challenge is single-atom-like isolated Pt included in thermally stable intermetallic compounds. For instance, the 1:1 compound of Pt and Ga with cubic $P2_13$ space group has thermal stability (ΔH_f = –55.6 kJ mol^{-1}) much greater than typical random alloys (–10 < $\Delta H_f \leq$ 0 kJ mol^{-1}) and a unique structure for this purpose.[18,19] The stable (111) surface of PtGa has four different terminations displaying isolated and three-fold Pt and Ga sites (hereafter signed Pt_1, Ga_1, Pt_3, and, Ga_3, Figure 20a). Here, the Ga_3 moiety can be regarded as a matrix to support the isolated Pt_1 atom; therefore, it may be possible to describe the Pt_1 site as “single-atom Pt”. Note that there are two enantiomeric forms of PtGa unit cell (PtGa:A and PtGa:B, the former is shown in Figure 20b), because the space group $P2_13$ is chiral. In an analogous system of PdGa (space group $P2_13$), such surface termination (Pd_3 and Pd_1, which were described as trimer and single atom, respectively) has actually been observed by surface science techniques.[20,21] For the PdGa system, Pd_3 is known to catalyze semihydrogenation of acetylene more selectively than Pd_1.[20] For PtGa in PDH, however, the Pt_3 site is expected to be more active for deep C–H(C) scission. Therefore, some modification that makes only Pt_3 sites disabled while Pt_1 sites available for the reaction is needed for achieving highly selective and stable PDH.

In this study, we design Pb-modified PtGa where the three-fold Pt is selectively blocked by Pb deposition while the single-atom Pt remains intact (Figure 20c). As demonstrated later, the convex Pt_1 site is unfavorable geometrically and energetically for Pb deposition. We prepare SiO_2-supported PtGa and PtGa–Pb (Pt/Pb = 2) catalysts by an impregnation method (reduced by H_2 at 700°C) and test in PDH at high temperatures (600 or 650°C; note that it is lower than the preparation temperature). Here, we show a different type of single-atom Pt and its outstandingly high catalytic performance in PDH at high temperature.

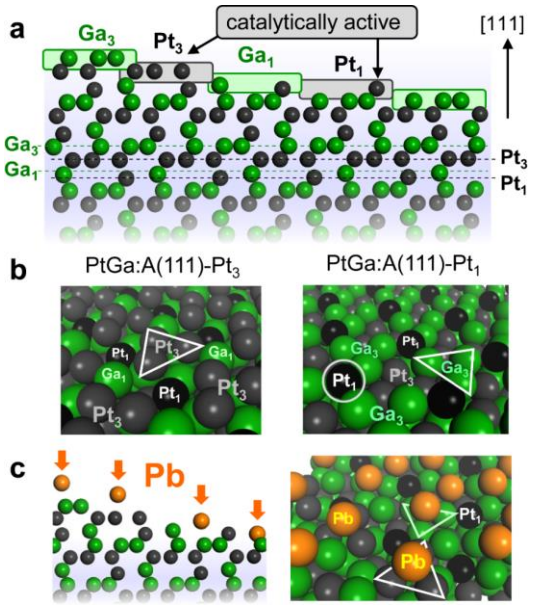

Figure 20. Catalyst design of single-atom Pt in PtGa. (a) Four different surface terminations of PtGa:A(111) viewed along [101] direction (ball model). (b) Diagonal view of Pt_3 and Pt_1 termination (space-filling model). Pt_1 is highlighted with black color. (c) Catalyst design by Pb deposition to block the Pt_3 (and Ga_3) sites and to keep the Pt_1 sites available.

3.2. Experimental

3.2.1. Catalyst Preparation.

SiO_2 (CARiACT G–6, Fuji Silysia, S_{BET} = *ca*. 500 $m^2\ g^{-1}$), Al_2O_3 (prepared by the calcination of boehmite [γ-AlOOH, supplied by SASOL chemicals] at 900°C for 3 h, γ phase), CeO_2 (JRC-CEO-2, S_{BET} = 123.1 $m^2\ g^{-1}$), ZrO_2 (JRC-ZRO-6, S_{BET} = 279.3 $m^2\ g^{-1}$), and TiO_2 (P-25, anatase). $MgAl_2O_4$ support was prepared by a co-precipitation method using urea as a precipitating agent. The precursors and urea were precisely weighted and dissolved together in deionized water so that urea/precursors atomic ratio was 20. Mixed aqueous solution of $Mg(NO_3)_3{\cdot}6H_2O$, $Al(NO_3)_3{\cdot}9H_2O$ and urea was stirred overnight at 90°C. After the precipitation, the solution was washed with water 5 times and dried overnight in oven at 90°C, followed by calcination at 800°C in the dry air for 5 h. $CeZrO_2$ and $CaZrO_3$ were prepared in a same co-precipitation method used to prepare $MgAl_2O_4$. $Ce(NO_3)_3{\cdot}6H_2O$, $Zr(NO_3)_2O{\cdot}2H_2O$, and $Ca(NO_3)_2{\cdot}4H_2O$ were used as precursors.

Pt-based bimetallic catalysts were prepared by the pore-filling co-impregnation method using SiO_2 as the support (Pt_3M/SiO_2, and PtM/SiO_2, where M = Ga, In, Sn, Pb; Pt: 3 wt%). $Ga(NO_3)_3{\cdot}nH_2O$ (n = 7–9), $SnCl_2$, $Pb(NO_3)_2$ were used as second metal precursors. The ratio of precursors was fixed at the desired ratio. Mixed aqueous solution of $Pt(NH_3)_2(NO_3)_2$ and second metal was added dropwise to ground dried SiO_2 so that the solutions just filled the pores of the SiO_2. The mixture was kept in a sealed round-bottom flask overnight at room temperature, followed by quick freezing with liquid nitrogen, freeze-drying in vacuum at −5°C. The resulting powder was further dried in an oven at 90°C overnight, calcined in dry air at 400°C for 1 h, and finally reduced by H_2 (0.1 MPa, 50 mL min^{-1}) at 700°C for 1 h. The catalysts except Pt/SiO_2 were further annealed at 400°C for 2 h under flowing H_2 (0.1 MPa, 50 mL min^{-1}) to enhance alloying without further sintering. Ga/SiO_2 catalyst with 5 wt% loading was prepared using a similar method (reduction was carried out at 900°C for 1 h). (2) The corresponding silica-supported trimetallic catalysts were also prepared using a same method with $PtGa/SiO_2$ [PtGa–Pb/SiO_2, where Pt/Pb = 5, 2.5, 2, and 1.5; PtGa–M/SiO_2, where M = In and Sn, Pt/M = 2; Pt: 3 wt%]. $In(NO_3)_3{\cdot}8.8H_2O$ (determined by ICP-AES), $SnCl_2$ and $Pb(NO_3)_2$ were used as third metal precursors. (3) A series of Pt-Ga bimetallic catalysts supported on various oxides (PtGa/*X*, where *X* = γ-Al_2O_3, $MgAl_2O_4$, CeO_2, $CeZrO_2$, ZrO_2, $CaZrO_3$, and TiO_2; Pt/Ga = 1; Pt: 3 wt%) was prepared by the conventional impregnation method. To prepare a precursor solution, $Pt(NH_3)_2(NO_3)_2$ and $Ga(NO_3)_3{\cdot}nH_2O$ (n = 7–9) were dissolved in an excess amount of water (*ca*. 25 mL of ion exchanged water per g of support). The oxide support was added to a vigorously stirred aqueous solution of the metal precursors and kept with stirring at 90°C for 3 h. The mixture was dried using a rotary evaporator at 50°C and further dried overnight in an oven at 90°C. The resulting powder was treated in a similar manner for the SiO_2-supported alloy catalysts as mentioned above.

3.2.2. Catalytic Reactions.

Propane dehydrogenation was carried out in a vertical, quartz fixed-bed reactor with 6 mm of internal diameter under an atmospheric pressure. Generally, 15 mg of catalysts diluted with quartz sand (total: 1.5 g) were charged in the reactor. Prior to the catalytic test, the catalyst was prereduced under flowing H_2 at 650°C and held at 650°C for 0.5 h. After the pretreatment, the temperature was kept at 650°C or decreased to 600°C, followed by feeding reactant gas mixture; C_3H_8:H_2:He = 3.9:5:40, a total of 48.9 mL min^{-1} (WHSV = 30.7 h^{-1}) The resulting product gas was analyzed by online TCD gas chromatograph (Shimadzu GC–8A with a column of Unipak S, GL Science) equipped downstream. For all the catalysts, C_3H_8, C_2H_4, C_2H_6, and CH_4 were detected as reaction products. The C_3H_8 conversion, C_3H_6 selectivity, C_3H_8 yield, and material balance were defined by Eqs (1) ~ (4), respectively. Material balance typically ranged between 95~105% for all the reactions.

$$C_3H_8 \text{ conversion } (\%) = \frac{[C_3H_8]_{inlet} - [C_3H_8]_{outlet}}{[C_3H_8]_{inlet}} \times 100 \quad (1)$$

$$C_3H_6 \text{ selectivity } (\%) = \frac{[C_3H_6]}{[C_3H_6] + \frac{2}{3}[C_2H_6] + \frac{2}{3}[C_2H_4] + \frac{1}{3}[CH_4]} \times 100 \quad (2)$$

$$C_3H_6 \text{ yield } (\%) = \frac{[C_3H_6]_{outlet}}{[C_3H_8]_{inlet}} \times 100 \quad (3)$$

$$\text{Material balance } (\%) = \frac{[C_3H_8]_{outlet} + [C_3H_6] + \frac{2}{3}[C_2H_6] + \frac{2}{3}[C_2H_4] + \frac{1}{3}[CH_4]}{[C_3H_8]_{inlet}} \times 100 \quad (4)$$

The first-order deactivation model was used to estimate the catalytic stability.[1] k_d (h^{-1}) and τ (h) were defined by the following equation. Here, lower k_d and higher τ values are indicative of higher stability.

$$k_d = \frac{\ln(\frac{1-conv._{end}}{conv._{end}}) - \ln(\frac{1-conv._{start}}{conv._{start}})}{t} \quad (5)$$

$$\tau = \frac{1}{k_d} \quad (6)$$

where, $conv._{start}$ and $conv._{end}$ indicates initial and final propane conversion, respectively. t represents the reaction time. k_d (h^{-1})[1] and τ (h) represent the deactivation rate constant and expected catalyst life, respectively.

3.2.3. Characterization.

XRD patterns of the Pt-based catalysts were obtained using a MiniFlex 700+D/teX Ultra (X–ray source: Cu Kα radiation). HAADF-STEM analysis was performed by an FEI Titan G2 or a JEOL JEM-ARM200 M microscope with an EDX detector. The volume averaged particle size in a TEM image (d_{TEM}) was used.

Pt dispersion in the catalysts (percentage of exposed Pt to the total amount of Pt) was measured by chemisorption of CO at room temperature. Prior to chemisorption, the catalyst (50 mg) was treated by 5% H_2/Ar (40 mL min^{-1}) at 300°C for 0.5 h, followed by cooling to room temperature with a He purge (40 mL min^{-1}) to remove chemisorbed hydrogen. We introduced a pulse of 10% CO/He into the reactor and quantified the CO passed through the catalyst bed using a TCD detector. This pulse measurement was repeated until no more CO was adsorbed. We estimated the amount of chemisorbed CO assuming a 1:1 stoichiometry for CO chemisorption on a surface Pt atom.

XPS study was conducted using a JEOL JPS-9010MC spectrometer (X–ray source: Mg-Kα radiation). The catalysts were treated by flowing H_2 at 650°C for 0.5 h in a quartz reactor, followed by transferring into the spectrometer in air. The surface of the catalyst was sputtered by Ar^+ (voltage: 400 V, rate: 20%, time: 1 s, at each cycle) for the depth analysis. Calibration of the binding energy was performed with the Si 2*p* emission of the SiO_2 support (103.9 eV).

Fourier-transform infrared (FT-IR) spectra of adsorbed CO were obtained with a JASCO FTIR-4100 spectrometer with a TGS detector in the transmission mode (resolution 4 cm^{-1}) under a dynamic condition. Prior to CO chemisorption, 50 mg of the catalyst was pressed into a pellet (diameter of 20 mm) and placed in a quartz cell equipped with CaF_2 windows and a Dewar vessel, followed by reduction under a flowing H_2 at 550˚C for 1 h. The reduced sample was then kept in vacuum at 550˚C for 1h, then the cell was cooled to ca. −196°C by liquid nitrogen. The sample was exposed to a pulse of low-pressure CO, then evacuated in vacuum to remove the gaseous CO and concentrated CO on the catalyst. This CO exposure was repeated several times until the CO saturation coverage.

TPO experiment was performed to quantify the amount of coke deposited on the spent catalysts after 20 h of PDH at 600°C (15 mg of the catalyst without quartz sand). The spent catalyst (10 mg) placed in a quartz tube reactor was treated under flowing He (40 mL min^{-1}) at 150°C for 30 min, followed by cooling to room temperature. Then, the catalyst bed temperature was increased (25~900°C, ramping rate: 5 °C min^{-1}) under flowing O_2/He (50%, 40 mL min^{-1}). The amount of CO_2 in the outlet gas was quantified by an online mass spectrometer.

XAFS spectra of the prepared catalysts were collected at the BL01B1 beamline of SPring-8, JASRI using a Si(111) double-crystal as a monochromator. Prior to the measurement, the catalyst was pelletized (ca. 150 mg with a diameter of 10 mm) and pretreated by H_2 at 650°C for 0.5 h in a quartz tube. After the pretreatment, the quartz tube containing the reduced pellet was sealed and transferred into an Ar grove box (O_2: < 0.1 ppm) without exposing to air. The pellet was sealed in a plastic film bag (Barrier Nylon) together with an oxygen absorber (ISO A500-HS: Fe powder). The Pt L_{III}- and Ga K-edges XAFS spectra was recorded in a transmission mode at room temperature. Athena and Artemis software ver. 0.9.25 implemented in the Demeter package[22] was used for the analysis of the obtained XAFS spectra. Fourier-transform of the Pt L_{III}-edge EXAFS oscillation was obtained in the *k* range of 3−16 $Å^{-1}$. The back Fourier-transform obtained in the *R* range of 1.5−3.5 Å was used for curve-fitting. FEFF8 was used for the calculation of the back-scattering amplitude and phase shift functions.[23] We defined the R-factor (R^2) for curve-fitting as follows:

$$R^2 = \Sigma_i\{k^3\chi_i^{exp}(k)-k^3\chi_i^{fit}(k)\}^2 \text{ per } \Sigma_i\{k^3\chi_i^{exp}(k)\}^2. \quad (7)$$

3.2.4. Computational Details.

DFT calculations were performed by using the CASTEP code.[24] We used Vanderbilt-type ultrasoft pseudopotentials[25] and the revised version of Perdew−Burke−Ernzerhof exchange−correlation functional[26,27] based on the generalized gradient approximation. A cut-off energy of 360 eV was used for the plane-wave basis set. A *k*-point mesh with a spacing of 0.04 $Å^{-1}$ generated by the Monkhorst−Pack scheme[28] was used to sample the Brillouin zone. In this study, the PtGa:A(111) and Pt_3Sn(111) planes were considered as the standard active surfaces for PDH. The supercell structure was constructed using a (2 × 2) unit cell slab with six atomic layers and a vacuum spacing of 15 Å. We performed geometry optimizations on the supercell structures using a Fermi smearing of 0.1 eV, the OBS method for dispersion correlations, and the following convergence criteria: (1) self-consistent field tolerance; 1.0×10^{-6} eV per atom, (2) energy tolerance; 1.0×10^{-5} eV per atom, (3) maximum force tolerance of 0.05 eV $Å^{-1}$, and (4) maximum displacement tolerance; 1.0×10^{-3} Å. Transition state search was carried out based on the complete linear synchronous transit/quadratic synchronous transit method[29,30] with the tolerance for all root-mean-square forces on an atom of 0.10 eV $Å^{-1}$.

3.3. Results

3.3.1. Characterization of PtGa–Pb/SiO_2.

Figure 21a shows the high-resolution HAADF-STEM image of PtGa–Pb/SiO_2 with a single nanoparticle. A crystal structure with interplanar distances of 2.07 Å and 2.25 Å and dihedral angle of 56° was observed, which

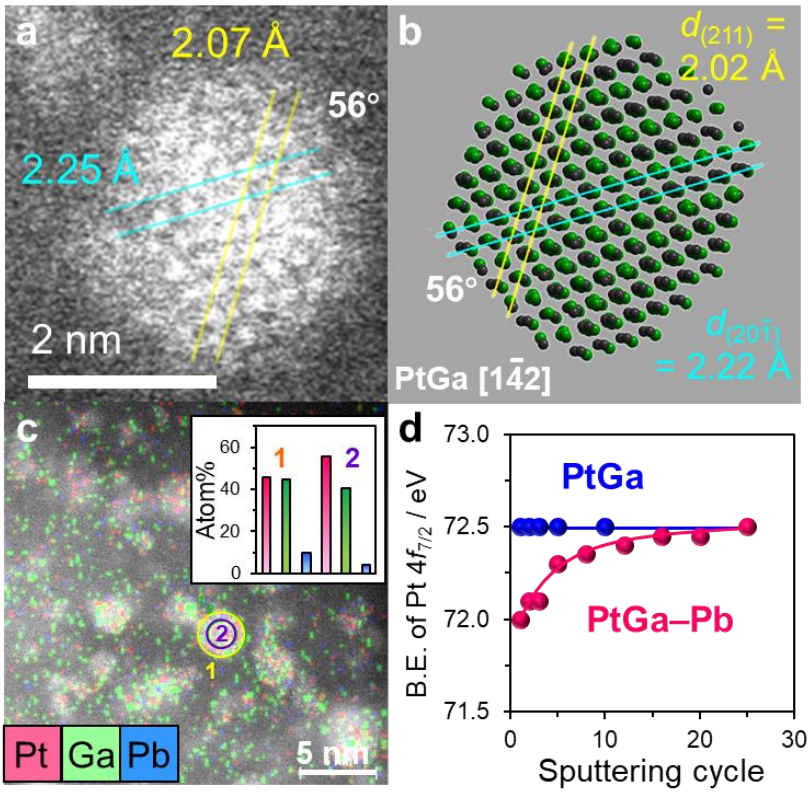

Figure 21. Characterization of PtGa–Pb/SiO_2. (a) HAADF-STEM image of a single nanoparticle in PtGa–Pb/SiO_2 (Pt/Pb = 2). (b) Crystal structure of intermetallic PtGa viewed along [1$\bar{4}$2] direction. (c) Elemental map of Pt, Ga, and Pb acquired by EDX. Inset shows their atom% included in areas 1 (yellow circle) and 2 (purple circle), corresponding to the whole and core region of a single nanoparticle. (d) Changes in Pt 4$f_{7/2}$ binding energy (B.E.) of PtGa/SiO_2 and PtGa–Pb/SiO_2 (Pt/Pb = 2) during sputtering cycles.

agreed with those of (211) and (20$\bar{1}$) planes of intermetallic PtGa viewed along with [1$\bar{4}$2] direction (Figure 21b).[31] Theparticle size distribution was narrow (mostly 1.5~3 nm) with an average of 2.8 ± 0.6 nm. The elemental map acquired by EDX analysis showed that Pt and Ga were homogeneously distributed in each nanoparticle with approximately 1:1 ratio (Figure 21c). Similar results of the HAADF-STEM-EDX analyses were also obtained for PtGa/SiO_2. On the contrary, the Pb distribution in PtGa–Pb/SiO_2 was focused on the shell part of nanoparticles (areas 1 and 2 in Figure 21c). Considering that the Pb content in the whole nanoparticle (area 1) is lower than those fed in the catalyst (Pt/Pb =2), a part of Pb may present on SiO_2 support. XPS analysis with Ar^+ sputtering revealed that the Pt4$f_{7/2}$ binding energy of PtGa–Pb was lower than that of PtGa (due to ligand effect of Pb[32]), but came close immediately after several sputtering (Figure 21d). This result strongly supports that Pb is located at the surface region of PtGa nanoparticles. We also performed XAFS analysis (Figures 22 and 23). Pt–Ga scattering with 2.50 ± 0.01 Å was observed for PtGa–Pb (Table 3), which is consistent finely with the interatomic distance of the nearest Pt and Ga in PtGa (2.499 Å).[31] This result suggests that Pb atoms are not substituted into the bulk of PtGa to increase the lattice constant. Pt–Pb scattering was also observed with a small *CN* of 1.0, which indicates that the

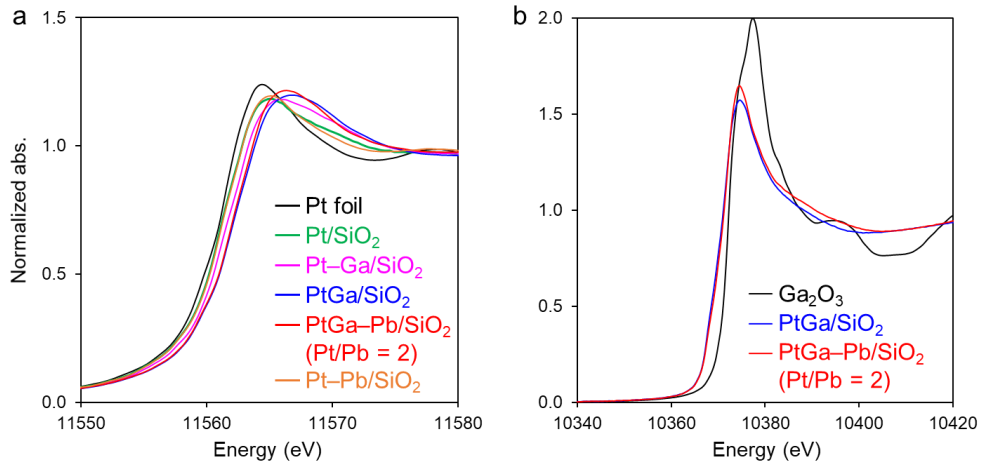

Figure 22. (a) Pt L_{III}- and (b) Ga K-edge XANES spectra of the reduced catalysts and reference compounds. The atomic ratio of Pt/M in Pt–M/SiO_2 (M = Ga and Pb) was 3.

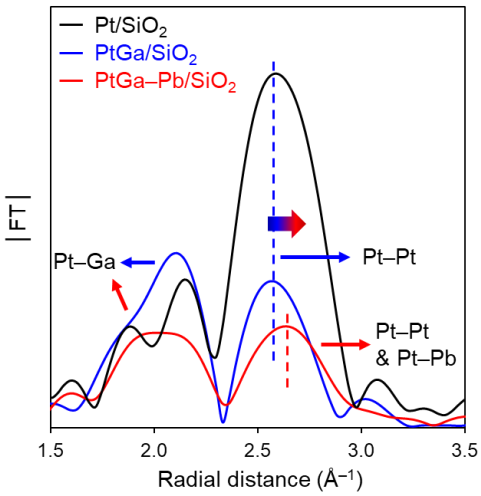

Figure 23. Magnitude of Fourier transform of the k^3-weighted EXAFS spectra of reduced catalysts. Δk = 3–16 Å.

Table 3. Summary of the Pt L_{III}-edge k^3-weighted EXAFS curve fitting for Pt-based catalysts and reference Pt foil.

Sample	Shell	S_o^{2}[a]	*CN*	*R* (Å)[b]	ΔE_o (eV)[c]	σ^2 (Å^2)[d]	R-factor (R^2)
Pt foil	Pt–Pt	0.91	12.0 (fix)	2.77 ± 0.00	4.8 ± 0.4	0.005 ± 0.000	0.002
Pt/SiO_2	Pt–Pt	0.91	7.0 ± 0.4	2.73 ± 0.00	3.9 ± 0.7	0.007 ± 0.000	0.009
$Pt–Ga/SiO_2$	Pt–Ga	0.91	1.6 ± 1.1	2.50 ± 0.01	−1.9 ± 1.3	0.013 ± 0.005	0.015
(Pt/Ga = 3)	Pt–Pt	0.91	5.2 ± 0.8	2.71 ± 0.01		0.008 ± 0.001	
$PtGa/SiO_2$	Pt–Ga	0.91	2.6 ± 0.5	2.49 ± 0.01	−4.4 ± 1.1	0.011 ± 0.001	0.010
	Pt–Pt	0.91	2.7 ± 0.4	2.70 ± 0.01		0.007 ± 0.001	
$PtGa–Pb/SiO_2$	Pt–Ga	0.91	1.8 ± 0.3	2.50 ± 0.01		0.010 ± 0.001	
	Pt–Pt	0.91	4.5 ± 1.3	2.75 ± 0.01	−1.7 ± 2.0	0.010 ± 0.001	0.007
	Pt–Pb	0.91	1.0 ± 1.0	2.88 ± 0.03		0.012 ± 0.006	
$Pt–Pb/SiO_2$ (Pt/Pb = 3)	Pt–Pt	0.91	7.5 ± 0.3	2.74 ± 0.01	2.3 ± 0.5	0.007 ± 0.000	0.004

[a]Amplitude factor. [b]Distance between absorber and backscatterer atoms. [c]Correction term in the absorption edge. [d]Disorder term (EXAFS Debye–Waller factor).

surface Pt sites are partly blocked by Pb deposition. CO pulse chemisorption experiment supported the partial coverage of surface Pt, where Pt dispersion decreased from 9.9% to 5.9% upon the Pb modification to $PtGa/SiO_2$. To obtain further information about the surface of $PtGa–Pb/SiO_2$, we then performed FT-IR spectroscopy with CO adsorption at −196°C (Figure 24). For $PtGa/SiO_2$, two peaks appeared at 2078 and 1885 cm^{-1} at the initial stage, which are assigned to stretching vibration of CO adsorbed on Pt with on-top and three-fold modes, respectively.[21] Upon the increase in CO pressure (P_{CO}), the threefold CO disappeared and the intensity of the on-top CO increased with an appearance of a small shoulder feature at around 2050 cm^{-1}. This change could be attributed to the migration of three-fold CO to on-top CO on the Pt_3 site due to the increase of CO coverage. The new shoulder at around 2050 cm^{-1} might be assigned to on-top CO adsorbed on Pt_1 site.[21] On the contrary, for $PtGa–Pb/SiO_2$, only a single symmetric adsorption band appeared at 2040 cm^{-1} with lower intensity even at saturation coverage, which implies that the Pt_3 sites are blocked by Pb while the remaining Pt_1 sites are open for CO adsorption. We then simulated the theoretical $\nu_{C=O}$ for the suggested conformations by DFT calculations. The calculated $\nu_{C=O}$ values were consistent finely (on-top CO) or roughly (threefold CO) with the corresponding experimental values, which strongly supports the assignment mentioned above. The observed trend agreed also with a relevant system of CO adsorption on PdGa:B(111) monitored by surface science techniques.[21] Only a slight red-shift in $\nu_{C=O}$ (2043 to 2037 cm^{-1}) was suggested when Pb was added near the Pt_1 site, likely because of electron-enriched Pt by the ligand effect of Pb as observed in Figure 24. Thus, we successfully prepared an ideal catalyst for PDH with single-atom-like isolated Pt without any Pt–Pt ensembles.

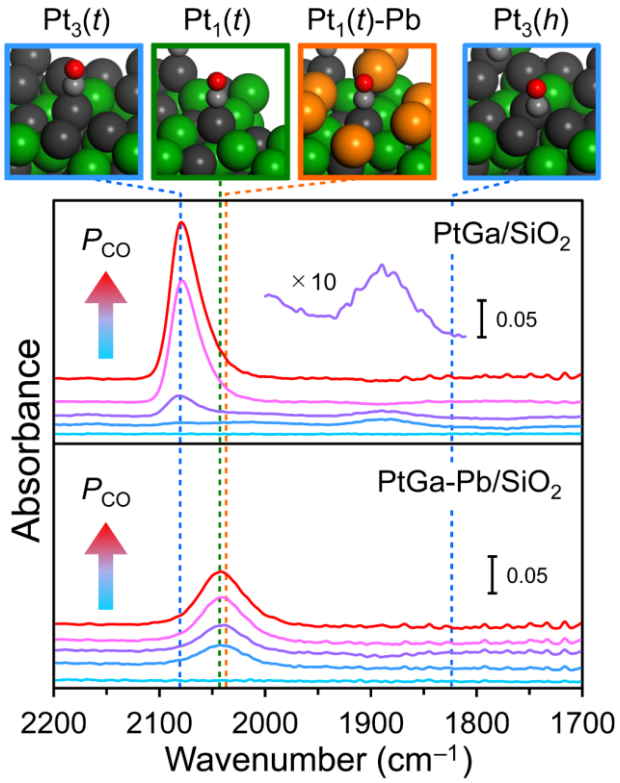

Figure 24. Surface characterization by FT-IR with CO adsorption. Changes in FT-IR spectra of CO adsorbed on $PtGa/SiO_2$ and $PtGa–Pb/SiO_2$ (Pt/Pb = 2) with increase in P_{CO} measured at −196°C are shown. Vertical dashed lines indicate $\nu_{C=O}$ values calculated by DFT. The upper pictures show the optimized structures of on-top CO (*t*) on Pt_3, Pt_1, and Pt_1-Pb sites, and threefold CO (*h*) on Pt_3 hollow site.

3.3.2. Catalytic Performance in PDH.

Next, we tested the catalytic performances of the prepared catalysts in PDH at 600°C (Figure 25). Although PtGa exhibited high conversion and selectivity at the initial stage (40% conv. 99.1% sel. at 0.5 h), conversion gradually decreased below half of its initial value within 50 h. Conversely, PtGa–Pb retained high conversion and excellent selectivity (>30% conv. >99.6% sel.) for 50 h even under the harsh condition. It should be noted that almost no deactivation was observed even at 96 h (Figure 26). Thus, the Pb-modification to PtGa significantly improved the stability and selectivity. We achieved the long-term, continuous, and highly selective propylene production in PDH at high temperatures without deactivation (>580°C: see Tables 4, 5, and Figure 27 for comparison with literatures). We also tested Pt_3Sn catalyst, the well-known catalyst selective for PDH,[1,7] which gave lower conversion, selectivity, and stability (higher deactivation rate, Table 6) than PtGa, highlighting the outstandingly high catalytic performance of PtGa–Pb. The spent catalysts were then analyzed by TPO and the HAADF-STEM-EDX analysis. PtGa and Pt_3Sn showed coke combustion peaks in their TPO profiles, while PtGa–Pb gave no peak (Figure 28). This is consistent with the stability trend in Figure 25 and suggests that the coke formation process is strictly inhibited. The HAADF-STEM-EDX analysis revealed that, despite the long-term operation (50 h) in the harsh condition, PtGa–Pb retained its small particles sizes (flesh: 2.8 ± 0.6 nm, spent: 3.0 ± 0.6 nm), intermetallic structure,

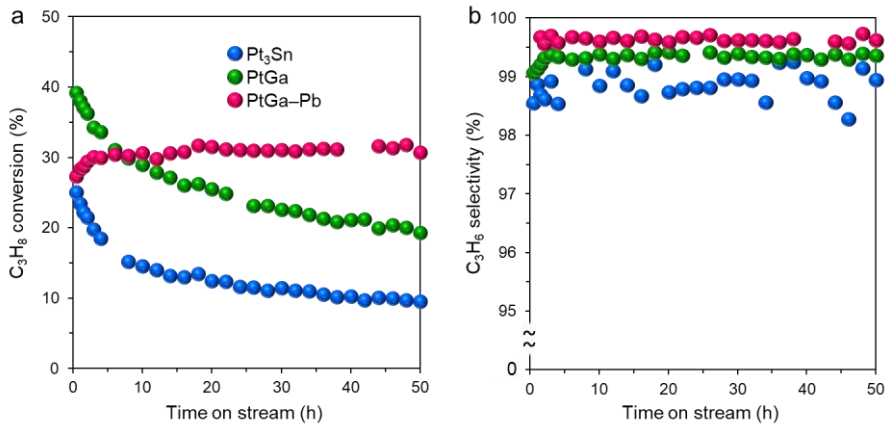

Figure 25. Catalytic performance in PDH. Changes in propane conversion (a) and propylene selectivity (b) in PDH catalyzed by $PtGa/SiO_2$, $PtGa–Pb/SiO_2$ (Pt/Pb = 2) and Pt_3Sn/SiO_2 are shown. Catalyst amount was adjusted so that the number of exposed Pt was identical (4.5 μmol): PtGa (9.0 mg), PtGa–Pb (Pt/Pb = 2) (15 mg), Pt_3Sn (3.7 mg), and diluted with quartz sand (total 1.5 g). Gas feed: C_3H_8:H_2:He = 3.9:5.0:40 mL min^{-1}. Temperature: 600°C.

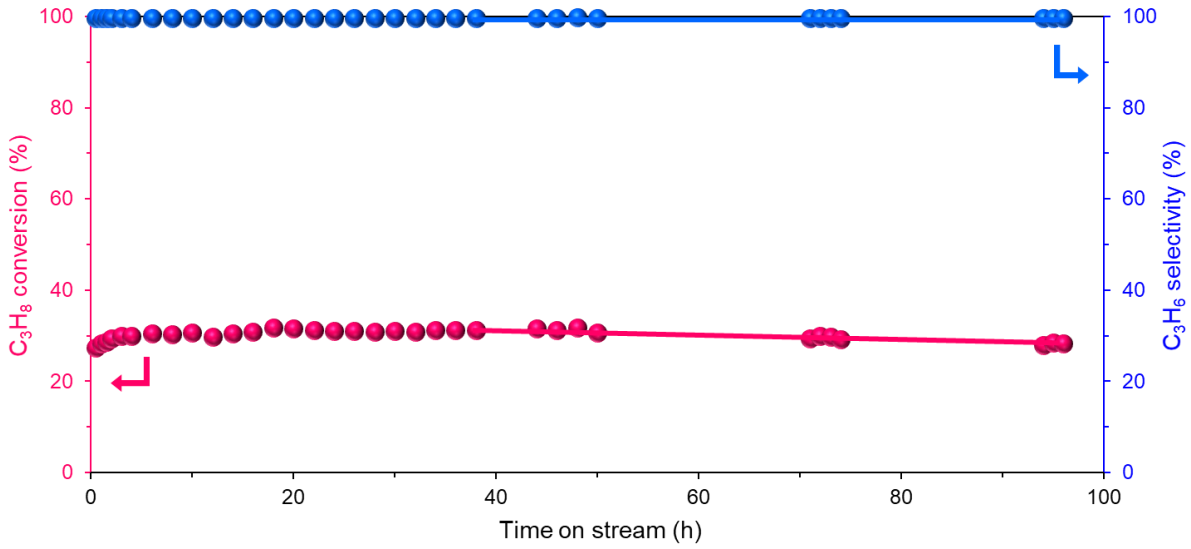

Figure 26. Long-term stability test in PDH on $PtGa–Pb/SiO_2$ (Pt/Pb = 2) at 600°C.

Table 4. Summary of the catalytic data of PtGa−Pb and other reported Pt-based catalysts for PDH.

Entry	Catalyst	Pt (wt%)	Temp. (°C)	Conversion (%)[a]	C_3H_6 Selectivity (%)[b]	Specific activity (s^{-1})[c]	k_d (h^{-1})[d]	Ref.
1	PtIn/Mg(Al)O-600	0.6	620	69–50	98	0.45	0.027	7
2	PtIn/Mg(Al)O-x	0.6	620	66.4–43.5	95	0.43	0.118	8
3	0.3PtSn/1.5In-Al	0.3	620	58.4–48.6	93.5	0.75	0.144	9
4	PtGa/SiO_2	3	600	44.7–24.5	98.8	0.56	0.018	This
5	PtGa−Pb/SiO_2 (Pt/Pb = 2)	3	600	30.0 (4 h)–28.4	99.6	0.38	0.001	Study
6	Pt/Mg(Sn)(Al)O	0.5	600	48.3–43.0	86.4	1.05	0.002	10
7	Pt_3In/SiO_2	0.3	600	17.5–17	92	0.08	0.018	11
8	Pt3Ga/CeAl	1	600	41.1–32.2	99.6	0.52	0.026	12
9	Pt3Ga/Al_2O_3	1	600	39.4–28.1	99.5	0.50	0.034	12
10	Pt/CeAl	1	600	47.1–22.2	62	0.59	0.076	12
11	PtSn/TS-1	0.5	600	53.5–47.7	92.5	0.41	0.033	13
12	15%Zn-0.1%/Al_2O_3	–	600	35–31	94	–	0.045	14
13	Pt/TA0	1	600	50.5–21.0	60	0.64	0.134	15
14	Pt/TA10	1	600	47.3–25.9	77	0.60	0.094	15
15	Pt/TA20	1	600	45.5–17.8	89	0.57	0.135	15
16	PtSnIn/08Zr-Al	0.3	600	57.7–51.7	98	0.74	0.097	16
17	0.1Pt10Cu/Al_2O_3	0.1	600	40–22	90	1.97	0.215	17
18	Pt-Sn/SAPO-34-500	0.5	595	34.6–43.9	66	0.48	0.149	18
19	Pt/Al_2O_3 sheet	0.36	590	42.7–15.9	93	1.38	0.058	19
20	PtSn/Al_2O_3 sheet	0.35	590	48.7–44.6	98	1.62	0.007	19
21	Pt-Sn-Na/Al-SBA-15	0.5	590	27.5–12.6	94	0.20	0.024	20
22	Pt-Na/Sn-ZSM-5	0.5	590	41.7–39.1	95.3	0.30	0.011	21
23	PtNa/Zn(1.0%)-ZSM-5	0.5	590	40.6–37.8	93	0.29	0.012	22
24	Pt-Sn/mesoporous Al_2O_3	0.5	590	29.8–24.6	92	0.22	0.044	23
25	Pt-Sn/ZSM-5	0.5	590	33.1–26.3	47.7	0.24	0.054	23
26	Pt-Sn/γ–Al_2O_3	0.5	590	29.4–22.7	76	0.21	0.058	23
27	Pt-Sn/SBA-15	0.5	590	11.0–6.0	80	0.08	0.110	23
28	PtSn$Al_{0.2}$/SBA-15	0.5	590	55.9–40.5	98.5	0.32	0.104	24
29	Pt-Cu/$MgAl_2O_4$	1	590	25.7–21.0	87.5	0.24	0.011	25
30	Pt-Ag/$MgAl_2O_4$	1	590	30.6–16.7	95.1	0.28	0.034	25
31	Pt-Au/$MgAl_2O_4$	1	590	33.7–16.6	60	0.31	0.040	25
32	Pt-Sn-2/$MgAl_2O_4$	0.55	580	44–18.7	92	0.23	0.014	26

33	Pt-Sn-3/$MgAl_2O_4$	0.53	580	42–18.7	97	0.23	0.013	26
34	Pt-Sn-4/$MgAl_2O_4$	0.5	580	50–31.5	98	0.29	0.009	26
35	Pt-Sn-5/$MgAl_2O_4$	0.42	580	45–37.6	98	0.31	0.003	26
36	Pt-Sn-6/$MgAl_2O_4$	0.39	580	44–38.9	99	0.33	0.002	26
37	Pt/0.5Sn-SBA-15	0.72	580	43.8–38.3	98.5	0.62	0.038	27
38	Pt-Sn/$MgAl_2O_4$-ALT	1	575	33–29	99	0.59	0.057	28
39	$Pt^0Zn^{\delta+}/SiO_2$	3.05	550	30.2–16.1	98.1	0.96	0.027	29
40	$Ga^{\delta+}Pt^0/SiO_2$	1.55	550	31.9–18.2	99	1.36	0.038	3
41		1.55	550	36.5–26.9	90.9	0.76	0.023	3
42		1.55	550	40.7–38.5	63.5	0.04	0.005	3
43	Pt/Mg(Sn)(Al)O	0.5	550	29.4–27.8	93.7	0.64	0.001	10
44	2Pt-0.6Sn/γ–Al_2O_3	2	540	42.9–39.2	93.7	0.09	0.020	30
45	2Pt-1.2Sn/γ–Al_2O_3	2	540	43.5–41.4	96.9	0.09	0.011	30
46	2Pt-2.4Sn/γ–Al_2O_3	2	540	42.8–41.7	98.3	0.09	0.006	30
47	2Pt-3.6Sn/γ–Al_2O_3	2	540	42.8–41.8	98.6	0.09	0.005	30
48	0.1Pt10Cu/Al_2O_3	0.1	520	13.1–12.4	90	0.65	0.001	17
49	Pt-Na-[Fe]/ZSM-5	0.1	520	33–13	98.3	1.51	0.008	31

[a]The first value was obtained at the beginning of the run, and the second at the end. [b]The C_3H_6 selectivity was obtained at the beginning of the run. [c]Defined as (mol reacted propane) per (mol Pt*t(s)). [d]The first-order deactivation model was used to estimate the catalytic stability.[3]

Table 5. Summary of the catalytic data of PtGa−Pb and other reported Pt-based catalysts for PDH.

Entry	catalyst	Pt (wt%)	Temp. (°C)	WHSV (h^{-1})[a]	Gas composition	τ (h)[b]	Operation time (h)[c]	Ref.
1	PtIn/Mg(Al)O-600	0.6	620	3.3	$C_3H_8/H_2/Ar$ = 8/7/35	37.5	41.0	7
2	PtIn/Mg(Al)O-x	0.6	620	3.3	$C_3H_8/H_2/Ar$ = 8/7/35	8.5	8.0	8
3	0.3PtSn/1.5In-Al	0.3	620	3.3	$C_3H_8/H_2/Ar$ = 8/7/35	7.0	2.8	9
4	$PtGa/SiO_2$	3	600	30.7	C_3H_8 = 3.9, H_2 = 5, He = 40	54.1	50.0	This study
5	$PtGa–Pb/SiO_2$ (Pt/Pb = 2)	3	600	30.7	C_3H_8 = 3.9, H_2 = 5, He = 40	1159.0	96.0	Study
6	Pt/Mg(Sn)(Al)O	0.5	600	14	$C_3H_8/H_2/Ar$ = 1/0.5/2	561.2	48.0	10
7	Pt_3In/SiO_2	0.3	600	3	C_3H_8/H_2 = 1/1, balance N_2	57.1	2.5	11
8	Pt3Ga/CeAl	1	600	10	C_3H_8/H_2 = 1/1, balance N_2	39.0	15.0	12
9	$Pt3Ga/Al_2O_3$	1	600	10	C_3H_8/H_2 = 1/1, balance N_2	29.5	15.0	12
10	Pt/CeAl	1	600	10	C_3H_8/H_2 = 1/1, balance N_2	13.2	15.0	12
11	PtSn/TS-1	0.5	600	3	$C_3H_8/H_2/N_2$ = 1/1/4	30.1	7.0	13
12	$15\%Zn-0.1\%/Al_2O_3$	–	600	3	C_3H_8/H_2 = 1/1, balance N_2	22.1	4.0	14
13	Pt/TA0	1	600	10	$C_3H_8/H_2/N_2$ = 13/13/24	7.4	10.0	15
14	Pt/TA10	1	600	10	$C_3H_8/H_2/N_2$ = 13/13/24	10.6	10.0	15
15	Pt/TA20	1	600	10	$C_3H_8/H_2/N_2$ = 13/13/24	7.4	10.0	15
16	PtSnIn/08Zr-Al	0.3	600	3.3	$C_3H_8/H_2/Ar$ = 8/7/35	10.3	2.5	16
17	$0.1Pt10Cu/Al_2O_3$	0.1	600	4.0	C_3H_8/H_2 = 1/1	4.7	4.0	17
18	Pt-Sn/SAPO-34-500	0.5	595	5.6	C_3H_8/H_2 = 4/1	6.7	8.0	18
19	Pt/Al_2O_3 sheet	0.36	590	9.4	$C_3H_8/H_2/N_2$ = 1:1.25:4	17.1	24.0	19
20	$PtSn/Al_2O_3$ sheet	0.35	590	9.4	$C_3H_8/H_2/N_2$ = 1:1.25:4	142.6	24.0	19
21	Pt-Sn-Na/Al-SBA-15	0.5	590	3.0	C_3H_8/H_2 = 75/25	41.3	40.0	20
22	Pt-Na/Sn-ZSM-5	0.5	590	3.0	C_3H_8/H_2 = 75/25	92.6	9.0	21
23	PtNa/Zn(1.0%)-ZSM-5	0.5	590	3.0	C_3H_8/H_2 = 4/1	85.1	9.0	22
24	Pt-Sn/mesoporous Al_2O_3	0.5	590	3.0	C_3H_8/H_2 = 4	22.8	6.0	23
25	Pt-Sn/ZSM-5	0.5	590	3.0	C_3H_8/H_2 = 4	18.4	6.0	23
26	$Pt-Sn/\gamma–Al_2O_3$	0.5	590	3.0	C_3H_8/H_2 = 4	17.2	6.0	23
27	Pt-Sn/SBA-15	0.5	590	3.0	C_3H_8/H_2 = 4	9.1	6.0	23
28	$PtSnAl_{0.2}$/SBA-15	0.5	590	2.5	C_3H_8/Ar = 1/5	9.6	6.0	24
29	$Pt-Cu/MgAl_2O_4$	1	590	6.8	C_3H_8 = 19, H_2 = 19, He = 2	89.2	24.0	25
30	$Pt-Ag/MgAl_2O_4$	1	590	6.8	C_3H_8 = 19, H_2 = 19, He = 2	29.8	24.0	25
31	$Pt-Au/MgAl_2O_4$	1	590	6.8	C_3H_8 = 19, H_2 = 19, He = 2	25.1	24.0	25
32	$Pt-Sn-2/MgAl_2O_4$	0.55	580	2.4	C_3H_8 = 2, H_2 = 2, He = 16	73.3	90.0	26
33	$Pt-Sn-3/MgAl_2O_4$	0.53	580	2.4	C_3H_8 = 2, H_2 = 2, He = 16	78.5	90.0	26
34	$Pt-Sn-4/MgAl_2O_4$	0.5	580	2.4	C_3H_8 = 2, H_2 = 2, He = 16	115.9	90.0	26

35	Pt-Sn-5/$MgAl_2O_4$	0.42	580	2.4	C_3H_8 = 2, H_2 = 2, He = 16	294.2	90.0	26
36	Pt-Sn-6/$MgAl_2O_4$	0.39	580	2.4	C_3H_8 = 2, H_2 = 2, He = 16	427.8	90.0	26
37	Pt/0.5Sn-SBA-15	0.72	580	8.3	C_3H_8/Ar = 7/3	26.4	6.0	27
38	Pt-Sn/$MgAl_2O_4$-ALT	1	575	14.7	C_3H_8/H_2 = 1.2, balance He	17.6	3.3	28
39	$Pt^0Zn^{\delta+}/SiO_2$	3.05	550	75	C_3H_8/Ar = 10/40	36.8	3.5	29
40	$Ga^{\delta+}Pt^0/SiO_2$	1.55	550	98.3	C_3H_8/Ar = 1:4	26.5	20.0	3
41		1.55	550	43.3	C_3H_8/Ar = 1:4	44.2	20.0	3
42		1.55	550	2.0	C_3H_8/Ar = 1:4	214.1	20.0	3
43	Pt/Mg(Sn)(Al)O	0.5	550	14	C_3H_8/H_2/Ar = 1/0.5/2	1531.2	240.0	10
44	2Pt-0.6Sn/γ–Al_2O_3	2	540	3.5	$C_3H_8/H_2/N_2$ = 6/2/42	49.0	6.0	30
45	2Pt-1.2Sn/γ–Al_2O_3	2	540	3.5	$C_3H_8/H_2/N_2$ = 6/2/42	87.2	6.0	30
46	2Pt-2.4Sn/γ–Al_2O_3	2	540	3.5	$C_3H_8/H_2/N_2$ = 6/2/42	166.4	6.0	30
47	2Pt-3.6Sn/γ–Al_2O_3	2	540	3.5	$C_3H_8/H_2/N_2$ = 6/2/42	183.0	6.0	30
48	0.1Pt10Cu/Al_2O_3	0.1	520	4.0	C_3H_8/H_2 = 1/1	1906.6	120.0	17
49	Pt-Na-[Fe]/ZSM-5	0.1	520	15.1	C_3H_8/He = 25/75	125.0	166.0	31

[a]WHSV: weight hourly space velocity (h^{-1}). [b]Expected catalyst life defined as $\tau = k_d^{-1}$. [c]operation time: total time tested for a single run.

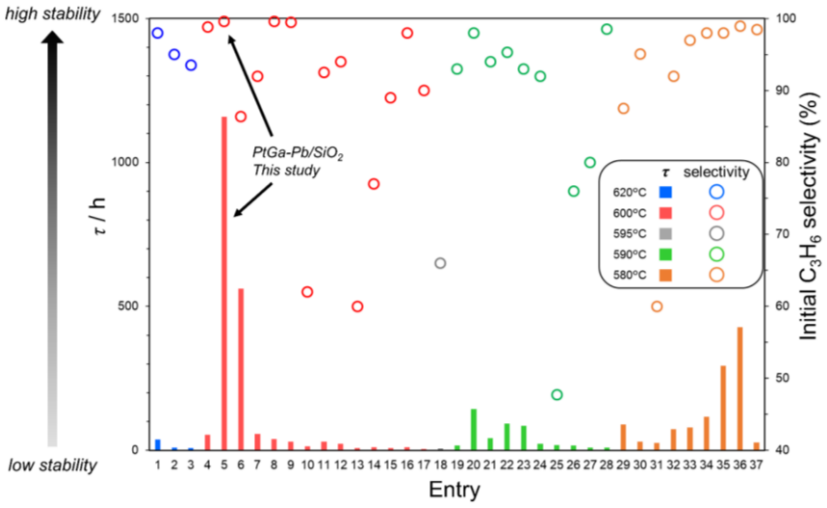

Figure 27. At-a-glance chart of the catalytic performance of PtGa–Pb/SiO_2 (Pt/Pb = 2) and existing Pt-based catalysts in PDH (references are listed in Tables 4 and 5). Expected catalyst life ($\tau = k_d^{-1}$) and initial C_3H_6 selectivity are categorized by reaction temperature (580~620°C). The results of previous studies conducted at temperatures lower than 570°C and higher than 630°C were omitted due to low C_3H_8 conversion or production rate and the lack of long-term stability, respectively.

Table 6. Summary of catalytic performance of SiO_2-supported Pt-based materials in PDH at 600°C. [a] Deactivation rate constant. [b] Expected catalyst life.

Catalyst	C_3H_8 conversion (%)		k_d (h^{-1})[a]	τ (h)[b]	C_3H_6 selectivity (%) at 0.5 h
	at 0.5 h	at 50 h			
Pt	30.7	10.8	0.026	38.2	86.8
Pt–Ga (Pt/Ga = 3)	38.9	17.7	0.022	45.6	89.8
PtGa	44.7	24.5	0.018	54.1	98.8
PtGa–Pb (Pt/Pb = 2)	30.3 (4 h)	28.4 (96 h)	0.001	1159	99.6
Pt_3Sn	39.1	18.0	0.022	46.1	97.5
PtSn	33.6	21.0	0.013	76.9	99.2
Pt_3In	34.6	13.9	0.024	41.7	94.9
Pt–Pb (Pt/Pb = 3)	28.8	13.7	0.019	53.0	96.1

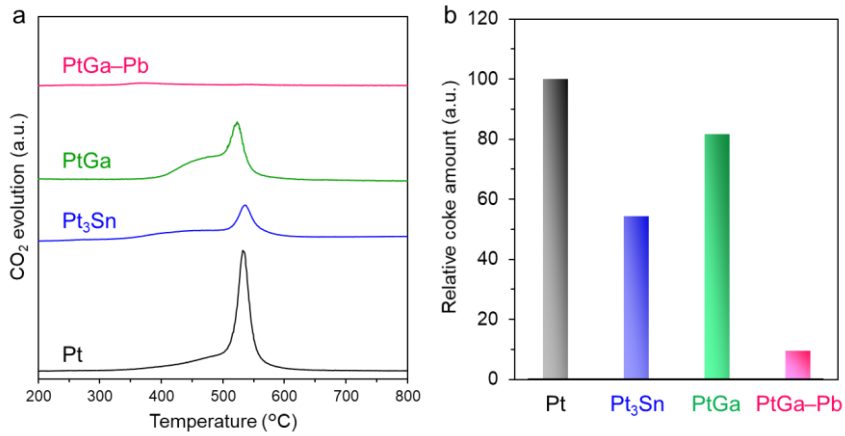

Figure 28. (a) TPO profiles of the spent catalysts (without quartz sand) in the dehydrogenation of propane at 600°C for 20 h. (b) The relative coke amount accumulated on the catalysts (200–800°C) estimated from TPO experiment.

and elemental distribution, demonstrating the high thermal stability and resistance to sintering. The stability test was also conducted at 650°C, where PtGa–Pb retained high conversion (37~38%) for several hours and then gradually decreased to approximately 20% over 50 h. The gradual deactivation can be attributed to the contribution of thermal (noncatalytic) cracking.[58] This was confirmed by a control experiment using SiO_2, in which small amount of C_1 and C_2 were formed at 650°C, while that was negligible at 600°C. Other bimetallic combinations that have been reported to be effective for PDH (PtSn[59] and Pt_3In[37]) were also tested at 600°C. However, they all showed deactivation trends similar to that of Pt_3Sn. Considering that Pt–Ga (Pt/Ga = 3) gave higher deactivation rate and lower selectivity than PtGa, using 1:1 PtGa phase is a significant factor to develop a highly efficient catalytic system for PDH. When the modifier for PtGa was changed from Pb to other metals such as In or Sn, no positive effects on activity and selectivity were obtained. We also tested the recyclability of PtGa–Pb catalyst. The spent PtGa–Pb catalyst could be regenerated by O_2 treatment to recover the original catalytic performance after some induction period, whereas some bimetallic or trimetallic other Sn-containing catalysts (Pt_3Sn, PtSn, and PtGa–Sn) did not. Therefore, the combination of intermetallic PtGa and the Pb modification is suitable for stabilizing single-atom-like isolated Pt at high temperature. This is probably because (1) PtGa itself is thermodynamically stable (ΔH_f = –55.6 kJ mol^{-1})[18,19] and (2) the atomic radius[60] of Pb (1.80 Å) is much larger than those of Pt (1.35 Å) and Ga (1.30 Å): the diffusion of Pb into the bulk of PtGa is likely to be unfavorable even at 600°C. Although several researchers have pointed that Ga works as a good promotor for Pt-based PDH as well as other typical element such as Sn or In,[55,61–66] our results indicate that the geometry and appropriate design of an active site is more significant rather than the individual chemical property of the additive element, that is, Pt should be strictly isolated. We also surveyed various Pt/Pb ratios and metal oxides as catalyst supports, which confirmed that PtGa–Pb/SiO_2 (Pt/Pb = 2) was the best. Ga itself has also been known to be active for PDH.[67] However, a control experiment using Ga/SiO_2 at 650°C showed very low conversion (<3%), indicating the negligible contribution of Ga itself to the catalysis of much more active Pt-based materials.

3.3.3. DFT Calculations.

Finally, we conducted DFT calculations for the step-wise C–H scissions of propane to clarify the detailed property of isolated Pt for selective PDH. Figure 29 summarizes the reaction scheme of PDH and the calculated energy barrier of each step (E_x: x = 1, 2, 3, and d; see Figures 30~32, Figure 33, and Table 7 for the detailed structures, energy diagram, and summarized activation energies, respectively). The adsorbed propylene (C_3H_6(a)) formed via the first and second C–H scissions undergoes desorption to gas phase (C_3H_6(g)) or further (third) C–H scission to trigger undesired side reactions.[6–10] Here, propylene selectivity depends on the difference in the two energy barriers ($\Delta E = E_3 - E_d$, shaded part in Figure 29): the larger ΔE is, the higher the selectivity is. PtGa-Pt_3 gave ΔE of 35.9 kJmol^{-1}, which was slightly larger than that of Pt_3Sn(111) (24.1 kJ mol^{-1}). Interestingly, PtGa-Pt_1 having the isolated Pt showed much larger ΔE of 64.9 kJ mol^{-1}. This is due to the remarkably high E_3 (173.2 kJ mol^{-1}) even though E_1 (typically the rate-determining step of PDH) and E_d did not differ significantly from those of PtGa-Pt_3 and Pt_3Sn-Pt_3 sites. The specifically high E_3 could be attributed to the molecular rotation from lying 1,2-π-C_3H_6 to vertically standing 2-σ-C_3H_5 conformations occurring at the convex Pt_1 site. Because of the molecular rotation and long Pt–Pt distance between the Pt_1 site and the nearest

neighboring Pt_3 site (3.06 Å), the hydrogen atom involved in the third C–H scission has to migrate a long distance toward the final state. The energy required for such an unfavorable path becomes significantly high. We also estimated the theoretical propylene selectivity based on the Arrhenius equation with ΔE, which are listed in Table 8 with the corresponding experimental values. The calculated values and their order were consistent with the experimental results, which demonstrates the validity of our calculation model. Thus, our calculation successfully reproduced the experimental trends in selectivity. The high propylene selectivity of Pt_1 sites minimizes the accumulation of coke, which leads to the outstandingly high catalyst stability. Finally, we investigated the affinity of Pb deposition to several Pt and Ga sites. Pb atoms adsorbed stably on the Pt_3, Ga_3, and concave Pt_1 (in PtGa-Pt_3 termination) sites with large adsorption energies (−462 ~ −337 kJ mol^{-1}, Figure 34), while could not on the convex Pt_1 site: the Pb atom placed on the top of the Pt_1 site migrated downward during structure optimization. This result indicates that the convex Pt_1 site is unfavorable for Pb deposition geometrically and energetically.

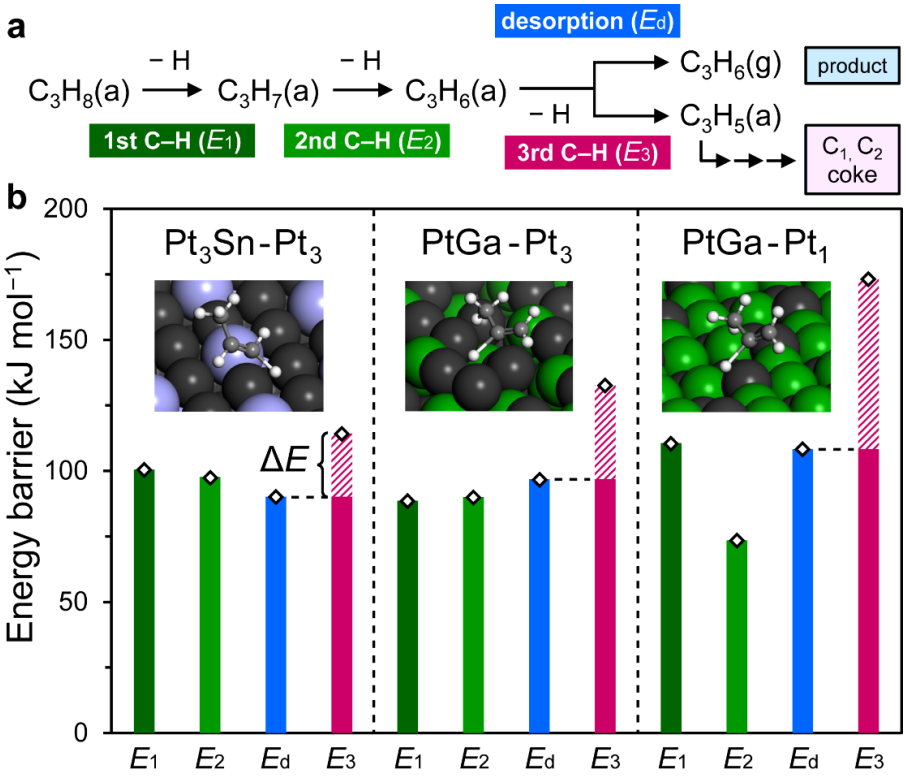

Figure 29. Theoretical interpretation of propylene selectivity. (a) The reaction scheme of PDH to generate propylene and undesired products. (b) The energy barriers of each C–H scission and propylene desorption on Pt_3Sn(111)-Pt_3, PtGa:A(111)-Pt_3, and PtGa:A(111)-Pt_3. Inset picture shows the transition state structure in the third C–H scission for each surface. Dark green, light green, magenta, and cyan bars represent the activation energies for first (E_1), second (E_2), third (E_3) C–H scissions, and propylene desorption (E_d), respectively. Shaded parts in magenta bars correspond to ΔE ($\Delta E = E_3 - E_d$).

Pt_3Sn-Pt_3 site

a $C_3H_8 \rightarrow C_3H_7 + H$

IS TS FS

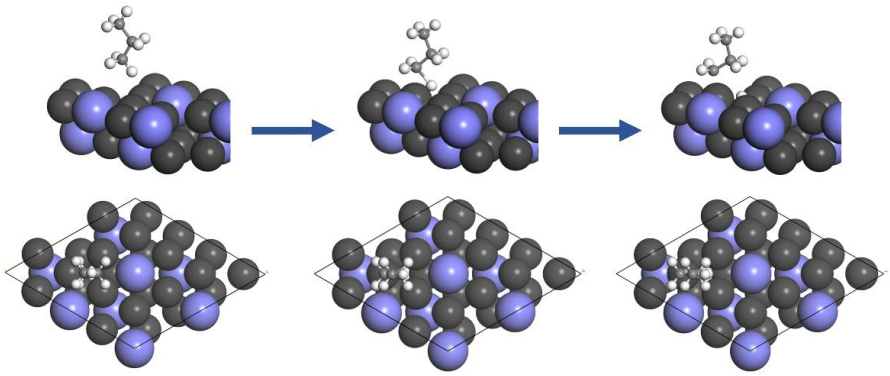

b $C_3H_7 \rightarrow C_3H_6 + H$

IS TS FS

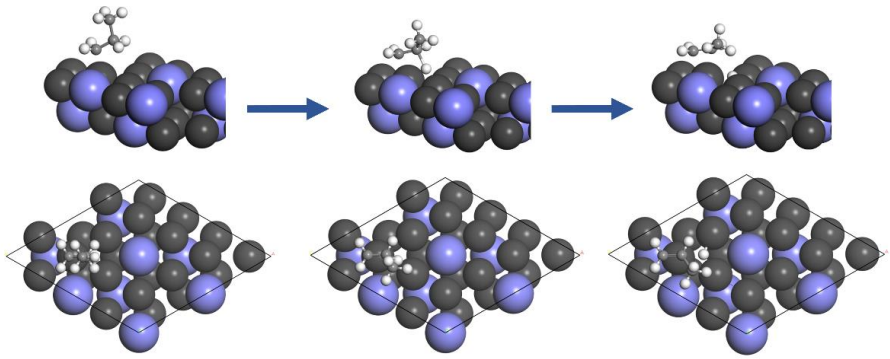

c $C_3H_6 \rightarrow C_3H_5 + H$

IS TS FS

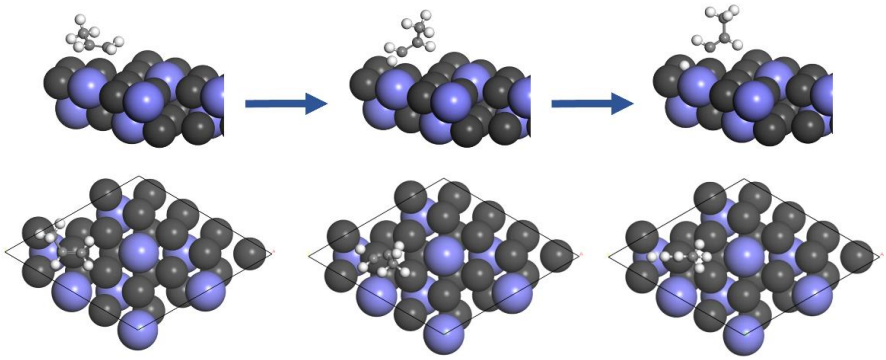

Figure 30. Structures of initial (IS), transition (TS), and final states (FS) of (a) 1st, (b) 2nd, and (c) 3rd C–H scissions in PDH on the $Pt_3Sn(111)$-Pt_3 site.

PtGa-Pt_3 site

a $C_3H_8 \rightarrow C_3H_7 + H$

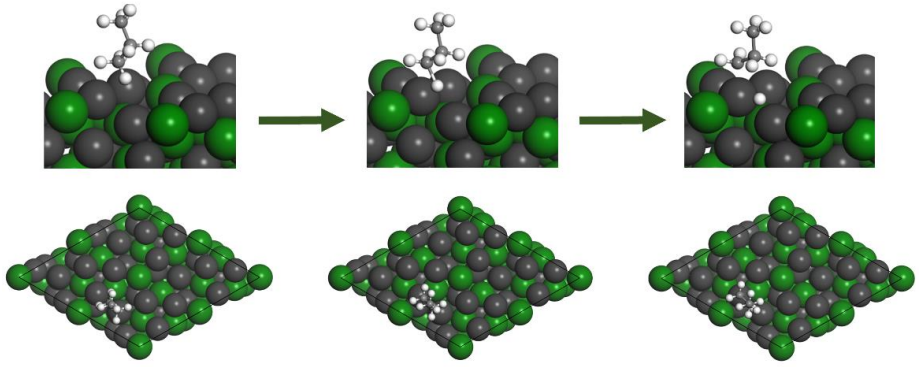

IS TS FS

b $C_3H_7 \rightarrow C_3H_6 + H$

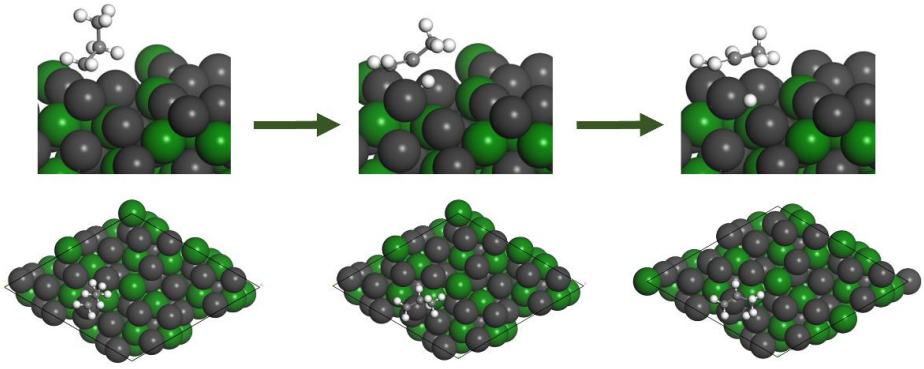

IS TS FS

c $C_3H_6 \rightarrow C_3H_5 + H$

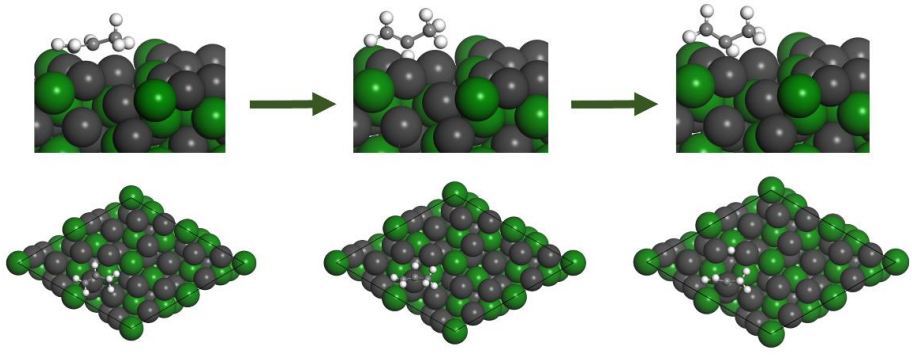

IS TS FS

Figure 31. Structures of initial (IS), transition (TS), and final states (FS) of (a) 1st, (b) 2nd, and (c) 3rd C–H scissions in PDH on the PtGa:A(111)-Pt_3 site.

PtGa-Pt_1 site

a $C_3H_8 \rightarrow C_3H_7 + H$

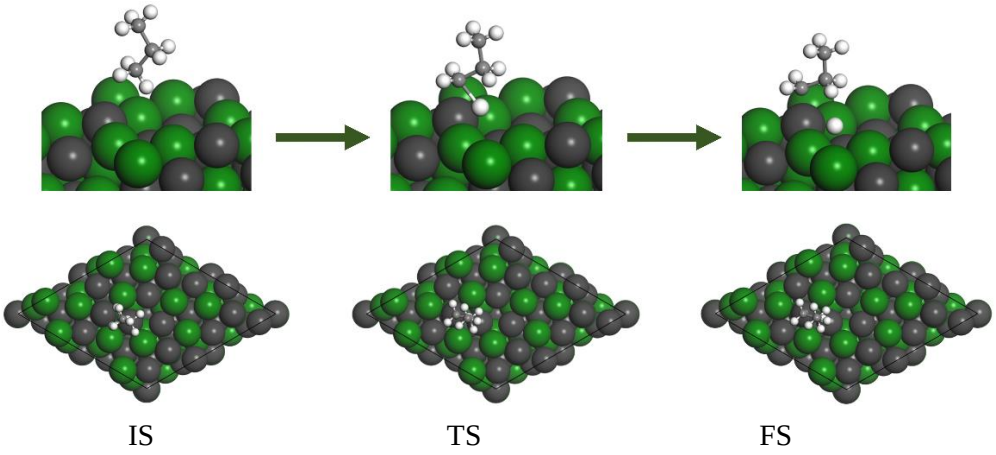

b $C_3H_7 \rightarrow C_3H_6 + H$

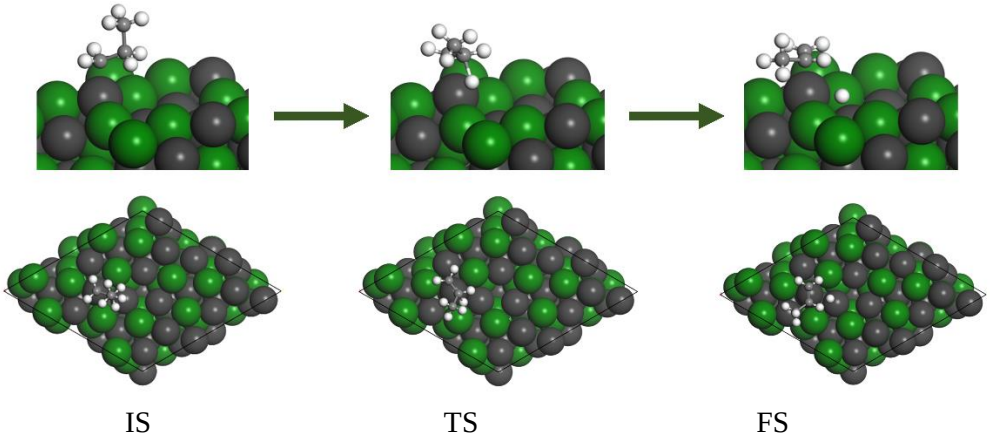

c $C_3H_6 \rightarrow C_3H_5 + H$

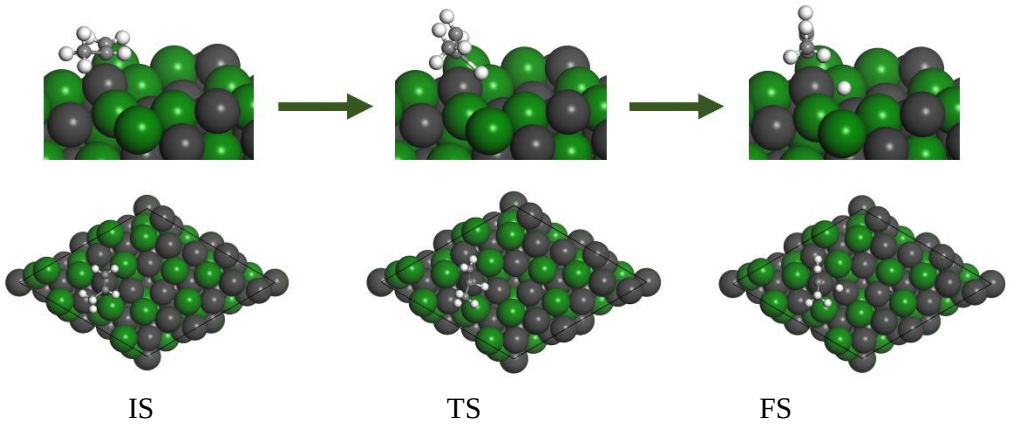

Figure 32. Structures of initial (IS), transition (TS), and final states (FS) of (a) 1st, (b) 2nd, and (c) 3rd C–H scissions in PDH on the PtGa:A(111)-Pt_1 site.

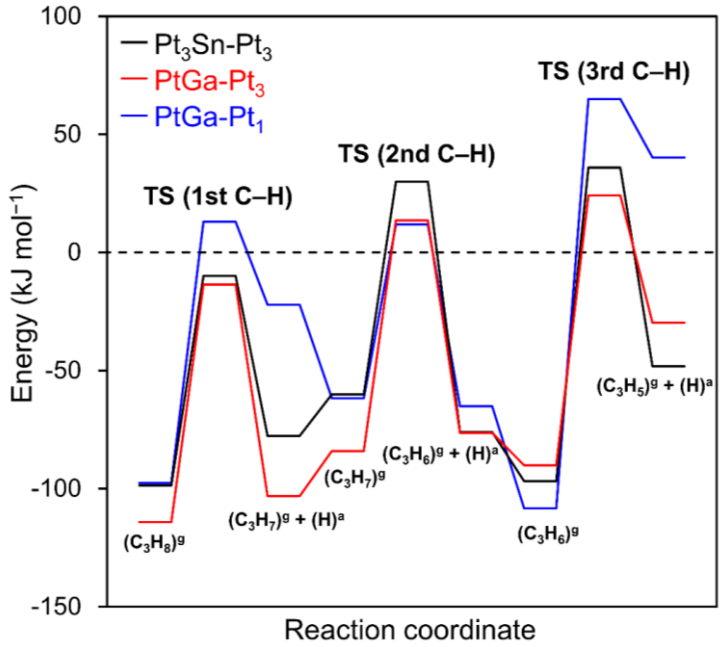

Figure 33. Energy diagram for PDH on the PtGa:A(111)-Pt_1, PtGa:A(111)-Pt_3, and Pt_3Sn(111)-Pt_3 sites calculated by DFT. The superscript "g" and "a" indicate the gaseous and adsorbed states of molecules, respectively.

Table 7. Calculated activation energy (E_a) for the dehydrogenation of propane on Pt-based surfaces.

	Activation energy (kJ mol^{-1})			
Surface	1st C–H scission ($E_a^{1st\ C–H}$)[a]	2nd C–H scission ($E_a^{2nd\ C–H}$)[b]	C_3H_6 desorption (E_a^{des})[c]	3rd C–H scission ($E_a^{3rd\ C–H}$)[d]
Pt_3Sn-Pt_3	100.5	97.6	90.1	114.3
PtGa-Pt_3	88.7	90.0	96.8	132.7
PtGa-Pt_1	110.6	73.6	108.3	173.2

[a]Activation energy for first C–H scission ($C_3H_8 \rightarrow C_3H_7 + H$). [b]Activation energy for second C–H scission ($C_3H_7 \rightarrow C_3H_6 + H$). [c]Activation energy for third C–H scission ($C_3H_6 \rightarrow C_3H_5 + H$). [d]Activation energy for C_3H_6 desorption.

Table 8. Theoretical and experimental C_3H_6 selectivity in PDH at 600°C.

Theoretical simulation			Experimental result	
Surface	ΔE (kJ mol^{-1})[a]	C_3H_6 sel. (%)	Catalyst	initial C_3H_6 sel. (%)[b]
Pt_3Sn-Pt_3	24.1	96.5	Pt_3Sn/SiO_2	98.6 (97.5)[c]
PtGa-Pt_3	35.9	99.3	$PtGa/SiO_2$	99.1
PtGa-Pt_1	64.9	>99.9	$PtGa–Pb/SiO_2$	99.6

[a]Difference between the activation energies of propylene desorption and the third C–H scission. [b]At 0.5 h of time on stream. [c]Catalyst amount: 15 mg.

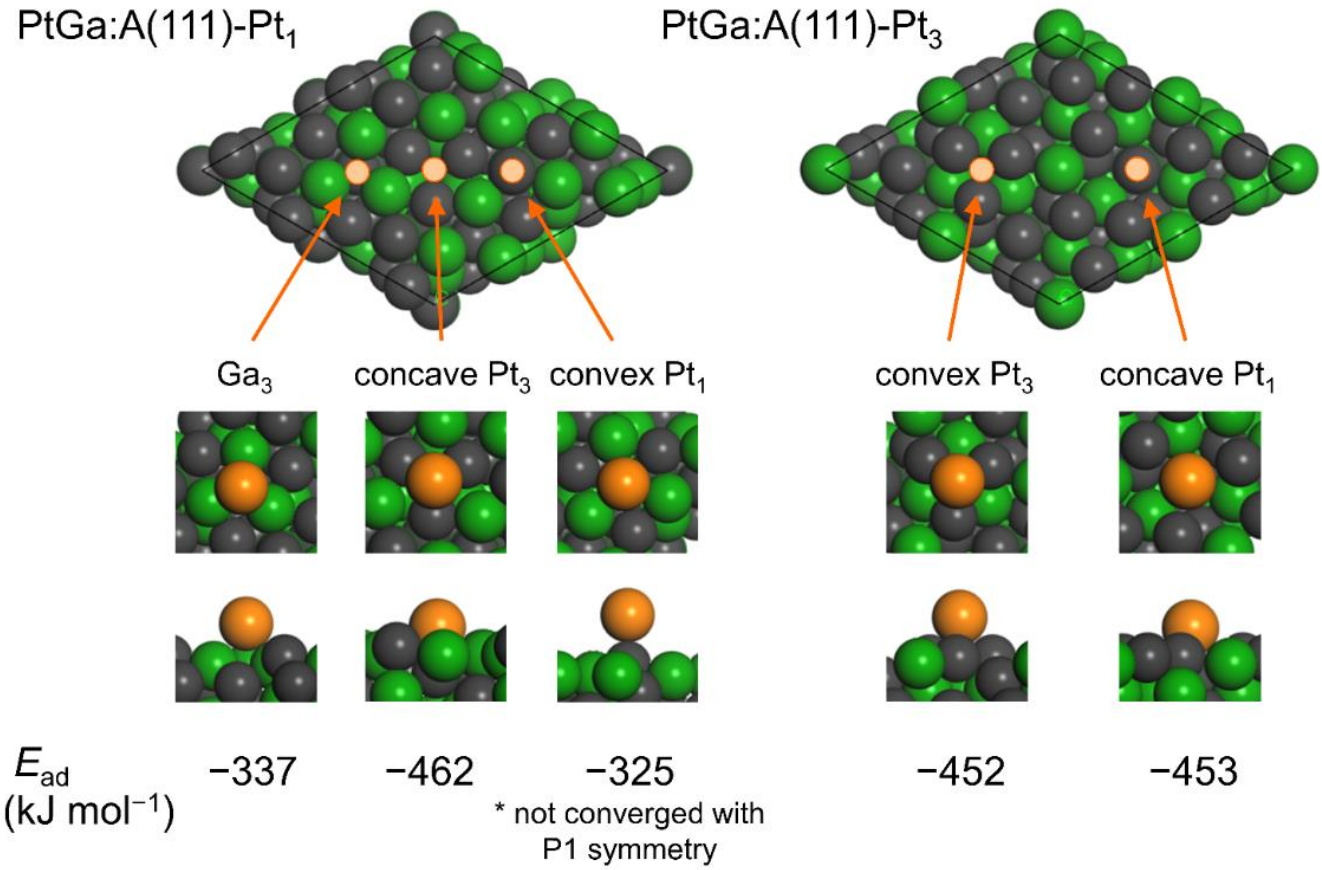

Figure 34. Adsorption energy (E_{ad}) and optimized structure of a Pb atom on various Ga_3, Pt_3, and Pt_1 sites of the two PtGa:A(111) surfaces. All calculations were done with P3 symmetry. Structure optimization for Pb on the convex Pt_1 site did not converged with P1 symmetry due to the complete migration of the Pb atom downward, which indicates that the convex Pt_1 site is actually unfavorable for Pb deposition.

3.4. Discussion

In summary, we designed and prepared the PtGa–Pb/SiO_2 catalyst for highly selective PDH, in which threefold hollow Pt_3 ensembles were successfully blocked by Pb deposition, while the single-atom-like isolated Pt_1 sites remained. The isolated Pt_1 is highly selective (99.6%) for propylene production and the catalyst is outstandingly stable for long-term operation at high temperature (96 h, 600°C). The catalytic performance in PDH is much superior to those of the reported systems. The combination of (1) the specific crystal structure of intermetallic PtGa providing isolated Pt, (2) its thermal stability, and (3) the large atomic size of Pb enables the remarkably high selectivity and stability even in harsh conditions. The results obtained in this study provide not only a highly efficient catalytic system for alkane dehydrogenation but also significant insights for material design to isolate and stabilize active metals.

Reference

1 J. J. H. B. Sattler, J. Ruiz-Martinez, E. Santillan-Jimenez and B. M. Weckhuysen, *Chem. Rev.*, 2014, **114**, 10613–10653.

2 O. O. James, S. Mandal, N. Alele, B. Chowdhury and S. Maity, *Fuel Process. Technol.*, 2016, **149**, 239–255.

3 Z. P. Hu, D. Yang, Z. Wang and Z. Y. Yuan, *Chin. J. Catal.*, 2019, **40**, 1233–1254.

4 M. M. Bhasin, J. H. McCain, B. V. Vora, T. Imai and P. R. Pujadó, *Appl. Catal. A Gen.*, 2001, **221**, 397–419.

5 D. Sanfilippo and I. Miracca, *Catal. Today*, 2006, **111**, 133–139.

6 A. W. Hauser, P. R. Horn, M. Head-Gordon and A. T. Bell, *Phys. Chem. Chem. Phys.*, 2016, **18**, 10906–10917.

7 M. L. Yang, Y. A. Zhu, X. G. Zhou, Z. J. Sui and D. Chen, *ACS Catal.*, 2012, **2**, 1247–1258.

8 S. Zha, G. Sun, T. Wu, J. Zhao, Z. J. Zhao and J. Gong, *Chem. Sci.*, 2018, **9**, 3925–3931.

9 Z. J. Zhao, C. C. Chiu and J. Gong, *Chem. Sci.*, 2015, **6**, 4403–4425.

10 L. Nykänen and K. Honkala, *ACS Catal.*, 2013, **3**, 3026–3030.

11 G. Sun, Z. J. Zhao, R. Mu, S. Zha, L. Li, S. Chen, K. Zang, J. Luo, Z. Li, S. C. Purdy, A. J. Kropf, J. T. Miller, L. Zeng and J. Gong, *Nat. Commun.*, 2018, **9**, 4454.

12 X. F. Yang, A. Wang, B. Qiao, J. Li, J. Liu and T. Zhang, *Acc. Chem. Res.*, 2013, **46**, 1740–1748.

13 Z. Zhang, Y. Zhu, H. Asakura, B. Zhang, J. Zhang, M. Zhou, Y. Han, T. Tanaka, A. Wang, T. Zhang and N. Yan, *Nat. Commun.*, 2017, **8**, 16100.

14 J. Jones, H. Xiong, A. T. DeLaRiva, E. J. Peterson, H. Pham, S. R. Challa, G. Qi, S. Oh, M. H. Wiebenga, X. I. P. Hernández, Y. Wang and A. K. Datye, *Science*, 2016, **353**, 150–154.

15 L. Lin, S. Yao, R. Gao, X. Liang, Q. Yu, Y. Deng, J. Liu, M. Peng, Z. Jiang, S. Li, Y. W. Li, X. D. Wen, W. Zhou and D. Ma, *Nat. Nanotechnol.*, 2019, **14**, 354.

16 M. D. Marcinkowski, M. T. Darby, J. Liu, J. M. Wimble, F. R. Lucci, S. Lee, A. Michaelides, M. Flytzani-Stephanopoulos, M. Stamatakis and E. C. H. Sykes, *Nat. Chem.*, 2018, **10**, 325–332.

17 S. Duan, R. Wang and J. Liu, *Nanotechnology*, 2018, **29**, 204002.

18 W. E. Liu and S. E. Mohney, *J. Electron. Mater.*, 2003, **32**, 1090–1099.

19 S. Furukawa and T. Komatsu, *ACS Catal.*, 2017, **7**, 735–765.

20 J. Prinz, C. A. Pignedoli, Q. S. Stöckl, M. Armbrüster, H. Brune, O. Gröning, R. Widmer and D. Passerone, *J. Am. Chem. Soc.*, 2014, **136**, 11792–11798.

21 J. Prinz, R. Gaspari, Q. S. Stöckl, P. Gille, M. Armbrüster, H. Brune, O. Gröning, C. A. Pignedoli, D. Passerone and R. Widmer, *J. Phys. Chem. C*, 2014, **118**, 12260–12265.

22 B. Ravel and M. Newville, *J. Synchrotron Rad.*, 2005, **12**, 537–541.

23 A. Ankudinov and B. Ravel, *Phys. Rev. B, Condens. Matter Mater. Phys.*, 1998, **58**, 7565–7576.

24 M. D. Segall, P. J. D. Lindan, M. J. Probert, C. J. Pickard, P. J. Hasnip, S. J. Clark and M. C. Payne, *J. Phys. Condens. Matter*, 2002, **14**, 2717–2744.

25 D. Vanderbilt, *Phys. Rev. B, Condens. Matter Mater. Phys.*, 1990, **41**, 7892–7895.

26 Y. Zhang and W. Yang, *Phys. Rev. Lett.*, 1998, **80**, 890.
27 B. Hammer, L. B. Hansen and J. K. Nørskov, *Phys. Rev. B, Condens. Matter Mater. Phys.*, 1999, **59**, 7413–7421.
28 H. J. Monkhorst and J. D. Pack, *Phys. Rev. B*, 1976, **13**, 5188–5192.
29 T. A. Halgren and W. N. Lipscomb, *Chem. Phys. Lett.*, 1977, **49**, 225–232.
30 N. Govind, M. Petersen, G. Fitzgerald, D. King-Smith and J. Andzelm, *Comput. Mater. Sci.*, 2003, **28**, 250–258.
31 M. K. Bhargava, A. A. Gadalla and K. Schubert, *J. Less-Common Met.*, 1975, **42**, 69–76.
32 S. Iihama, S. Furukawa and T. Komatsu, *ACS Catal.*, 2016, **6**, 742–746.
33 L. L. Shen, K. Xia, W. Z. Lang, L. F. Chu, X. Yan and Y. J. Guo, *Chem. Eng. J.*, 2017, **324**, 336–346.
34 P. P. Li, W. Z. Lang, K. Xia, L. Luan, X. Yan and Y. J. Guo, *Appl. Catal. A Gen.*, 2016, **522**, 172–179.
35 X. Liu, W. Z. Lang, L. L. Long, C. L. Hu, L. F. Chu and Y. J. Guo, *Chem. Eng. J.*, 2014, **247**, 183–192.
36 Y. Zhu, Z. An, H. Song, X. Xiang, W. Yan and J. He, *ACS Catal.*, 2017, **7**, 6973–6978.
37 S. Zha, G. Sun, T. Wu, J. Zhao, Z. J. Zhao and J. Gong, *Chem. Sci.*, 2018, **9**, 3925–3931.
38 T. Wang, F. Jiang, G. Liu, L. Zeng, Z. Zhao and J. Gong, *AIChE J.*, 2016, **62**, 4365–4376.
39 J. Li, J. Li, Z. Zhao, X. Fan, J. Liu, Y. Wei, A. Duan, Z. Xie and Q. Liu, *J. Catal.*, 2017, **352**, 361–370.
40 G. Liu, L. Zeng, Z. J. Zhao, H. Tian, T. Wu and J. Gong, *ACS Catal.*, 2016, **6**, 2158–2162.
41 F. Jiang, L. Zeng, S. Li, G. Liu, S. Wang and J. Gong, *ACS Catal.*, 2015, **5**, 438–447.
42 L. L. Long, K. Xia, W. Z. Lang, L. L. Shen, Q. Yang, X. Yan and Y. J. Guo, *J. Ind. Eng. Chem.*, 2017, **51**, 271–280.
43 Z. Nawaz, X. Tang, Y. Chu and F. Wei, *Cuihua Xuebao/Chinese J. Catal.*, 2010, **31**, 552–556.
44 L. Shi, G. M. Deng, W. C. Li, S. Miao, Q. N. Wang, W. P. Zhang and A. H. Lu, *Angew. Chem. Int. Ed.*, 2015, **54**, 13994–13998.
45 Y. Duan, Y. Zhou, Y. Zhang, X. Sheng and M. Xue, *Catal. Letters*, 2011, **141**, 120–127.
46 Y. Zhang, Y. Zhou, L. Huang, M. Xue and S. Zhang, *Ind. Eng. Chem. Res.*, 2011, **50**, 7896–7902.
47 Y. Zhang, Y. Zhou, L. Huang, S. Zhou, X. Sheng, Q. Wang and C. Zhang, *Chem. Eng. J.*, 2015, **270**, 352–361.
48 Y. Zhang, Y. Zhou, J. Shi, S. Zhou, X. Sheng, Z. Zhang and S. Xiang, *J. Mol. Catal. A Chem.*, 2014, **381**, 138–147.
49 X. Fan, J. Li, Z. Zhao, Y. Wei, J. Liu, A. Duan and G. Jiang, *Catal. Sci. Technol.*, 2015, **5**, 339–350.
50 G. Q. Ren, G. X. Pei, Y. J. Ren, K. P. Liu, Z. Q. Chen, J. Y. Yang, Y. Su, X. Y. Liu, W. Z. Li and T. Zhang, *J. Catal.*, 2018, **366**, 115–126.
51 H. Zhu, D. H. Anjum, Q. Wang, E. Abou-Hamad, L. Emsley, H. Dong, P. Laveille, L. Li, A. K. Samal and J. M. Basset, *J. Catal.*, 2014, **320**, 52–62.
52 B. Li, Z. Xu, W. Chu, S. Luo and F. Jing, *Cuihua Xuebao/Chinese J. Catal.*, 2017, **38**, 726–735.
53 Y. L. Shan, T. Wang, Z. J. Sui, Y. A. Zhu and X. G. Zhou, *Catal. Commun.*, 2016, **84**, 85–88.
54 L. Rochlitz, K. Searles, J. Alfke, D. Zemlyanov, O. V. Safonova and C. Copéret, *Chem. Sci.*, 2020, **11**, 1549–1555.

55 K. Searles, K. W. Chan, J. A. Mendes Burak, D. Zemlyanov, O. Safonova and C. Copéret, *J. Am. Chem. Soc.*, 2018, **140**, 11674–11679.

56 C. Sun, J. Luo, M. Cao, P. Zheng, G. Li, J. Bu, Z. Cao, S. Chen and X. Xie, *J. Energy Chem.*, 2018, **27**, 311–318.

57 T. Waku, J. A. Biscardi and E. Iglesia, *Chem. Commun.*, 2003, **3**, 1764–1765.

58 A. G. Buekens and G. F. Froment, *Ind. Eng. Chem. Process Des. Dev.*, 1968, **7**, 435–447.

59 L. Nykänen and K. Honkala, *J. Phys. Chem. C*, 2011, **115**, 9578–9586.

60 J. C. Slater, *J. Chem. Phys.*, 1964, **41**, 3199–3204.

61 E. A. Redekop, V. V. Galvita, H. Poelman, V. Bliznuk, C. Detavernier and G. B. Marin, *ACS Catal.*, 2014, **4**, 1812–1824.

62 T. Wang, F. Jiang, G. Liu, L. Zeng, Z. Zhao and J. Gong, *AIChE J.*, 2015, **61**, 857–866.

63 G. Siddiqi, P. Sun, V. Galvita and A. T. Bell, *J. Catal.*, 2010, **274**, 200–206.

64 J. Im and M. Choi, *ACS Catal.*, 2016, **6**, 2819–2826.

65 E. L. Jablonski, A. A. Castro, O. A. Scelza and S. R. De Miguel, *Appl. Catal. A Gen.*, 1999, **183**, 189–198.

66 Y. Xu, J. Chen, X. Yuan, Y. Zhang, J. Yu, H. Liu, M. Cao, X. Fan, H. Lin and Q. Zhang, *Ind. Eng. Chem. Res.*, 2018, **57**, 13087–13093.

67 K. Searles, G. Siddiqi, O. V. Safonova and C. Copéret, *Chem. Sci.*, 2017, **8**, 2661–2666.

Chapter 4

Electronic Modification of Single-atom Pt in Surface-modified Intermetallics for Propane Dehydrogenation

4.1. Introduction

Propylene is one of the most essential basic raw materials in the chemical industry that is suddenly scarce and demanded for the shale gas revolution.[1–3] Among the propylene production processes, on-purpose propylene production *via* catalytic PDH has attracted tremendous interest as a strategy for satisfying the growing global demand for propylene. Pt is widely utilized for alkane, including propane, dehydrogenation because of its high performance in C–H scissions and relatively low performance in C–C cleavage. However, a high reaction temperature (>600°C) is required to obtain sufficient propylene yield because of the high endothermicity of PDH. Thus, the Pt-based catalysts are inevitably deactivated by coking and/or nanoparticle sintering at such a high temperature and must be regenerated in short cycles. In this context, the development of a perfectly stable catalytic system that does not require regeneration, even at >600°C, is a great challenge, yet highly attractive for practical applications. Although several researchers have attempted to resolve this challenge, no catalyst has been reported, which exhibits month-long stability for PDH at >600°C. Therefore, to achieve this milestone, an innovative catalyst design must be developed to completely inhibit the occurrences of undesired side reactions.

The geometric and electronic effects are known to be pivotal to most catalytic systems, including the PDH one. Regarding the geometric effect, a catalyst design that is based on the alloying of Pt is generally applied. Furthermore, PDH is a structure-insensitive reaction, whereas, side reactions, such as hydrogenolysis, isomerization, and polymerization, are structure-sensitive reactions.[1–3] Moreover, since large Pt–Pt ensembles are well-known activators of undesired side reactions, the dilution of such ensembles (also known as the "ensemble effect") by alloying Pt with inactive metals such as Sn,[4–6] Ga,[7–9] In,[10] and Zn[11,12] has been generally applied to prevent side reactions. The ensemble effect can also be maximized by completely isolating the Pt atoms by the second metals, thus favoring the first and second C–H scissions, whereas the subsequent C–H scission would be successfully inhibited.[8,13,14] J. Gong *et al*. designed an isolated Pt site utilizing a Pt–Cu SAA, which exhibited high stability at 520°C.[13] However, the Pt–Cu SAA catalyst was severely deactivated at 600°C by nanoparticle sintering. Thus, materials possessing isolated Pt sites with high thermal stability should be utilized for continuous working at a high temperature (≥600°C).[8,10,15–21] In the previous study, we observed that an isolated Pt atom (single-atom-like Pt, Pt_1) included in thermally stable intermetallic PtGa (Pt:Ga = 1:1, Space group of $P2_13$)[22] functioned as a highly selective and durable active site for PDH without sintering even at 600°C (refer Chapter 3).[8] Although PtGa contains the isolated Pt_1 and Pt_3 ensembles at the most stable (111) surface, the latter can be selectively blocked by Pb decoration (Scheme 2).

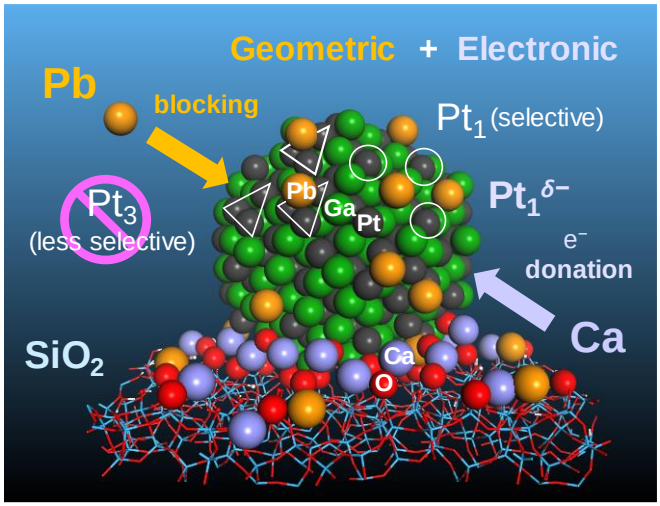

Scheme 2. Catalyst design concept of the double decoration of the nanoparticulate intermetallic PtGa supported on SiO_2. The synergy of the geometric and electronic effects is expected to greatly enhances propylene selectivity and the stability of the catalyst.

As well as the geometric property, the electronic properties of Pt, contribute to the adsorption strength of propylene on the Pt site. For instance, an increase in the electron density of Pt induces its electrostatic repulsion to propylene, thereby promoting propylene desorption and improving stability.[23–25] Hence, tuning the electronic properties of Pt can be another approach for increasing the lifetime of PDH catalysts. Therefore, the double modification of PtGa to synergize the geometric and electronic promotion effects can be a promising catalyst design concept to construct an ultra-stable catalytic system for PDH. Crucially, the considered geometric and electronic effects for the double decoration concept should be compatible and not change the parent PtGa intermetallic structure. Scheme 2 shows a possible approach that satisfies this guideline. The surface of the intermetallic PtGa nanoparticles on SiO_2 was decorated with Pb for the geometric modification to block the Pt_3 sites. Pb remains at the surface of PtGa and is not diffused into the PtGa bulk, even at a high temperature, because of its large atomic size and the high thermal stability of PtGa.[8] Moreover, a certain alkali or alkaline earth cation, such as Ca^{2+},[26–28] is deposited around the PtGa nanoparticles as an electron-donating agent. Notably, such a cation that exhibits high ionization tendency is not easily reduced and alloyed with PtGa. Hence, the resulting electron-enriched Pt_1 site is expected to function as an ideal active site that can almost perfectly suppress side reactions in PDH.

In this study, we report a novel catalyst design concept, the “double decoration of intermetallics,” where PtGa was modified with Pb and Ca. This strategy enabled the synergy of the geometric and electronic promotion effects without changing the parent PtGa structure, thereby affording, for the first time, an innovative catalyst with outstandingly high catalytic stability in PDH for up to one month at 600°C.

4.2. Experimental

4.2.1. Catalyst Preparation.

Preparation of Pt-based catalysts supported on silica (without Ca). PtGa/SiO_2 (Pt:Ga =1:1) and PtGa–Pb/SiO_2 (Pt:Ga:Pb = 1:1:0.75) catalysts were synthesized by the pore-filling co-impregnation method, which can deposit all the metal components on the SiO_2 support without loss.[29] $Pt(NH_3)_2(NO_3)_2$ (Furuya Metal Co. Ltd., 4.60 wt% of Pt in HNO_3 solution), $Ga(NO_3)_3{\cdot}nH_2O$ (n = 7-9, Wako, 99.9%), and $Pb(NO_3)_2$ (Wako, 99.5%) were used as metal precursors. The loading amount of Pt was fixed at 3 wt%. Mixed aqueous solution of the metal precursors was first added dropwise to SiO_2 (CARiACT G–6, Fuji Silysia, S_{BET} = *ca*. 500 $m^2\ g^{-1}$) so that the solutions just filled the pore of the SiO_2 (*ca*. 1.6 mL of solution per g of SiO_2). The obtained mixtures were sealed by three pieces of plastic film and kept overnight at room temperature, followed by transferring to a round-bottom flask and subsequent freezing using liquid nitrogen. The frozen mixtures were dried in vacuum at ca. −5°C and further dried in an oven at 90°C overnight. The resulting powder was calcined at 400°C for 1 h in dry air with ramping rate of 20 °C min^{-1}. The calcined powder was then reduced under flowing H_2 (0.1 MPa, 50 mL min^{-1}) at 700°C for 1 h with ramping rate of 20 °C min^{-1}.

Preparation of PtGa-based catalysts supported on silica with Ca. The corresponding Ca containing catalysts were also prepared using $Ca(NO_3)_2{\cdot}4H_2O$ (Wako, 98.5%) as Ca source in a similar method to that of PtGa: PtGa–Ca (Pt:Ga:Ca = 1:1:5) and PtGa–Pb–Ca (Pt:Ga:Ca:Pb = 1:1:5:0.55); Pt: 3 wt%. All the samples were calcined at 600°C instead of 400°C.

Preparation of PtGa catalysts supported on silica with M (M = Na, K, Rb, Cs, Mg, Sr, Y, La, Ce, Nd, and Sm). The corresponding M containing catalysts were also prepared in a same method to that of PtGa–Ca/SiO_2; Pt: 3 wt%. $NaNO_3$ (Sigma-Aldrich, 99.5%), KNO_3 (Wako, 99.0%), Rb_2CO_3 (Wako, >97.0%), $CsNO_3$ (KANTO CHEMICAL CO., INC., 99.99%), $Mg(NO_3)_2{\cdot}6H_2O$ (KANTO CHEMICAL CO., INC., >99.2%), $Sr(NO_3)_2$ (KANTO CHEMICAL CO., INC., >98%), $Y(NO_3)_3{\cdot}6H_2O$ (Mitsuwa Chemicals Co., Ltd., >99.9%), $La(NO_3)_3{\cdot}6H_2O$ (Mitsuwa Chemicals Co., Ltd., >99.9%), $Ce(NO_3)_3{\cdot}6H_2O$ (Wako, >98.0%), $Nd(NO_3)_3{\cdot}6H_2O$ (Mitsuwa Chemicals Co., Ltd., >99.9%), and $Sm(NO_3)_3{\cdot}6H_2O$ (Mitsuwa Chemicals Co., Ltd., 99.9%) were used as precursors of M.

Preparation of PtGa catalysts supported on other supports. CaO support was synthesized by a precipitation method using urea (CH_4N_2O, Wako, >99.0%) as a precipitating agent. First, $Ca(NO_3)_2{\cdot}4H_2O$ and urea (urea/Ca molar ratio = 20) were dissolved together in deionized water. The mixed solution was stirred at 90°C for 50 h, then centrifuged and washed with water five times. The resulting powder was dried overnight in oven at 90°C, then calcined at 800°C in dry air for 3 h. $MgAl_2O_4$ support was synthesized in a similar manner using $Mg(NO_3)_2{\cdot}6H_2O$ and $Al(NO_3)_3{\cdot}9H_2O$ (Wako, >98.0%) as precursors.

A series of the PtGa/X catalysts (X = CaO, MgO (JRC-MGO-4 500A), CeO_2 (JRC-CEO-2), ZrO_2 (JRC-ZRO-6), γ-Al_2O_3 (prepared by calcination of boehmite [γ-AlOOH, supplied by SASOL chemicals] at 900°C for 3 h, γ-phase), and $MgAl_2O_4$) were prepared by the conventional impregnation method. Firstly,

$Pt(NH_3)_2(NO_3)_2$ and $Ga(NO_3)_3{\cdot}nH_2O$ (n = 7-9) were dissolved in an excess amount of deionized water (25 mL/$g_{support}$). Then, the support was added to the vigorously stirred mixed solution and kept with stirring at 90°C for 30 min. The resulting mixture was dried using a rotary evaporator at 50°C and further dried overnight in an oven at 90°C. Finally, the obtained powder was calcined and reduced, in a similar manner to that of PtGa–Ca/SiO_2.

4.2.2. Catalytic Reactions.

The PDH reactions were performed in a vertical, quartz fixed-bed reactor with an internal diameter of 8 mm under an atmospheric pressure. Generally, 10 mg of catalysts, diluted with quartz sand (total: 1.5 g) were charged in the reactor. Prior to the catalytic test, the catalyst was reduced under flowing H_2 at 600°C for 0.5 h, and the reactant gas mixture was subsequently fed; C_3H_8:He = 2.5:5, a total of 7.5 mL min^{-1} (WHSV = 29.5 h^{-1}; calculated based on the weight of catalyst except the quartz sand: $WHSV_{Pt}$ = 984 h^{-1}; calculated based on the weight of Pt). The product gas was analyzed by an online TCD gas chromatograph (Shimadzu GC–8A with a column of Unipak S or Gaskuropak 54, GL Science) equipped downstream. For all the catalysts, C_3H_8, C_2H_4, C_2H_6, and CH_4 were detected as reaction products. C_3H_8 conversion, C_3H_6 selectivity, C_3H_8 yield, and material balance were calculated as shown in Chapter 3, respectively. Material balance typically ranged between 97~103% for all the reactions.

To estimate the catalyst stability, the first-order deactivation model was employed.[1] k_d (h^{-1}) and τ (h) were used as shown in Chapter 3. k_d (h^{-1})[1] and τ (h) represent the deactivation rate constant and mean catalyst life, respectively. Here, lower k_d and higher τ values represent higher catalyst stability.

4.2.3. Catalytic Reactions.

The crystalline phase in the prepared catalysts were obtained using powder XRD (MiniFlex 700+D/teX Ultra; Cu Kα X–ray source).

HAADF-STEM was used to investigate the particle size distribution and the crystal structure of the prepared catalyst using a FEI Titan G2 microscope equipped with an EDX analyzer. Prior to the observation, a catalyst was firstly reduced at 600°C for 0.5 h under flowing H_2 (10 mL min^{-1}) with a ramping rate of 20 °C min^{-1}. Then, the catalyst was ground and dispersed in ethanol by ultrasonic, which was deposited on a molybdenum grid and dried in vacuum. The volume averaged mean particle size (d_{TEM}) was used.

The dispersion of Pt in the catalyst was estimated by CO-pulse chemisorption at −100°C using BELCAT-II (Microtrac BEL) instrument. Prior to chemisorption, 50 mg of the catalyst was reduced under a 5% H_2/Ar flow (20 mL min^{-1}) at 600°C for 30 min, then cooled to −100°C using CATCryo-II under a He flow (20 mL min^{-1}). A pulse of 10% CO/He was introduced into the reactor and CO passed thought the catalyst bed was quantified by a TCD equipped downstream. This CO pulse introduction was repeated until the amount of chemisorbed CO reached saturation. For the calculation of Pt dispersion, the amount of chemisorbed CO was estimated using an assumption of 1:1 chemisorption of CO on a Pt atom.

H_2 temperature-programmed reduction (H_2-TPR) was performed using BELCAT-II (Microtrac BEL) instrument. Prior to the H_2-TPR, 30 mg of the as-calcined (not reduced) catalyst was pretreated under a flow

of Ar (20 mL min^{-1}) at 300°C for 30 min. After the pretreatment, the catalyst was cooled to room temperature and further cooled to −120°C using CATCryo-II, and then heated from −120°C to 900°C with a ramping rate of 5 °C min^{-1} under a flow of 5% H_2/Ar (20 mL min^{-1}). The H_2 consumption was quantified by a TCD equipped in BELCAT-II.

The FT–IR spectra of adsorbed CO were obtained using a JASCO FTIR-4100 spectrometer with a mercury-cadmium-telluride detector in a transmission mode (resolution 4 cm^{-1}) under a dynamic condition. Prior to CO chemisorption, 100 mg of the catalyst was pressed into a pellet (diameter: 20 mm) and placed in a quartz cell equipped with CaF_2 windows and a Dewar vessel, followed by reduction under flowing H_2 at 600°C for 1 h. The reduced sample was then kept in vacuum at 600°C for 1h, then the cell was cooled to ca. −196°C by liquid nitrogen. The sample was exposed to 10% CO/He flow, then evacuated in vacuum to remove CO in gas phase and physiosorbed on the catalyst.

The amount of coke accumulated on the spent catalysts (without quartz sand: 30 mg) after propane dehydrogenation at 600°C for several hours (0.5, 1, 2, 5, and 20 h) was quantified by TPO. The spent catalyst (25 mg) was transferred into a quartz tube reactor. Prior to the TPO experiment, the catalyst was first heated to 150°C under flowing He (10 mL min^{-1}) and held at 150°C for 30 min, and then cooled to 100°C. After cooling, the catalyst was heated from 100°C to 800°C with a ramping rate of 2 °C min^{-1} under flowing 2% O_2/He (50 mL min^{-1}) and kept at 800°C for 10 min. The outlet gas (typically CO_2; m/z = 44) was analyzed online by quadrupole mass spectrometer (BELMASS) equipped downstream.

XAFS measurements of the catalysts and reference samples were carried out at BL01B1 and BL1402 beamlines of SPring-8, Japan Synchrotron Radiation Research Institute. XAFS spectra were recorded at the Pt L_{III}- and Ga K-edges in transmission mode at room temperature using a Si(111) double-crystal monochromator. Prior to pelletization, the catalyst was crushed using agate mortar. Then, the crushed catalyst was pressed into a pellet (diameter of 7 mm). For *in-situ* XAFS measurement (PtGa, PtGa–Ca, PtGa–Y, PtGa–Pb, and PtGa–Ca–Pb), the pelletized sample was transferred into a quartz cell and pre-reduced at 600°C for 20 min under flowing 5% H_2/N_2 (40 mL min^{-1}), and then cooled to room temperature under N_2 gas flow. For *ex-situ* XAFS measurement, the pelletized sample was transferred into a quartz cell and pre-reduced at 600°C for 30 min under flowing H_2 (50 mL min^{-1}), and then cooled to room temperature. After the pretreatment, the quartz tube containing the reduced pellet was sealed and transferred into an Ar grove box (O_2 : <0.1 ppm) without exposing to air. The pellet was sealed in a plastic film bag (Barrier Nylon) together with an oxygen absorber (ISO A500-HS: Fe powder).

The obtained XAFS spectra were analyzed using Athena and Artemis software ver. 0.9.25 implemented in the Demeter package.[30] Pt L_{III}-edge EXAFS oscillation was Fourier-transformed in the k range of 3−15 $Å^{-1}$. Curve-fitting was performed using the back Fourier-transforms between 1.5−3.5 Å. The back-scattering amplitude and phase shift functions were calculated by FEFF8.[31] R-factor (R^2) for curve-fitting was defined as follows: $R^2 = \Sigma_i\{k^3\chi_i^{exp}(k)-k^3\chi_i^{fit}(k)\}^2/\Sigma_i\{k^3\chi_i^{exp}(k)\}^2$.

4.2.4. Computational Details.

Periodic DFT calculations were performed using the CASTEP code[32] with Vanderbilt-type ultrasoft pseudopotentials and the revised version of Perdew−Burke−Ernzerhof exchange−correlation functional based on the generalized gradient approximation.[33] The plane-wave basis set was truncated at a kinetic energy of 360 eV. A Fermi smearing of 0.1 eV was utilized. Dispersion correlations were considered using the Tkatchenko–Scheffler method with a scaling coefficient of s_R = 0.94 and a damping parameter of d = 20.[34] The reciprocal space was sampled using a *k*-point mesh with a spacing of typically 0.04 $Å^{-1}$, as generated by the Monkhorst−Pack scheme.[35] Geometry optimizations were performed on supercell structures using periodic boundary conditions. We chose PtGa:A(111) as the most stable surface according to the relevant system of PdGa.[36,37] The surfaces were modeled using the PtGa:A(111)–(1 × 1) metallic slabs with a thickness of four atomic layers with 13 Å of vacuum spacing. For the Ca decoration, a CaO moiety was adsorbed vertically on the Ga_3 hollow site adjacent to the Pt_1 site so that the Ca–O–Ga_3 linkage was formed. Note that this simple model was made for a qualitative evaluation of the Ca decoration on the electronic state of Pt and that the results do not directly reflect the actual electronic state of Pt at the real system of the metal-support interface. For the Pb decoration, a Pb atoms was placed on the hollow site of Pt_3 site. The unit cell size of the bulk material (PtGa) was firstly optimized, followed by modeling the slab structure and surface relaxation with the size of the supercell fixed. The convergence criteria for structure optimization and energy calculation were set to (a) an SCF tolerance of 1.0×10^{-6} eV per atom, (b) an energy tolerance of 1.0×10^{-5} eV per atom, (c) a maximum force tolerance of 0.05 eV $Å^{-1}$, and (d) a maximum displacement tolerance of 1.0×10^{-3} Å. For all calculations, the net charge was set to zero and spin polarization was considered.

The adsorption energy was defined as follows: $E_{ad} = E_{A\text{-}S} - (E_S + E_A)$, where $E_{A\text{-}S}$ is the energy of the slab together with the adsorbate, E_A is the total energy of the free adsorbate, and E_S is the total energy of the bare slab.

4.3. Results

4.3.1. Characterization of PtGa–Ca/SiO_2.

First, we prepared and characterized PtGa–Ca/SiO_2 to elucidate the effect of Ca. HAADF-STEM image of PtGa–Ca and its particle size distribution are shown in Figure 35. The nanoparticles with a mean particle size of 2.4 ± 0.5 nm were uniformly distributed. EDX analysis revealed that Pt and Ga co-existed in each nanoparticle in a ratio of ~1:1 (Figures 36a and b). The quantitative analysis on the EDX maps revealed that the Ca ratio became much higher when the surrounding areas of nanoparticles were included (odd No. >> even No., Figure 36b). The high-resolution (HR) HAADF-STEM image (Figure 36c) revealed an ordered crystal structure with interplanar distances of 1.98 Å and 2.29 Å and a dihedral angle (56°), which agree with those of the (211) and $(20\bar{1})$ planes of intermetallic PtGa that were viewed along the $[1\bar{4}2]$ direction (Figure 36d). These results indicate that Ca is present at the metal-support interface rather than on nanoparticles and does not change the bulk structure of intermetallic PtGa. To obtain further structural information, XAFS analysis was performed. Pt–Ga scattering with 2.47 Å was observed, and this is consistent with the interatomic distance of the closest Pt and Ga atoms in intermetallic PtGa (2.50 Å).[22] Similar results were also obtained for the

undecorated PtGa/SiO_2 catalyst. Furthermore, Figures 36e and f show the Pt L_{III}- and Ga K-edge XANES spectra of PtGa and PtGa–Ca, respectively. The absorption edge in Pt L_{III}-edge XANES shifted to lower energy than that of PtGa, indicating the electron donation from Ca to Pt upon Ca decoration.[38] Contrarily, the white line intensity of Ga K-edge XANES slightly increased upon Ca decoration, indicating that a part of Ga had been oxidized. This is probably due to the formation of a Ga–O–Ca linkage and suggests the close contact of the PtGa nanoparticles with the CaO species. Note that the Ca decoration did not decrease Pt dispersion (Table 9); therefore, the active Pt sites are still open for reaction despite the close contact with CaO.

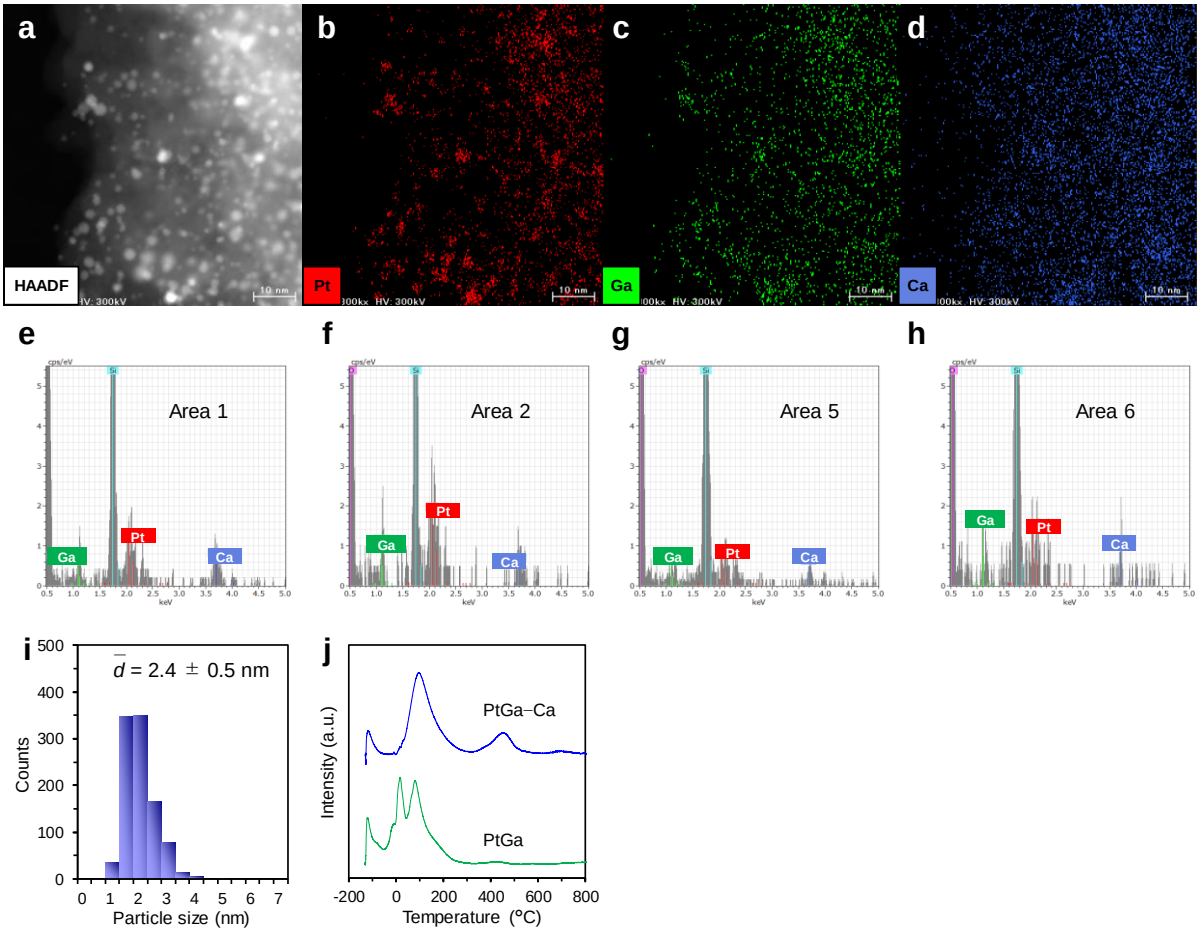

Figure 35. (a) HAADF-STEM image of the PtGa–Ca/SiO_2 catalyst and the corresponding elemental maps of (b) Pt; (c) Ga; and (d) Ca acquired using EDX for the region designated in (a). EDX spectra obtained in (e) Area 1; (f) Area 2; (g) Area 5; and (h) Area 6; designated in Figure 1c. (i) Particle size distribution of the PtGa–Ca/SiO_2 catalyst for more than 900 nanoparticles. The particle size was narrow with small and uniform nanoparticles ranging from 1 nm to 4 nm (typically smaller than 2.5 nm) with a volume weighted average of 2.4 ± 0.5 nm. (j) H_2-TPR profiles of as-calcined (not reduced) PtGa/SiO_2 and PtGa–Ca/SiO_2.

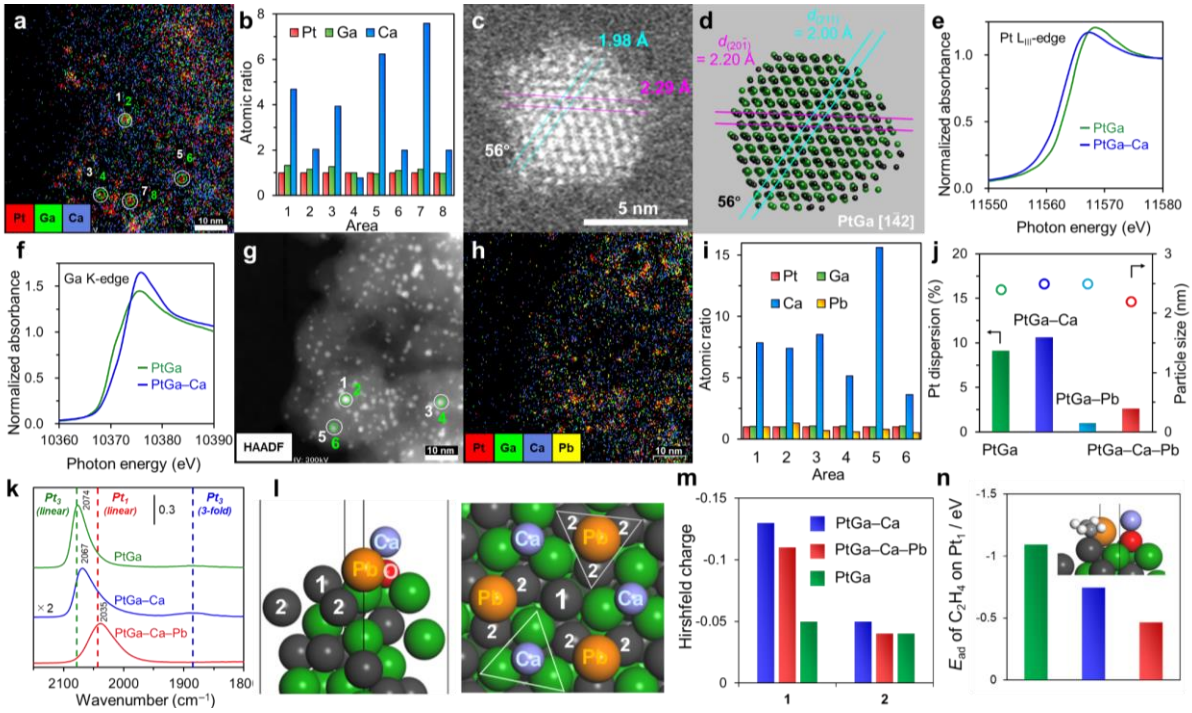

Figure 36. (a) Elemental maps of the Pt+Ga+Ca overlay in PtGa–Ca/SiO_2. (b) Atomic ratio of Pt, Ga, and Ca in areas designated by white/green circles in (a). (c) High-angle annular dark field scanning transmission microscopy (HAADF-STEM) image of a single nanoparticle of the PtGa–Ca/SiO_2 catalyst. (d) Crystal structure of an intermetallic PtGa nanoparticle that was viewed along the [1$\bar{4}$2] direction. (e) Pt L_{III}- and (f) Ga K-edge XANES spectra of PtGa/SiO_2 and PtGa–Ca/SiO_2. (g) HAADF-STEM image of PtGa–Ca–Pb/SiO_2 and (h) the corresponding elemental maps of Pt+Ga+Pb+Ca overlay. (i) Atomic ratio of Pt, Ga, Ca, and Pb in areas designated by white/green circles in (g). (j) Pt dispersion and the mean particle size of the Pt-based catalysts. (k) FT–IR spectra of CO that was adsorbed on PtGa, PtGa–Ca, and PtGa–Ca–Pb at −196°C. The vertical dashed lines indicate the vibrational frequency, as observed in the previous study.[8] (l) Optimized structure of PtGa:A(111)–OCa–Pb as a model of PtGa–Pt_1 that was modified with CaO and Pb (left: side view, right: top view). (m) Hirshfeld charges of the Pt atoms in (l). (n) E_{ad} of C_2H_4 adsorbed on the Pt_1 site (1) of PtGa:A(111) with and without modifications by CaO and/or Pb. The inset figure illustrates the adsorbed structure of C_2H_4 on PtGa:A(111)–OCa–Pb.

Table 9. Summary of the Pt dispersion and mean particle size of the silica-supported PtGa-based catalysts.

Catalyst	Pt	Ga	Ca	Pb	Pt dispersion (%)[a]	Blocked surface Pt (%)[b]	Mean particle size (nm)[c]
$PtGa/SiO_2$	1	1	0	0	9.1	–	2.4 ± 0.6
$PtGa–Ca/SiO_2$	1	1	5	0	10.6	0	2.4 ± 0.5
$PtGa–Pb/SiO_2$	1	1	0	0.75	1.0	89	2.5 ± 0.5
$PtGa–Ca–Pb/SiO_2$	1	1	5	0.55	2.6	7	2.2 ± 0.5
$PtGa–Mg/SiO_2$ (Mg/Pt = 5)	1	1	0	0	13.2	0	–[d]
$PtGa–Na/SiO_2$ (Na/Pt = 5)	1	1	0	0	0	100	–[d]
$PtGa–K/SiO_2$ (K/Pt = 5)	1	1	0	0	0	100	–[d]
$PtGa–Rb/SiO_2$ (Rb/Pt = 5)	1	1	0	0	0	100	–[d]
$PtGa–Cs/SiO_2$ (Cs/Pt = 5)	1	1	0	0	0	100	–[d]
$PtGa–Sm/SiO_2$ (Sm/Pt = 5)	1	1	0	0	3.0	67	–[d]
PtGa/CaO	1	1	0	0	1.4	85	–[d]
PtGa/MgO	1	1	0	0	3.6	60	–[d]

[a]Pt dispersion (D_{Pt}) was calculated using CO-pulse chemisorption at −100°C. [b]$(1 - D_{Pt(PtGa–M)}/D_{Pt(PtGa)}) \times 100$: negative values were regarded as zero. [c]Mean particle size was estimated based on HAADF-STEM images. [d]Not evaluated.

4.3.2. Characterization of $PtGa–Ca–Pb/SiO_2$.

Next, we prepared the doubly decorated $PtGa–Ca–Pb/SiO_2$ catalyst and thoroughly analyzed its structure. The HAADF-STEM-EDX analysis revealed that the particles size, Pt–Ga elemental distribution, and the bulk crystal structure were similar to those of $PtGa–Ca/SiO_2$ (2.2 ± 0.5 nm, Pt:Ga = ~1:1, and intermetallic PtGa, respectively (Figures 36g-i, and 37)), thus confirming that the parent PtGa structure was retained (not changed). The formation of the intermetallic PtGa phase was also suggested by EXAFS curve fitting (Pt–Ga, 2.46 Å). The quantitative analysis on the EDX map revealed that the Ca ratio was higher when the surrounding areas was included (odd No. >> even No.) as observed for PtGa–Ca, whereas the Pb ratio did not change (Figures 36h, i, and 37). Therefore, unlike the Ca species, Pb atoms seem to be present mainly on the surface of PtGa. This result was also supported by the change in the dispersions of Pt, as shown in Figure 36j and Table 9. Pt dispersion was not changed by Ca modification, although it was reduced by Pb deposition, which strongly

suggests that Pb was deposited on some of the Pt sites,[8] whereas Ca was not. A similar trend was observed in the distribution of Pb in PtGa–Pb. The electron density of Pt was higher in PtGa–Ca–Pb than in PtGa–Pb, as observed in Pt L_{III}-edge XANES (Figure 38). This result is consistent with the aforementioned trend between PtGa and PtGa–Ca. Similarly, the Ga K-edge XANES analysis revealed the slight oxidation of Ga probably because of its close contact with Ca (Ga–O–Ca interaction, Figure 38). These results indicate that PtGa–Pb can be modified by Ca similarly to PtGa. Thereafter, FT-IR spectroscopy with CO adsorption was conducted at −196°C to obtain information about the surface structure (Figure 36k). The PtGa–Ca catalyst exhibited absorption bands, which were assignable to the stretching vibrations of CO that was adsorbed on the Pt_3 sites, and a small shoulder that corresponds to CO on the Pt_1 sites,[8] which is similar to that of the PtGa catalyst. However, the peak position of PtGa–Ca was at a lower wavenumber than that of PtGa and indicated the electron donation from the interfacial CaO to the surface Pt. Conversely, only CO that was adsorbed on the Pt_1 sites appeared in PtGa–Ca–Pb, thus supporting the blockage of Pt_3 sites and the exposure of the Pt_1 ones *via* Pb deposition. These results confirm that Ca located at the PtGa–SiO_2 interface, whereas Pb was deposited on the surface of the PtGa nanoparticles. Thus, the electronic and geometric effects of Ca and the deposited Pb, respectively, on the catalyst are compatible because of their different locations and roles therein. Thus, we have successfully synthesized the doubly decorated intermetallic compound catalyst, in which the electron-enriched Pt_1 active sites are present according to the rational catalyst design (Scheme 2).

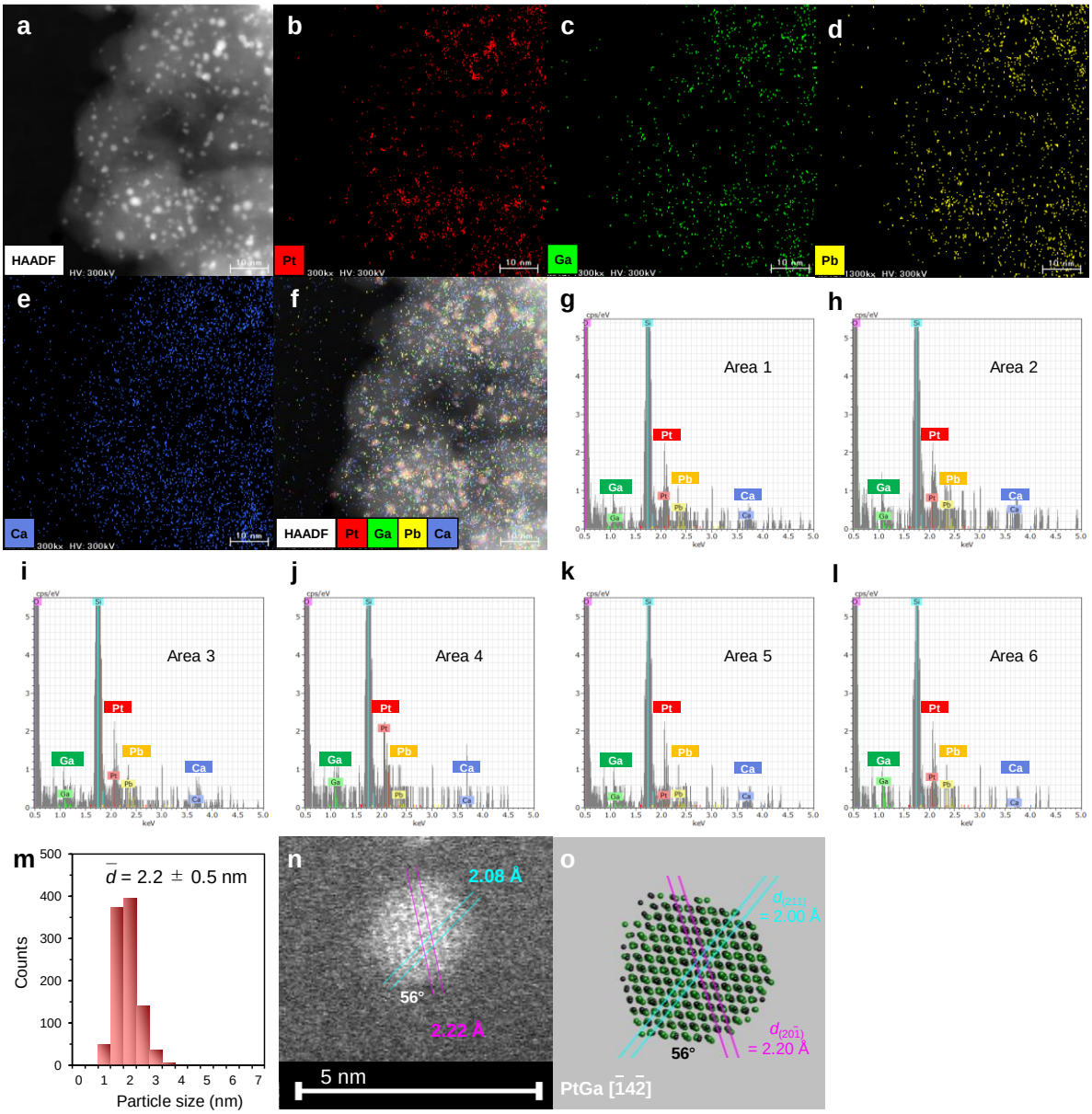

Figure 37. (a) HAADF-STEM image of the PtGa–Ca–Pb/SiO_2 (Pt:Ca:Pb = 1:5:0.55) catalyst and corresponding elemental maps of (b) Pt; (c) Ga; (d) Pb; (e) Ca; and (f) HAADF+Pt+Ga+Pb+Ca acquired using EDX for the region designated in (a). EDX spectra obtained in (g) Area 1; (h) Area 2; (i) Area 3; (j) Area 4; (k) Area 5; and (l) Area 6; designated in Figure 1f. (m) Size distribution of nanoparticles of the PtGa–Ca–Pb/SiO_2 (Pt:Ca:Pb = 1:5:0.55) catalyst. The particle size was narrow with small and uniform nanoparticles ranging from 1 nm to 3 nm (typically smaller than 2 nm) with a volume weighted average of 2.2 ± 0.5 nm. (n) High-resolution HAADF-STEM image of a single nanoparticle in PtGa–Pb–Ca/SiO_2. (o) Crystal structure of an intermetallic PtGa nanoparticle that was viewed along the [$\bar{1}4\bar{2}$] direction.

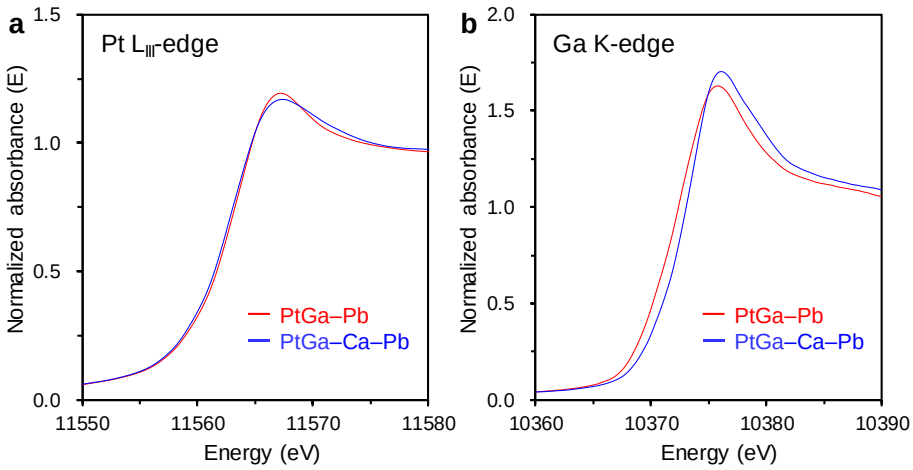

Figure 38. (a) Pt L_{III}- and (b) Ga K-edge XANES spectra of PtGa–Pb/SiO_2 (Pt:Pb = 1:0.75) and PtGa–Ca–Pb/SiO_2 (Pt:Ca:Pb = 1:5:0.55).

4.3.3. DFT Calculations.

Next, DFT calculations were conducted to elucidate the effect of Ca and Pb on the electronic structure of Pt and the adsorption property of the product, alkene. Figure 36l shows the optimized model structure of the PtGa(111)–Pt_1 surface modified with CaO and Pb. The CaO moiety was situated on the Ga_3 hollow site with a Ca–O–Ga linkage, while the Pb atom was placed on the hollow site of the Pt_3 site. Similar model without Pb deposition was also considered. The surface Pt atoms became more negatively charged upon the CaO modification, indicating the electron transfer from CaO to Pt. The electron donation was prominent at the Pt_1 site (Figure 36m, charge: < -0.1). Moreover, the adsorption of ethylene as a model light alkene was considered (Figure 36n). Upon Ca modification, the adsorption energy (E_{ad}) increased from −1.09 to −0.75 eV, indicating promoted desorption, which is unfavorable to side reactions that form cokes. Furthermore, the density of states (DOS), which were projected on the *d*-orbitals of the model structures with and without CaO, were calculated. However, no significant difference was observed in the *d*-band structures, and this confirmed that the electron donation from Ca to Pt was crucial to promoting alkene desorption. Interestingly, the Pb deposition further increased E_{ad} of ethylene (−0.47 eV), which is probably due to the steric hindrance by the large Pb atom.

4.3.4. Catalytic Performance in PDH.

Then, we tested the catalytic performances of the prepared catalysts for PDH. Figure 39a shows the normalized C_3H_8 conversion, in which a considerably harsh condition was applied to investigate the stability in a short time (600°C without co-feeding H_2, refer to Figures 40 and 41 for the original catalytic performances). PtGa–Ca, which possesses electron-enriched Pt atoms, exhibited higher C_3H_6 selectivity and stability compared with those of PtGa. Thus, tuning the electronic property of the intermetallics was effective in prolonging the lifetime of the catalyst. Pb deposition, as well as the Ca decoration, enhanced the stability of the catalyst.[8] More importantly, the combination of Pb and Ca exerted a synergistic effect on the stability of the catalyst. The mean catalyst lifetime (reciprocal deactivation constant: $k_d^{-1} = \tau = 233$ h) of PtGa–Ca–Pb was much longer than that of PtGa–Pb ($\tau = 149$ h), thus highlighting the further enhancement of the catalytic stability *via* the double decoration by Ca–Pb, which afforded the electron-enriched Pt_1. Regarding the Pb-containing catalysts, a short induction period (~10 h) was observed. This was probably due to the redistribution of excess Pb from a part of the Pt_1 sites to the Ga sites or SiO_2 support. Figure 39b shows the amount of coke after 20 h of reaction. The trend of the amount of coke was very consistent with that of the catalytic stability. Notably, the catalytic performance of spent PtGa–Ca–Pb could be recovered by a simple regeneration process (O_2–H_2 treatment). The spent catalyst after regeneration process was evaluated and no aggregation of nanoparticles was not observed even after long-term reaction and regeneration process, revealing the high thermal stability against nanoparticles sintering. Despite the excellent stability of PtGa–Ca–Pb, its catalytic activity gradually decreased probably because of the thermal cracking of propane. Afterward, the catalytic performance of PtGa–Ca–Pb/SiO_2 was tested by co-feeding H_2 (a typically applied condition for PDH[2]) to suppress the accumulation of coke. Co-feeding H_2 drastically decreased coke formation (Figure 39b), thereby improving the catalytic stability. PtGa–Ca–Pb/SiO_2 was barely deactivated for 1 month at least, thus highlighting its much greater stability compared with those of previously reported catalysts (refer to Tables 10-11 and Figure 42 for comparisons). Noteworthily, the mean catalyst life ($\tau = 3067$ h) was 2.6 times higher than the highest ever reported mean catalyst life ($\tau = 1159$ h). Finally, PtGa–Ca–Pb/SiO_2 was tested in PDH at 580°C utilizing undiluted neat C_3H_8 (a more industrially favorable condition, Figure 43). Therein, PtGa–Ca–Pb achieved 36.6% initial conversion of C_3H_8 and retained 25.2% conversion after 10.5 days of reaction ($\tau = 465$ h), indicating its much greater stability than that of the recently reported stable catalyst (PtLa/mz-deGa with $\tau = 380$ h).[39] To the best of our knowledge, our PtGa–Ca–Pb/SiO_2 catalyst afforded the highest stability in PDH under different conditions. We also tested other basic additives or supports instead of Ca or Ca–SiO_2, respectively, of which results are summarized in Table 12. However, none of them showed positive effects on the catalytic activity and stability of PtGa in PDH.

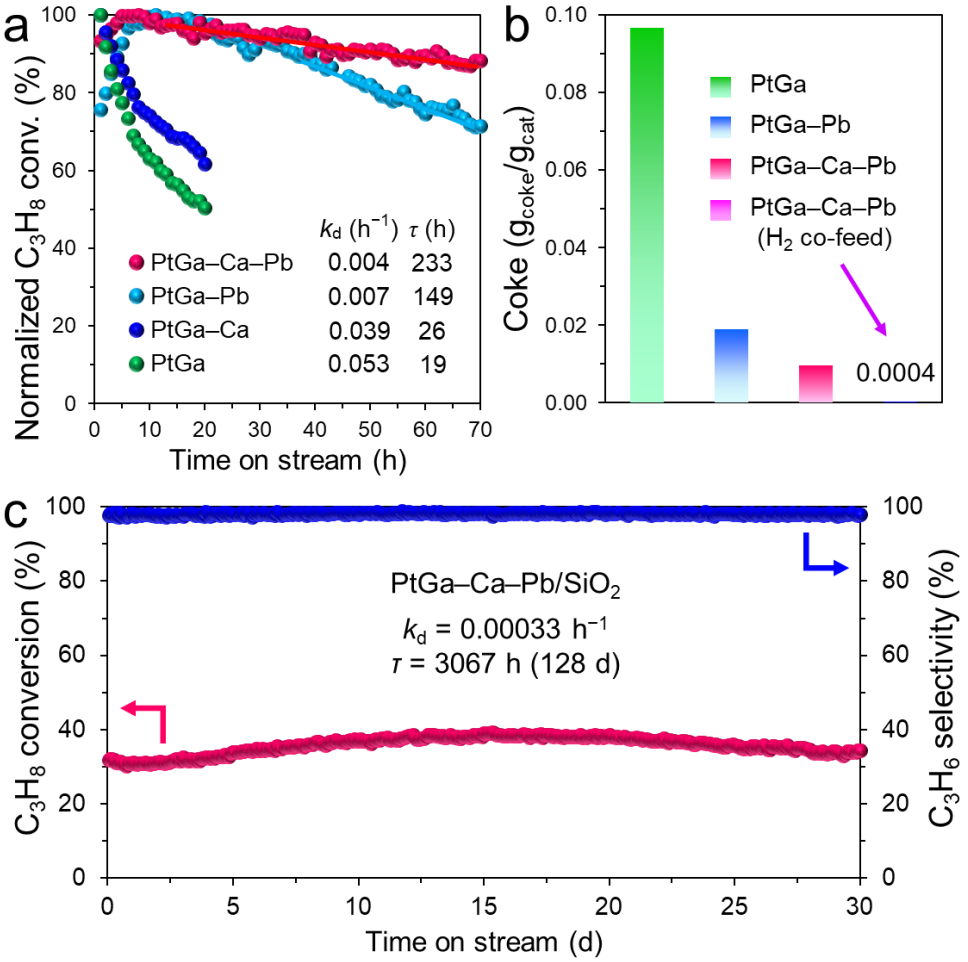

Figure 39. (a) Normalized C_3H_8 conversion during PDH at 600°C (C_3H_8:He = 2.5:5.0 mL min^{-1}). (b) Amount of coke that was accumulated on the catalyst that was applied for PDH after 20 h at 600°C. (c) Long-term stability test of PtGa–Ca–Pb/SiO_2 for PDH at 600°C (C_3H_8:H_2:He = 2.5:1.25:3.75 mL min^{-1}).

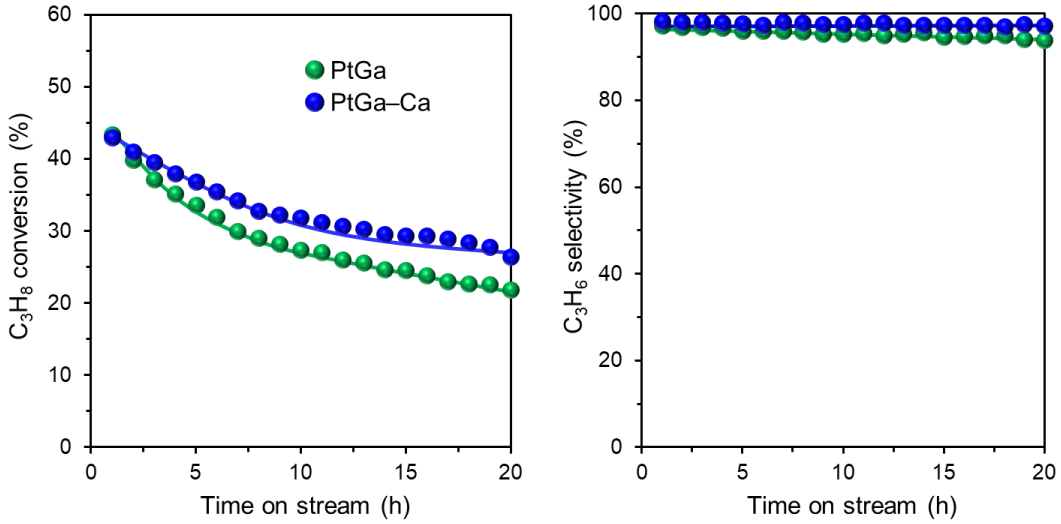

Figure 40. Catalytic performances of $PtGa/SiO_2$ (Pt:Ga = 1:1) and $PtGa–Ca/SiO_2$ (Pt:Ga:Ca = 1:1:5) in PDH (WHSV = 29.5 h^{-1}) at 600°C.

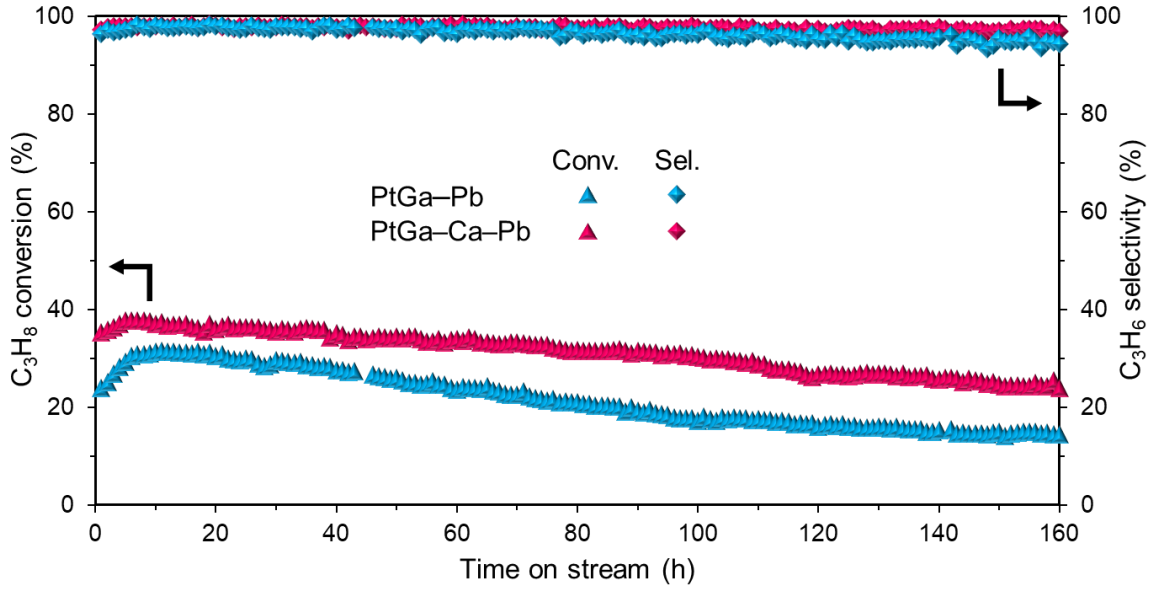

Figure 41. Long-term stability test for $PtGa–Pb/SiO_2$ (Pt:Ga:Pb = 1:1:0.75) and $PtGa–Ca–Pb/SiO_2$ (Pt:Ga:Ca:Pb = 1:1:5:0.55) in PDH (WHSV = 9.8 h^{-1}) at 600°C.

Table 10. Summary of the catalytic performance of PtGa–Ca–Pb/SiO_2 and other reported Pt-based catalysts in PDH in the presence of H_2.

Entry	Catalyst	Temp. (°C)	Conversion (%)[a]	C_3H_6 sel. (%)[b]	Specific activity (s^{-1})[c]	Catalyst τ (h)[d]	Ref.
1	PtIn/Mg(Al)O-600	620	69–50	98	0.436	37	40
2	0.3PtSn/1.5In-Al	620	58.4–48.6	93.5	0.705	7	41
3	PtGa–Ca–Pb/SiO_2	600	37.6 (300 h)–34.4	98.3–98.1	0.089	3067	This study
4	PtGa–Pb/SiO_2	600	30.0 (4 h)–28.4	99.6	0.376	1159	8
5	PtGa/SiO_2	600	44.7–24.5	98.8	0.556	54	8
6	Pt0.1Zn0.17/SiO_2	600	36–28	97–97.2	4.055	433	42
7	PtZn@S-1	600	46.6–39.8	98.5–99.4	0.813	324	43
8	Pt/Mg(Sn)(Al)O@Al_2O_3	600	48.3–43.0	86.4–98.1	1.439	224	5
9	0.6PtSn/1.5In-Al	600	55–42	96	0.341	101	41
10	PtSnIn/1.5Ca-Al	600	60.1–34.0	96.6	0.749	93	28
11	$Pt_{0.5}$-$Ge_{1.5}$/Al_2O_3-CaO	600	21–17	98.5	1.201	92	26
12	$Pt_{0.5}$-$Ge_{1.5}$/Al_2O_3	600	62–52	92.5–96.5	0.191	24	44
13	PtZn/0.02TS-170	600	54.4–20.5	98.2–96.3	1.551	63	45
14	Pt_3In/SiO_2	600	17.5–17	92	0.218	57	46
15	Pt3Ga/CeAl	600	41.1–32.2	98.5–99.6	0.509	39	47
16	PtSn/TS-1	600	53.5–47.7	92.5	0.359	30	48
17	15%Zn-0.1%Pt/Al_2O_3	600	35–31	94–97	1.194	22	49
18	Pt/Nb1Al2-O	600	37–29	92–96	0.293	20	50
19	Pt-Sn/SBA-15	600	40–25	92	0.997	12	51
20	Pt/TA10	600	47.3–25.9	77	0.458	10	52
21	PtSnIn/08Zr-Al	600	57.7–51.7	98	0.730	10	53
22	0.1Pt10Cu/Al_2O_3	600	40–22	90	1.672	5	13
23	Pt-Sn/SAPO-34-500	595	34.6–43.9	66	0.315	7	54
24	Pt-Cu/$MgAl_2O_4$	590	25.7–21.0	87.5	0.188	89	55
25	PtSn/Al_2O_3 sheet	590	48.7–44.6	99.1	1.601	143	4
26	PtNa/Zn(1.0%)-ZSM-5	590	40.6–37.8	93	0.274	85	56
27	PtNa/Sn-ZSM-5	590	41.7–39.1	95.3	0.288	83	57
28	PtSnNaLa(1.4%)/ZSM-5	590	41.5–37.5	97.1–97.5	0.292	30	58
29	PtSnCa(0.9%)/ZSM-5	590	34.9–27.5	51.4–62	0.139	23	27
30	Pt-Sn/mesoporous Al_2O_3	590	29.8–24.6	92	0.249	23	59

31	PtSnNa(1.0%)/Al-SBA-	590	27.5–12.6	94.1	0.188	12	[60]
32	Pt-Sn-6/$MgAl_2O_4$	580	45.0–38.9	99–99.7	0.332	359	[61]
33	Pt-Sn-5/$MgAl_2O_4$	580	47.0–37.6	98–99.5	0.318	233	[61]
34	Pt-Sn-4/$MgAl_2O_4$	580	50.0–31.5	98–99.6	0.285	116	[61]
35	Pt-Sn-3/$MgAl_2O_4$	580	42.0–18.7	97–99	0.223	78	[61]
36	Pt-Sn-2/$MgAl_2O_4$	580	45.0–18.7	92–98.3	0.219	71	[61]
37	Pt-Sn/$MgAl_2O_4$-ALT	575	33–29	99	0.593	18	[62]
38	Pt/Mg(Sn)(Al)O@Al_2O_3	550	29.4–27.8	93.7–99.2	0.950	3062	[5]
39	0.1Pt10Cu/Al_2O_3	550	13.1–12.7	90–94	0.548	3640	[13]
40	Pt/Nb_2CT_x	550	15.5–6.5	88	–	1	[63]
41	Pt/$Ti_3C_2T_x$	550	15.5–5.5	95	–	1	[63]

[a]The first value was obtained at the beginning of the run, and the second at the end. [b]The C_3H_6 selectivity was obtained at the beginning of the run. [c]Defined as (mol of reacted propane per second) per mol of total Pt. [d]Mean catalyst life defined as $\tau = k_d^{-1}$.

Table 11. Summary of the catalytic performance of PtGa–Ca–Pb/SiO_2 and other reported Pt-based catalysts in PDH in the presence of H_2.

Entry	Catalyst Pt (wt%)	Temp. (°C)	Gas composition (%)	WHSV (h^{-1})[a]		k_d (h^{-1})[d]	Operation time (h)[c]	Ref.
1	PtIn/Mg(Al)O-600	0.6	620	$C_3H_8/H_2/Ar$ = 8/7/35	3.1	0.027	30	[40]
2	0.3PtSn/1.5In-Al	0.3	620	$C_3H_8/H_2/Ar$ = 8/7/35	3.1	0.144	2.8	[41]
3	PtGa–Ca–Pb/SiO_2	3	600	C_3H_8/H_2/He =	5.9	0.0003	720 (30 d)	This
4	PtGa–Pb/SiO_2 (Pt/Pb =	3	600	C_3H_8/H_2/He =	30.7	0.001	96	[8]
5	PtGa/SiO_2	3	600	C_3H_8/H_2/He =	30.7	0.018	50	[8]
6	Pt0.1Zn0.17/SiO_2	0.1	600	C_3H_8/H_2 = 2/1	9.4	0.002	160	[42]
7	PtZn@S-1	0.41	600	$C_3H_8/H_2/N_2$ = 1/1/2	5.9	0.003	90	[43]
8	Pt/Mg(Sn)(Al)O@Al_2O_3	0.5	600	$C_3H_8/H_2/Ar$ = 1/0.5/2	14.0	0.004	48	[5]
9	0.6PtSn/1.5In-Al	0.6	600	$C_3H_8/H_2/Ar$ = 8/7/35	3.1	0.010	53	[41]
10	PtSnIn/1.5Ca-Al	0.3	600	$C_3H_8/H_2/Ar$ = 8/7/35	3.1	0.011	100	[28]
11	$Pt_{0.5}$-$Ge_{1.5}$/Al_2O_3-CaO	0.5	600	$C_3H_8/H_2/N_2$/Ar =	23.6	0.011	24	[26]
12	$Pt_{0.5}$-$Ge_{1.5}$/Al_2O_3	0.5	600	$C_3H_8/H_2/N_2$/Ar =	1.4	0.041	10	[44]
13	PtZn/0.02TS-170	0.5	600	$C_3H_8/H_2/N_2$ = 1/1/4	11.8	0.016	96.8	[45]
14	Pt_3In/SiO_2	0.3	600	$C_3H_8/H_2/N_2$ = 7/7/36	3.3	0.018	2.3	[46]
15	Pt3Ga/CeAl	1	600	C_3H_8/H_2/N = 13/13/24	10.2	0.026	15	[47]
16	PtSn/TS-1	0.5	600	$C_3H_8/H_2/N_2$ = 1/1/4	3.0	0.033	7	[48]
17	15%Zn-0.1%Pt/Al_2O_3	0.1	600	C_3H_8/H_2 = 1/1,	3.0	0.045	4	[49]
18	Pt/Nb1Al2-O	0.92	600	C_3H_8/H_2/N = 1/1/3	6.4	0.050	8	[50]
19	Pt-Sn/SBA-15	0.75	600	C_3H_8/H_2/N = 14/14/72	16.5	0.087	8	[51]
20	Pt/TA10	1	600	$C_3H_8/H_2/N_2$ =	10.2	0.098	10	[52]
21	PtSnIn/08Zr-Al	0.3	600	$C_3H_8/H_2/Ar$ = 8/7/35	3.1	0.097	2.5	[53]
22	0.1Pt10Cu/Al_2O_3	0.1	600	C_3H_8/H_2 = 1/1	3.8	0.215	4	[13]
23	Pt-Sn/SAPO-34-500	0.5	595	C_3H_8/H_2 = 4/1	5.6	0.149	8	[54]
24	Pt-Cu/$MgAl_2O_4$	1	590	C_3H_8/H_2/He = 19/19/2	6.8	0.011	24	[55]
25	PtSn/Al_2O_3 sheet	0.35	590	$C_3H_8/H_2/N_2$ =	9.4	0.007	24	[4]
26	PtNa/Zn(1.0%)-ZSM-5	0.5	590	C_3H_8/H_2 = 4/1	3.0	0.012	10	[56]
27	PtNa/Sn-ZSM-5	0.5	590	C_3H_8/H_2 = 75/25	3.0	0.012	9	[57]
28	PtSnNaLa(1.4%)/ZSM-5	0.5	590	C_3H_8/H_2 = 4/1	3.0	0.033	5	[58]
29	PtSnCa(0.9%)/ZSM-5	0.5	590	C_3H_8/H_2 = 4/1	3.1	0.043	8	[27]
30	Pt-Sn/mesoporous Al_2O_3	0.4	590	C_3H_8/H_2 = 4/1	3.0	0.044	6	[59]
31	PtSnNa(1.0%)/Al-SBA-	0.5	590	C_3H_8/H_2 = 4/1	3.0	0.084	7	[60]

32	Pt-Sn-6/$MgAl_2O_4$	0.39	580	$C_3H_8/H_2/He$ = 2/2/16	2.4	0.003	90	[61]
33	Pt-Sn-5/$MgAl_2O_4$	0.42	580	$C_3H_8/H_2/He$ = 2/2/16	2.4	0.004	90	[61]
34	Pt-Sn-4/$MgAl_2O_4$	0.50	580	$C_3H_8/H_2/He$ = 2/2/16	2.4	0.009	90	[61]
35	Pt-Sn-3/$MgAl_2O_4$	0.53	580	$C_3H_8/H_2/He$ = 2/2/16	2.4	0.013	90	[61]
36	Pt-Sn-2/$MgAl_2O_4$	0.55	580	$C_3H_8/H_2/He$ = 2/2/16	2.4	0.014	90	[61]
37	Pt-Sn/$MgAl_2O_4$-ALT	1	575	C_3H_8/H_2 = 1.25,	14.8	0.057	3.3	[62]
38	Pt/Mg(Sn)(Al)O@Al_2O_3	0.5	550	$C_3H_8/H_2/Ar$ = 1/0.5/2	14	0.0003	240	[5]
39	0.1Pt10Cu/Al_2O_3	0.1	550	C_3H_8/H_2 = 1/1	3.8	0.0003	120	[13]
40	Pt/Nb_2CT_x	2	550	$C_3H_8/H_2/N_2$ =	–	1.004	1	[63]
41	Pt/$Ti_3C_2T_x$	2	550	$C_3H_8/H_2/N_2$ =	–	1.188	1	[63]

[a]WHSV: weight hourly space velocity based on propane gas flow (h^{-1}). [b]The first-order deactivation model was used to estimate the catalyst stability.[1] [c]operation time: total time tested for a single run.

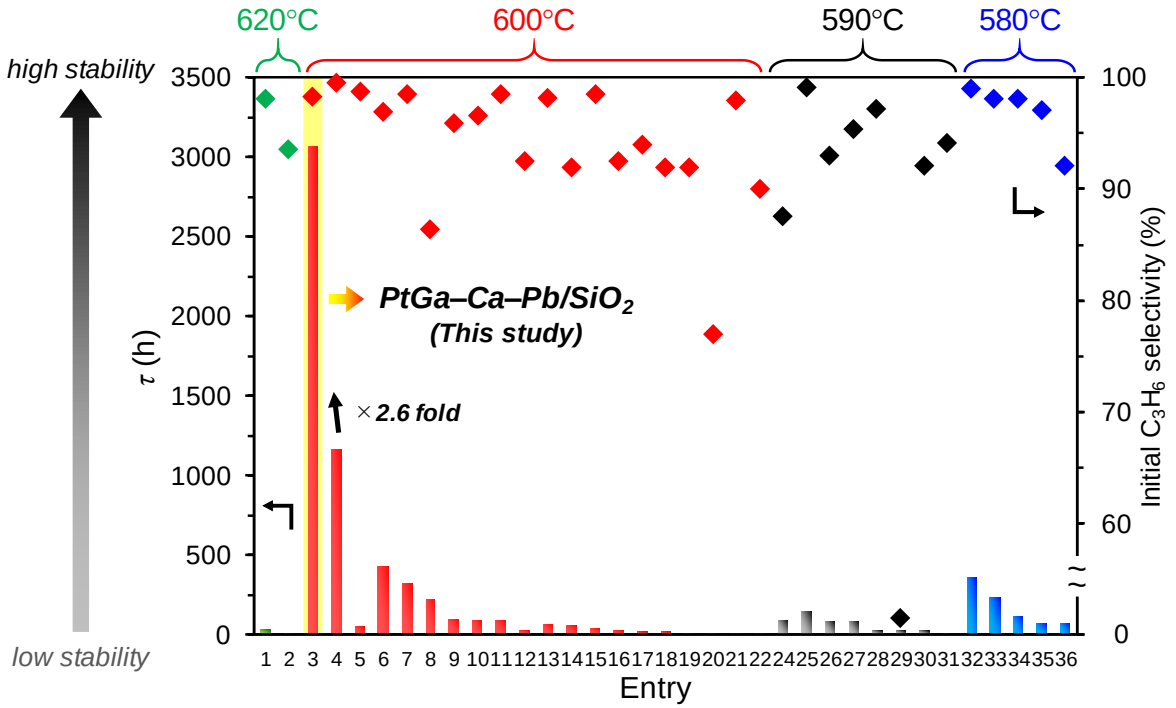

Figure 42. At-a-glance chart of the catalytic performance of PtGa–Ca–Pb/SiO_2 and the ever reported Pt-based catalysts in PDH with co-feeding H_2 (references are listed in Tables 10 and 11). Mean catalyst life (defined as $\tau = k_d^{-1}$) and initial C_3H_6 selectivity are categorized by several reaction temperatures (580°C~620°C). The results of the catalytic performance of the ever reported catalysts at temperatures lower than 570°C and higher than 630°C were omitted owing to low C_3H_8 conversion or production rate and the lack of long-term stability, respectively.

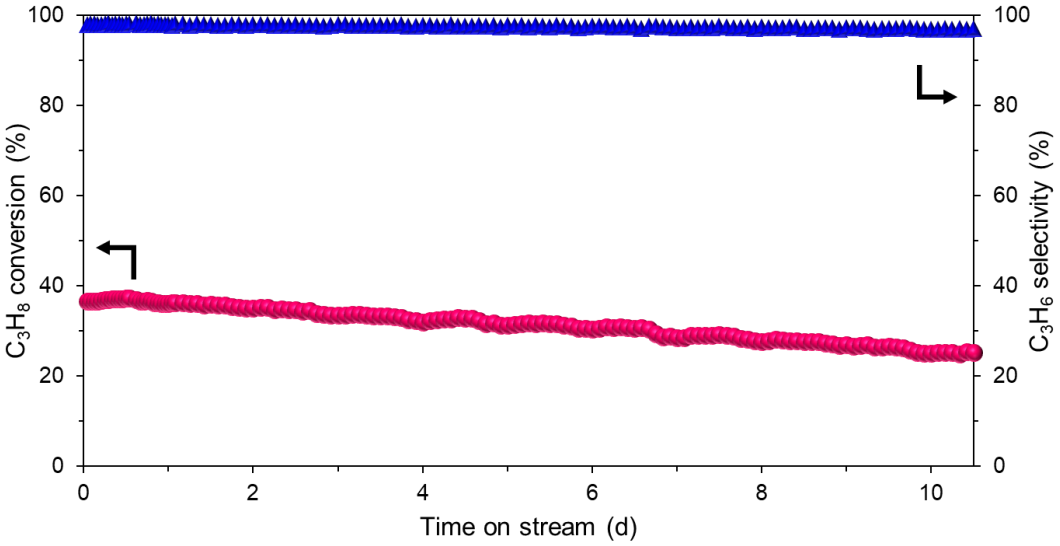

Figure 43. Long-term stability of PtGa–Ca–Pb/SiO_2 in PDH (WHSV = 5.9 h^{-1}) at 580°C using undiluted neat C_3H_8.

Table 12. Summary of the effects of additives and supports on PtGa and PDH.

Additive / Support	Alloying[a]	Availability of Pt[b]	Activity[c]	Electron-donation[d]
Ca	⊕	⊕	⊕	⊕
Mg	⊕	⊕	⊕	⊖
Sr, Y, La, Nd, Sm	⊕	⊖	⊖	⊖ / ⊗
Na, K, Rb, Cs	⊕	⊗	⊗	⊕ / ⊖
CaO, MgO, Al_2O_3, $MgAl_2O_4$, ZrO_2, CeO_2	⊕	⊖	⊗	⊖ / ⊗

[a]+: PtGa phase was formed. [b]Decrease of Pt dispersion upon decoration +: 0%, ─:60–85%, ×: 100%. [c]Initial propane conversion. +: >40%, ─: 25–40%, ×: <10%. [d]XANES negative shift: +: > 0.5 eV, ─: 0.1–0.3 eV, ×: 0 eV.

4.4. Discussion

Summarily, we designed and successfully synthesized doubly decorated intermetallics applying Ca and Pb to modify the geometric and electronic characters of PtGa. Pb was deposited on the three-fold Pt (and Ga) sites of the PtGa nanoparticles, whereas Ca was placed around the nanoparticles to impart them with an electron-enriched Pt_1 site (an active site for highly selective PDH). The effects of these modifications were synergistic and remarkably improved the catalytic stability in PDH. The PtGa–Ca–Pb/SiO_2 catalyst exhibited much superior stability to those of reported PDH catalysts (month-long stability, even at 600°C) was achieved. No other basic additives and supports than Ca did not work as effective modifiers for PtGa intermetallics, highlighting the specific character of Ca for the double-decoration strategy. The catalyst design concept, which was established in this study exposes a new horizon to enhance the catalytic performance of intermetallics in alkane dehydrogenation.

Reference

1 J. J. H. B. Sattler, J. Ruiz-Martinez, E. Santillan-Jimenez and B. M. Weckhuysen, *Chem. Rev.*, 2014, **114**, 10613–10653.

2 S. Chen, X. Chang, G. Sun, T. Zhang, Y. Xu, Y. Wang, C. Pei and J. Gong, *Chem. Soc. Rev.*, 2021, **50**, 3315–3354.

3 Y. Dai, X. Gao, Q. Wang, X. Wan, C. Zhou and Y. Yang, *Chem. Soc. Rev.*, 2021, **50**, 5590–5630.

4 L. Shi, G. M. Deng, W. C. Li, S. Miao, Q. N. Wang, W. P. Zhang and A. H. Lu, *Angew. Chem. Int. Ed.*, 2015, **54**, 13994–13998.

5 Y. Zhu, Z. An, H. Song, X. Xiang, W. Yan and J. He, *ACS Catal.*, 2017, **7**, 6973–6978.

6 L. Nykänen and K. Honkala, *ACS Catal.*, 2013, **3**, 3026–3030.

7 K. Searles, K. W. Chan, J. A. Mendes Burak, D. Zemlyanov, O. Safonova and C. Copéret, *J. Am. Chem. Soc.*, 2018, **140**, 11674–11679.

8 Y. Nakaya, J. Hirayama, S. Yamazoe, K. Shimizu and S. Furukawa, *Nat. Commun.*, 2020, **11**, 2838.

9 E. A. Redekop, V. V. Galvita, H. Poelman, V. Bliznuk, C. Detavernier and G. B. Marin, *ACS Catal.*, 2014, **4**, 1812–1824.

10 S. Zha, G. Sun, T. Wu, J. Zhao, Z. J. Zhao and J. Gong, *Chem. Sci.*, 2018, **9**, 3925–3931.

11 L. Rochlitz, K. Searles, J. Alfke, D. Zemlyanov, O. V. Safonova and C. Copéret, *Chem. Sci.*, 2020, **11**, 1549–1555.

12 Q. Sun, N. Wang, Q. Fan, L. Zeng, A. Mayoral, S. Miao, R. Yang, Z. Jiang, W. Zhou, J. Zhang, T. Zhang, J. Xu, P. Zhang, J. Cheng, D. C. Yang, R. Jia, L. Li, Q. Zhang, Y. Wang, O. Terasaki and J. Yu, *Angew. Chem. Int. Ed.*, 2020, **59**, 19450–19459.

13 G. Sun, Z. J. Zhao, R. Mu, S. Zha, L. Li, S. Chen, K. Zang, J. Luo, Z. Li, S. C. Purdy, A. J. Kropf, J. T. Miller, L. Zeng and J. Gong, *Nat. Commun.*, 2018, **9**, 4454.

14 E. C. Wegener, B. C. Bukowski, D. Yang, Z. Wu, A. J. Kropf, W. N. Delgass, J. Greeley, G. Zhang and J. T. Miller, *ChemCatChem*, 2020, **12**, 1325–1333.

15 S. C. Purdy, P. Ghanekar, G. Mitchell, A. J. Kropf, D. Y. Zemlyanov, Y. Ren, F. Ribeiro, W. N. Delgass, J. Greeley and J. T. Miller, *ACS Appl. Energy Mater.*, 2020, **3**, 1410–1422.

16 Z. Wu, B. C. Bukowski, Z. Li, C. Milligan, L. Zhou, T. Ma, Y. Wu, Y. Ren, F. H. Ribeiro, W. N. Delgass, J. Greeley, G. Zhang and J. T. Miller, *J. Am. Chem. Soc.*, 2018, **140**, 14870–14877.

17 N. J. LiBretto, C. Yang, Y. Ren, G. Zhang and J. T. Miller, *Chem. Mater.*, 2019, **31**, 1597–1609.

18 C. Ye, M. Peng, Y. Wang, N. Zhang, D. Wang, M. Jiao and J. T. Miller, *ACS Appl. Mater. Interfaces*, 2020, **12**, 25903–25909.

19 L. G. Cesar, C. Yang, Z. Lu, Y. Ren, G. Zhang and J. T. Miller, *ACS Catal.*, 2019, **9**, 5231–5244.

20 J. Zhu Chen, Z. Wu, X. Zhang, S. Choi, Y. Xiao, A. Varma, W. Liu, G. Zhang and J. T. Miller, *Catal. Sci. Technol.*, 2019, **9**, 1349–1356.

21 G. Zhang, C. Ye, W. Liu, X. Zhang, D. Su, X. Yang, J. Z. Chen, Z. Wu and J. T. Miller, *Nano Lett.*, 2019, **19**, 4380–4383.

22 M. K. Bhargava, A. A. Gadalla and K. Schubert, *J. Less-Common Met.*, 1975, **42**, 69–76.

23 J. Liu, Y. Yue, H. Liu, Z. Da, C. Liu, A. Ma, J. Rong, D. Su, X. Bao and H. Zheng, *ACS Catal.*, 2017, **7**, 3349–3355.
24 M. L. Yang, Y. A. Zhu, X. G. Zhou, Z. J. Sui and D. Chen, *ACS Catal.*, 2012, **2**, 1247–1258.
25 L. Nykänen and K. Honkala, *J. Phys. Chem. C*, 2011, **115**, 9578–9586.
26 S. Rimaz, L. Chen, A. Monzón, S. Kawi and A. Borgna, *Chem. Eng. J.*, 2021, **405**, 126656.
27 L. Bai, Y. Zhou, Y. Zhang, H. Liu and M. Tang, *Catal. Letters*, 2009, **129**, 449–456.
28 L. L. Long, W. Z. Lang, X. Liu, C. L. Hu, L. F. Chu and Y. J. Guo, *Chem. Eng. J.*, 2014, **257**, 209–217.
29 Y. Nakaya, M. Miyazaki, S. Yamazoe, K. Shimizu and S. Furukawa, *ACS Catal.*, 2020, **10**, 5163–5172.
30 B. Ravel and M. Newville, *J. Synchrotron Rad.*, 2005, **12**, 537–541.
31 A. Ankudinov and B. Ravel, *Phys. Rev. B, Condens. Matter Mater. Phys.*, 1998, **58**, 7565–7576.
32 M. D. Segall, P. J. D. Lindan, M. J. Probert, C. J. Pickard, P. J. Hasnip, S. J. Clark and M. C. Payne, *J. Phys. Condens. Matter*, 2002, **14**, 2717–2744.
33 B. Hammer, L. B. Hansen and J. K. Nørskov, *Phys. Rev. B, Condens. Matter Mater. Phys.*, 1999, **59**, 7413–7421.
34 A. Tkatchenko and M. Scheffler, *Phys. Rev. Lett.*, 2009, **102**, 6–9.
35 H. J. Monkhorst and J. D. Pack, *Phys. Rev. B*, 1976, **13**, 5188–5192.
36 R. Jana and S. C. Peter, *J. Solid State Chem.*, 2016, **242**, 133–139.
37 J. Ye, C. Liu and Q. Ge, *Phys. Chem. Chem. Phys.*, 2012, **14**, 16660–16667.
38 J. Yu, R. Wang, S. Ren, X. Sun, C. Chen, Q. Ge, W. Fang, J. Zhang, H. Xu and D. S. Su, *ChemCatChem*, 2012, **4**, 1376–1381.
39 R. Ryoo, J. Kim, C. Jo, S. W. Han, J. C. Kim, H. Park, J. Han, H. S. Shin and J. W. Shin, *Nature*, 2020, **585**, 221–224.
40 L. L. Shen, K. Xia, W. Z. Lang, L. F. Chu, X. Yan and Y. J. Guo, *Chem. Eng. J.*, 2017, **324**, 336–346.
41 X. Liu, W. Z. Lang, L. L. Long, C. L. Hu, L. F. Chu and Y. J. Guo, *Chem. Eng. J.*, 2014, **247**, 183–192.
42 S. Chen, Z. Zhao, S. Chen, Z. Zhao, R. Mu, X. Chang, J. Luo, S. C. Purdy, A. J. Kropf, G. Sun, C. Pei, J. T. Miller, X. Zhou, E. Vovk, Y. Yang and J. Gong, *Chem*, 2021, **7**, 1–19.
43 B. Zhang, G. Li, Z. Zhai, D. Chen, Y. Tian, R. Yang, L. Wang, X. Zhang and G. Liu, *AIChE J.*, 2021, 1–12.
44 S. Rimaz, C. Luwei, S. Kawi and A. Borgna, *Appl. Catal. A Gen.*, 2019, **588**, 117266.
45 X. Zhu, X. Wang and Y. Su, *Catal. Sci. Technol.*
46 S. Zha, G. Sun, T. Wu, J. Zhao, Z. J. Zhao and J. Gong, *Chem. Sci.*, 2018, **9**, 3925–3931.
47 T. Wang, F. Jiang, G. Liu, L. Zeng, Z. Zhao and J. Gong, *AIChE J.*, 2016, **62**, 4365–4376.
48 J. Li, J. Li, Z. Zhao, X. Fan, J. Liu, Y. Wei, A. Duan, Z. Xie and Q. Liu, *J. Catal.*, 2017, **352**, 361–370.
49 G. Liu, L. Zeng, Z. J. Zhao, H. Tian, T. Wu and J. Gong, *ACS Catal.*, 2016, **6**, 2158–2162.
50 T. Zhao, S. Shen, Y. Jia, C. W. Pao, J. L. Chen, Y. Guo, X. Liu, S. Dai and Y. Wang, *New J. Chem.*, 2020, **44**, 20115–20121.

51 J. Wang, X. Chang, S. Chen, G. Sun, X. Zhou, E. Vovk, Y. Yang, W. Deng, Z.-J. Zhao, R. Mu, C. Pei and J. Gong, *ACS Catal.*, 2021, **11**, 4401–4410.

52 F. Jiang, L. Zeng, S. Li, G. Liu, S. Wang and J. Gong, *ACS Catal.*, 2015, **5**, 438–447.

53 L. L. Long, K. Xia, W. Z. Lang, L. L. Shen, Q. Yang, X. Yan and Y. J. Guo, *J. Ind. Eng. Chem.*, 2017, **51**, 271–280.

54 Z. Nawaz, X. Tang, Y. Chu and F. Wei, *Cuihua Xuebao/Chinese J. Catal.*, 2010, **31**, 552–556.

55 G. Q. Ren, G. X. Pei, Y. J. Ren, K. P. Liu, Z. Q. Chen, J. Y. Yang, Y. Su, X. Y. Liu, W. Z. Li and T. Zhang, *J. Catal.*, 2018, **366**, 115–126.

56 Y. Zhang, Y. Zhou, L. Huang, S. Zhou, X. Sheng, Q. Wang and C. Zhang, *Chem. Eng. J.*, 2015, **270**, 352–361.

57 Y. Zhang, Y. Zhou, L. Huang, M. Xue and S. Zhang, *Ind. Eng. Chem. Res.*, 2011, **50**, 7896–7902.

58 Y. Zhang, Y. Zhou, H. Liu, Y. Wang, Y. Xu and P. Wu, *Appl. Catal. A Gen.*, 2007, **333**, 202–210.

59 Y. Zhang, Y. Zhou, J. Shi, S. Zhou, X. Sheng, Z. Zhang and S. Xiang, *J. Mol. Catal. A Chem.*, 2014, **381**, 138–147.

60 Y. Duan, Y. Zhou, Y. Zhang, X. Sheng and M. Xue, *Catal. Letters*, 2011, **141**, 120–127.

61 H. Zhu, D. H. Anjum, Q. Wang, E. Abou-Hamad, L. Emsley, H. Dong, P. Laveille, L. Li, A. K. Samal and J. M. Basset, *J. Catal.*, 2014, **320**, 52–62.

62 Y. L. Shan, T. Wang, Z. J. Sui, Y. A. Zhu and X. G. Zhou, *Catal. Commun.*, 2016, **84**, 85–88.

63 Z. Li, L. Yu, C. Milligan, T. Ma, L. Zhou, Y. Cui, Z. Qi, N. Libretto, B. Xu, J. Luo, E. Shi, Z. Wu, H. Xin, W. N. Delgass, J. T. Miller and Y. Wu, *Nat. Commun.*, 2018, **9**, 5258.

Chapter 5

Single-Atom Pt in High-Entropy Intermetallics as an Ultrastable Catalyst for Propane Dehydrogenation

5.1. Introduction

Propylene is one of the most important basic raw materials in the petrochemical industry, which has been increasingly scarce due to the shale gas revolution.[1–6] On-purpose propylene production *via* selective PDH into propylene has been regarded as the most promising propylene production technology compared with other methanol-to-olefins and Fischer-Tropsch-to-olefins because of high propylene selectivity to meet the increasing global demand for propylene. However, due to its endothermicity, PDH requires high operation temperatures (>600°C) to obtain sufficient propylene yield, in which severe catalyst deactivation by coking and/or sintering inevitably occurs in short periods. In this context, developing an innovative PDH catalyst that exhibits high propylene selectivity and catalyst stability even at ≥600°C is incredibly beneficial for the chemical industry. Although numerous efforts have been made to overcome this obstacle, no outstandingly stable catalyst has yet been found to function for several months without deactivation.

PDH is a structure-insensitive reaction, whereas the undesired side reactions leading to deactivation, such as hydrogenolysis, cracking, and coking, are structure-sensitive.[1–6] Active metal-metal ensembles such as Pt–Pt sites are known to induce these side reactions. Therefore, the dilution or isolation of Pt–Pt ensembles by an inert metal has been commonly employed as a standard catalyst design concept for selective and stable PDH.[1–7] SAAs,[8] where Pt atoms are isolated by excess counterpart metal such as Cu, are the representative material/approach for this purpose; the undesired propylene decomposition is successfully inhibited over Pt@Cu SAA. However, SAAs typically undergo significant aggregation at ≥600°C due to the insufficient thermal stability, resulting in an irreversible deactivation of the catalyst. Therefore, a novel material that serves isolated Pt with high thermal stability is required to develop an ultrastable catalytic system for PDH. The thermal stability of an alloy can be improved by increasing the number of constituent elements due to the significant contribution of mixing entropy, as observed for high-entropy alloys (HEAs: solid-solution alloys comprising five or more elements with near equimolar ratio).[9–11] Because of the unique characteristics and remarkable performances, the catalytic application of HEAs has received significant attention and amid the "gold rush" in recent years.[12] However, for a random alloy structure, a large excess (>20 equiv.) of counterpart metals is needed for the complete isolation of Pt.[8,13] Therefore, there remain some Pt–Pt sites in a common (quinary to octonary) HEA. Thus, a multimetallic alloy with a particular ordered structure should be constructed to overcome this challenge.

A possible candidate for such an ideal active site structure is high-entropy intermetallics (HEIs). Unlike HEAs, the constituent metals of an HEI are distributed separately to two (or more) crystallographically distinct sites, depending on the parent intermetallic structure.[14–18] Scheme 3 illustrates the specific catalyst design concept employed in this regard. We focused on PtGe as the parent binary intermetallics (FeAs-type structure, space group: *Pnma*) due to its unique ordered surface structure and significantly negative formation enthalpy ($\Delta H_f = -90.8$ kJ mol^{-1}).[19] The former provides one-dimensionally aligned Pt columns separated by Ge columns, where the surface

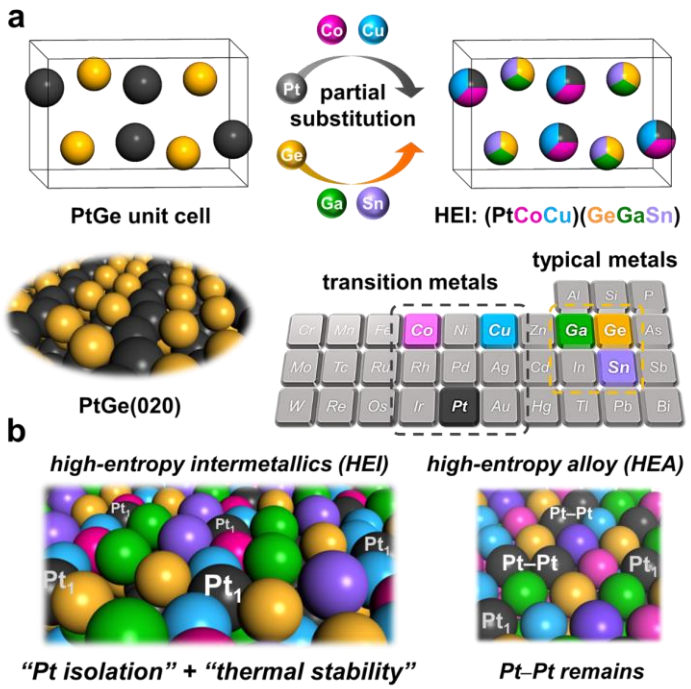

Scheme 3. The catalyst design concept for thermally stable isolated Pt site using HEI. (a) Pt and Ge sites in intermetallic PtGe are partially substituted by Co(Cu) and Ga(Sn), respectively, resulting in the formation of PtGe-type HEI (PtCoCu)(GeGaSn). (b) Illustrations of the (020) surface of (PtCoCu) (GeGaSn) HEI (left) and (111) surface of Pt-based senary HEA (right).

Pt–Pt coordination number is only two (Scheme 3a). Besides, the latter can be the driving force to retain the ordered structure upon multi-metallization. Here, the Pt and Ge sites in PtGe are partially substituted by much less-active transition (Co and Cu) and inert typical (Ga and Sn) metals, respectively to form a senary HEI, *i.e.*, $(Pt_xCo_{0.5-x/2}Cu_{0.5-x/2})(Ge_{0.33}Ga_{0.33}Sn_{0.33})$ (hereafter, denoted as HEI(x)). These diluent metals were chosen based on the following guidelines; (1) analogous to Pt and Ge (near in the periodic table, Scheme 1a), (2) catalytically less active or inert, and (3) no volatility and toxicity. This site-specific multi-metallization allows the isolation of Pt by Co and Cu and further enhancement in thermal stability by Ga and Sn. Moreover, the degree of Pt isolation can be tuned by changing the Pt fraction x. As a result, the isolated Pt sites surrounded by other inert constituent metals functioned as a highly selective and stable PDH catalyst at high reaction temperatures. This study reports a novel catalyst material and design concept based on HEIs, providing thermally stable isolated Pt and working as an outstandingly stable catalyst for high-temperature PDH.

5.2. Experimental

5.2.1. Catalyst Preparation.

(PtCoCu)(GeGaSn)/Ca–SiO_2, namely, high-entropy intermetallic(0.25) [HEI(0.25)] was synthesized by the pore-filling co-impregnation method, which can deposit all the metal components on the SiO_2 support without loss.[20] $Pt(NH_3)_2(NO_3)_2$ (Furuya Metal Co. Ltd., 4.60 wt% of Pt in HNO_3 solution), $Co(NO_3)_2{\cdot}6H_2O$ (Wako, ≥98.0%),

$Cu(NO_3)_2 \cdot 3H_2O$ (Sigma-Aldrich, ≥99%), $(NH_4)_2GeF_6$ (Sigma-Aldrich, 99.99%), $Ga(NO_3)_3 \cdot nH_2O$ (n = 7-9, Wako, 99.9%) $(NH_4)_2SnCl_6$ (Alfa Aesar, 98%), and $Ca(NO_3)_2 \cdot 4H_2O$ (Wako, 98.5%), were used as precursors. The loading amount of Pt was fixed at 1 wt%. The detailed molar ratios of metals are given in Table S1. Mixed aqueous solution of the metal precursors was first added dropwise to SiO_2 (CARiACT G–6, Fuji Silysia, SBET = *ca.* 500 $m^2\ g^{-1}$) so that the solutions just filled the pore of the SiO_2 (*ca.* 1.6 mL of solution per g of SiO_2). The obtained mixtures were sealed by three pieces of plastic film and kept overnight at room temperature, followed by transferring to a round-bottom flask and subsequent freezing using liquid nitrogen. The frozen mixtures were dried in vacuum at ca. −5°C and further dried in an oven at 90°C overnight. The resulting powder was calcined at 400°C for 1 h in dry air with ramping rate of 1 °C min^{-1}. The calcined powder was then reduced under flowing H_2 (0.1 MPa, 50 mL min^{-1}) at 700°C for 1 h with ramping rate of 20 °C min^{-1}. The metal content of HEI(0.25) was estimated using inductively coupled plasma atomic emission spectroscopy as follows: Pt: 0.96 wt%, Co: 0.45 wt%, Cu: 0.53, Ge: 0.44 wt%, Ga: 0.53 wt%, Sn: 0.89 wt%, Ca: 3.01 wt%, which were close to the fed compositions (Pt: 1.00 wt%, Co: 0.45 wt%, Cu: 0.49, Ge: 0.56 wt%, Ga: 0.71 wt%, Sn: 0.91 wt%, Ca: 3.08 wt%)

PtFeCoCuGa/Ca–SiO_2 (high-entropy alloy: HEA), (PtCoCu)Ge/Ca–SiO_2, and PtCoCuGa/Ca–SiO_2 catalysts were also prepared in a similar method to that of HEI. The loading amount of Pt was fixed at 1 wt%. $Fe(NO_3)_3 \cdot 6H_2O$ (Sigma-Aldrich, ≥98%) was used as a precursor for HEA.

$Pt_{0.5}M_{0.5}$/Ca–SiO_2 (solid solution alloys, M = Co and Cu) and PtM'/Ca–SiO_2 (intermetallic compounds, M' = Ge, Ga, and Sn) catalysts were also prepared in a similar method to that of HEI. The loading amount of Pt was fixed at 1 wt%. The detailed molar ratios of metals are summarized in Table S1.

Pt–Cu/Ca–SiO_2, namely, SAA catalyst was also prepared in a similar method to that of HEI. The loading of Pt and ratio of Cu/Pt were fixed at 1 wt% and 25, respectively. Pt–Cu/Ca–SiO_2 catalysts with different Cu/Pt ratios were also prepared in a similar method to that of SAA catalyst.

Bulk PtGe powder was synthesized by mixing aqueous solutions of $Pt(NH_4)_4(OH)_{2(aq)}$ and $(NH_4)_2GeF_{6(aq)}$. First, an aqueous solution (total 4.0 g) containing 114.2 mg of $(NH_4)_2GeF_6$ (Thermo Scientific, 99.99%) was added dropwise to a vigorously stirred aqueous solution of $Pt(NH_4)_4(OH)_{2(aq)}$ (4.87 g, Furuya Metal, Pt: 2.05 wt%), followed by stirring for 30 min. Then, the precipitate was corrected by centrifugation and washed by water 3 times. The resultant mixture was dried in an oven at 90°C overnight, followed by reduction under flowing H_2 (0.1 MPa, 50 mL $min^{-1)}$ at 700°C for 1 h with a ramping rate of 20 °C min^{-1}.

5.2.2. Catalytic Reactions.

The PDH reactions were performed in a vertical, quartz fixed-bed reactor with an internal diameter of 4 mm under an atmospheric pressure. Typically, 20~100 mg of catalysts was charged in the reactor. Prior to the catalytic test, the catalyst was reduced under flowing H_2 at 600°C for 0.5 h, and the reactant gas mixture was subsequently fed; C_3H_8:He = 2.5:5.0, a total of 7.5 mL min^{-1} (WHSV = 3.0~14.8 h^{-1}). WHSV was calculated based on the weight of C_3H_8 and catalyst. For the long-term stability tests of the HEI catalyst at 600°C with co-feeding H_2, 150 mg of catalyst was used to obtain over 30% propane conversion (WHSV = 2.0 h^{-1}). Prior to the catalytic test, the catalyst was pretreated under flowing H_2 (10 mL min^{-1}) at 600°C for 0.5 h, the reactant gas mixture was subsequently fed; C_3H_8:H_2:He = 2.5:1.3:3.7, a total of 7.5 mL min^{-1}.. The product gas was analyzed by online gas chromatography equipped downstream with a TCD (Shimadzu GC–8A) and a column of Gaskuropak 54 (GL Science). For all the catalysts, C_3H_8, C_2H_4, C_2H_6, and CH_4 were detected as reaction products. C_3H_8 conversion, C_3H_6 selectivity, C_3H_8 yield, and material balance were calculated as shown in Chapter 3, respectively. Material balance typically ranged between 98~102% for all the reactions.

To estimate the catalyst stability, the first-order deactivation model was employed.[1] k_d (h^{-1}) and τ (h) were used as shown in Chapter 3. k_d (h^{-1})[1] and τ (h) represent the deactivation rate constant and mean catalyst life, respectively. Here, lower k_d and higher τ values represent higher catalyst stability. C_3H_8 conversion, C_3H_6 selectivity, C_3H_8 yield, and material balance were defined by Eqs (1) ~ (4), respectively. Material balance typically ranged between 98~102% for all the reactions. To estimate the catalyst stability, the first-order deactivation model was employed (refer to Experimental in Chapter 2).[1] k_d (h^{-1}) and τ (h) were used (refer to Experimental in Chapter 2). k_d (h^{-1})[1] and τ (h) represent the deactivation rate constant and mean catalyst life, respectively. Here, lower k_d and higher τ values represent higher catalyst stability. The rate constant for the forward direction (k_f) of PDH was estimated by Eq 7.

$$k_f = \frac{R}{P_{C_3H_8}\left(1 - \frac{1}{K_e}\frac{P_{C_3H_6}P_{H_2}}{P_{C_3H_8}}\right)} \qquad (7)$$

where, R, P_X, and K_e are the specific activity [mol_{C3H6} g_{Pt}^{-1} h^{-1}], partial pressure of X [bar], and equilibrium constant [bar].[7,21]

5.2.3. Characterization.

The crystalline phase in the prepared catalysts were analyzed in an *ex-situ* mode using powder XRD (Rigaku, MiniFlex 700+D/teX Ultra; Cu Kα X–ray source).

Synchrotron XRD measurement was carried out for the HEI catalyst at BL19B2 beamlines of SPring-8, JASRI. Wavelength of 0.5 Å (25 keV) was utilized as X-ray source.

HAADF-STEM was used to investigate the particle size distribution and the crystal structure of the prepared catalyst using a FEI Titan G2 microscope equipped with an EDX analyzer operated at 300 kV. Prior to the observation, the as-reduced catalyst was firstly ground and dispersed in ethanol by ultrasonic. Then, the dispersed catalyst was deposited on a molybdenum grid and dried in vacuum. The particle size distribution was estimated by using length mean particle size.

H_2-TPR was performed using BELCAT-II (Microtrac BEL) instrument. Prior to the H_2-TPR, 30 mg of the as-calcined (not reduced) catalyst was heated under a flow of Ar (20 mL min^{-1}) at 300°C for 30 min to remove the physically absorbed species (such as H_2O). Then, the catalyst was cooled to 100°C, subsequently heated from 100°C to 900°C with a ramping rate of 2 °C min^{-1} under a flow of 5% H_2/Ar (20 mL min^{-1}). The H_2 consumption was quantified by a TCD equipped downstream in BELCAT-II.

The dispersion of Pt in the catalyst was estimated by CO-pulse chemisorption at −100°C using BELCAT-II (Microtrac BEL) instrument. Prior to chemisorption, 100 mg of the catalyst was reduced under a 5% H_2/Ar flow (20 mL min^{-1}) at 600°C for 30 min, then cooled to −100°C using CATCryo-II under a He flow (20 mL min^{-1}). Afterward, a pulse of 10% CO/He was introduced into the reactor and CO passed thought the catalyst bed was quantified by a TCD equipped downstream. This CO pulse introduction was repeated until the TCD signal due to the effluent CO gas unchanged (the amount of chemisorbed CO reached saturation). For the calculation of Pt dispersion, the stoichiometry of chemisorbed CO/Pt was estimated as 1.

The FT-IR spectra of adsorbed CO were obtained using a JASCO FTIR-4100 spectrometer with a mercury-cadmium-telluride (MCT) detector in a transmission mode (resolution 4 cm^{-1}) under a dynamic condition. Prior to CO chemisorption, 100 mg of the catalyst was pressed into a pellet (diameter: 20 mm) and placed in a pretreatment room (quartz). The catalyst was heated to 600°C and kept at same temperature under flowing H_2 at 600°C for 1 h. The reduced sample was then evacuated in vacuum at 600°C for 1h, then the cooled to room temperature, subsequently transferred to a measurement room, equipped with CaF_2 windows and a vessel, without exposure to air. Then the sample was then cooled to ca. −100°C using cooled ethanol. The sample was subsequently exposed to 10% CO/He flow, then evacuated in vacuum to remove CO in gas phase and physisorbed on the catalyst. During the measurement, infrared ray was cut by 20% using a filter.

XPS analysis was performed using a JEOL JPS-9010MC spectrometer (X-ray source: Mg-Kα radiation). First, the as-reduced catalysts were re-reduced at 700°C for 30 min under flowing H_2 (50 mL min^{-1}), then cooled to room temperature, subsequently transferred into an Ar grove box (O_2 : <0.1 ppm) without exposing to air. Afterward, the catalysts were loaded on carbon tape and transferred into the spectrometer using transfer vessel without air exposure. The obtained spectra were calibrated with the Si 2*p* emission of the SiO_2 support (103.9 eV).

The amount of coke accumulated on the spent catalysts after PDH was quantified by TPO. Firstly, 60 mg of the fresh catalyst (Pt 1 wt%) was used for PDH at 600°C for 20 h. Then, the spent catalyst (30 mg) was transferred into a quartz tube reactor. Prior to the TPO experiment, the catalyst was first pretreated at 300°C for 0.5 h under flowing He (10 mL min^{-1}), and then cooled to 100°C, subsequently heated from 100°C to 700°C with a ramping rate of 2 °C min^{-1} under flowing 2% O_2/He (50 mL min^{-1}) and kept at 700°C for 10 min. The outlet gas (typically CO_2; m/z = 44) was analyzed online by quadrupole mass spectrometer (BELMASS) equipped downstream.

Temperature-programmed desorption of C_3H_6 (C_3H_6-TPD) was carried out using BELCAT-II (Microtrac BEL) instrument. Prior to the C_3H_6-TPD, the as-reduced catalyst (100 mg) was heated to 600C under 5%H_2/Ar gas mixture (20 mL min^{-1}) with a ramping rate of 20 °C min^{-1}, then kept at same temperature for 0.5 h. After the reduction, the catalyst was cooled to −35°C using CATCryo-II under a He flow (20 mL min^{-1}), then kept at −35°C for 0.5 h, subsequently exposed to 5%C_3H_6/He gas mixture (20 mL min^{-1}) at same temperature for 5 minutes. The catalyst was then purged under He (50 mL min^{-1}) at −35°C for 1.5 h, subsequently heated from −35°C to 300°C with a ramping rate of 2 °C min^{-1}. The outlet gas (C_3H_6; m/z = 41) was analyzed online by quadrupole mass spectrometer (BELMASS) equipped downstream.

CO-TPD was performed using a JASCO FTIR-4100 spectrometer with a MCT detector in a transmission mode (resolution 4 cm^{-1}) under a dynamic condition. First, 100 mg of the catalyst was pressed into a pellet (diameter: 20 mm) and placed in a measurement room (pyrex). The catalyst was then heated to 500°C with a ramping rate of 20 °C min^{-1} and kept at same temperature under flowing 15%H_2/He (70 mL min^{-1}). After the reduction, the sample was cooled to room temperature, subsequently purged under He (60 mL min^{-1}) for 10 minutes. Afterward, the sample was exposed to 10% CO/He flow for 10 minutes, then purged under He (60 mL min^{-1}) to remove CO in gas phase and physisorbed on the catalyst. Finally, the sample was heated with a ramping rate of 10 °C min^{-1}. During the measurement, infrared ray was cut by 20% using a filter.

The actual metal content of HEI(0.25) was measured using ICP-AES at the Instrumental Analysis Division, Global Facility Center, Creative Research Institution, Hokkaido University.

XAFS measurements of the catalysts and reference samples were carried out at BL01B1 and BL14B2 beamlines of SPring-8, JASRI. XAFS spectra were recorded at the Pt L_{II}- and Co K-, Cu K-, Ge K-, Ga K-, and Sn K-edges in transmission mode at room temperature using a Si(111) double-crystal monochromator. Typically, XAFS spectra for Pt-containing catalyst is performed at the Pt L_{III}-edge. However, Ge K-edge oscillation interfered the Pt L_{III}-edge XAFS spectra, therefore Pt L_{II}-edge spectra was chosen in this study. Besides, the Pt L_{III}- and Pt L_I-edge oscillations also interfere the Ge K-edge and Pt L_{II}-edge spectra, respectively. Therefore, the XAFS oscillations for Pt L_{II}- and Ge K-edges at high *k* values (> *ca*. 11) do not provide the important information for structural analysis due to the overlap of the adjacent XANES spectra. Prior to pelletization, the catalyst was crushed using agate mortar for more than 40 min to suppress the hole effect. Then, the crushed catalyst was pressed into a pellet (diameter of 7 mm). For *in-situ* XAFS measurement, the pelletized sample of as-calcined (not reduced) catalyst was transferred into a quartz cell and pre-reduced at 700°C for 60 min under flowing 50% H_2/He (50 mL min^{-1}), and then cooled to room temperature under He gas flow (25 mL min^{-1}). For *ex-situ* XAFS measurement, the pelletized sample of as-reduced catalyst was transferred into a quartz cell and pre-reduced at 700°C for 30 min

(bulk PtGe: 650°C for 1 h) under flowing H_2 (50 mL min^{-1}), and then cooled to room temperature. After the pretreatment, the quartz tube containing the reduced pellet was sealed and transferred into an Ar grove box (O_2 : <0.1 ppm) without exposing to air. The pellet was sealed in a plastic film bag (Barrier Nylon) together with an oxygen absorber (ISO A500-HS: Fe powder). The spectra were recorded several times and merged at each measurement step to obtain good signal-to-noise (*S*/*N*) ratio. The obtained XAFS spectra were analyzed using Athena and Artemis software ver. 0.9.25 implemented in the Demeter package.[22] The back-scattering amplitude and phase shift functions were calculated by FEFF8.[23] *R*-factor (R^2) for curve-fitting was defined as follows: $R^2 = \Sigma i\{k^3\chi_i^{exp}(k)-k^3\chi_i^{fit}(k)\}^2/\Sigma i\{k^3\chi_i^{exp}(k)\}^2$.

5.2.4. Computational Details.

Periodic DFT calculations were performed using the CASTEP code[24] with Vanderbilt-type ultrasoft pseudopotentials and the revised version of Perdew−Burke−Ernzerhof exchange−correlation functional based on the generalized gradient approximation.[25] The plane-wave basis set was truncated at a kinetic energy of 360 eV. A Fermi smearing of 0.1 eV was utilized. Dispersion correlations were considered using the Tkatchenko–Scheffler method with a scaling coefficient of $s_R = 0.94$ and a damping parameter of $d = 20$.[26] The reciprocal space was sampled using a k-point mesh with a spacing of typically 0.04 $Å^{-1}$, as generated by the Monkhorst−Pack scheme.[27] Geometry optimizations were performed on supercell structures using periodic boundary conditions. The surfaces were modeled with a thickness of four atomic layers with 13 Å of vacuum spacing. The unit cell size of the bulk crystal was first optimized, followed by modeling the slab structure and surface relaxation with the size of the supercell fixed. The convergence criteria for structure optimization and energy calculation were set to (a) an SCF tolerance of 1.0×10^{-6} eV per atom, (b) an energy tolerance of 1.0×10^{-5} eV per atom, (c) a maximum force tolerance of 0.05 eV $Å^{-1}$, and (d) a maximum displacement tolerance of 1.0×10^{-3} Å. For all calculations, the net charge was set to zero and spin polarization was considered. The adsorption energy was defined as follows: $E_{ad} = E_{A\text{-}S} - (E_S + E_A)$, where $E_{A\text{-}S}$ is the energy of the slab together with the adsorbate, E_A is the total energy of the free adsorbate, and E_S is the total energy of the bare slab. Surface energy calculations were conducted for densely packed low-index planes of PtGe such as (211), (202), (112), (002), (020), (102), (103). The surface energy was defined as follows: $\gamma = (E_S - NE_B)/2A$, where E_B is the energy of bulk unit cell, A is the surface area, and *N* is the number of unit cells in the slab. Transition state search was carried out based on the complete linear synchronous transit/quadratic synchronous transit method[28,29] with the tolerance for all root-mean-square forces on an atom of 0.10 eV $Å^{-1}$.

For constructing the HEI(0.25) structure, a PtGe–(2×2×2) supercell was considered as a base structure. Some Pt and Ge atoms in the supercell were substituted with Co/Cu and Ga/Sn atoms, respectively so that the Pt/(Pt+Co+Cu) and Ge/(Ga+Ge+Sn) ratios were 0.25 and 0.33, respectively (total numbers; Pt: 8, Co: 12, Cu: 12, Ga: 11, Ge: 11, and Sn: 10). The configuration of each element (Pt, Co, Cu in the Pt sites and Ga, Ge, Sn in the Ge sites) was randomly determined using the RAND and RANK functions in Excel. Besides, the following restrictions were employed to maximize the configuration entropy, which cannot be considered by the conventional DFT and is expected to be thermodynamically likely: (1) all the Pt atoms in each (040) plane are isolated (no Pt–Pt) and (2)

the number of each element in each (040) plane is almost same (Pt: 2, Co: 3, Cu: 3, Ga: 2 or 3, Ge: 2 or 3, and Sn: 2 or 3) (mode A). In addition, purely random distributions without these restrictions were also considered (mode B). We generated forty (twenty for modes A and B) configurations that were geometrically optimized and chose the most energetically stable one as a likely structure. The first (HEI(040):A) and the second (HEI(040):B) top layers of the (040) plane of the supercell were selected as the model surfaces of HEI(0.25) (Figure S50). There are four isolated Pt atoms and eight Pt–Co(Cu) bridge sites (A1–A4 and B1–B4) as the H adsorption sites. The stepwise C–H scissions of propane were considered for the eight different active sites so that the eliminated hydrogen atom was captured by the bridge site, whereas the carbon moiety was placed on the Pt atom.

5.3. Results

5.3.1. Characterization of (PtCoCu)(GeGaSn)/Ca–SiO_2.

The HEI and the related alloy catalysts were prepared by a pore-filling impregnation method as supported nanoparticles using Ca-modified amorphous silica (Ca–SiO_2). The HAADF-STEM analysis showed that nanoparticle size ranged mainly 1.5–3 nm (average: 2.2 nm, Figure 44). Figure 45a shows the elemental maps of a single nanoparticle obtained using the EDX analysis, confirming that the nanoparticle comprised Pt, Co, Cu, Ge, Ga, and Sn. Quantitative analysis for some small nanoparticles revealed that the atomic ratios of (Pt+Co+Cu)/(Ge+Ga+Sn) were close to unity (Figure 46). Figure 45b shows the synchrotron XRD pattern of the HEI(0.25) catalyst, showing a PtGe-type diffraction pattern, unlike *fcc*- or *hcp*-type HEAs.[12] The diffraction angles for the HEI were higher than those of the parent PtGe, which can be attributed to lattice shrinkage by substituting Pt with the smaller size elements, Co and Cu. This experimental lattice shrinkage (5.6%) was consisted finely with the theoretical value estimated by Vegard's rule and each atomic radius (5.4%, supporting the formation of the HEI structure. The intensity of 011 diffraction (observed at 9° for PtGe) was lowered for HEI, which can be attributed to lattice distortion caused by mixing several elements with different atomic radii. Such a decrease in the diffraction intensity was also observed in *fcc* HEA systems.[30–32]

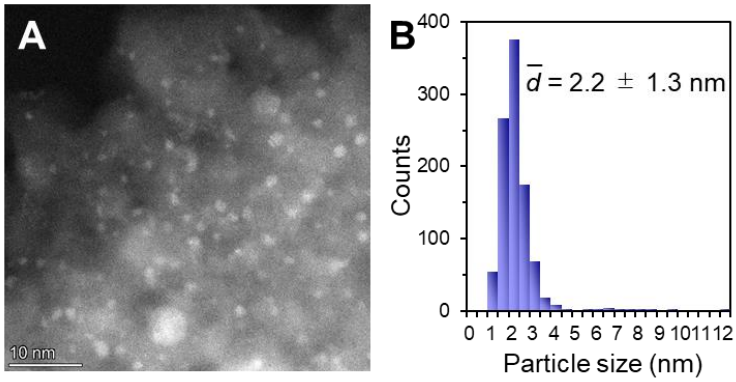

Figure 44. (a) HAADF-STEM image of the HEI(0.25) catalyst (Pt 1 wt%) and (b) the particle size distribution for 1000 nanoparticles.

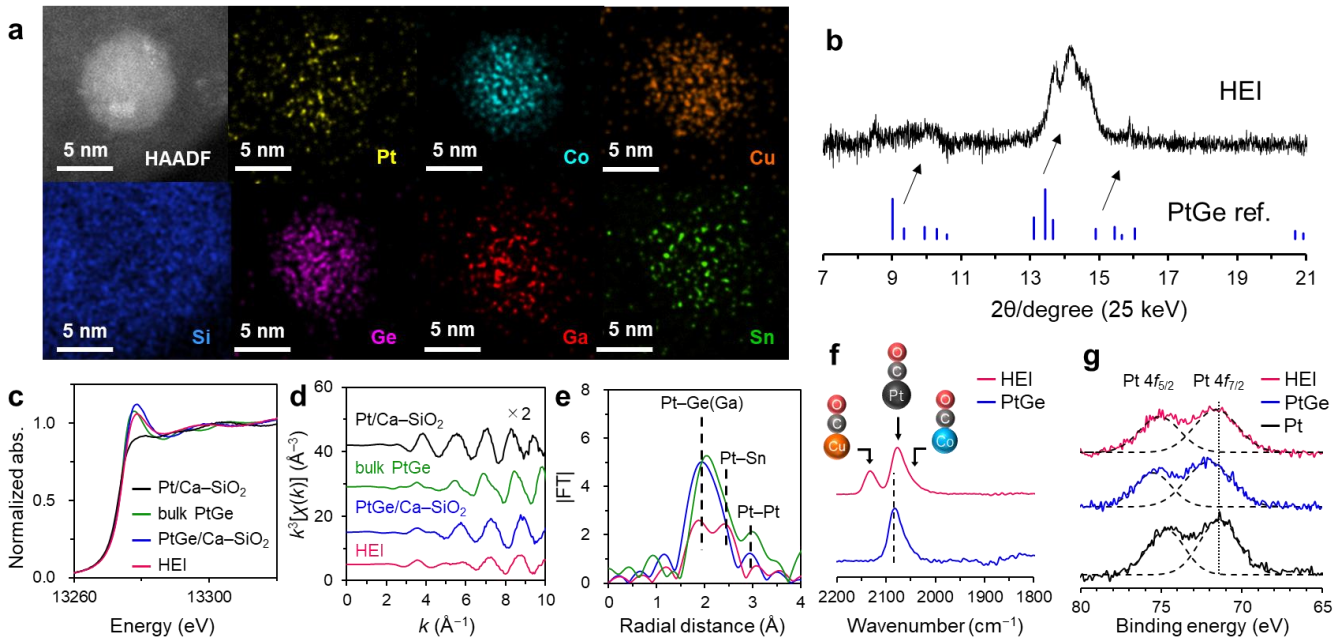

Figure 45. Characterization of the HEI(0.25) catalyst. (a) HAADF-STEM image and the corresponding elemental maps for a single nanoparticle. (b) Synchrotron XRD pattern. Pt L_{II}-edge (c) XANES, (d) k^3-weighted EXAFS oscillations, and (e) Fourier-transformed EXAFS of Pt/Ca–SiO_2, bulk PtGe, PtGe/Ca–SiO_2, and HEI(0.25). (f) FT-IR spectra of CO adsorbed on PtGe/Ca–SiO_2 and HEI(0.25) at −100°C. (g) XPS of Pt/Ca–SiO_2, PtGe/Ca–SiO_2, and HEI(0.25).

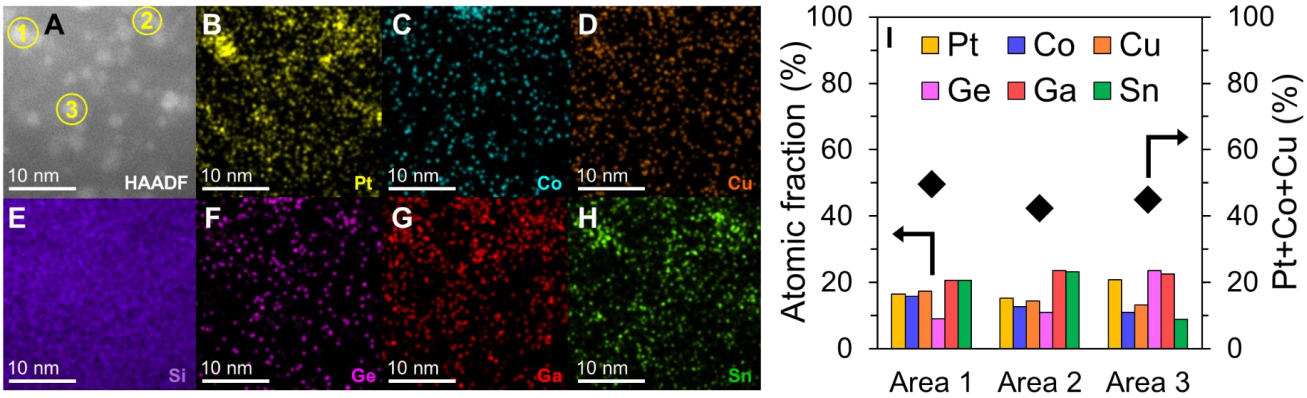

Figure 46. (a) HAADF-STEM image of the HEI(0.25) catalyst and corresponding elemental maps of (b) Pt, (c) Co, (d) Cu, (e) Si, (f) Ge, (g) Ga, and (h) Sn. (i) Quantitative analysis of the HEI(0.25) catalyst. The atomic ratio of (Pt+Co+Cu)/(Ge+Ga+Sn) was approximately 1/1, which is consistent with the PtGe-type HEI structure, in which Pt and Ge sites were substituted by Co(Cu) and Ga(Sn), respectively. The elemental maps acquired by EDX did not clearly reflect the shapes of nanoparticles, which was due to the too small size and the insufficient resolution

We also performed XAFS analysis to obtain further structural information. Figure 45c shows the Pt L_{II}-edge XANES spectra of Pt/Ca–SiO_2, bulk PtGe, PtGe/Ca–SiO_2, and HEI(0.25) (see Figure 47 for other edges). The bulk PtGe and PtGe/Ca–SiO_2 have diffraction patterns characteristic to intermetallic PtGe (Figure 48 and 49), hence can be used as references for bulk and nanoparticulate PtGe, respectively (the size of nanoparticle size was 1.8 nm in average). HEI(0.25) has a XANES characteristic that was similar to bulk PtGe and PtGe/Ca–SiO_2 but different from Pt/Ca–SiO_2. In the raw EXAFS oscillations, a similar tendency was seen (Figure 45d). Although a small difference in the oscillation feature was observed at k = 3–6 $Å^{-1}$, this can be attributed to the overlap of the Pt–Sn scattering (Figure 50). Notably, the EXAFS oscillation of HEI(0.25) did not match with those of PtGa/Ca–SiO_2 and PtSn/Ca–SiO_2 (Figure 49), supporting that the HEI retained the PtGe-type crystal structure. Further structural information is presented in the Fourier-transformed EXAFS spectra. Unlike PtGe, HEI(0.25) showed two peaks at 2.0 Å and 2.5 Å (Figure 45e), which could be assigned to Pt–Ge(Ga) and Pt–Sn scatterings, respectively, demonstrating that Sn is doped into the Ge site. Besides, the Pt–Pt scattering at 3.0 Å, observed for PtGe, disappeared upon the multi-metallization. This suggests that Pt atoms were sufficiently isolated by substitution with Co and Cu. We also performed comparable analyses for absorption edges other than Pt L_{II}, where curve fitting allowed use to assign all of the associated transition–typical metal scatterings (for example, Co–Ge(Ga), Cu–Sn, Ga–Co(Cu), and Sn–Pt). These results comprehensively support the formation of the (PtCoCu)(GeGaSn) HEI structure.

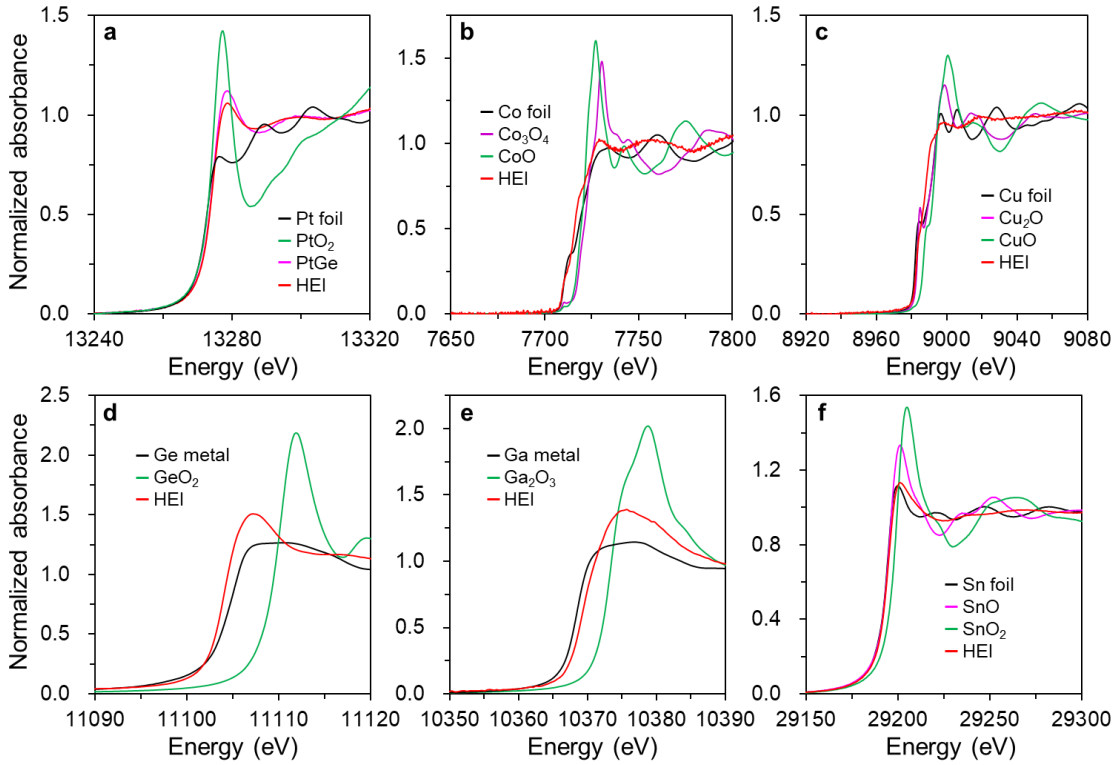

Figure 47. (a) Pt L_{II}-, (b) Co K-, (c) Cu K-, (d) Ge K-, (e) Ga K-, and (f) Sn K-edges XANES spectra of HEI(0.25) recorded at room temperature. *In-situ*; Ge K-, Ga K-, and Sn K-edges. *Ex-situ*: Pt L_{II}-, Co K- and Cu K-edges.

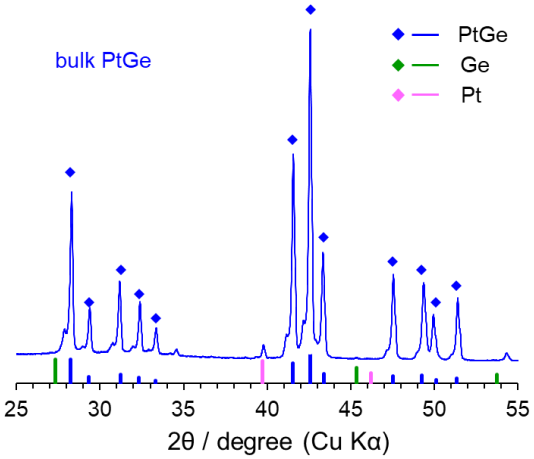

Figure 48. XRD pattern of PtGe bulk. The sharp diffraction peaks of PtGe intermetallic were mainly observed.

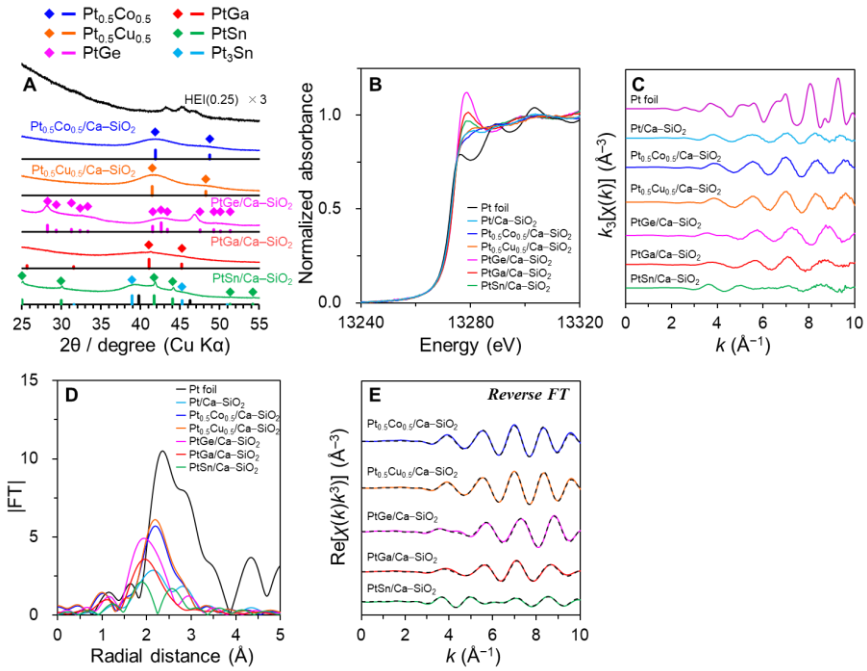

Figure 49. (a) XRD patterns of SiO_2-supported Pt-based bimetallic catalysts (Pt 6 wt%, Ca/Pt = 2.5). The vertical lines and the rhombus indicate the diffraction angles of references. References: Pt[33], $Pt_{0.5}Co_{0.5}$[34], $Pt_{0.5}Cu_{0.5}$ (calculated based on Vegard's law using Pt[33] and Cu[35] as references), PtGe[36], PtGa[37], PtSn[38], and Pt_3Sn[38]. The unknown peak, centered at 47°, was observed for PtGe/Ca–SiO_2. The unknown peak did not match with those of other Pt-Ge intermetallics. (b) Pt L_{II}-edge XANES spectra, (c) Pt L_{II}-edge k^3-weighted raw EXAFS oscillations, and (d) magnitude of Fourier transform of Pt L_{II}-edge k^3-weighted raw EXAFS spectra (Δk = 3−10) of SiO_2-supported Pt-based bimetallic catalysts (Pt 1 wt%, Ca/Pt = 15) and reference Pt foil. (e) Curve-fitting for the Pt L_{II}-edge k^3-weighted EXAFS of SiO_2-supported Pt-based bimetallic catalysts and reference Pt foil. Solid and pink dashed lines indicate the results of experiment and simulation, respectively. The fitting ranges are Δk = 3−10 Å^{-1} and Δr = 1.1−3.5 Å (for PtSn, Δk = 3−10 Å^{-1} and Δr = 1.3−3.5 Å).

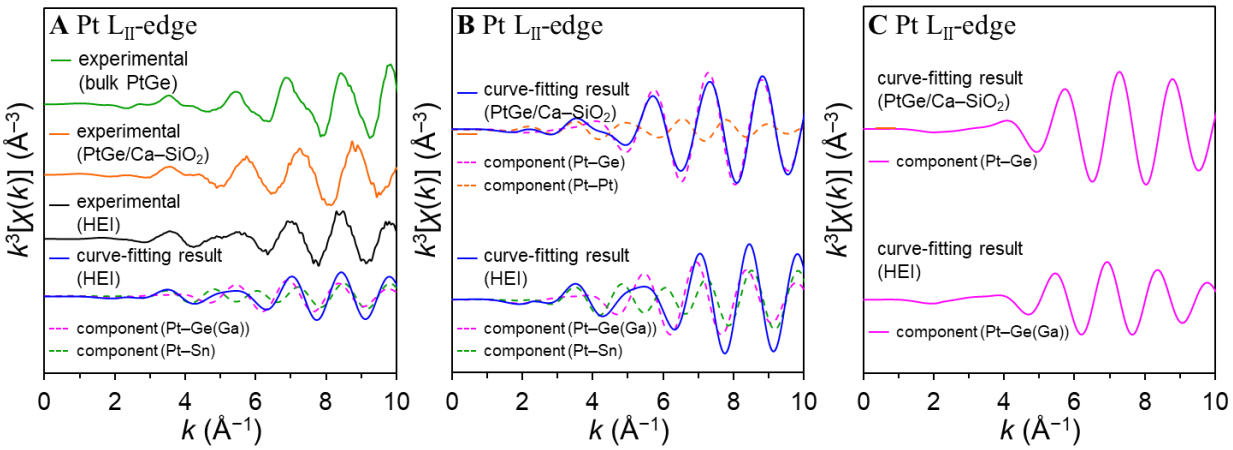

Figure 50. (a) Pt L$_{II}$-edges k^3-weighted raw EXAFS oscillation of PtGe bulk (solid green line), PtGe/Ca–SiO$_2$ (solid orange line) and HEI(0.25) (solid black line). Corresponding curve-fitting results of HEI(0.25) (solid blue line), and the component Pt–Ge(Ga) (dashed pink lines) and Pt–Sn paths (dashed green lines) are also shown. (b) Curve-fitting results of PtGe/Ca–SiO$_2$ and HEI(0.25) (solid blue lines), and the component Pt–Ge(Ga) (dashed pink lines) and Pt–Sn paths (dashed green lines) are also shown. (c) The component Pt–Ge(Ga) (solid pink lines) of PtGe/Ca–SiO$_2$ and HEI(0.25).

Next, the surfaces of PtGe and HEI were analyzed by FT-IR spectroscopy with CO adsorption (Figure 45f). The adsorption temperature was set to −100°C because CO did not adsorb on HEI at near room temperature (50°C). For PtGe, a peak assigned to linearly adsorbed CO on Pt atoms appeared at 2080 cm^{-1},[39,40] which was consistent with the previous study of intermetallic PtGe.[41] For HEI(0.25), two kinds of linear CO were observed at 2070 cm^{-1} and 2150 cm^{-1}, assignable to those on Pt[39,40] and Cu,[42] respectively. The broad shoulder peak at 2024 cm^{-1} may be attributed to linear CO on Co.[43] For both catalysts, no absorption was observed below 2000 cm^{-1}, indicating the absence of three-fold Pt ensembles. These findings are consistent with the substitution of the Pt site in PtGe with Co and Cu. The electronic state of Pt was also investigated using XPS analysis (Figure 45g). The Pt 4$f_{7/2}$ binding energy of PtGe (72.1 eV) was higher than that of Pt (71.4 eV), depicting that the electron density of Pt was decreased by alloying with Ge and is consistent with the observation in literature.[44,45] On the contrary, the binding energy shifted lower from PtGe to HEI(0.25) (71.6 eV), which suggests that the electron density of Pt 4*f* state was slightly recovered upon multi-metallization. Similar trends in the electron density were also observed in the XANES (white line intensity; PtGe > HEI(0.25) >> Pt, Figure 45c) and FT-IR studies (frequency of linear CO on Pt; PtGe > HEI, Figure 45f). However, as observed in XANES, the difference in the *d*-electron density of Pt between PtGe and HEI(0.25) was much smaller than that between PtGe and Pt (Figure 45c). This indicates that the electronic effect of multi-metallization on the Pt *d*-state is limited.

We also prepared an SAA (Cu–Pt/Ca–SiO$_2$, Cu/Pt = 25) and quinary HEA (PtFeCoCuGa/Ca–SiO$_2$) catalyst as control catalysts. The XRD, XAFS (Figure 51 and 52), and HAADF-STEM analyses confirmed that each catalyst had an *fcc* structure with high phase purity. Moreover, Pt atoms in the SAA were sufficiently isolated. Besides, the corresponding quaternary alloys (PtCoCuGe/Ca–SiO$_2$ and PtCoCuGa/Ca–SiO$_2$) and binary alloys or intermetallics

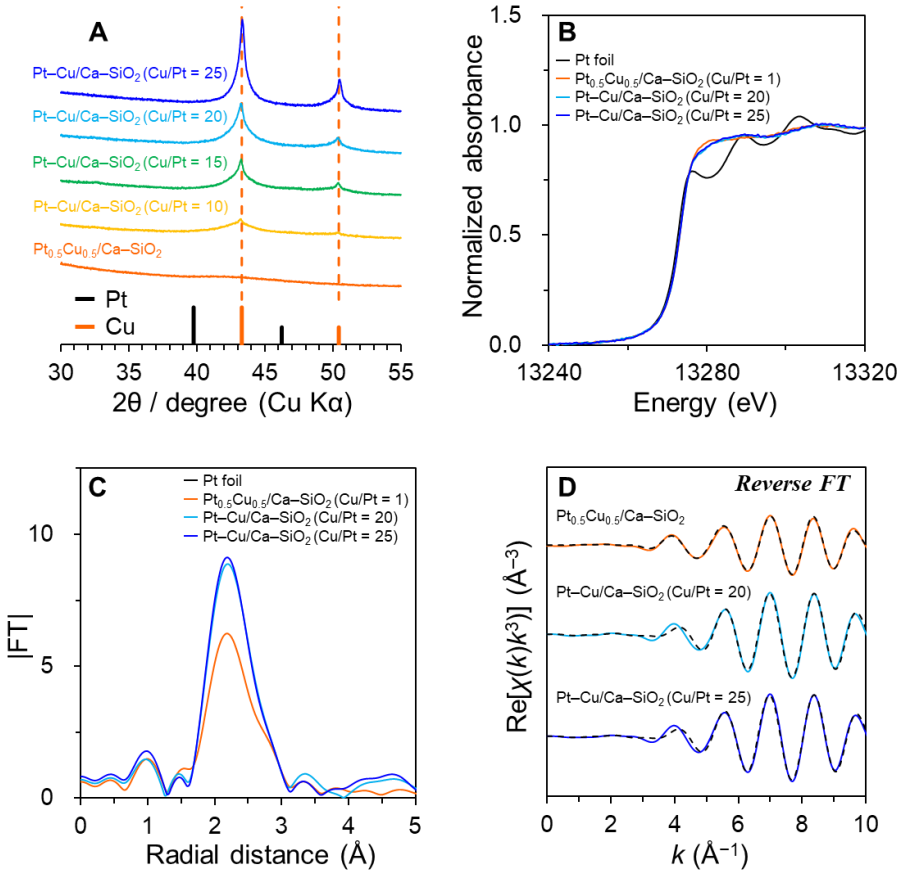

Figure 51. (a) XRD patterns of the Pt–Cu/Ca–SiO_2 (Pt 1 wt%) catalysts with different Cu/Pt ratios. Pt LII-edge (b) XANES and (c) Fourier transforms of k^3-weighted raw EXAFS spectra (Δk = 3–10) of SiO_2-supported Pt–Cu bimetallic catalysts (Pt 1 wt%) and reference Pt foil. (D) Curve-fitting for the Pt L_{II}-edge k^3-weighted EXAFS of SiO_2-supported Pt–Cu bimetallic catalysts and reference Pt foil. Solid and dashed lines indicate the experiment and simulation, respectively. The fitting ranges were Δk = 3−10 Å−1 and Δr = 1.5−3.5 Å (for $Pt_{0.5}Cu_{0.5}$/Ca–SiO_2; Δk = 3−10 $Å^{-1}$ and Δr = 1.1−3.5 Å).

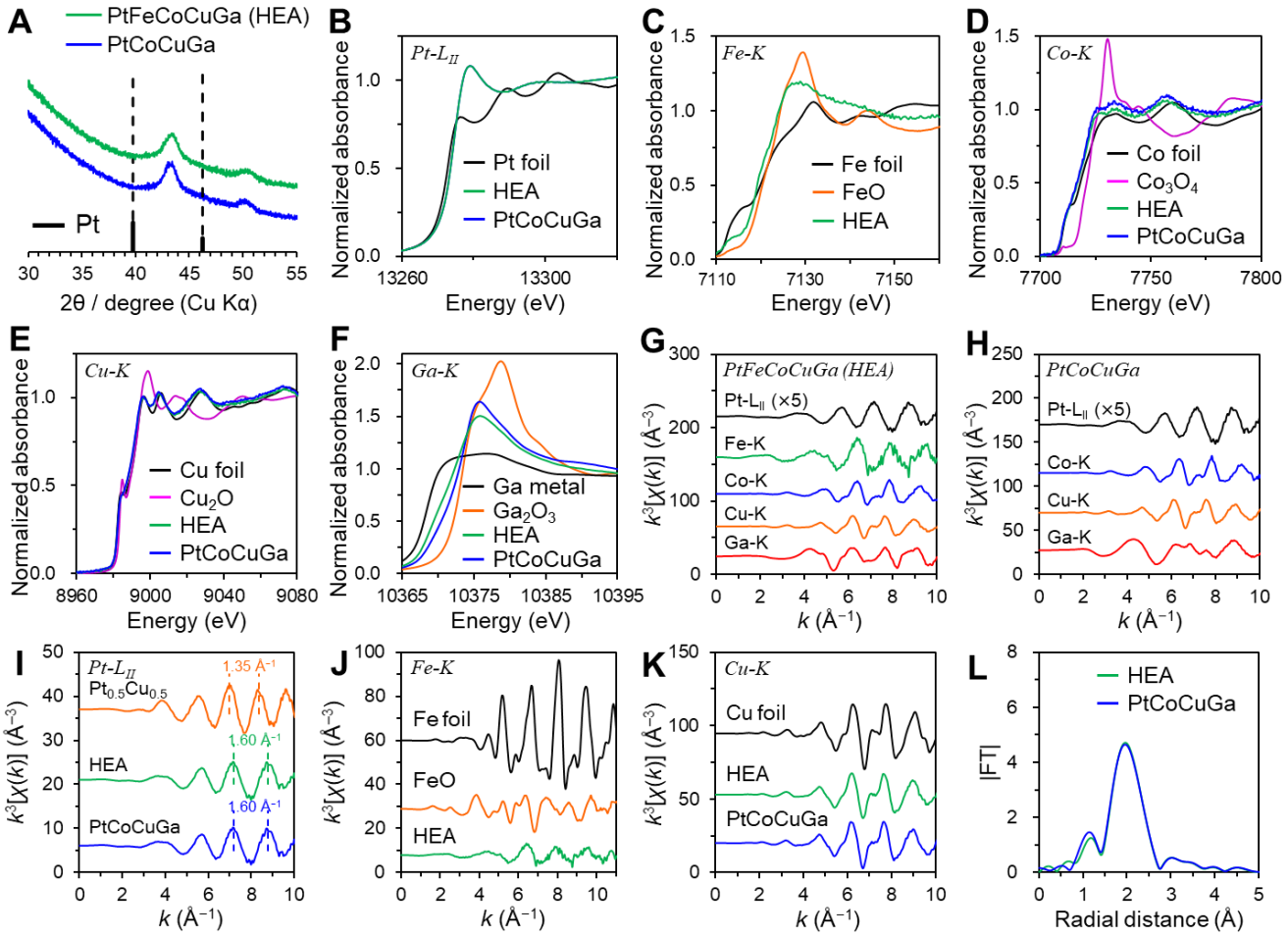

Figure 52. (a) XRD pattern of the PtFeCoCuGa/Ca–SiO_2 (HEA) and PtCoCuGa/Ca–SiO_2 catalysts (Pt 1 wt%). (b) Pt L_{II}-, (c) Fe-, (d) Co K-, (e) Cu K-, and (f) Ga K-edges *ex-situ* XANES spectra of the HEA and PtCoCuGa/Ca–SiO_2 catalysts (Pt 1wt%). Summary of the k^3-weighted raw EXAFS oscillations in k space for (g) HEA and (h) PtCoCuGa/Ca–SiO_2. (i) Pt L_{II}-edge k^3-weighted raw EXAFS oscillations in k space of $Pt_{0.5}Cu_{0.5}$/Ca–SiO_2, HEA, and PtCoCuGa/Ca–SiO_2. (j) Fe K-edge k^3-weighted raw EXAFS oscillations in k space of Fe foil, FeO, and HEA. (k) Cu K-edge k^3-weighted raw EXAFS oscillations in k space of Cu foil, HEA, and PtCoCuGa/Ca–SiO_2. (g) Magnification of Fourier transform of the Pt L_{II}-edge k^3-weighted EXAFS spectra (Δk = 3–10) for HEA and PtCoCuGa/Ca–SiO_2.

(PtM/Ca–SiO_2; M = Co, Cu, Ga, Ge, Sn) were prepared. Interestingly, the Ge-containing quaternary alloy had the PtGe-type intermetallic structure, *i.e.*, (PtCoCu)Ge (Figure 53), whereas the Ga-containing one showed an *fcc* solid solution phase. This is probably due to the large difference in ΔH_f between PtGe (−90.8 kJ mol^{-1})[19] and PtGa (−55.6 kJ mol^{-1}).[46] As mentioned for Scheme 1, the significant contribution of the enthalpic term of PtGe seemed to prevail over the entropic effect to form a solid-solution phase upon multi-metallization, while that of PtGa did not. This interpretation is also valid to understand the difference between HEI(0.25) and the quinary HEA. A similar characterization was also performed on a series of binary catalysts, revealing that the desired bimetallic phases were formed with high phase purities.

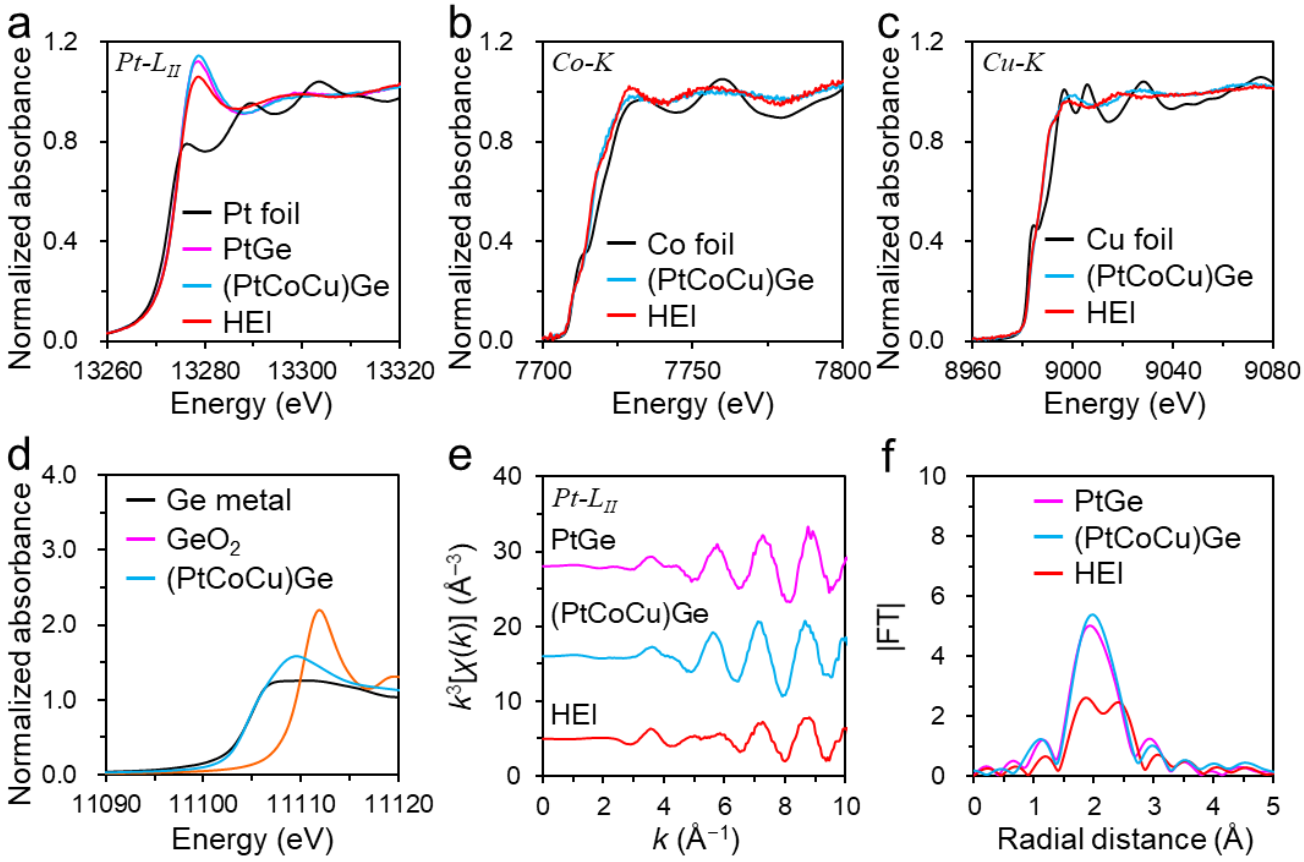

Figure 53. (a) Pt L_{II}-, (b) Co K-, (c) Cu K-, and (d) Ge K-edges *ex-situ* XANES spectra of the (PtCoCu)Ge/Ca–SiO_2 catalyst. (e) Pt L_{II}-edge k^3-weighted raw EXAFS oscillations in k space and (f) magnification of Fourier transform of the Pt L_{II}-edge k^3-weighted EXAFS spectra (Δk = 3–10) for PtGe/Ca–SiO_2, (PtCoCu)Ge/Ca–SiO_2, and (PtCoCu)(GeGaSn)/Ca–SiO_2 (HEI).

We also used an *in-situ* XAFS approach to explore the stability of the HEI phase at high temperatures, implying that the original structure of HEI(0.25) was preserved even at 700°C (Figure 54). Besides, the EXAFS features of HEI and the *fcc* HEA was still distinct at 700°C (Figures 55 and 56). Similar trends were also observed in the XANES region (Figure 56). Thus, we successfully synthesized the PtGe-type HEI, which provides thermally stable single-atom Pt as an ideal active site for high-temperature PDH.

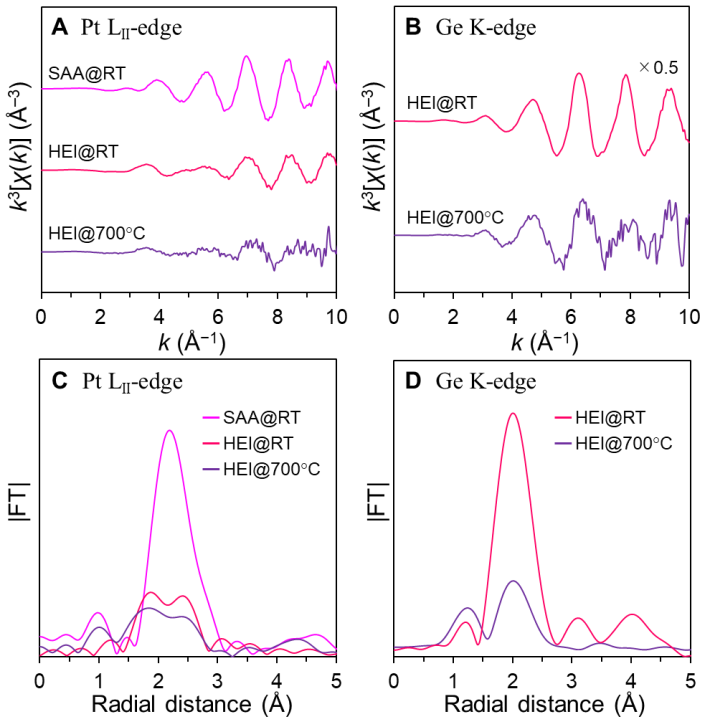

Figure 54. (a) Pt L_{II}- and (b) Ge K-edges k^3-weighted raw EXAFS oscillations of HEI(0.25) recorded at 700°C and RT. Magnification of Fourier transform of the (c) Pt L_{II}- and (d) Ge K-edges k^3-weighted EXAFS spectra of HEI(0.25) recorded at 700°C and RT. For HEI(0.25), as-calcined sample was reduced at 700°C for 1 h under flowing 50% H_2/He (50 mL min^{-1}), and then cooled to room temperature under flowing He (25 mL min^{-1}). The spectra of HEI@700°C were collected during the H_2 treatment (after 35 min). The Pt L_{II}-edge k^3-weighted raw EXAFS oscillation of SAA (SAA@RT) was also shown for the comparison of the PtGe-type and fcc structures. Although the oscillation strength and *S*/*N* ratio decreased at 700°C due to the large contribution of the Debye–Waller factor, the EXAFS features in Pt L_{II}- and Ge K-edges were not changed, demonstrating that the PtGe-type structure of HEI was retained even at high temperatures.

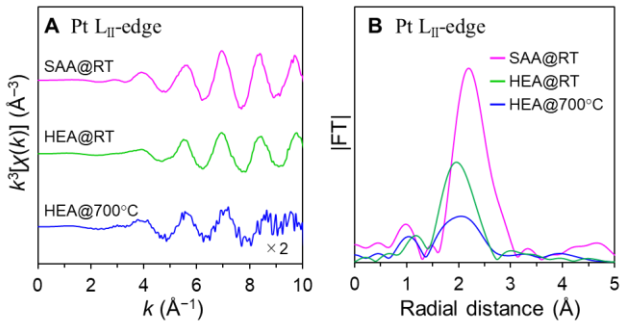

Figure 55. (a) Pt L_{II}-edges k^3-weighted raw EXAFS oscillations and (b) magnification of Fourier transform of the Pt L_{II}-edges k^3-weighted EXAFS spectra of HEA recorded at 700°C and RT. For HEA, as-calcined sample was reduced at 700°C for 1 h under flowing 50% H_2/He (50 mL min^{-1}), and then cooled to room temperature under flowing He (25 mL min^{-1}). The spectra of HEA@700°C were collected during the H_2 treatment (after 25 min). The Pt L_{II}-edge k^3-weighted raw EXAFS oscillation of SAA (SAA@RT) was also shown for the comparison. Although the oscillation strength and *S*/*N* ratio decreased at 700°C due to the large contribution of the Debye–Waller factor, the EXAFS features in Pt L_{II}-edges showed similar oscillation with those in HEA@RT and SAA@RT, demonstrating that the fcc-type structure of HEA was retained even at high temperatures.

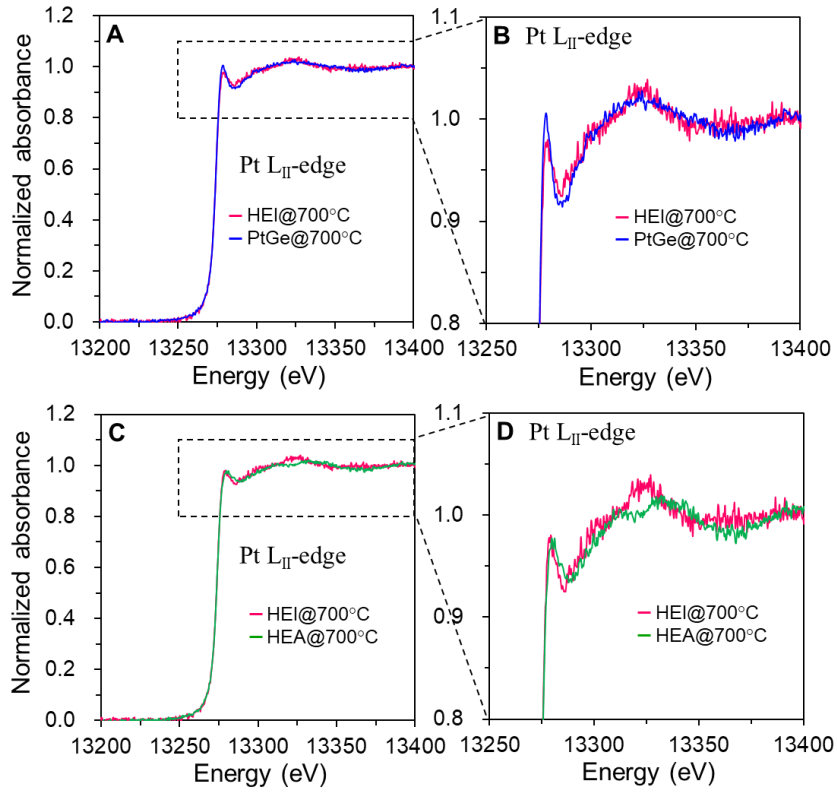

Figure 56. Pt L_{II}-edge XANES spectra of HEI(0.25) recorded at 700°C and the comparison with (a, b) PtGe/Ca–SiO_2 and (c, d) HEA. The spectra were collected during the H_2 treatment. b and d are the magnification of the region designated by dashed lines in a and c, respectively.

5.3.2. Catalytic Performance in PDH.

Then, we tested the catalytic performances of the prepared catalysts in PDH under a considerably harsh condition (600°C, without co-feeding H_2). The SAA catalyst and PtGe were deactivated within 20 h (Figure 57a) due to the aggregation of nanoparticles and coke accumulation, respectively. The quinary HEA (Figure 57a), quaternary (Figure 58), and binary (Figure 59) catalysts also showed slow deactivation due to coking. Conversely, HEI(0.25) was not deactivated within 100 h (Figure 57a) and retained >30% conversion and 99% propylene selectivity up to 260 h (Figure 60), where the mean catalyst life τ (reciprocal deactivation constant k_d^{-1}) was 628 h (Table 13). Moreover, HEI(0.25) still exhibited good stability at 620°C (>40% conv. for 120 h). To the best of our knowledge, the HEI catalyst exhibited the highest stability in PDH in the absence of H_2 (Figure 57b, details are listed in Tables 14–15), which is highly beneficial for practical application. The particle size distribution did not change before and after the 100-hour catalytic run, indicating high thermal stability and strong resistance to sintering HEI, according to the HAADF-STEM analysis. Interestingly, HEI(0.25) showed a short induction period in propane conversion at the initial stage of reaction (<10 h). Since no change in the bulk structure was observed during this period, the increase in conversion might be attributed to the change in the Pt:Co:Cu composition ratio at the surface. A possible interpretation is that Pt, Co, and Cu atoms can migrate gradually in the subsurface region under the high-temperature condition; therefore, the Pt:Co:Cu ratio at the surface is gradually optimized by contacting with hydrocarbons. We also tested another control experiment using HEI(0.25) without Ca, which resulted in lower stability than HEI(0.25) with Ca. Ca is known to acts as a spacer for metallic species,[47] which enhances homogeneous distribution and alloying of metallic species, thus promoting sufficient alloying. Therefore, the lower stability may be due to incomplete formation of the HEI structure. Next, we tested HEI(0.375) and HEI(0.5) in PDH, which resulted in lower selectivity and stability. As shown in Figure 57c, a strong positive correlation was observed between the Pt fraction x and the mean catalyst life τ, indicating that the degree of Pt isolation in HEI determines the selectivity and stability in PDH. Thus, these results demonstrated the validity of our catalyst design concept based on HEIs for high-temperature PDH. Control experiments using the Ca–SiO_2 and unmodified SiO_2 support were also performed at 600°C, where a small amount of propane was converted to propylene with low selectivity (conv., ~5%; sel., ~60%). This is probably due to a small contribution of noncatalytic thermal cracking.[47]

We subsequently investigated the reusability of the prepared catalysts through repeated regeneration processes (O_2–H_2 treatments, Figure 57d). The catalytic activity of PtGe was recovered after the first regeneration procedure, indicating that this treatment could combust the accumulated coke. However, it was not fully recovered despite repeated regeneration, most likely due to irreversible catalyst decomposition. Conversely, HEI(0.25) showed no deactivation after the repeated regeneration procedures, revealing its high durability in repeated regeneration and reuse. Indeed, the XRD patterns of HEI(0.25) showed no changes after PDH reaction and regeneration process, indicating that the original crystal structure of HEI(0.25) was retained. Then, the long-term stability of HEI(0.25) was examined in the presence of co-fed H_2 to minimize the coke formation, which is a more common condition for PDH. Notably, HEI(0.25) exhibited outstandingly high stability at 600°C for the first time; little deactivation was observed for at least two months (Figure 57e), where the mean catalyst life (τ = 4146 h) was 1.4 times higher than the highest ever reported (τ = 3067 h). Thus, the

HEI(0.25) catalyst is the most stable PDH catalyst under different conditions to the best of our knowledge. The coke amount was drastically decreased by co-feeding H_2 due to the decoking effect of H_2 (coke hydrogenation).[47] We also focused on the relationship between catalytic activity and stability, because a negative correlation between them is often suggested. For this purpose, we calculated the rate constant for the forward direction (k_f) as a universal scale covering the influences of space velocity and the degree of approach to equilibrium,[7,21] which was plotted against the mean catalyst life ($\tau = k_d^{-1}$) for reported Pt-based catalysts (Figure 61). Although a weak negative correlation was observed between activity and stability, HEI(0.25) deviated from this correlation significantly and exceptionally. Therefore, it is unlikely that the outstandingly high stability of HEI was achieved at the expense of activity, but rather due to the combination of site-isolation and entropy effects. However, further increase in the catalytic activity might be required for practical application with efficient propylene productivity.

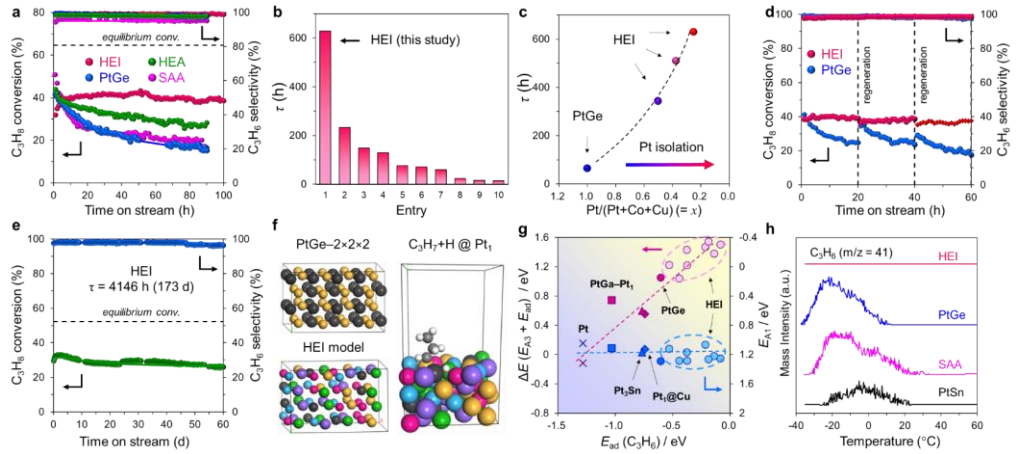

Figure 57. Catalytic performance of HEI in PDH and DFT calculations. (a) Catalytic performances of PtGe, HEI(0.25), SAA, and HEA in PDH at 600°C without co-feeding H_2. (b) Mean catalyst life ($\tau = k_d^{-1}$) of reported catalysts and HEI(0.25) in PDH without co-fed H_2 (references are listed in Tables S8-9). (c) Relationship between mean catalyst life ($\tau = k_d^{-1}$) and the degree of Pt isolation represented by x as Pt/(Pt+Co+Cu) molar ratio in PtGe and HEI. (d) Reusability of PtGe and HEI(0.25) in PDH at 600°C after repeated regeneration processes. (e) Long-term stability test of the HEI(0.25) in PDH at 600°C with co-feeding H_2 (catalyst: 150 mg, C_3H_8:H_2:He = 2.5:1.3:3.7 mL min^{-1}, WHSV = 2.0 h^{-1}). (f) Model structure of HEI (left bottom) derived from PtGe (left top) for DFT calculations. An example of the HEI slab model for PDH: C_3H_7+H at a Pt_1 site (right). (g) Relationship between E_{ad} (C_3H_6) and ΔE or E_{A1} for various Pt-based surfaces. (h) C_3H_6-TPD for Pt-based catalysts (adsorption temperature: −35°C).

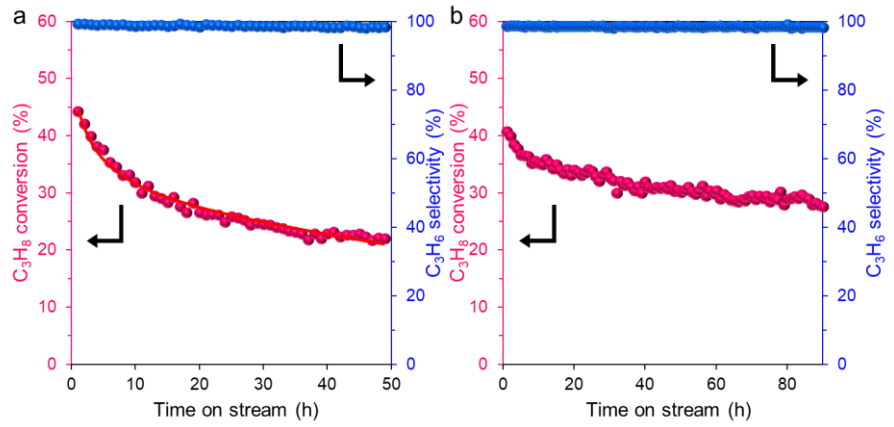

Figure 58. Long-term stability test of the (a) (PtCoCu)Ge/Ca–SiO_2 (Pt 1 wt%) and (b) PtCoCuGa/Ca–SiO_2 (Pt 1 wt%) catalysts in PDH at 600°C (C_3H_8/He = 2.5/5.0, F = 7.5 mL min^{-1}). 60 mg of catalyst, WHSV = 4.9 h^{-1}.

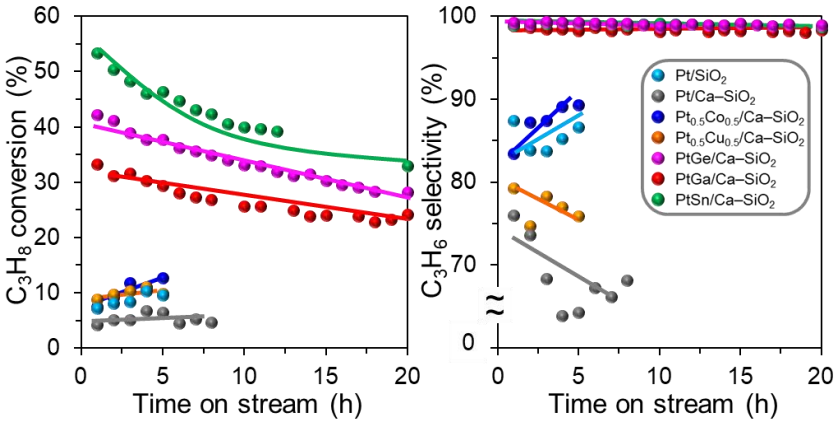

Figure 59. Catalytic performances of Pt-based bimetallic catalysts (Pt 1 wt%) in PDH at 600°C. Conditions: C_3H_8/He = 2.5/5.0, F = 7.5 mL min^{-1}, 20 mg of catalyst, WHSV = 14.8 h^{-1}. C_3H_6 and by-products (CH_4 and C_2H_4) were detected due to the dehydrogenation and thermal cracking of C_3H_8, respectively.

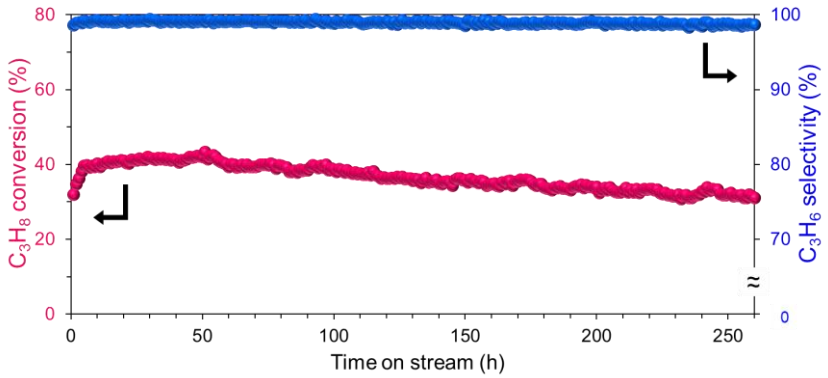

Figure 60. Long-term stability test of the HEI(0.25) catalyst (Pt 1 wt%) in PDH at 600°C (C_3H_8/He = 2.5/5.0, F = 7.5 mL min^{-1}, 100 mg of catalyst, WHSV = 3.0 h^{-1}).

Table 13. Summary of the catalytic performances of the silica-supported Pt-based catalysts at 600°C.

Catalyst	Time (h)		C_3H_8 conversion (%)		C_3H_6 selectivity (%)		k_d (h^{-1})[a]	τ (h)[b]
	initial	final	initial	final	initial	final		
(PtCoCu)(GeGaSn)/Ca–SiO_2[c] (HEI(0.25), Pt/Pt+Co+Cu) = 1/4, Pt 1 wt%)	10	260	40.3	31.2	99.3	98.7	0.002	628
(PtCoCu)(GeGaSn)/Ca–SiO_2[d] (HEI(0.375), Pt/Pt+Co+Cu) = 1.5/4, Pt 1.5 wt%)	10	119	32.2	27.7	98.6	98.4	0.002	509
(PtCoCu)(GeGaSn)/Ca–SiO_2[e] (HEI(0.5), Pt/Pt+Co+Cu) = 2/4, Pt 2 wt%)	10	120	39.4	32.1	98.7	98.9	0.003	343
(PtCoCu)Ge/Ca–SiO_2[f]	1	49	44.2	22.0	99.3	98.5	0.021	47
PtCoCuGa/Ca–SiO_2[f]	1	90	40.7	27.6	98.6	98.3	0.007	152
PtFeCoCuGa/Ca–SiO_2[f]	1	90	44.0	28.3	98.6	98.0	0.008	130
PtGe/Ca–SiO_2[e]	1	90	42.1	15.3	99.3	97.9	0.016	64
PtGa/Ca–SiO_2[e]	1	20	33.2	24.1	98.8	98.3	0.024	43
PtSn/Ca–SiO_2[e]	1	60	53.3	14.4	98.9	97.0	0.032	31
Pt–Cu/Ca–SiO_2 (SAA, Cu/Pt = 25)[c]	1	90	50.8	16.6	94.5	95.2	0.018	54

[a]Deactivation rate constant. [b]Mean catalyst lifetime. [c]WHSV = 3.0 h^{-1}. [d]WHSV = 5.9 h^{-1}. [e]WHSV = 14.8 h^{-1}. [f] WHSV = 4.9 h^{-1}.

Table 14. Summary of the catalytic performance of HEI and other representative reported Pt-based catalysts in PDH in the absence of H_2.

Entry	Catalyst.	Temp.	Conversion (%)[a]	Gas composition	C_3H_6 (%)[b]	Specific activity (s^{-1})[c]	k_f (mol_{C3H6} g_{Pt}^{-1} h^{-1} bar^{-1})[d]	Catalyst τ (h)[e]	Ref.
0	(PtCoCu)(GeGaSn)/Ca–SiO_2: HEI	620	49.3 (11 h)–40.8	C_3H_8/He = 2.5/5	97.4–96.7	0.174	29	318	This study
1	(PtCoCu)(GeGaSn)/Ca–SiO_2: HEI	600	40.3 (10 h)–31.2	C_3H_8/He = 2.5/5	99.3–98.7	0.145	20	628	
2	PtGa–Ca–Pb/SiO_2	600	37.8 (8 h)-	C_3H_8/He =	98.0–	0.149	19	233	26
3	PtGa–Pb/SiO_2	600	31.6 (11 h)-	C_3H_8/He =	97.9–	0.125	13	149	26
4	1.5Ga0.1@S-1	600	45.9–41.5	C_3H_8/N_2 =	92.1	0.667	495	129	32
5	K-PtSn@MFI-600H_2-	600	38.7 (2 h)–	C_3H_8/He =	>97	3.406	573	77	33
6	K-PtSn@MFI	600	20–17	C_3H_8/N_2 =	97	0.340	–	72	34
7	PtZn4@S-1-H	600	66.7–43.2	C_3H_8/N_2 = 1/3	90.8–	0.370	834	60	35
8	Pt/Sn-ZSM-5	600	70–45	C_3H_8/N_2 =	99	0.472	–	23	36
9	0.3PtZn0.5@S-1	600	31.0–26.0	C_3H_8/N_2 =	97	1.044	99	16	37
10	Zn10Pt0.1/HZ	600	80–50	C_3H_8/N_2 =	56	0.130	476	14	38
11	PtSn$Al_{0.2}$/SBA-15	590	55.9–40.5	C_3H_8/Ar = 1/5	98.5	0.320	149	10	39
12	PtSn$Al_{0.1}$/SBA-15	590	55.1–38.8	C_3H_8/Ar = 1/5	97.8	0.313	139	9	39
13	0.7Pt0.7Zn/MZ	580	35-20	C_3H_8	98–95	0.782	–	626	40
14	PtGa–Ca–Pb/SiO_2	580	36.6-25.2	C_3H_8	98.0–	0.087	–	465	26
15	PtLa/mz-deGa	580	42–417	C_3H_8	95	0.539	–	380	2
16	PtY/mz-deGa	580	42–5	C_3H_8	96	0.544	–	119	2
17	InPt/SSF	580	46.9–40.9	C_3H_8/Ar = 1/4	98	0.200	59	135	41
18	CePt/SSF	580	44.9–37.5	C_3H_8/Ar = 1/4	92	0.180	48	108	41
19	LaPt/SSF	580	44.4–35.2	C_3H_8/Ar = 1/4	92	0.178	46	86	41
20	FePt/SSF	580	56.8–44.0	C_3H_8/Ar = 1/4	90	0.223	143	64	41
21	PtSn/SiO_2	580	35.2–30.3	C_3H_8	>99	1.629	–	90	42
22	PtSn/SiO_2	580	34.5–27.6	C_3H_8	>9	2.434	–	62	42

23	Pt/0.8Sn-SBA-15	580	43.8–38.3	C_3H_8/Ar = 7/3	98.5	0.438	192	26	[43]
24	1Pt1Zn/MZ	580	30-27	C_3H_8	96–96	4.599	–	20	[40]
25	PtZn4@S-1-H	550	47.4–40.4	C_3H_8/N_2 = 1/3	93.2–	0.270	337	759	[35]
26	PtZn4@S-1-H	550	40.0–21.8	C_3H_8/N_2 = 1/3	99.1–	1.816	552	121	[35]
27	PtZn4@S-1-H	550	34.7–29.6	C_3H_8/N_2 = 1/3	99.1–	3.151	633	41	[35]
28	PtZn4@S-1-H	550	21.2–11.8	C_3H_8/N_2 = 1/3	98.3–	3.890	438	14	[35]
29	K-PtSn@MFI-600H_2-	550	20–17	C_3H_8	>97	7.040	822	351	[33]
30	$Ga^{\delta+}Pt^0/SiO_2$	550	40.7–38.5	C_3H_8/Ar = 1/4	63.5	0.016	5	217	[44]
31	$Ga^{\delta+}Pt^0/SiO_2$	550	36.5–26.9	C_3H_8/Ar = 1/4	90.9	0.408	99	45	[44]
32	$Ga^{\delta+}Pt^0/SiO_2$	550	31.9–18.2	C_3H_8/Ar = 1/4	99	0.847	170	27	[44]
33	0.1Pt-2Zn/Si-Beta	550	65–36	C_3H_8/He = 1/9	98	1.849	–	126	[45]
34	0.3Pt/0.5Sn-Si-Beta	550	27.5–25.2	C_3H_8/Ar =	99.1–	0.152	82	101	[46]
35	$Pt^0Zn^{\delta+}/SiO_2$	550	35.3–26.6	C_3H_8/Ar = 1/4	97.6–	1.147	261	73	[47]
36	$Pt^0Zn^{\delta+}/SiO_2$	550	30.2–16.1	C_3H_8/Ar = 1/4	98.1–	0.422	76	37	[47]
37	Zn10Pt0.1/HZ	550	56.2–48.2	C_3H_8/N_2 =	78	0.127	–	62	[38]

[a]The first value was obtained at the beginning of the run, and the second at the end. [b]The C_3H_6 selectivity was obtained at the beginning of the run. [c]Defined as (mol of formed propylene per second) per mol of total Pt. [e]Although the k_f value was negative in some references, values are not listed in the table in such cases. This is mainly because the actual propane conversion was somehow higher than the estimated equilibrium conversion. [e]Mean catalyst life defined as $\tau = k_d^{-1}$.

Table 15. Summary of the catalytic performance of HEI and other representative reported Pt-based catalysts in PDH in the absence of H_2.

Entry	Catalyst	Pt (wt%)	Temp. (°C)	WHSV (h^{-1})[a]	k_d (h^{-1})[b]	Operation time (h)[c]	Ref.
0	(PtCoCu)(GeGaSn)/Ca–SiO_2: HEI	1	620	3.0	0.003	120	This study
1	(PtCoCu)(GeGaSn)/Ca–SiO_2: HEI	1	600	3.0	0.002	260	
2	PtGa–Ca–Pb/SiO_2	3	600	9.8	0.004	160	26
3	PtGa–Pb/SiO_2	3	600	9.8	0.007	160	26
4	1.5Ga0.1@S-1	0.092	600	1.2	0.008	24	32
5	K-PtSn@MFI-600H2-22h	0.4	600	29.5	0.013	25	33
6	K-PtSn@MFI	0.42	600	1.8	0.014	67	34
7	PtZn4@S-1-H	0.72	600	3.6	0.017	58.3	35
8	Pt/Sn-ZSM-5	0.32	600	1.8	0.044	24	36
9	0.3PtZn0.5@S-1	0.23	600	6.5	0.061	5	37
10	Zn10Pt0.1/HZ	0.1	600	0.2	0.069	20	38
11	$PtSnAl_{0.2}$/SBA-15	0.5	590	2.4	0.104	6	39
12	$PtSnAl_{0.1}$/SBA-15	0.5	590	2.4	0.110	6	39
13	0.7Pt0.7Zn/MZ	0.7	580	13	0.002	480	40
14	PtGa–Ca–Pb/SiO_2	3	580	5.9	0.002	252	26
15	PtLa/mz-deGa	1	580	11.0	0.003	480	2
16	PtY/mz-deGa	1	580	11.0	0.008	312	2
17	InPt/SSF	1	580	3.5	0.007	33	41
18	CePt/SSF	1	580	3.5	0.009	33	41
19	LaPt/SSF	1	580	3.5	0.012	33	41
20	FePt/SSF	1	580	3.5	0.016	33	41
21	PtSn/SiO_2	0.5	580	19	0.011	20	42
22	PtSn/SiO_2	0.5	580	29	0.016	20	42
23	Pt/0.8Sn-SBA-15	1	580	8.3	0.038	6	43
24	1Pt1Zn/MZ	1	580	130	0.049	3	40
25	PtZn4@S-1-H	0.72	550	3.6	0.001	216.7	35
26	PtZn4@S-1-H	0.72	550	26.8	0.008	105.9	35
27	PtZn4@S-1-H	0.72	550	53.7	0.024	10.3	35
28	PtZn4@S-1-H	0.72	550	109.4	0.072	10.3	35

29	K-PtSn@MFI-600H2-22h	0.4	550	118.1	0.003	70	33
30	$Ga^{\delta+}Pt^{0}/SiO_2$	4.37	550	2.1	0.005	20	44
31	$Ga^{\delta+}Pt^{0}/SiO_2$	4.37	550	43.7	0.022	20	44
32	$Ga^{\delta+}Pt^{0}/SiO_2$	4.37	550	98.4	0.037	20	44
33	0.1Pt-2Zn/Si-Beta	1	550	2.4	0.008	150	45
34	0.3Pt/0.5Sn-Si-Beta	0.26	550	1.2	0.010	12	46
35	$Pt^{0}Zn^{\delta+}/SiO_2$	3.05	550	82.6	0.014	30	47
36	$Pt^{0}Zn^{\delta+}/SiO_2$	3.05	550	35.4	0.027	30	47
37	Zn10Pt0.1/HZ	0.1	550	0.2	0.016	20	38

[a]WHSV: weight hourly space velocity based on propane gas flow (h^{-1}). [b]The first-order deactivation model was used to estimate the catalyst stability.[1] [c]Operation time: total time tested for a single run.

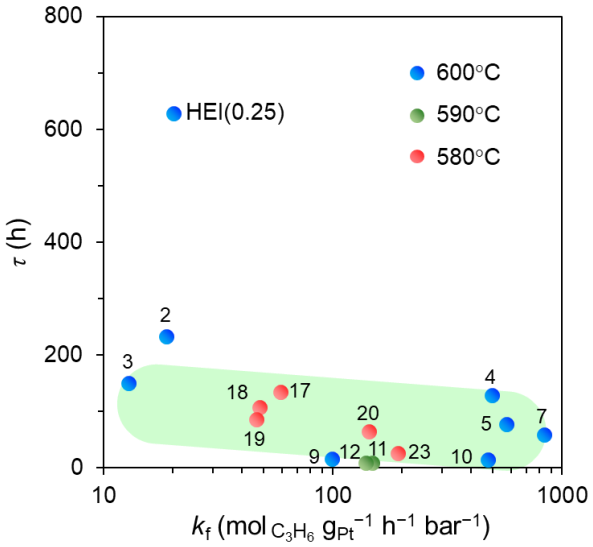

Figure 61. Relationship between activity (k_f) and stability ($\tau = k_d^{-1}$) obtained in PDH over Pt-based catalysts in literature and this study. Numbers correspond to the entries in Tables S8 and S9. To minimize the effect of temperature, values at 580°C~600°C were shown.

5.3.3. DFT Calculations.

Finally, we used DFT computations to ascertain the origin of HEI's exceptional catalytic performance. For PtGe, the (020) plane was considered as the main active surface because it is one of the major facets of PtGe crystal (see Figure S62 the result of Wulff construction) and much more active for C–H scissions than the most stable (211) and the second stable (112) planes (Figures 63-72 and Table 16). The HEI(0.25) structure was modeled based on the PtGe–(2×2×2) supercell, where the Pt and Ge sites were substituted partially and randomly with Co/Cu and Ga/Sn, respectively, such that the Pt faction *x* was 0.25 (Figure 57f). Here, we randomly generated forty structures (Figure 73) and chose the most stable one as an energetically favorable

model (Figure 74). The segregation energies of Pt atoms were also calculated for each isolated Pt site, which were mostly positive. This indicates that the isolated Pt state is electronically preferable to the segregated state. Then, for slab models, two HEI(040) surfaces (equivalent to PtGe(020) plane) were considered, each with four distinct isolated Pt atoms and eight Pt–Co/Cu bridge sites for H adsorption (Figure 74). On each Pt–Co/Cu site, the stepwise C–H scissions from C_3H_8 to C_3H_5 were calculated (Figure 57f right, Figures. 75–98, and Table 16). Similar computations were also executed on the (111) surfaces of Pt, Pt_3Sn, and Cu–Pt_1 for comparison (Figures. 97–107 and Table 16, results of PtGa were reproduced from the previous study[64]). The third C–H scission triggers propylene decomposition, leading to selectivity decrease, coke formation, and consequent catalyst deactivation (Scheme 4). Therefore, the propylene selectivity (and catalyst stability) generally depends on the difference in the energy barriers between the third C–H scission and propylene desorption ($\Delta E = E_{A3} - E_d = E_{A3} + E_{ad}$).[8,64,65] The calculated ΔE were in the following order; Pt (−0.11 eV) << Pt_1@Cu (0.55 eV) ≈ Pt_3Sn (0.60 eV) < Pt_1@PtGa (0.74 eV) < PtGe(020) (1.05 eV) < HEI(040) (1.04~1.54 eV) (Figure 57g and Table 16), which is consistent with the experimental trend in propylene selectivity (Table 13). Although the ΔE values for HEI varied depending on the site, they were much higher than those on other bimetallic surfaces, indicating exceptional selectivity and stability. Overall, ΔE linearly increased with the E_{ad} (Figure 57g), indicating that the adsorption strength of propylene on the surface indicates ΔE. Figure 57g also describes that E_{A1} did not vary depending on the surface, consistent with the structure-insensitivity of PDH. These results suggest that the single-atom Pt on HEI can selectively catalyze propane's first and second C–H scissions, while effectively inhibiting the third one and subsequent side reactions by facile propylene desorption. Notably, no significant difference was observed in the *d*-band shapes and centers between PtGe and HEI(0.25) (Figure 108). Therefore, the weakened propylene adsorption can be attributed to a geometric ensemble effect due to the Pt isolation rather than an electronic effect upon multi-metallization. We also calculated the *d*-band structure of Pt–Cu SAA, of which *d*-band center was much closer to the Fermi level than those of PtGe and HEI. This is consistent with the more negative E_{ad} of SAA (Figure 57g) and the lower propylene selectivity in PDH (Figure 2a).

Guided by the theoretical study outlined above, we conducted C_3H_6-TPD (Figure 57h) with an adsorption temperature of −35°C (12°C above the boiling point). PtGe, PtSn, and Cu–Pt SAA exhibited broad desorption peaks between at −40~20°C, where the peak tops appeared in this order. Conversely, no desorption was observed on HEI(0.25), indicating that propylene could not be adsorbed even at −35°C. This trend agrees with that of E_{ad} and demonstrates the remarkably easy desorption of propylene from HEI. We also used CO-TPD, which revealed a similar pattern (Figure 109). As a result, the Pt isolation using HEIs allows for months of selective and continuous propylene production *via* PDH.

On the other hand, the DFT model considered in this study were the bulk and slab structures, but not a nanoparticle on an oxide support. Considering the small size and the interaction with silica support, the trends in selectivity and thermal stability may be influenced by the nanosizing and support effects. To obtain the insights closer to the real HEI/SiO_2 catalyst, more sophisticated theoretical studies based on a supported nanoparticle model are preferred.[66–70] Although modeling and studying such a complex system is highly challenging, success in this approach will advance the chemistry of HEI-based catalysis.

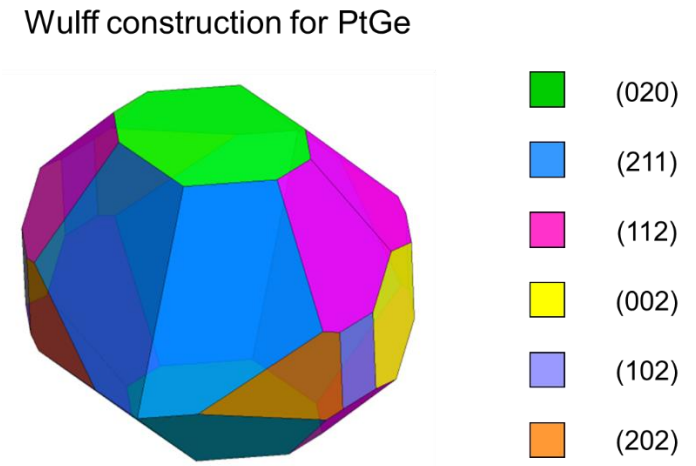

Figure 62. Equilibrium crystal shape of PtGe determined by Wulff construction.

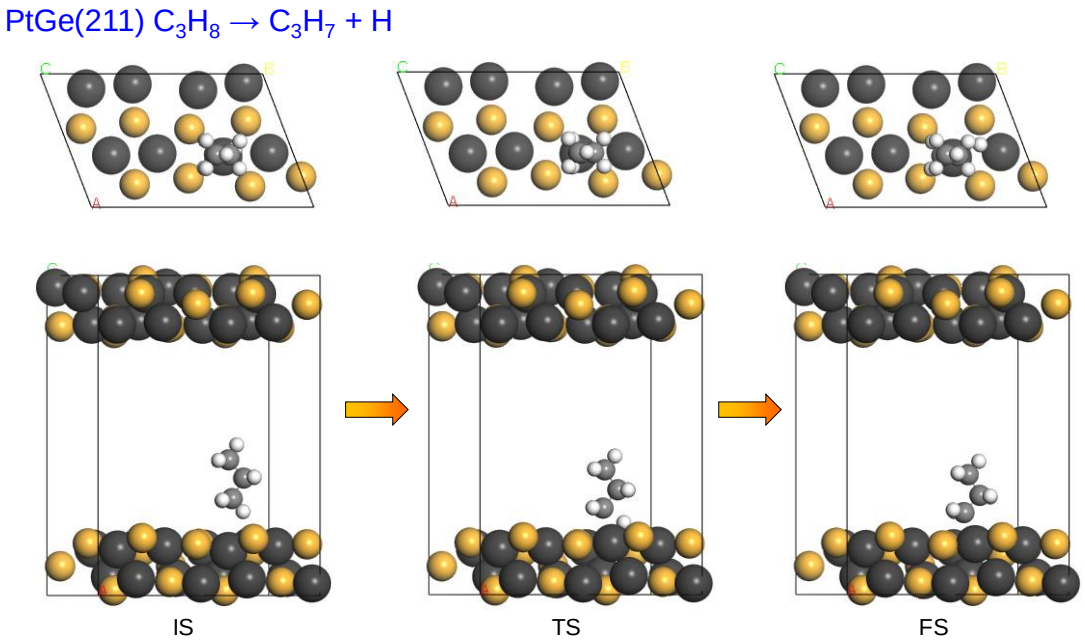

Figure 63. Structures of initial (IS), transition (TS), and final states (FS) of 1st C–H scissions in PDH on the PtGe(211) site.

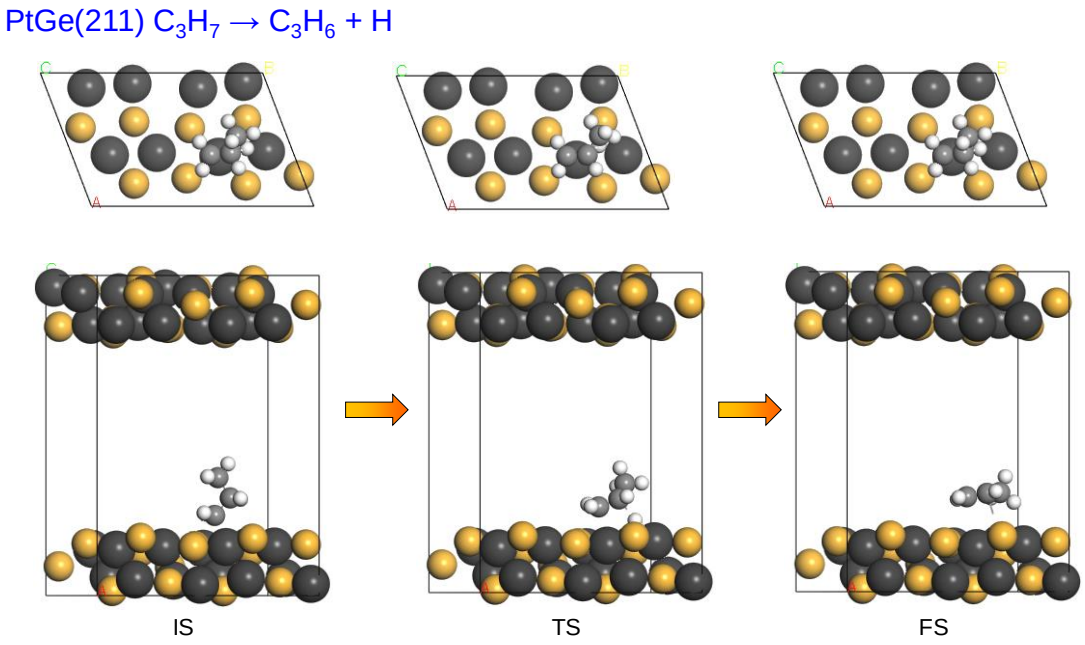

Figure 64. Structures of initial (IS), transition (TS), and final states (FS) of 2nd C–H scissions in PDH on the PtGe(211) site.

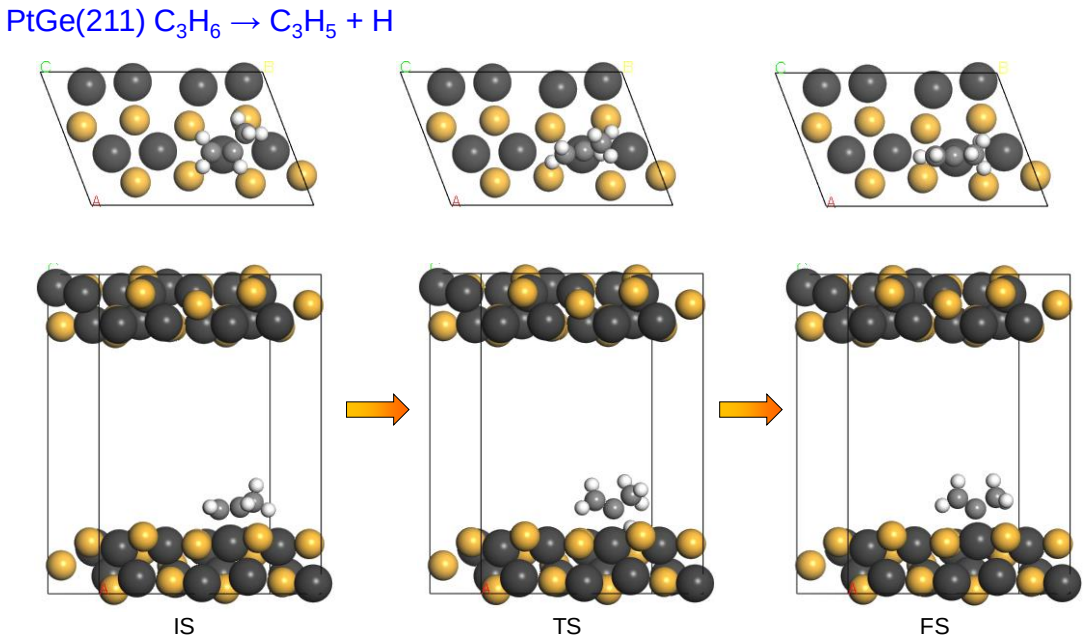

Figure 65. Structures of initial (IS), transition (TS), and final states (FS) of 3rd C–H scissions in PDH on the PtGe(211) site.

PtGe(112) $C_3H_8 \rightarrow C_3H_7 + H$

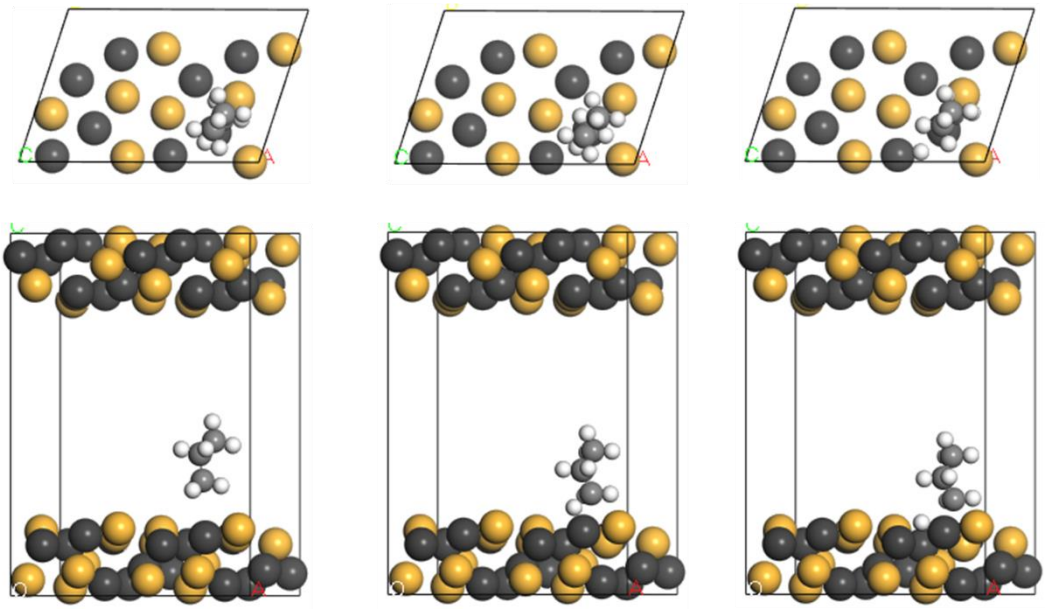

Figure 66. Structures of initial (IS), transition (TS), and final states (FS) of 2nd C–H scissions in PDH on the PtGe(112) site.

PtGe(112) $C_3H_7 \rightarrow C_3H_6 + H$

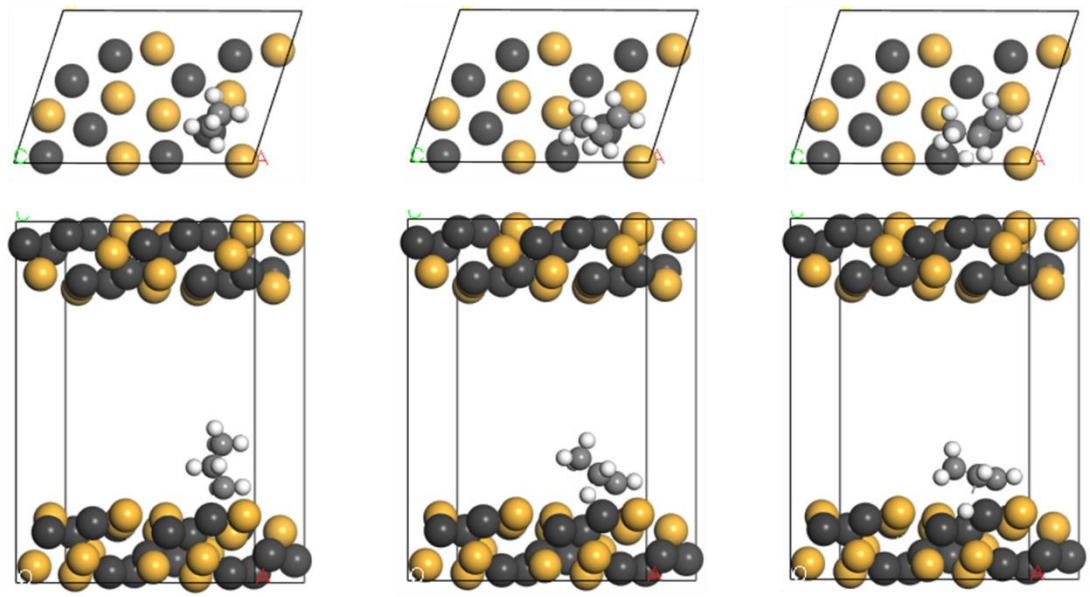

Figure 67. Structures of initial (IS), transition (TS), and final states (FS) of 2nd C–H scissions in PDH on the PtGe(112) site.

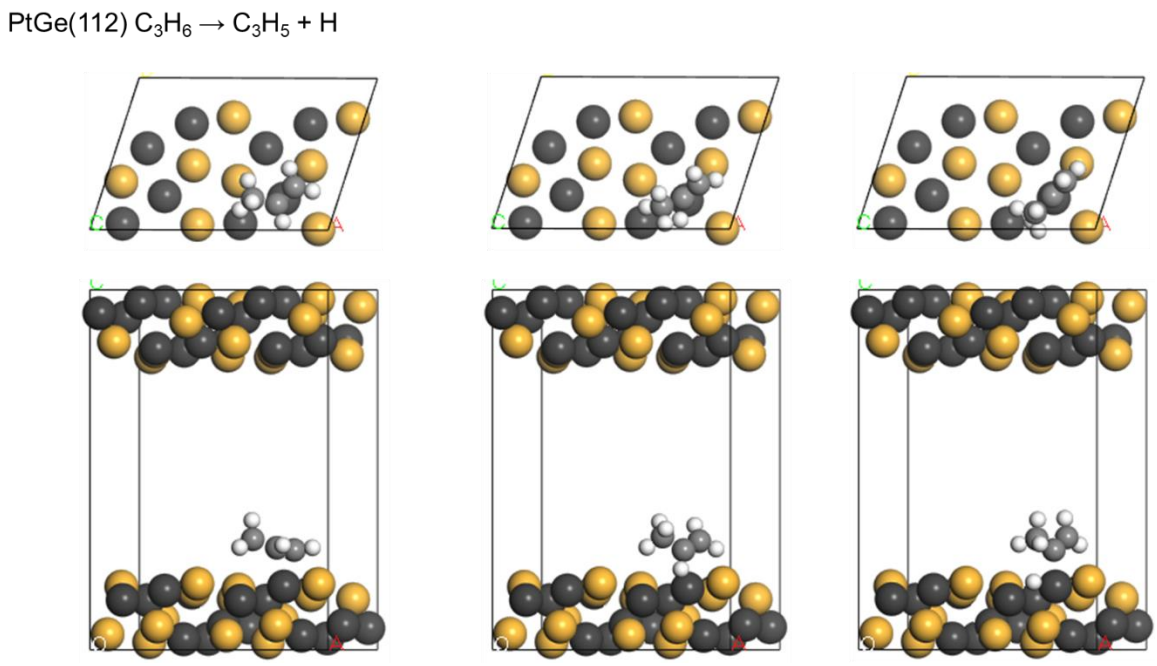

Figure 68. Structures of initial (IS), transition (TS), and final states (FS) of 3rd C–H scissions in PDH on the PtGe(112) site.

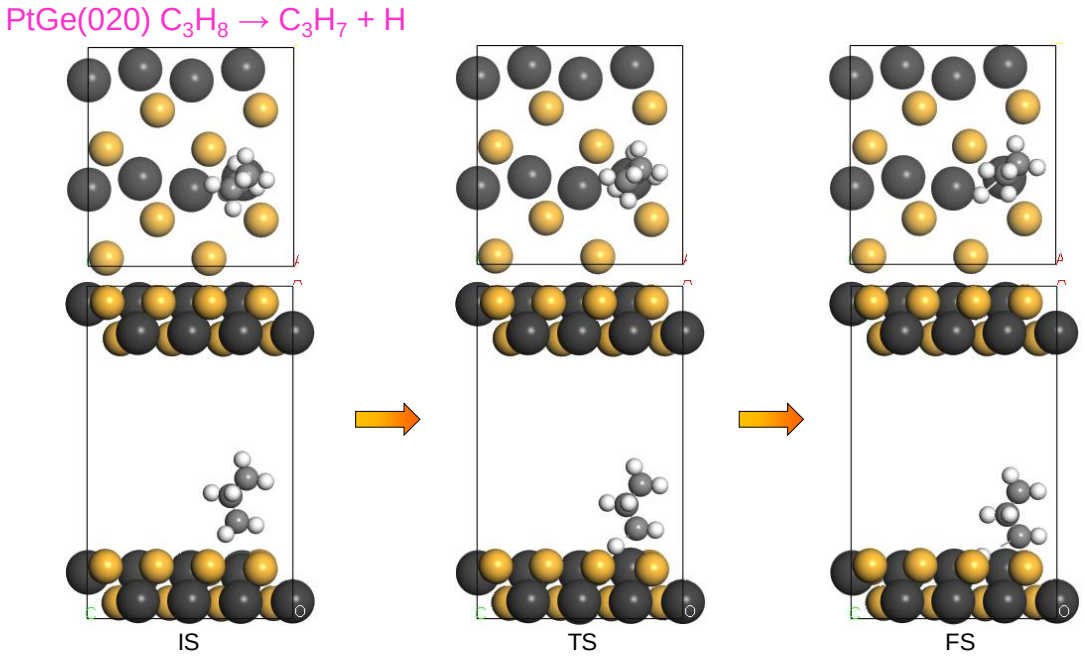

Figure 69. Structures of initial (IS), transition (TS), and final states (FS) of 1st C–H scissions in PDH on the PtGe(020) site.

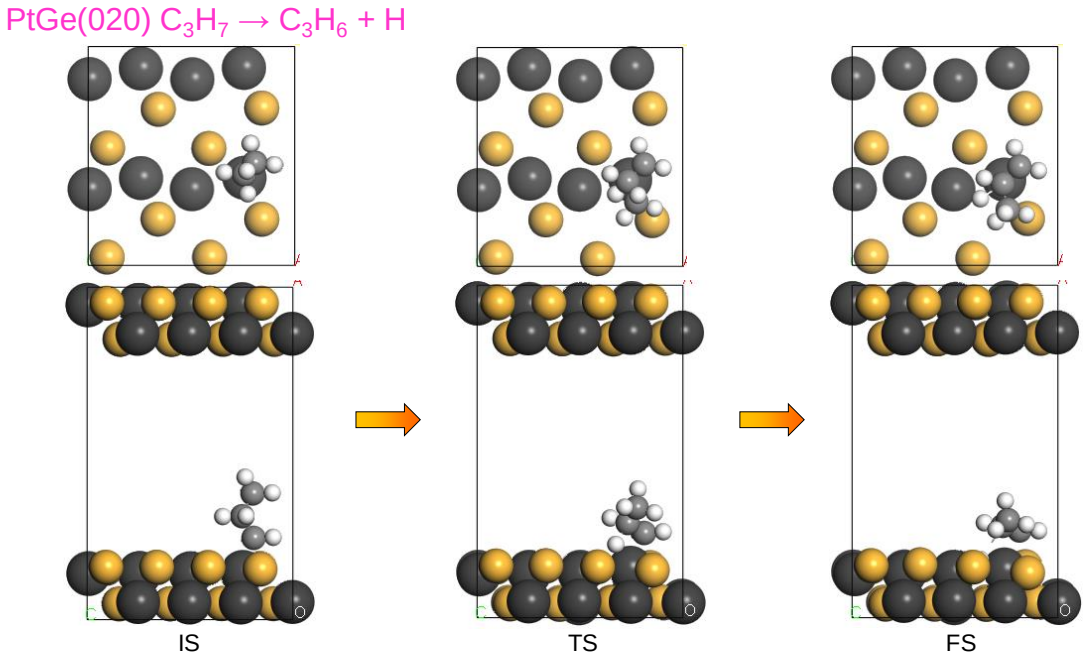

Figure 70. Structures of initial (IS), transition (TS), and final states (FS) of 2nd C–H scissions in PDH on the PtGe(020) site.

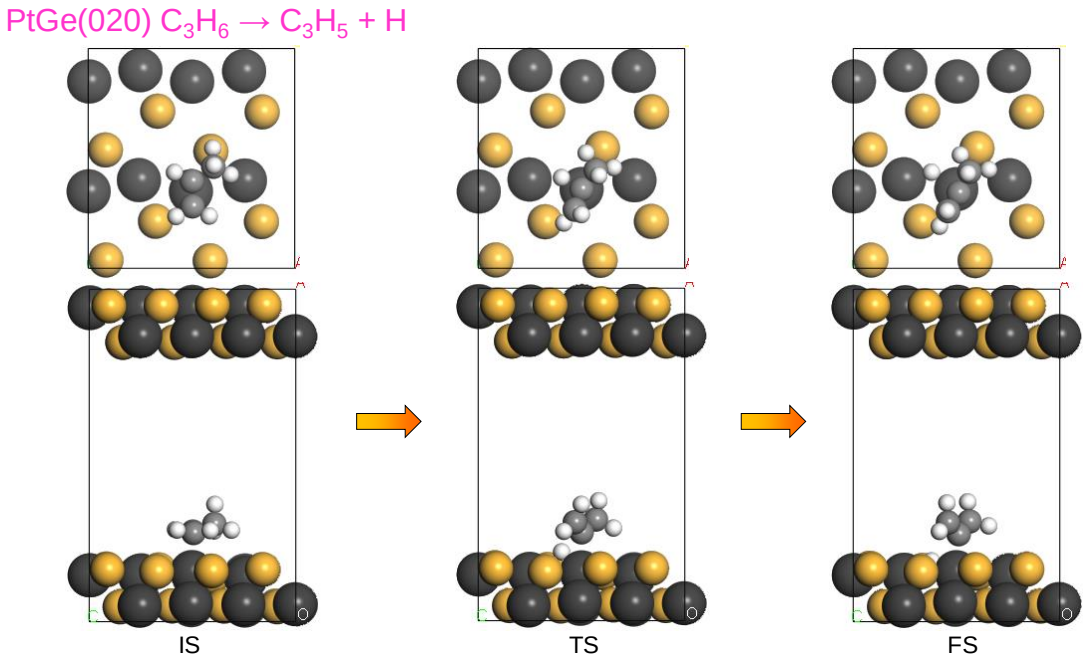

Figure 71. Structures of initial (IS), transition (TS), and final states (FS) of 3rd C–H scissions in PDH on the PtGe(020) site.

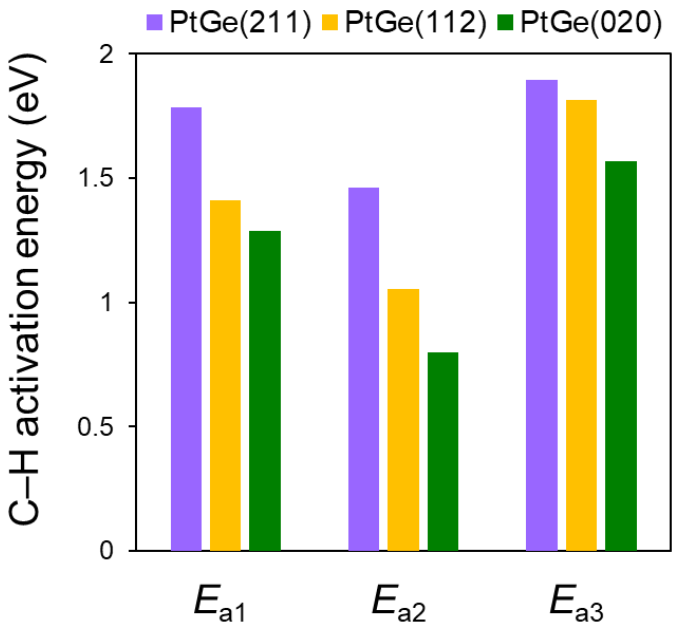

Figure 72. Activation barriers of 1st, 2nd, and 3rd C–H scissions (E_{A1}, E_{A2} and E_{A3}) from propane over the major facets of PtGe. PtGe(020) was more active than (211) and (112) for C–H scissions, indicating that the (020) surface is the most active surface of PtGe. This is probably because (211) and (112) are more stable than (020).

Table 16. Calculated activation energy (EA) for the dehydrogenation of propane on PtGe(211) and PtGe(020).

Surface	Activation energy (eV)		
	1st C–H scission (E_{A1}) ($C_3H_8 \rightarrow C_3H_7 + H$)	2nd C–H scission (E_{A2}) ($C_3H_7 \rightarrow C_3H_6 + H$)	3rd C–H scission (E_{A3}) ($C_3H_6 \rightarrow C_3H_5 + H$)
PtGe(211)	1.78	1.46	1.90
PtGe(112)	1.41	1.05	1.82
PtGe(020)	1.29	0.80	1.65

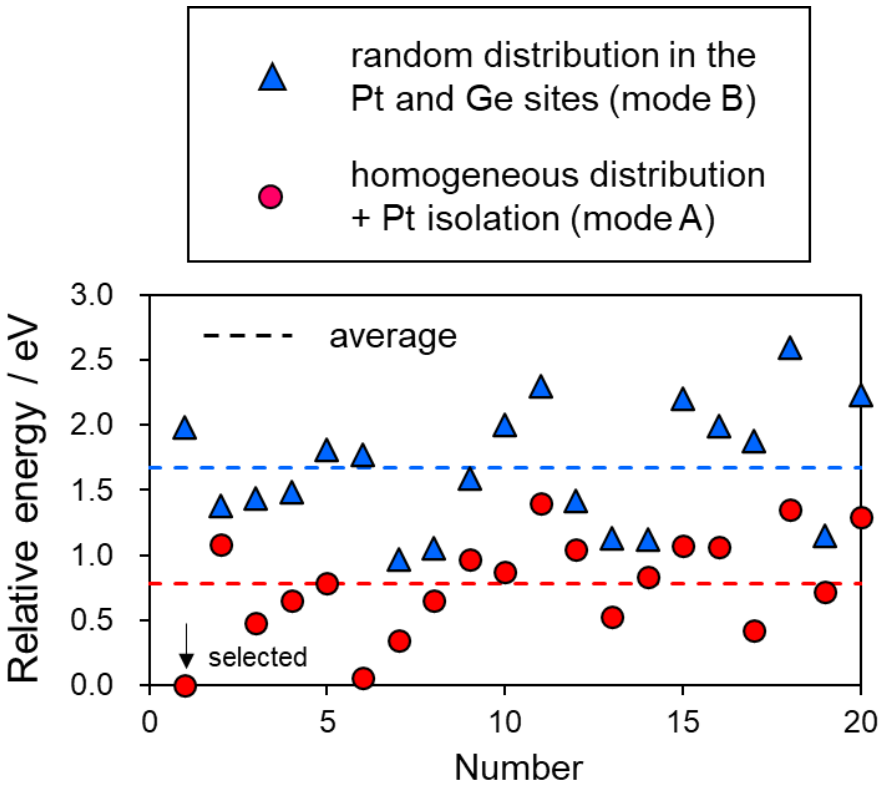

Figure 73. Difference in the electronic energies of various atomic configurations of the supercell of bulk HEI. The energy of the lowest one (selected for the model structure) was set to zero. Mode A: all the Pt atoms in each (040) plane are isolated (no Pt–Pt) and the number of each element in each (040) plane is almost same (Pt: 2, Co: 3, Cu: 3, Ga: 2 or 3, Ge: 2 or 3, and Sn: 2 or 3), mode B: random distribution without the restriction in mode A (mode B). Two or three Pt–Pt pair sites are typically included in mode B.

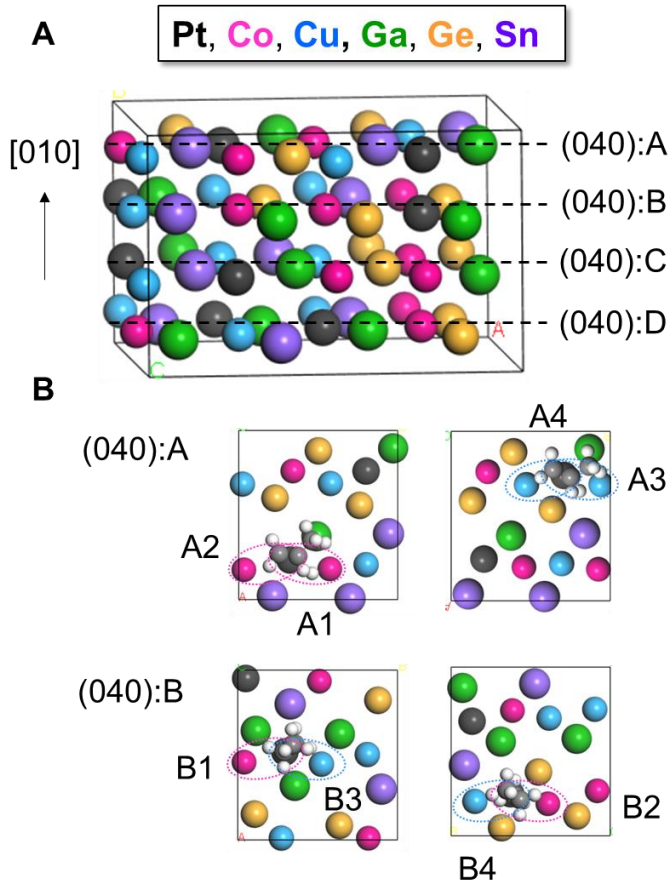

Figure 74. (a) The optimized structure of HEI(0.25) with the most stable atomic configuration. The first (HEI(040):A) and the second (HEI(040):B) top layers of the (040) plane were selected as the model surfaces for catalysis. (b) The atomic arrangements of the HEI(040):A/B surfaces. Eight different Pt–Co and Pt–Cu sites (A1–A4 and B1–B4) were designated by magenta and cyan dotted lines, respectively. The optimized structures of C_3H_6+H on (040):A and C_3H_7 on (040):B were also shown as example.

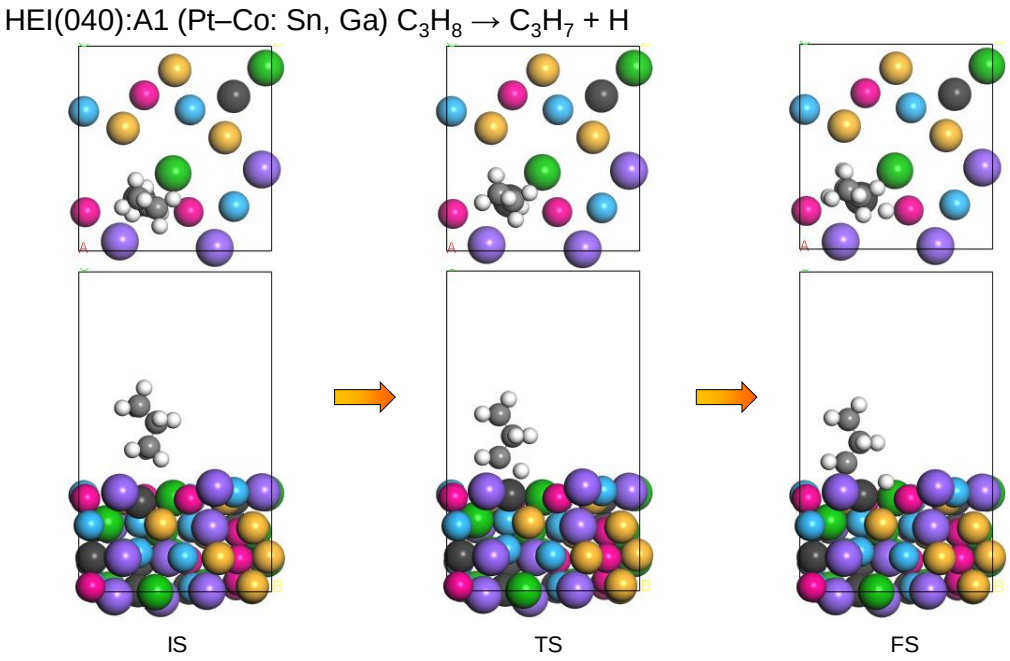

Figure 75. Structures of initial (IS), transition (TS), and final states (FS) of 1st C–H scissions in PDH on the HEI(040):A1 site.

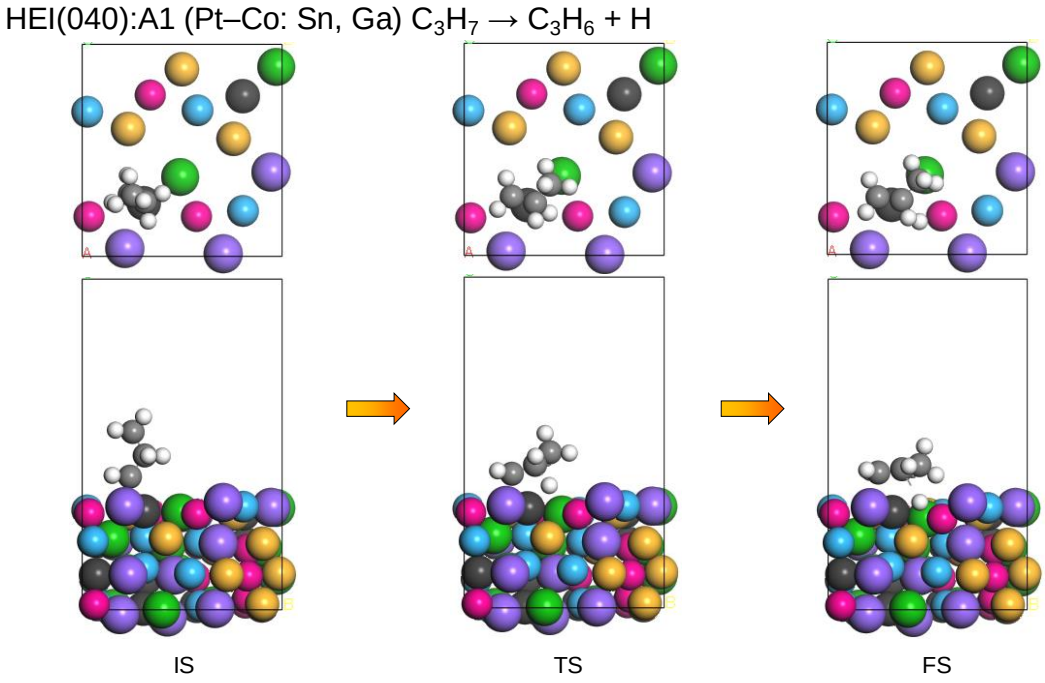

Figure 76. Structures of initial (IS), transition (TS), and final states (FS) of 2nd C–H scissions in PDH on the HEI(040):A1 site.

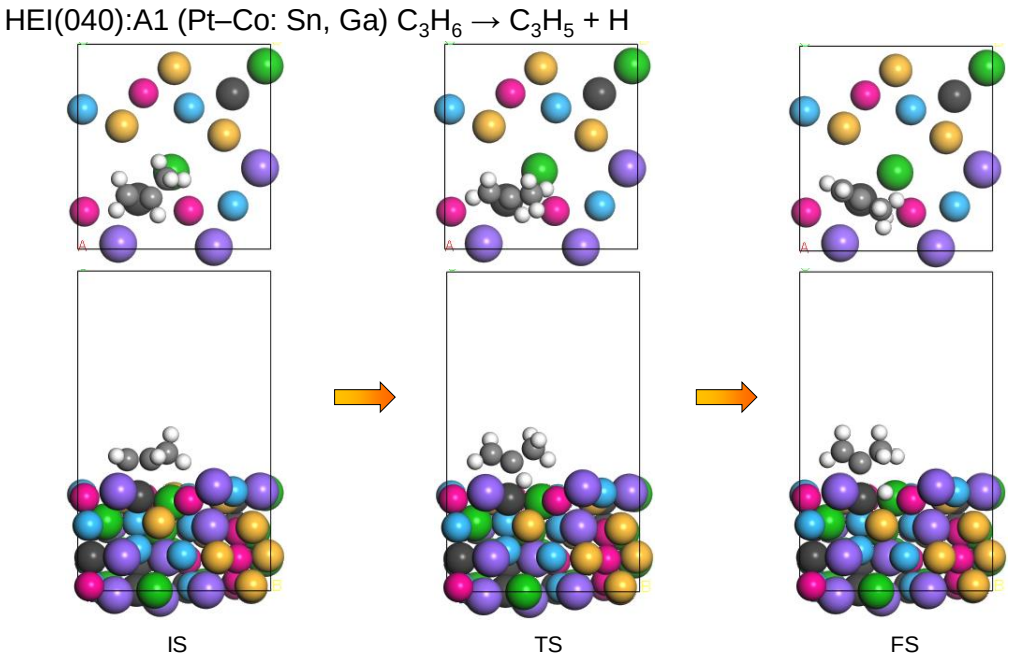

Figure 77. Structures of initial (IS), transition (TS), and final states (FS) of 3rd C–H scissions in PDH on the HEI(040):A1 site.

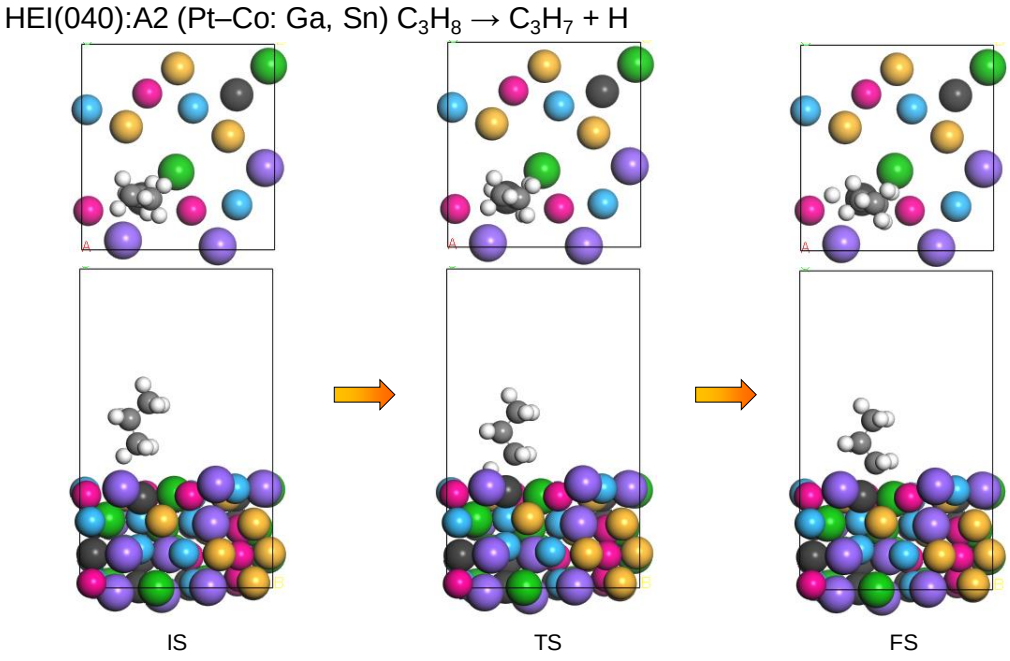

Figure 78. Structures of initial (IS), transition (TS), and final states (FS) of 1st C–H scissions in PDH on the HEI(040):A2 site.

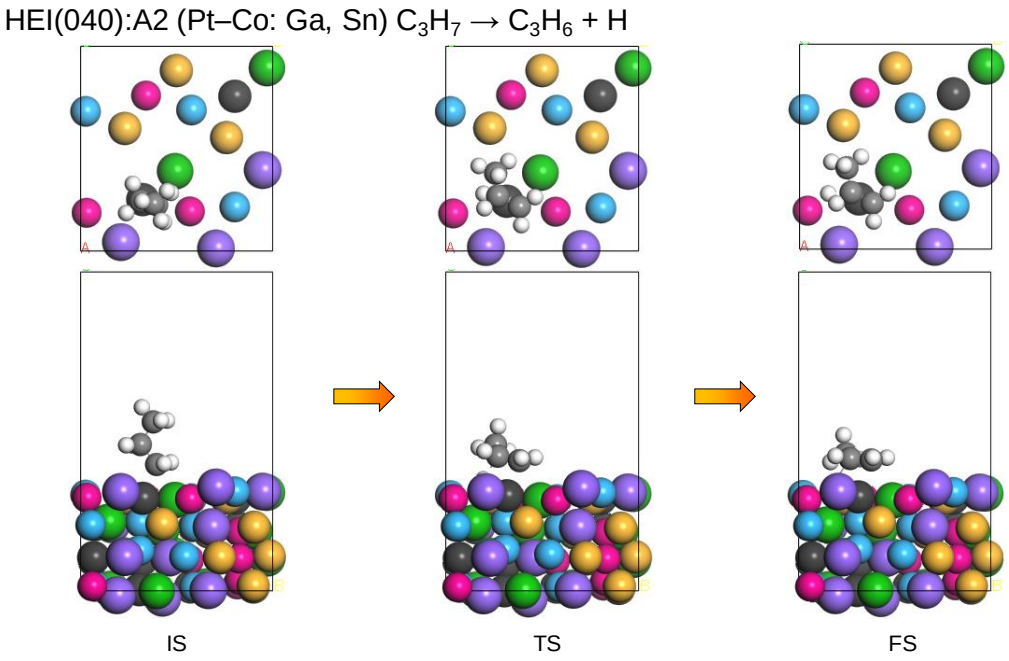

Figure 79. Structures of initial (IS), transition (TS), and final states (FS) of 2nd C–H scissions in PDH on the HEI(040):A2 site.

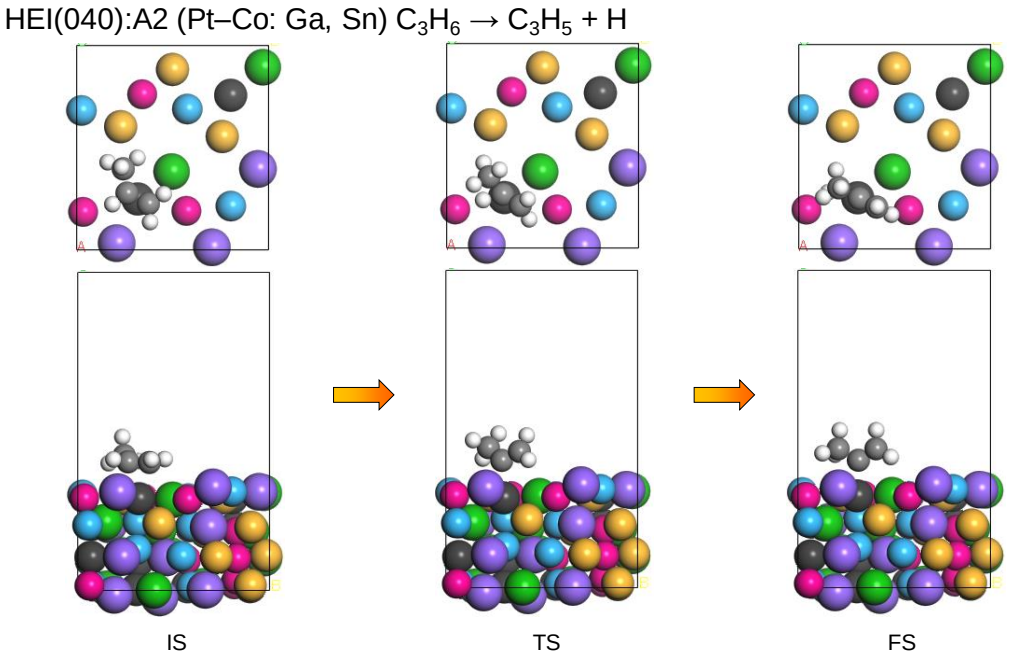

Figure 80. Structures of initial (IS), transition (TS), and final states (FS) of 3rd C–H scissions in PDH on the HEI(040):A2 site.

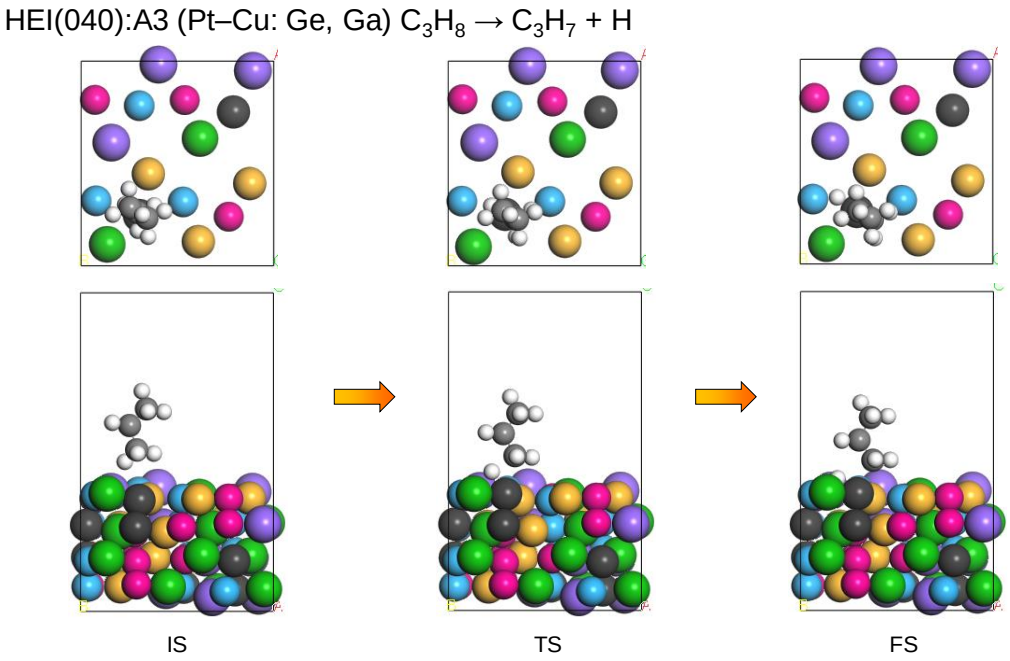

Figure 81. Structures of initial (IS), transition (TS), and final states (FS) of 1st C–H scissions in PDH on the HEI(040):A3 site.

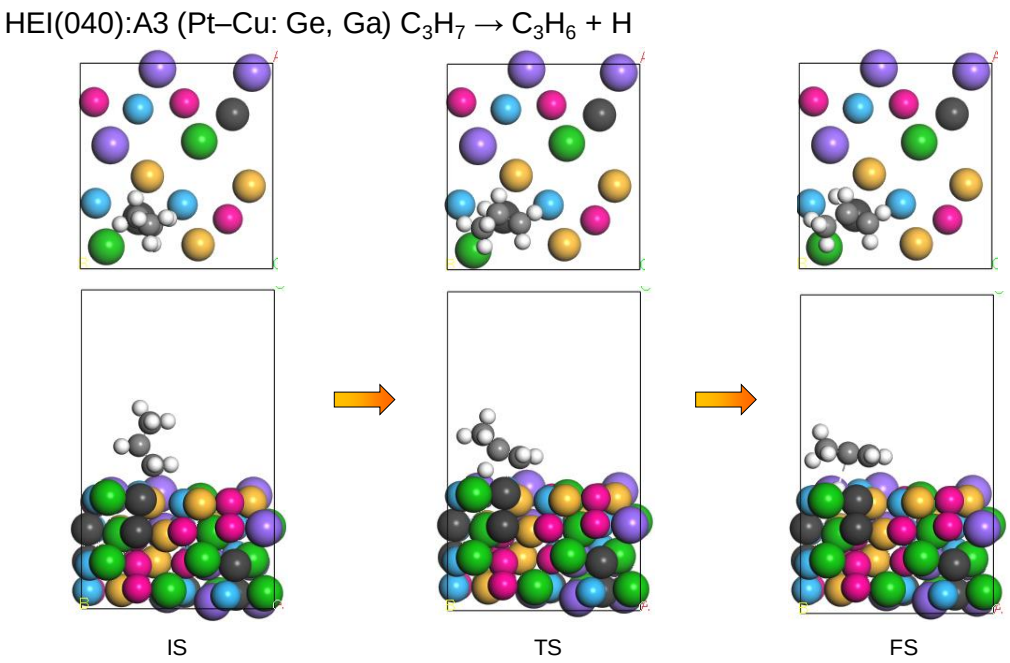

Figure 82. Structures of initial (IS), transition (TS), and final states (FS) of 2nd C–H scissions in PDH on the HEI(040):A3 site.

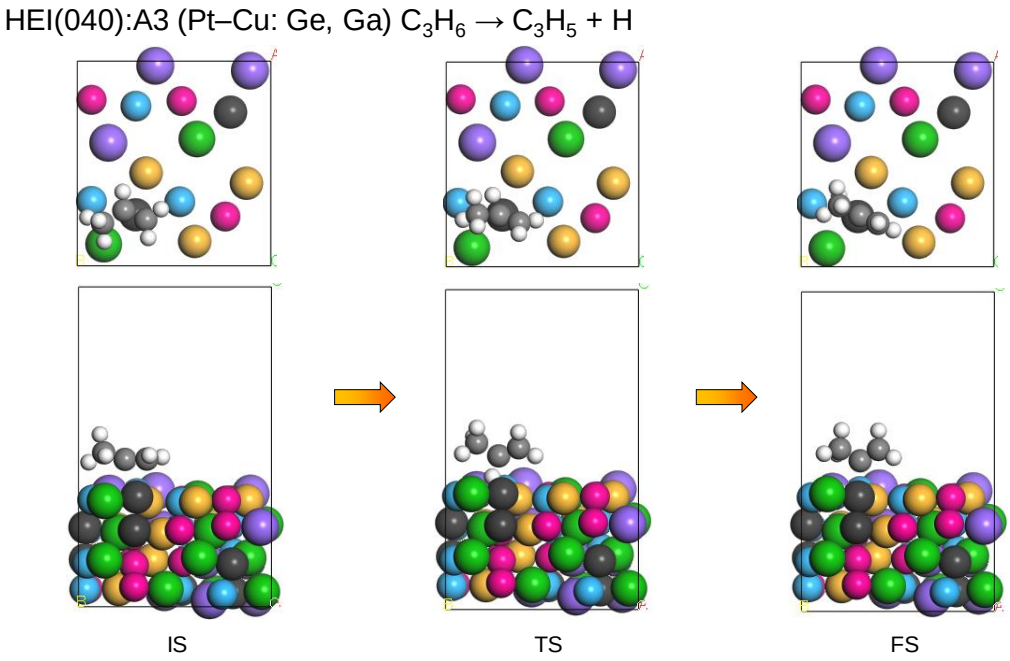

Figure 83. Structures of initial (IS), transition (TS), and final states (FS) of 3rd C–H scissions in PDH on the HEI(040):A3 site.

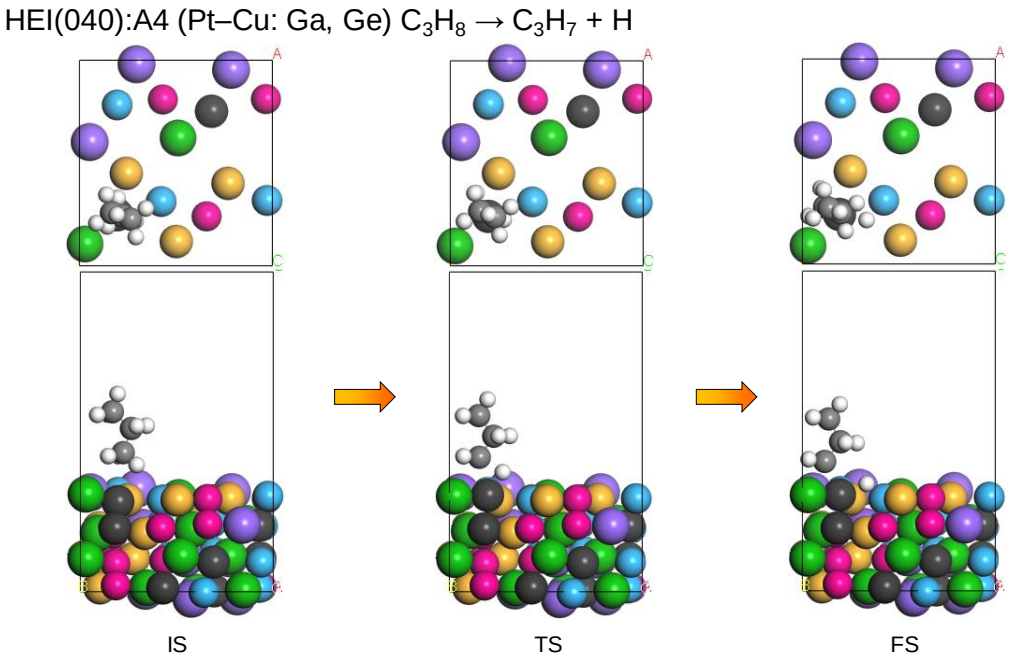

Figure 84. Structures of initial (IS), transition (TS), and final states (FS) of 1st C–H scissions in PDH on the HEI(040):A4 site.

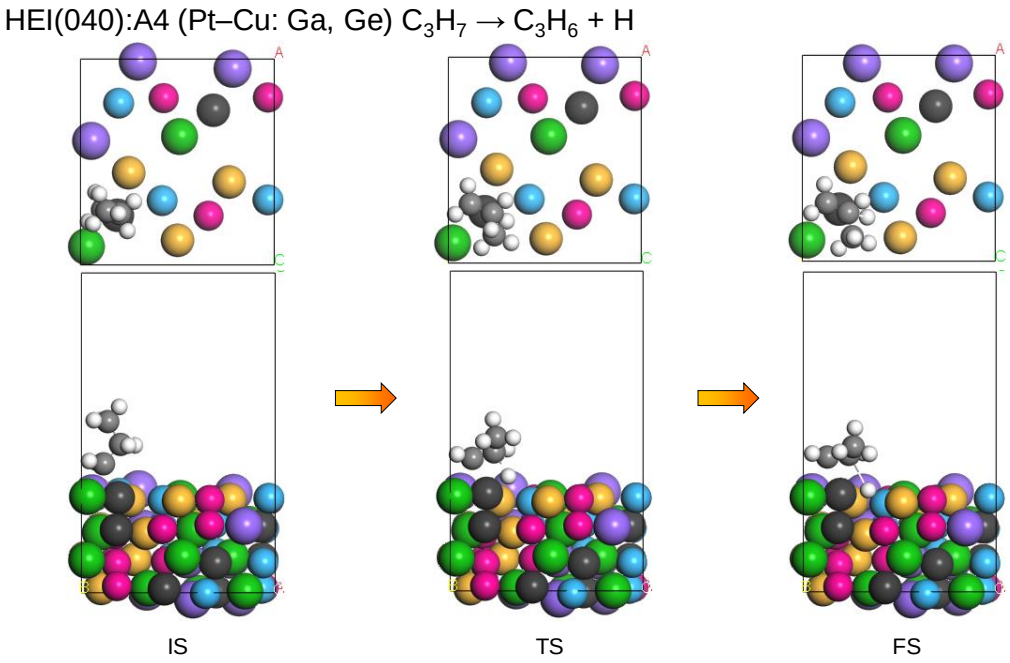

Figure 85. Structures of initial (IS), transition (TS), and final states (FS) of 2nd C–H scissions in PDH on the HEI(040):A4 site.

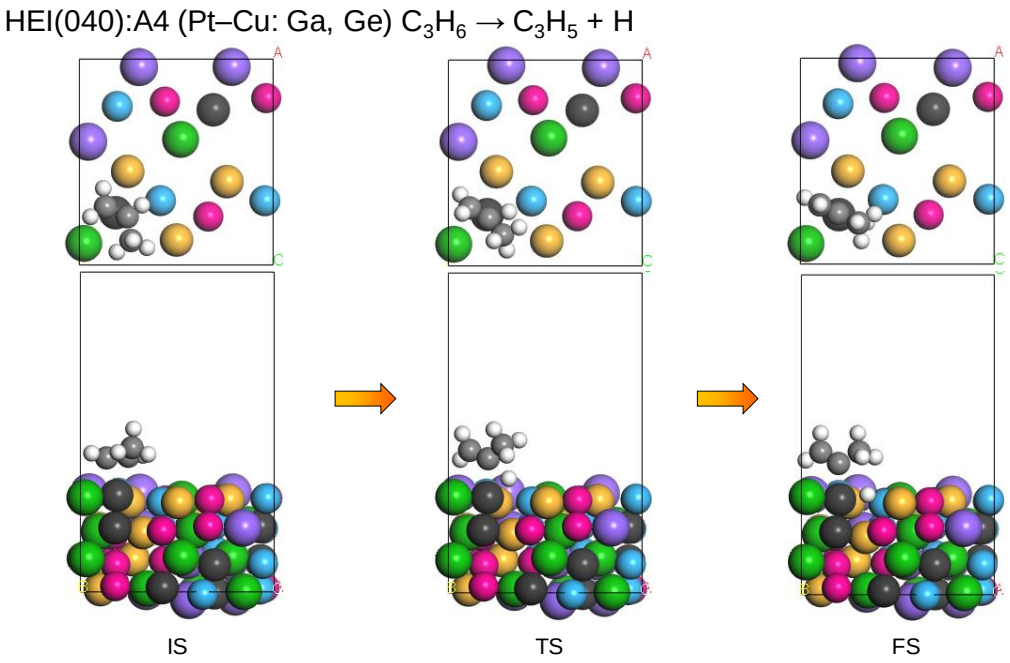

Figure 86. Structures of initial (IS), transition (TS), and final states (FS) of 3rd C–H scissions in PDH on the HEI(040):A3 site.

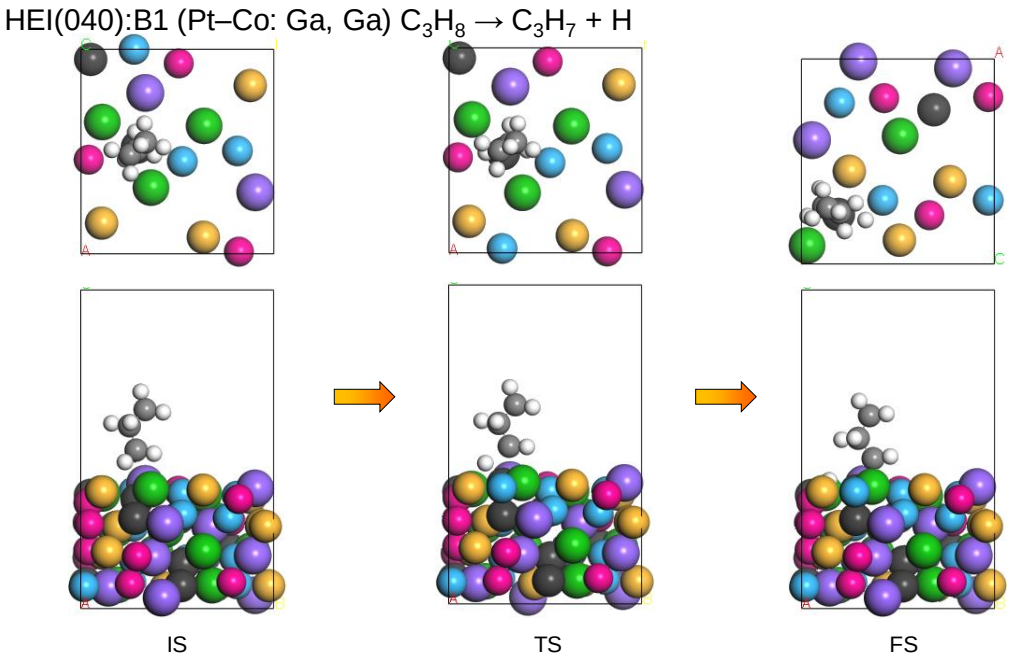

Figure 87. Structures of initial (IS), transition (TS), and final states (FS) of 1st C–H scissions in PDH on the HEI(040):B1 site.

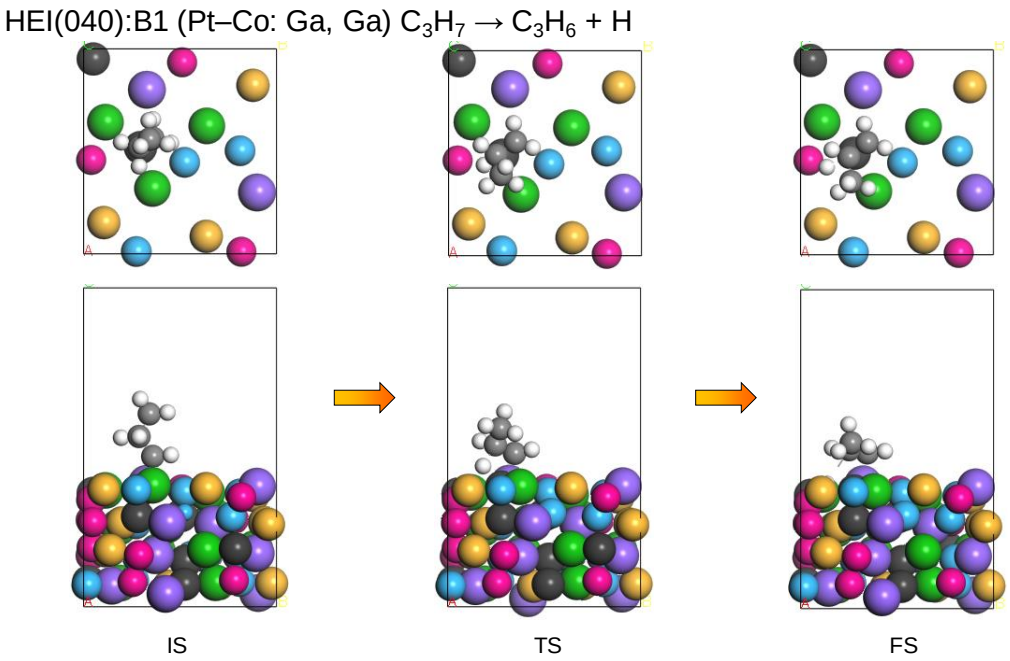

Figure 88. Structures of initial (IS), transition (TS), and final states (FS) of 2nd C–H scissions in PDH on the HEI(040):B1 site.

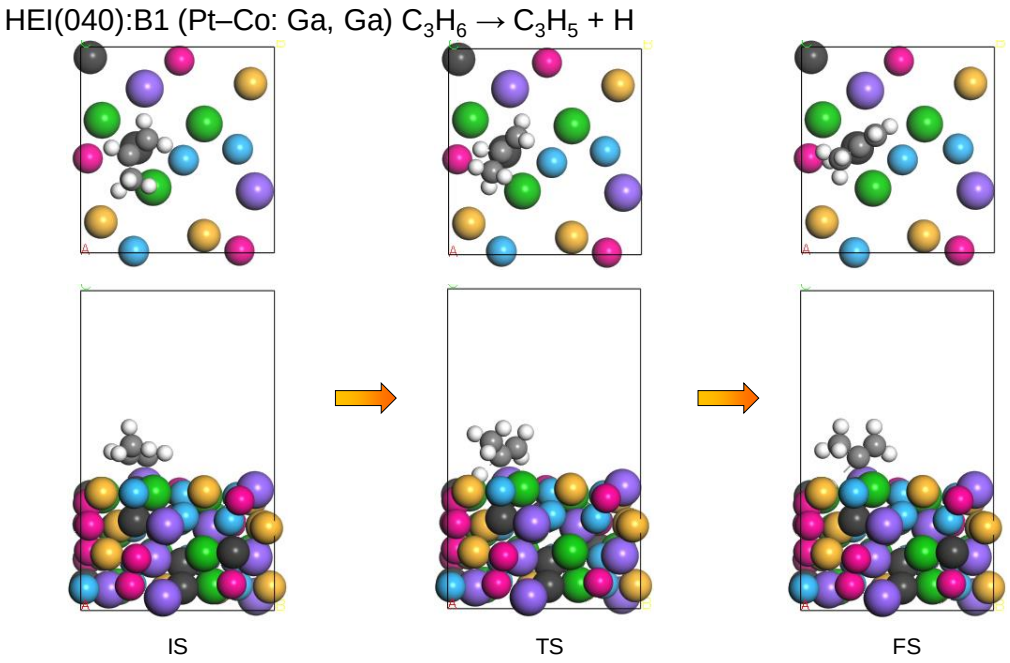

Figure 89. Structures of initial (IS), transition (TS), and final states (FS) of 3rd C–H scissions in PDH on the HEI(040):B1 site.

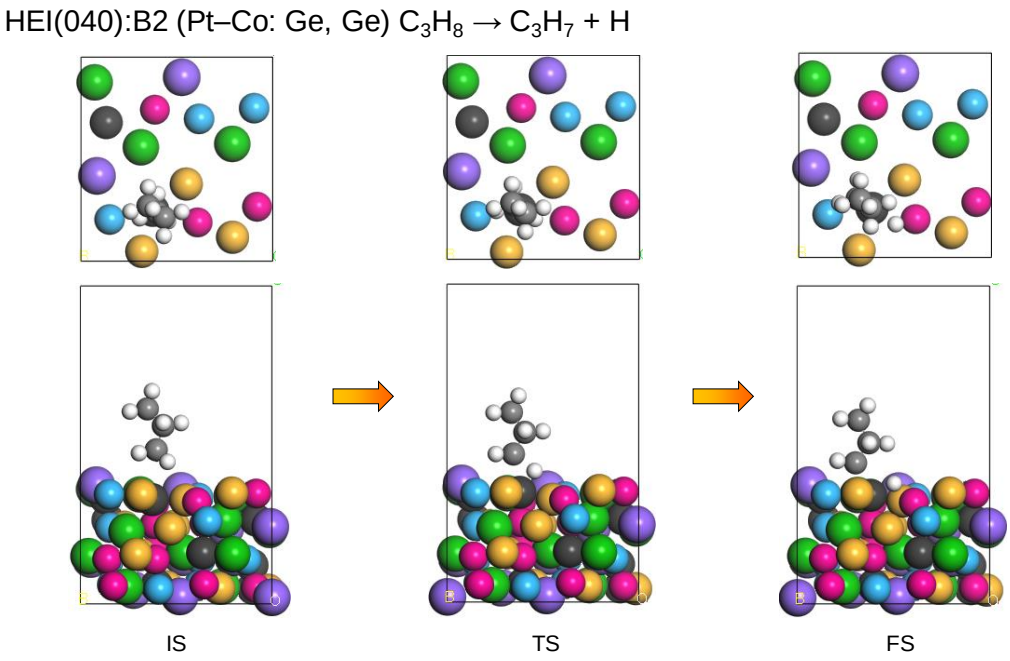

Figure 90. Structures of initial (IS), transition (TS), and final states (FS) of 1st C–H scissions in PDH on the HEI(040):B2 site.

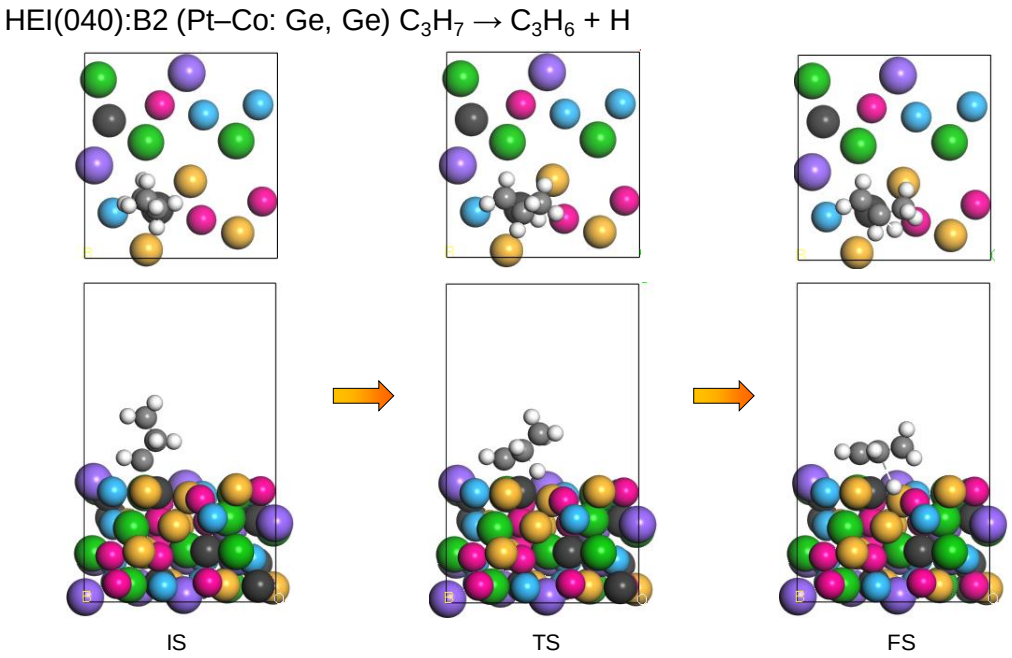

Figure 91. Structures of initial (IS), transition (TS), and final states (FS) of 2nd C–H scissions in PDH on the HEI(040):B2 site.

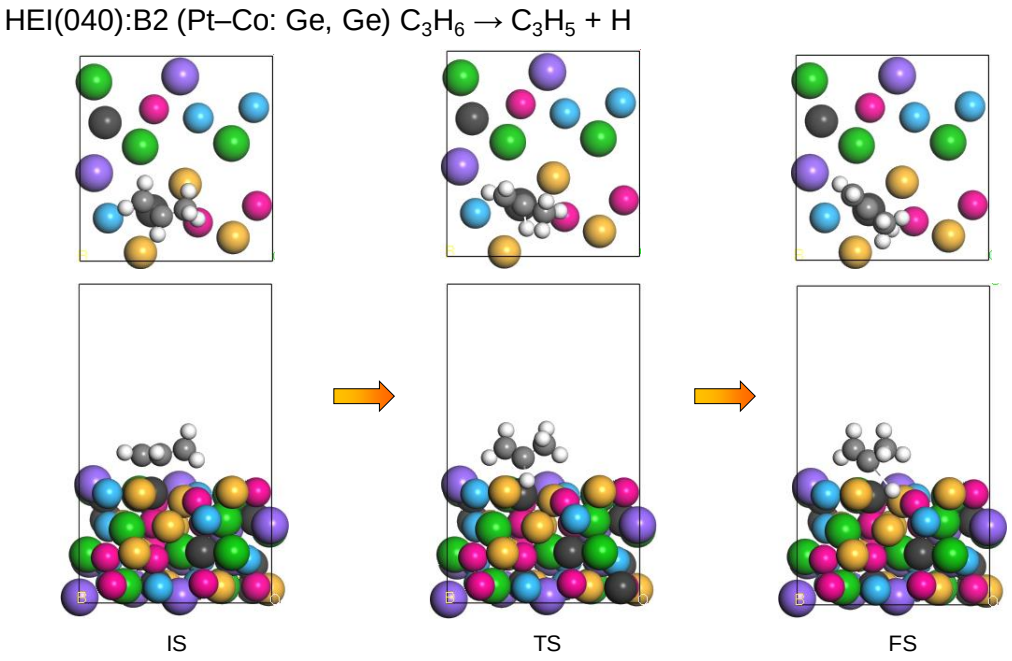

Figure 92. Structures of initial (IS), transition (TS), and final states (FS) of 3rd C–H scissions in PDH on the HEI(040):B2 site.

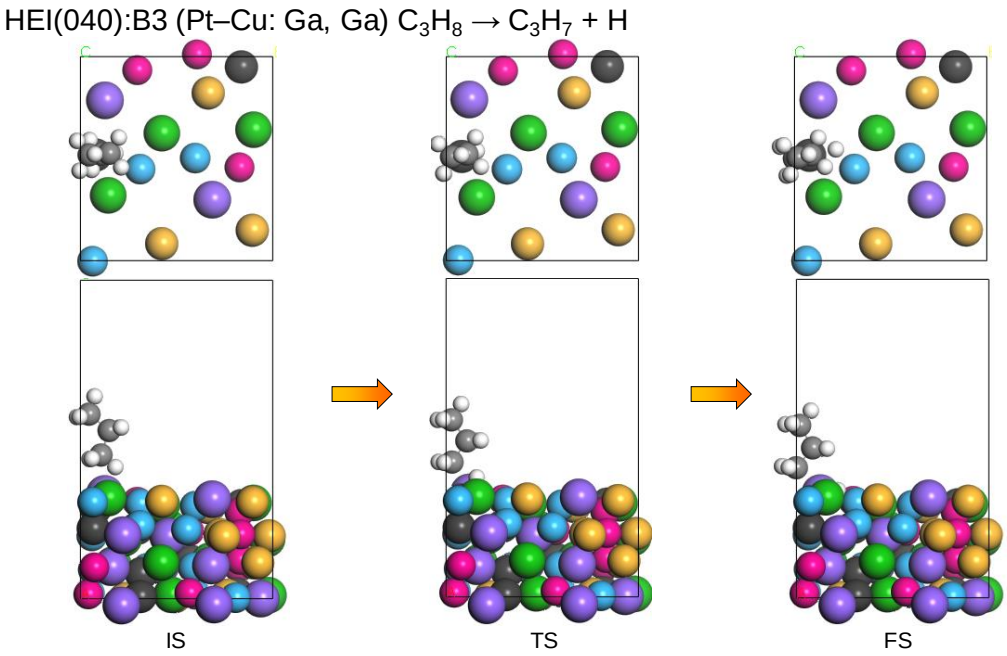

Figure 93. Structures of initial (IS), transition (TS), and final states (FS) of 1st C–H scissions in PDH on the HEI(040):B3 site.

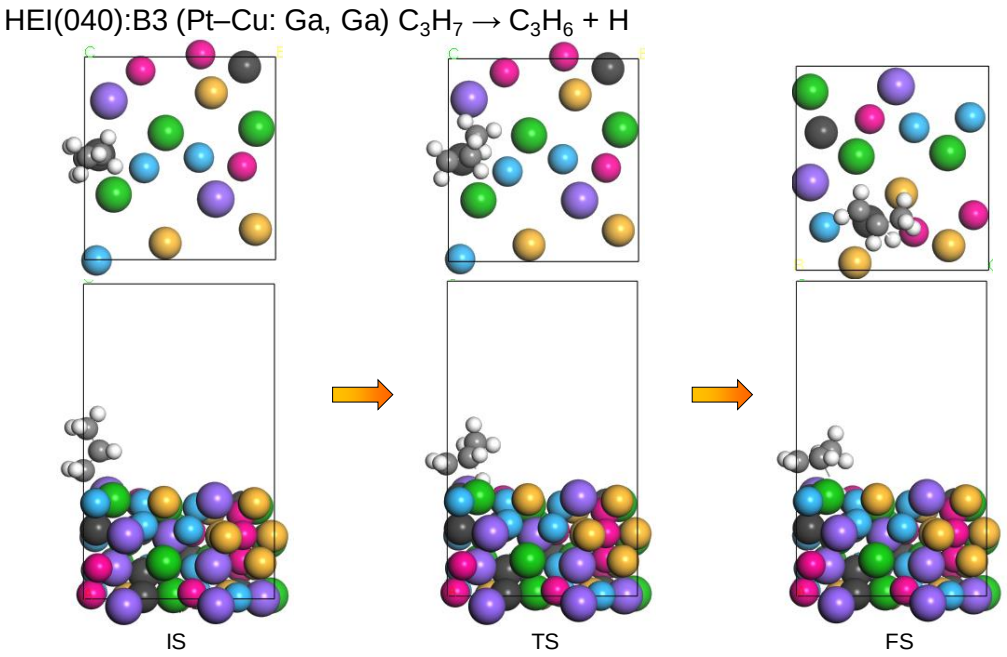

Figure 94. Structures of initial (IS), transition (TS), and final states (FS) of 2nd C–H scissions in PDH on the HEI(040):B3 site.

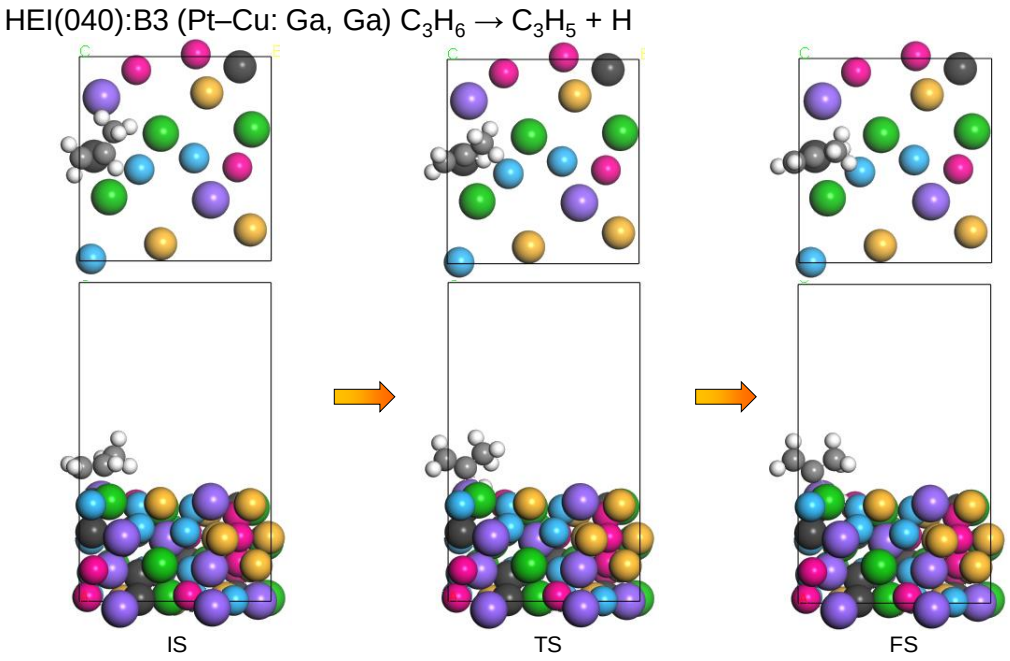

Figure 95. Structures of initial (IS), transition (TS), and final states (FS) of 3rd C–H scissions in PDH on the HEI(040):B3 site.

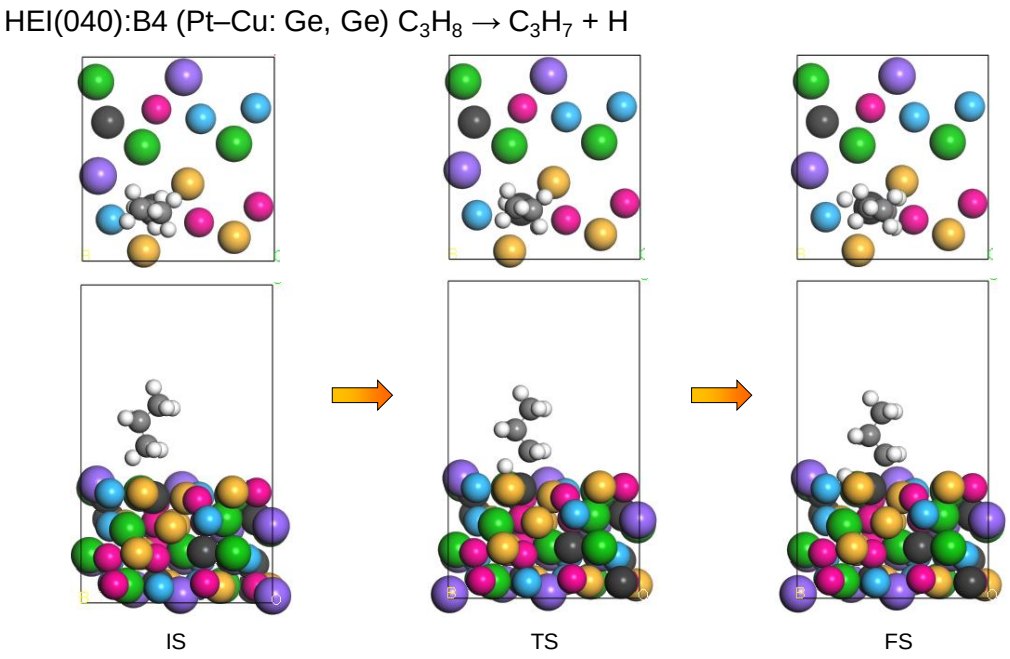

Figure 96. Structures of initial (IS), transition (TS), and final states (FS) of 1st C–H scissions in PDH on the HEI(040):B4 site.

HEI(040):B4 (Pt–Cu: Ge, Ge) $C_3H_7 \rightarrow C_3H_6 + H$

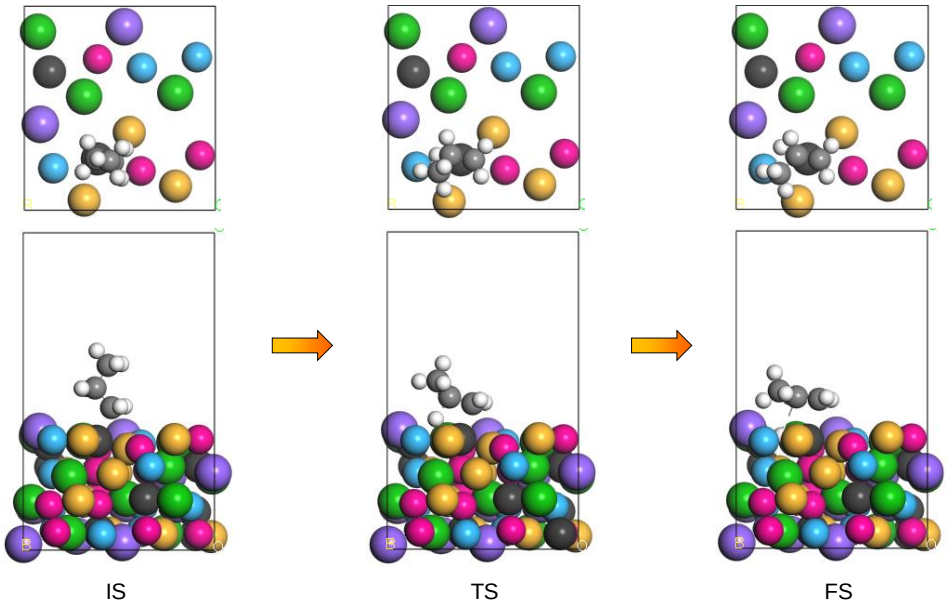

Figure 97. Structures of initial (IS), transition (TS), and final states (FS) of 2nd C–H scissions in PDH on the HEI(040):B4 site.

HEI(040):B4 (Pt–Cu: Ge, Ge) $C_3H_6 \rightarrow C_3H_5 + H$

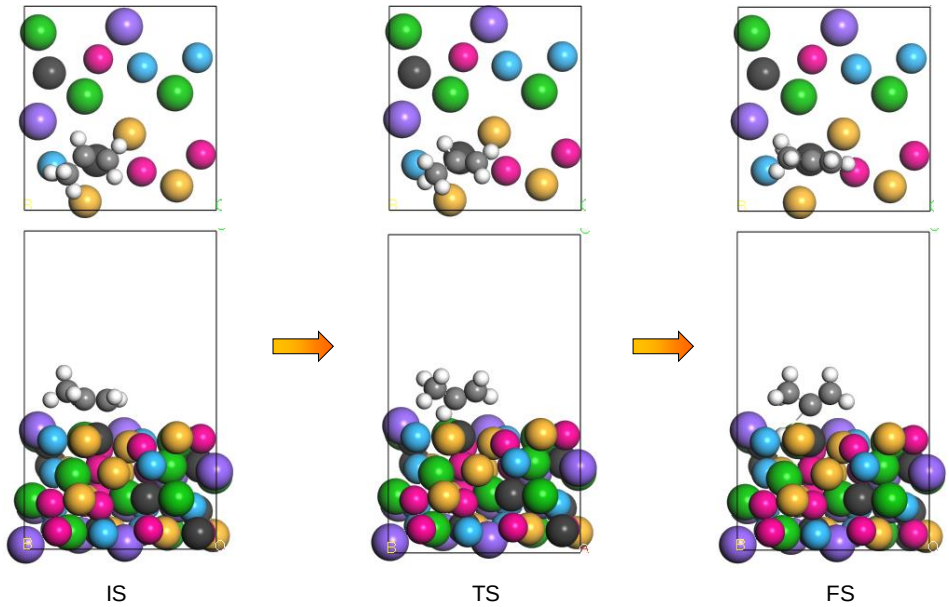

Figure 98. Structures of initial (IS), transition (TS), and final states (FS) of 3rd C–H scissions in PDH on the HEI(040):B4 site.

Table S16. Summary of DFT calculation for PDH on various metallic surfaces.

Surface active sites	Energy barrier (eV)			E_{ad}	Reaction energy (eV)			ΔE[a]
(constituent metals)	E_{A1}	E_{A2}	E_{A3}	(eV)	ΔE_{r1}	ΔE_{r2}	ΔE_{r3}	(eV)
HEI(040)								
A1 (Sn, Pt, Ga, Co)	1.17	0.97	1.81	-0.38	0.42	0.49	1.06	1.43
B1 (Ga, Pt, Ga, Co)	1.07	0.62	1.69	-0.22	0.40	0.21	0.85	1.47
A2 (Ga, Pt, Sn, Co)	1.28	0.66	1.48	-0.44	0.74	0.26	0.83	1.04
B2 (Ge, Pt, Ge, Co)	1.28	0.86	1.60	-0.38	0.74	0.60	1.34	1.22
A3 (Ge, Pt, Ga, Cu)	1.26	0.59	1.59	-0.08	0.96	0.34	1.26	1.50
B3 (Ga, Pt, Ga, Cu)	1.22	0.92	1.52	-0.14	0.85	0.65	0.96	1.38
A4 (Ga, Pt, Ge, Cu)	1.26	0.68	1.73	-0.19	0.80	0.66	1.31	1.54
B4 (Ge, Pt, Ge, Cu)	1.12	0.60	1.76	-0.53	0.73	0.39	1.33	1.23
PtGe(020)	1.29	0.80	1.65	-0.60	0.81	0.43	1.33	1.05
PtGe(112)	1.41	1.05	1.82	-0.38	0.80	0.24	0.85	1.43
PtGe(211)	1.78	1.46	1.90	0.21	1.36	0.64	0.97	2.11
Pt_1@PtGa(111) [b]	1.11	0.76	1.77	-1.03	0.81	0.10	1.50	0.74
Pt_1@Cu(111)	1.13	0.98	1.29	-0.74	0.61	0.24	1.02	0.55
Pt_3Sn(111)	1.17	0.76	1.36	-0.77	0.23	0.23	0.70	0.60
Pt(111)	1.04	0.98	1.17	-1.28	0.31	0.24	0.67	-0.11

[a]$\Delta E = E_{A3} - E_d = E_{A3} + E_{ad}$. [b]Reproduced from the previous study[64].

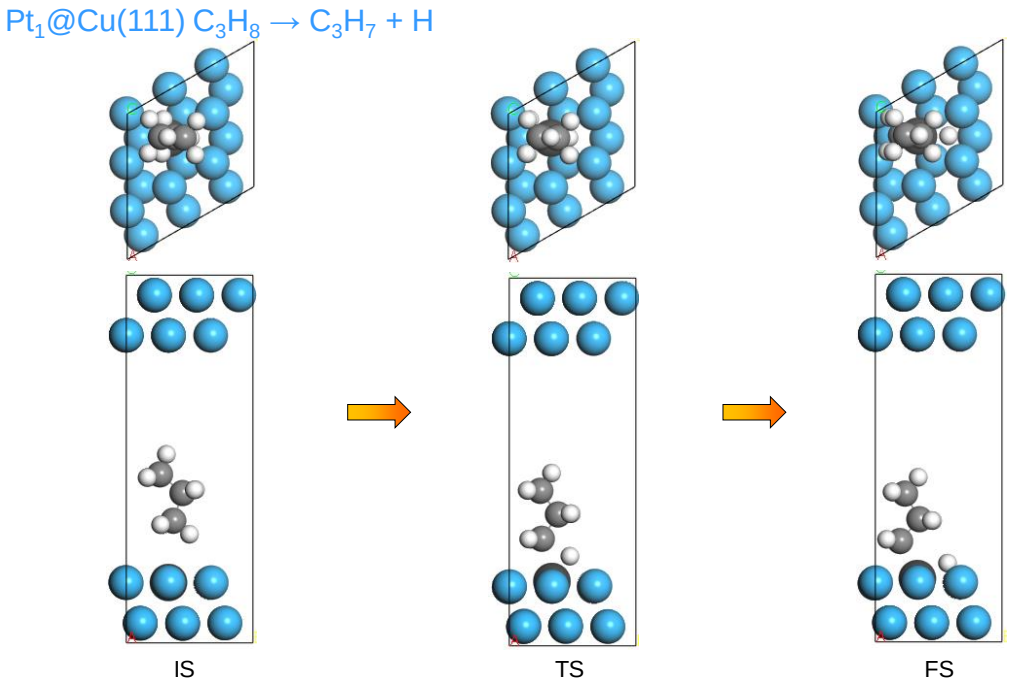

Figure 99. Structures of initial (IS), transition (TS), and final states (FS) of 1st C–H scissions in PDH on the Pt–Cu SAA; Pt_1@Cu(111) site.

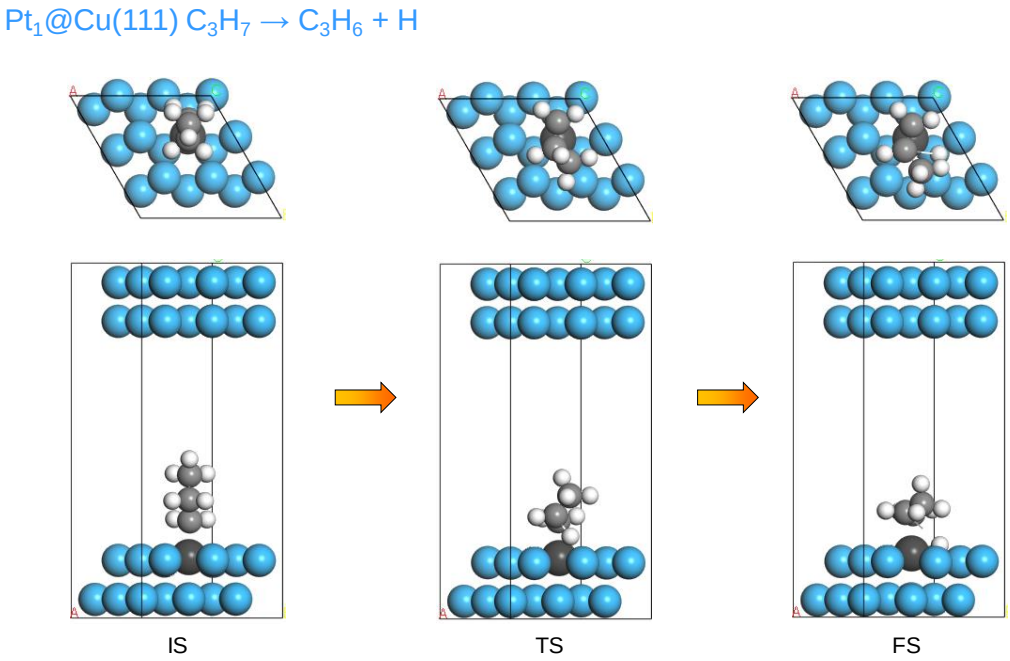

Figure 100. Structures of initial (IS), transition (TS), and final states (FS) of 2nd C–H scissions in PDH on the Pt–Cu SAA; Pt_1@Cu(111) site.

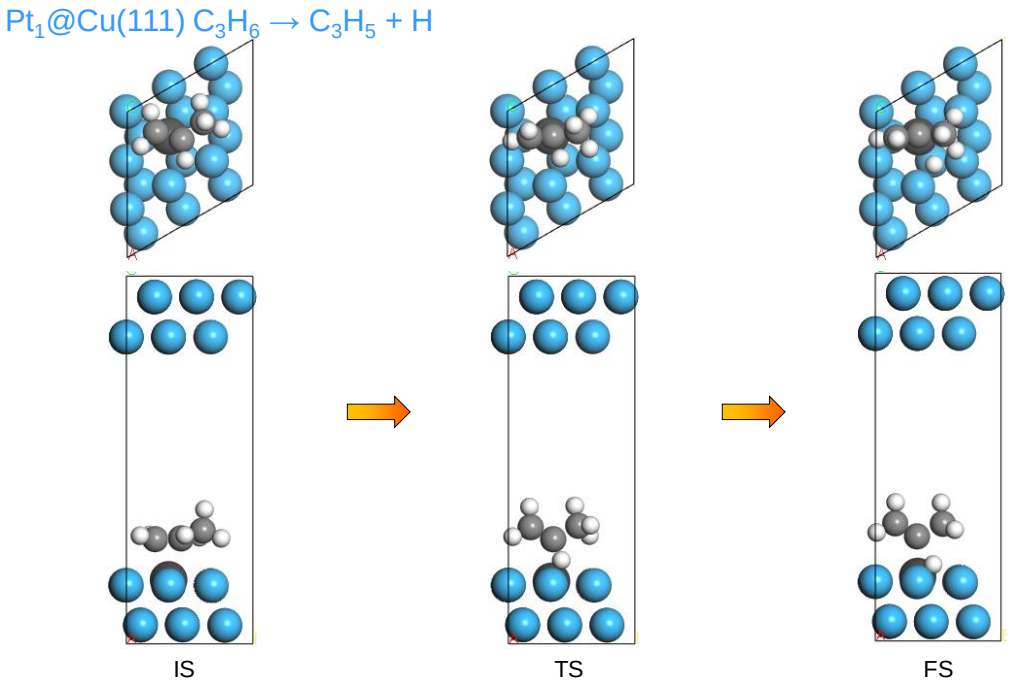

Figure 101. Structures of initial (IS), transition (TS), and final states (FS) of 3rd C–H scissions in PDH on the Pt–Cu SAA; Pt_1@Cu(111) site.

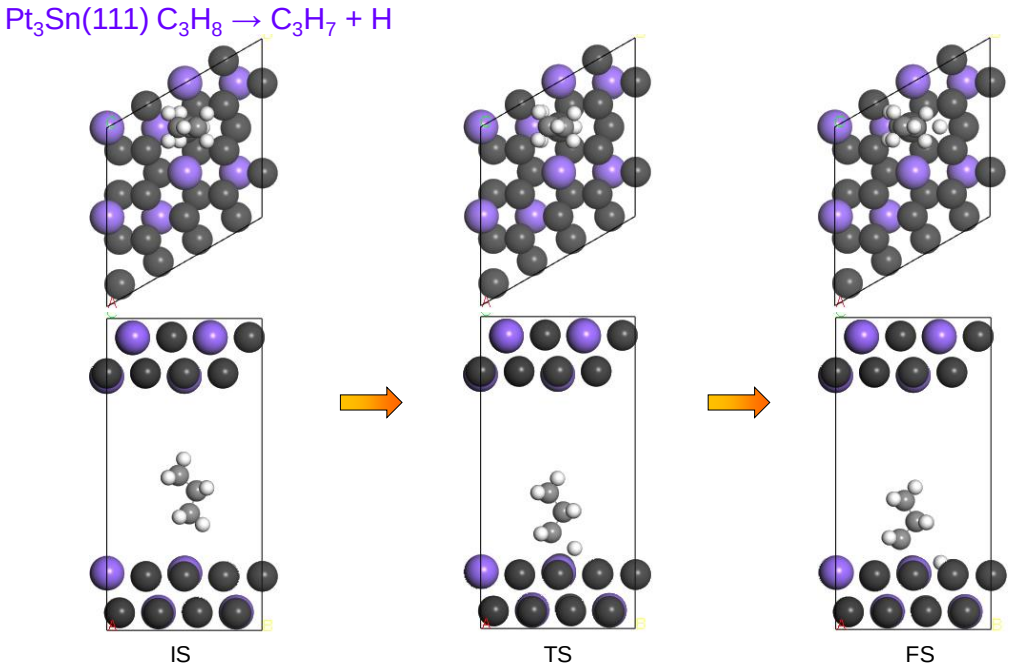

Figure 102. Structures of initial (IS), transition (TS), and final states (FS) of 1st C–H scissions in PDH on the Pt_3Sn(111) site.

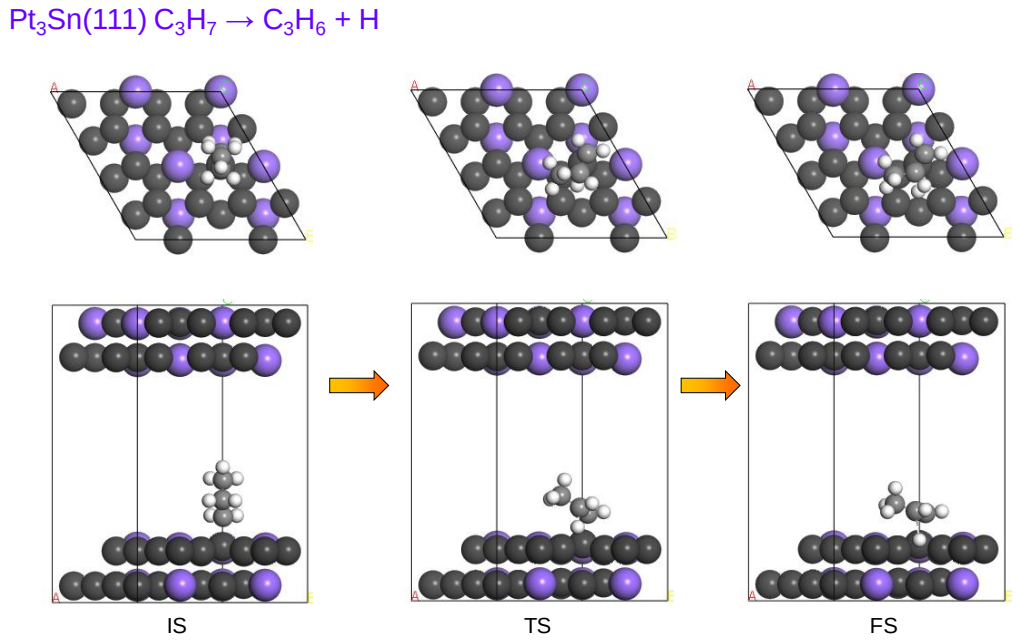

Figure 103. Structures of initial (IS), transition (TS), and final states (FS) of 2nd C–H scissions in PDH on the $Pt_3Sn(111)$ site.

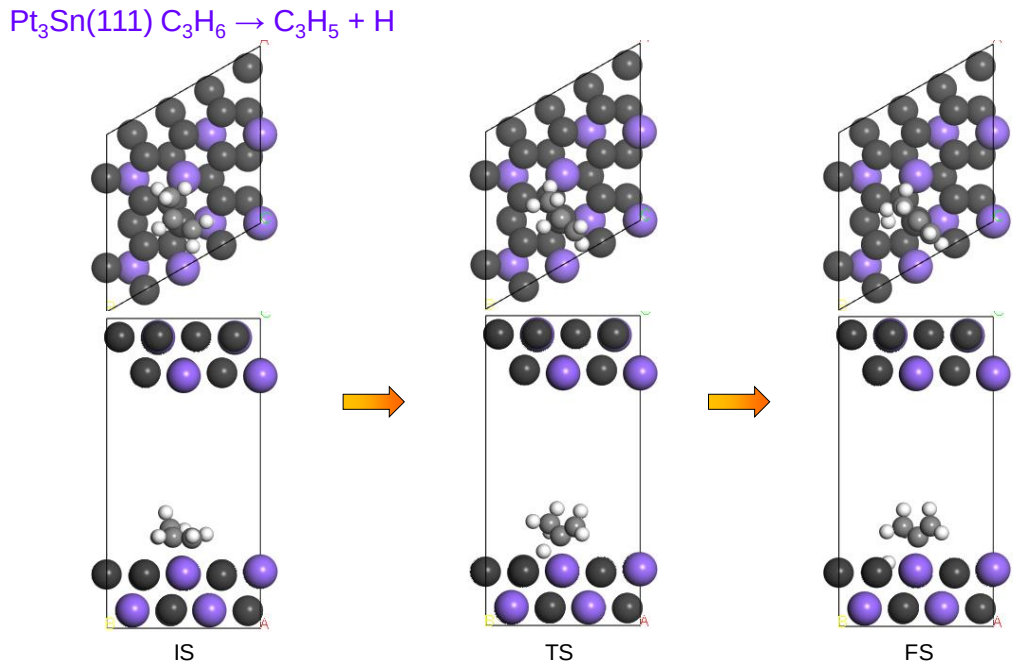

Figure 104. Structures of initial (IS), transition (TS), and final states (FS) of 3rd C–H scissions in PDH on the $Pt_3Sn(111)$ site.

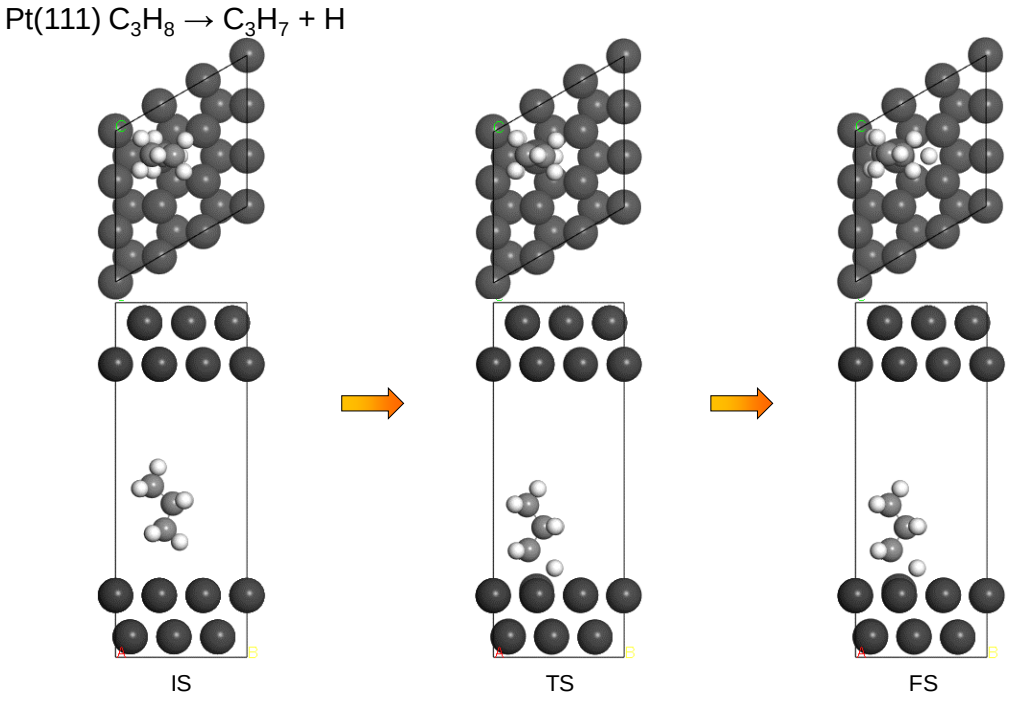

Figure 105. Structures of initial (IS), transition (TS), and final states (FS) of 1st C–H scissions in PDH on the Pt(111) site.

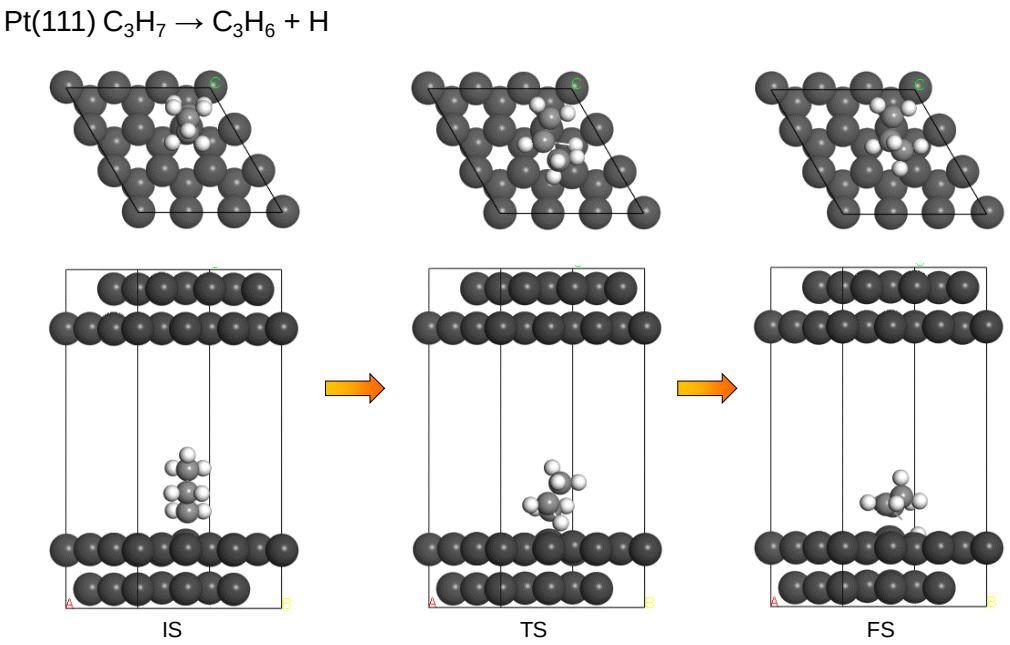

Figure 106. Structures of initial (IS), transition (TS), and final states (FS) of 2nd C–H scissions in PDH on the Pt(111) site.

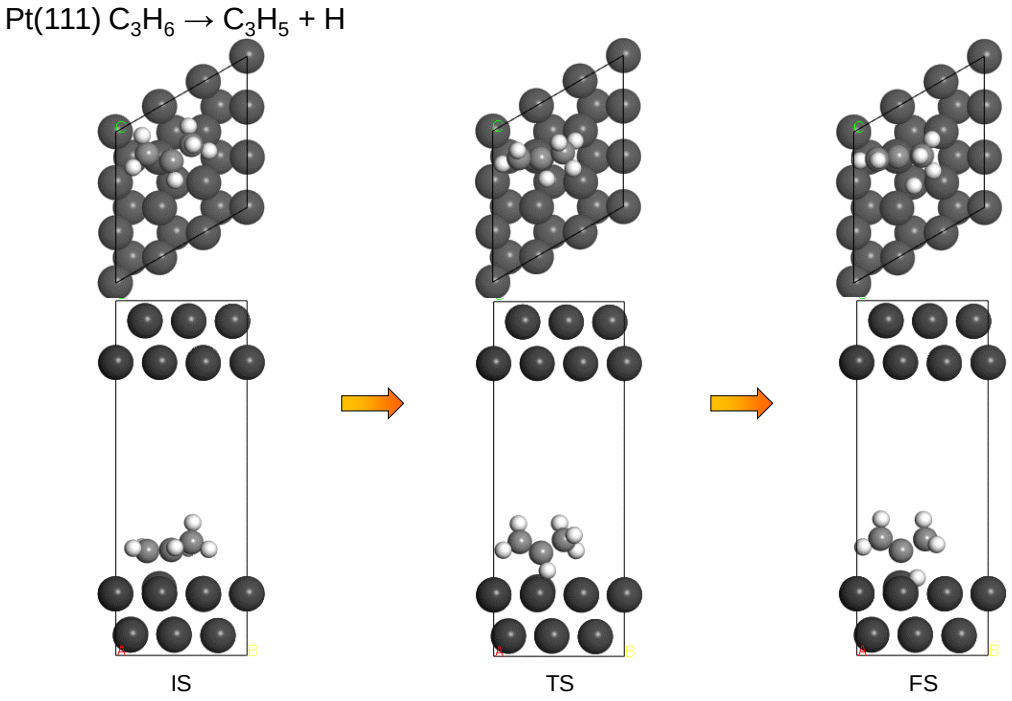

Figure 107. Structures of initial (IS), transition (TS), and final states (FS) of 3rd C–H scissions in PDH on the Pt(111) site.

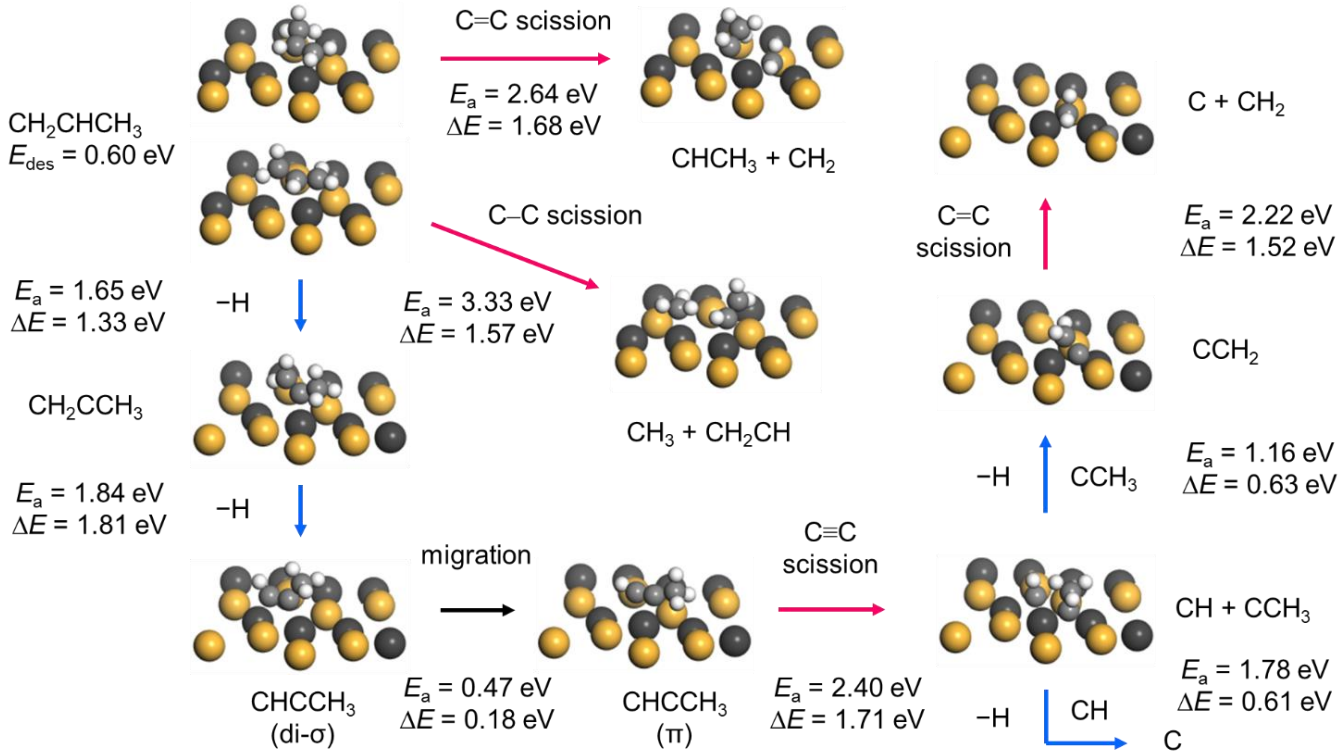

Scheme 4. Reaction scheme and energetics from C_3H_6 to carbon over PtGe(020) surface.

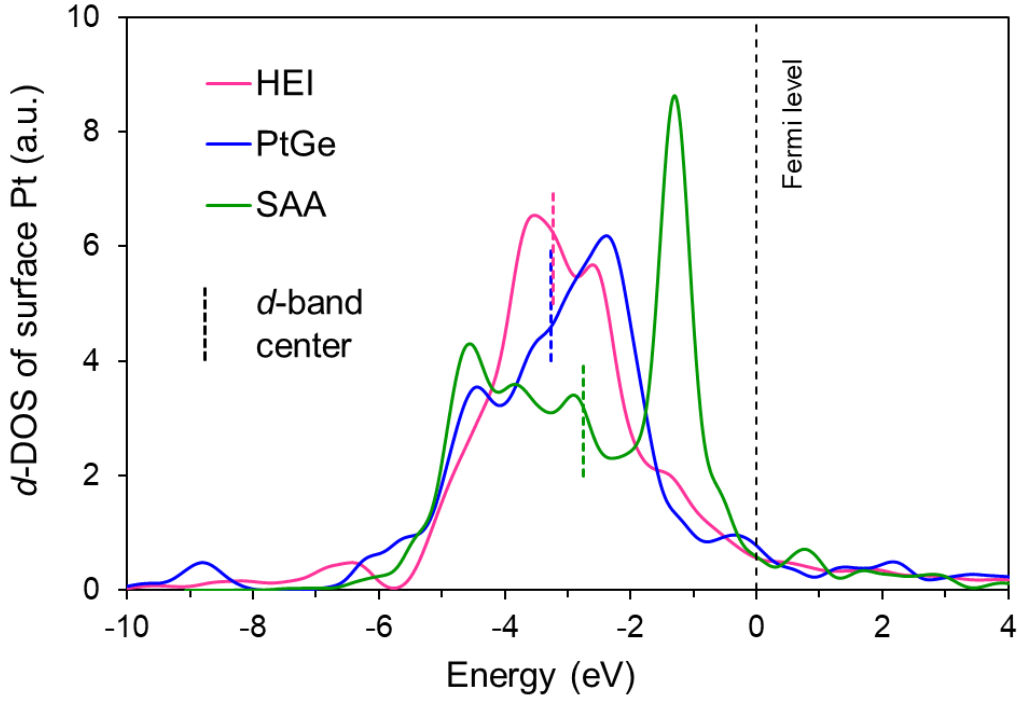

Figure 108. Density of states (DOS) of PtGe, HEI, and Pt–Cu SAA projected on d orbitals of surface Pt atoms.

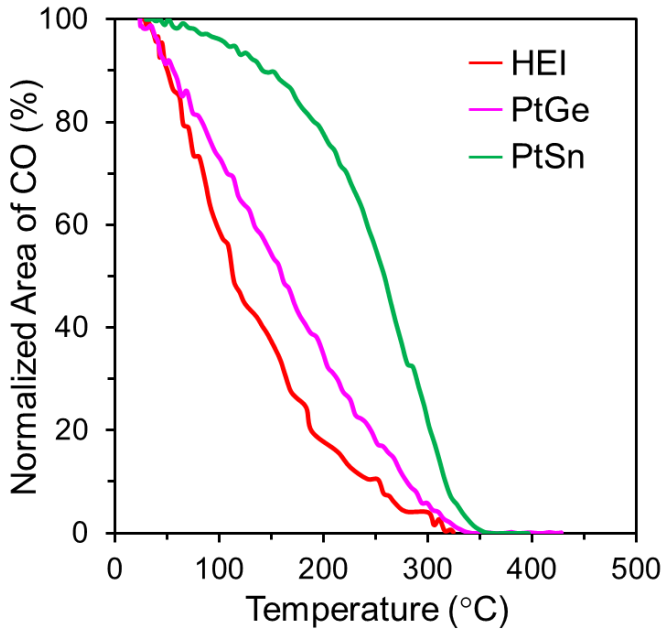

Figure 109. TPD profiles of linearly chemisorbed CO on PtSn, PtGe, and HEI(0.25) measured by FT-IR.

5.4. Discussion.

In the present study, we designed the PtGe-type HEIs to construct thermally stable single-atom Pt sites for PDH. The Pt and Ge sites of intermetallic PtGe were substituted with Co/Cu and Ga/Sn, respectively, which formed the nanoparticulate (PtCoCu)(GeGaSn) HEI on Ca–SiO_2 support. The degree of Pt isolation can be tuned by the Pt fraction in the Pt site (Pt/(Pt+Co+Cu) ratio), in which Pt atoms are sufficiently isolated at the ratio of 0.25. The single-atom-like Pt sites in HEI(0.25) effectively promotes the desorption of as-generated propylene to inhibit undesired side reactions. The HEI(0.25) catalyst is capable of working in PDH at 600°C for at least two months for the first time.

The role of each metal element is summarized as follows: (1) Pt works as the main active metal for C–H activation. (2) Ge, which is catalytically inactive, is the parent counterpart metal that determines the intermetallic PtGe structure and reduces the surface Pt–Pt coordination number to 2. (3) less active Co and Cu further dilute the Pt–Pt bridge sites in the transition metal site of HEI and provide isolated Pt sites. (4) Ga and Sn partially substitute the Ge site, which does not directly affect the catalysis, while increase the thermal stability of the HEI phase due to the entropy effect. (5) Ca works as a spacer to enhance the metal dispersion and alloying.

Thus, the multi-metallization strategy based on HEI is an ideal design concept for thermally stable single-atom Pt sites for light alkane activation.

Reference

1 J. J. H. B. Sattler, J. Ruiz-Martinez, E. Santillan-Jimenez and B. M. Weckhuysen, *Chem. Rev.*, 2014, **114**, 10613–10653.

2 Z. P. Hu, D. Yang, Z. Wang and Z. Y. Yuan, *Chinese J. Catal.*, 2019, **40**, 1233–1254.

3 S. Chen, C. Pei, G. Sun, Z.-J. Zhao and J. Gong, *Accounts Mater. Res.*, 2020, **1**, 30–40.

4 G. Wang, X. Zhu and C. Li, *Chem. Rec.*, 2020, **20**, 604–616.

5 S. Liu, B. Zhang and G. Liu, *React. Chem. Eng.*

6 S. Chen, X. Chang, G. Sun, T. Zhang, Y. Xu, Y. Wang, C. Pei and J. Gong, *Chem. Soc. Rev.*, 2021, **50**, 3315–3354.

7 A. H. Motagamwala, R. Almallahi, J. Wortman, V. O. Igenegbai and S. Linic, *Science*, 2021, **373**, 217–222.

8 G. Sun, Z. J. Zhao, R. Mu, S. Zha, L. Li, S. Chen, K. Zang, J. Luo, Z. Li, S. C. Purdy, A. J. Kropf, J. T. Miller, L. Zeng and J. Gong, *Nat. Commun.*, 2018, **9**, 4454.

9 J. W. Yeh, S. K. Chen, S. J. Lin, J. Y. Gan, T. S. Chin, T. T. Shun, C. H. Tsau and S. Y. Chang, *Adv. Eng. Mater.*, 2004, **6**, 299–303.

10 B. Cantor, I. T. H. Chang, P. Knight and A. J. B. Vincent, *Mater. Sci. Eng. A*, 2004, **375**–**377**, 213–218.

11 E. P. George, W. A. Curtin and C. C. Tasan, *Acta Mater.*, 2020, **188**, 435–474.

12 Y. Xin, S. Li, Y. Qian, W. Zhu, H. Yuan, P. Jiang, R. Guo and L. Wang, *ACS Catal.*, 2020, **10**, 11280–11306.

13 P. N. Duchesne, Z. Y. Li, C. P. Deming, V. Fung, X. Zhao, J. Yuan, T. Regier, A. Aldalbahi, Z. Almarhoon, S. Chen, D. en Jiang, N. Zheng and P. Zhang, *Nat. Mater.*, 2018, **17**, 1033–1039.

14 G. Firstova, A. Timoshevski, T. Kosorukova, Y. Koval, Y. Matviychuk and P. Verhovlyuk, *MATEC Web Conf.*, 2015, **33**, 0–3.

15 N. Zhou, S. Jiang, T. Huang, M. Qin, T. Hu and J. Luo, *Sci. Bull.*, 2019, **64**, 856–864.

16 K. Yao, L. Liu, J. Ren, Y. Guo, Y. Liu, Y. Cao, R. Feng, F. Wu, J. Qi, J. Luo, P. K. Liaw and W. Chen, *Scr. Mater.*, 2021, **194**, 113674.

17 Z. Jia, T. Yang, L. Sun, Y. Zhao, W. Li, J. Luan, F. Lyu, L. C. Zhang, J. J. Kruzic, J. J. Kai, J. C. Huang, J. Lu and C. T. Liu, *Adv. Mater.*, 2020, **32**, 2000385.

18 T. A. Kosorukova, G. Gerstein, V. V. Odnosum, Y. N. Koval, H. J. Maier and G. S. Firstov, *Materials (Basel).*

19 W. G. Jung and O. J. Kleppa, *J. Alloys Compd.*, 1991, **176**, 301–308.

20 Y. Nakaya, M. Miyazaki, S. Yamazoe, K. Shimizu and S. Furukawa, *ACS Catal.*, 2020, **10**, 5163–5172.

21 L. Qi, M. Babucci, Y. Zhang, A. Lund, L. Liu, J. Li, Y. Chen, A. S. Hoffman, S. R. Bare, Y. Han, B. C. Gates and A. T. Bell, *J. Am. Chem. Soc.*, 2021, **143**, 21364–21378.

22 B. Ravel and M. Newville, *J. Synchrotron Rad.*, 2005, **12**, 537–541.

23 A. Ankudinov and B. Ravel, *Phys. Rev. B, Condens. Matter Mater. Phys.*, 1998, **58**, 7565–7576.

24 M. D. Segall, P. J. D. Lindan, M. J. Probert, C. J. Pickard, P. J. Hasnip, S. J. Clark and M. C. Payne, *J. Phys. Condens. Matter*, 2002, **14**, 2717–2744.

25 B. Hammer, L. B. Hansen and J. K. Nørskov, *Phys. Rev. B, Condens. Matter Mater. Phys.*, 1999, **59**, 7413–7421.
26 A. Tkatchenko and M. Scheffler, *Phys. Rev. Lett.*, 2009, **102**, 6–9.
27 K. Hu, M. Wu, S. Hinokuma, T. Ohto, M. Wakisaka, J. I. Fujita and Y. Ito, *J. Mater. Chem. A*, 2019, **7**, 2156–2164.
28 T. A. Halgren and W. N. Lipscomb, *Chem. Phys. Lett.*, 1977, **49**, 225–232.
29 N. Govind, M. Petersen, G. Fitzgerald, D. King-Smith and J. Andzelm, *Comput. Mater. Sci.*, 2003, **28**, 250–258.
30 J. Y. He, H. Wang, H. L. Huang, X. D. Xu, M. W. Chen, Y. Wu, X. J. Liu, T. G. Nieh, K. An and Z. P. Lu, *Acta Mater.*, 2016, **102**, 187–196.
31 J. Joseph, N. Stanford, P. Hodgson and D. M. Fabijanic, *J. Alloys Compd.*, 2017, **726**, 885–895.
32 R. J. Vikram, B. S. Murty, D. Fabijanic and S. Suwas, *J. Alloys Compd.*, 2020, **827**, 154034.
33 S. N. Tripathi and M. S. Chandrasekharaiah, *J. Less-Common Met.*, 1983, **91**, 251–260.
34 C. Leroux, M. C. Cadeville, V. Pierron-Bohnes, G. Inden and F. Hinz, *J. Phys. F Met. Phys.*, 1988, **18**, 2033–2051.
35 R. P. Van Ingen, R. H. J. Fastenau and E. J. Mittemeijer, *J. Appl. Phys.*, 1994, **76**, 1871–1883.
36 E. J. Graeber, R. J. Baughman and B. Morosin, *Acta Crystallogr. Sect. B Struct. Crystallogr. Cryst. Chem.*, 1973, **29**, 1991–1994.
37 M. K. Bhargava, A. A. Gadalla and K. Schubert, *J. Less-Common Met.*, 1975, **42**, 69–76.
38 R. Massara, *J. Alloys Compd.*, 1994, **215**, 175–179.
39 F. Zaera, *Probing catalytic reactions at surfaces*, 2001, vol. 69.
40 K. Ding, A. Gulec, A. M. Johnson, N. M. Schweitzer, G. D. Stucky, L. D. Marks and P. C. Stair, *Science*, 2015, **350**, 189–192.
41 T. Komatsu, K. Sou and K. ichi Ozawa, *J. Mol. Catal. A Chem.*, 2010, **319**, 71–77.
42 X. Zheng, H. Lin, J. Zheng, X. Duan and Y. Yuan, *ACS Catal.*, 2013, **3**, 2738–2749.
43 M. J. Dees, T. Shido, Y. Iwasawa and V. Ponec, *J. Catal.*, 1990, **124**, 530–540.
44 R. Bouwman and P. Biloen, *J. Catal.*, 1977, **48**, 209–216.
45 S. Rimaz, C. Luwei, S. Kawi and A. Borgna, *Appl. Catal. A Gen.*, 2019, **588**, 117266.
46 W. E. Liu and S. E. Mohney, *J. Electron. Mater.*, 2003, **32**, 1090–1099.
47 Y. Nakaya, F. Xing, H. Ham, K. Shimizu and S. Furukawa, *Angew. Chem. Int. Ed.*, 2021, **60**, 19715–19719.
48 Y. Wang, Y. Suo, X. Lv, Z. Wang and Z. Y. Yuan, *J. Colloid Interface Sci.*, 2021, **593**, 304–314.
49 L. Liu, M. Lopez-Haro, C. W. Lopes, S. Rojas-Buzo, P. Concepcion, R. Manzorro, L. Simonelli, A. Sattler, P. Serna, J. J. Calvino and A. Corma, *Nat. Catal.*, 2020, **3**, 628–638.
50 L. Liu, M. Lopez-Haro, C. W. Lopes, C. Li, P. Concepcion, L. Simonelli, J. J. Calvino and A. Corma, *Nat. Mater.*, 2019, **18**, 866–873.

51 Q. Sun, N. Wang, Q. Fan, L. Zeng, A. Mayoral, S. Miao, R. Yang, Z. Jiang, W. Zhou, J. Zhang, T. Zhang, J. Xu, P. Zhang, J. Cheng, D. C. Yang, R. Jia, L. Li, Q. Zhang, Y. Wang, O. Terasaki and J. Yu, *Angew. Chem. Int. Ed.*, 2020, **59**, 19450–19459.

52 J. Zhu, R. Osuga, R. Ishikawa, N. Shibata, Y. Ikuhara, J. N. Kondo, M. Ogura, J. Yu, T. Wakihara, Z. Liu and T. Okubo, *Angew. Chem. Int. Ed.*, 2020, **59**, 19669–19674.

53 Y. Wang, Z. P. Hu, X. Lv, L. Chen and Z. Y. Yuan, *J. Catal.*, 2020, **385**, 61–69.

54 C. Chen, M. Sun, Z. Hu, J. Ren, S. Zhang and Z. Y. Yuan, *Catal. Sci. Technol.*, 2019, **9**, 1979–1988.

55 X. Fan, J. Li, Z. Zhao, Y. Wei, J. Liu, A. Duan and G. Jiang, *Catal. Sci. Technol.*, 2015, **5**, 339–350.

56 S. W. Han, H. Park, J. Han, J. Kim, J. Lee, C. Jo and R. Ryoo, *ACS Catal.*, 2021, **11**, 9233–9241.

57 R. Ryoo, J. Kim, C. Jo, S. W. Han, J. C. Kim, H. Park, J. Han, H. S. Shin and J. W. Shin, *Nature*, 2020, **585**, 221–224.

58 Y. Qiu, X. Li, Y. Zhang, C. Xie, S. Zhou, R. Wang, S. Z. Luo, F. Jing and W. Chu, *Ind. Eng. Chem. Res.*, 2019, 10804–10818.

59 B. Li, Z. Xu, W. Chu, S. Luo and F. Jing, *Cuihua Xuebao/Chinese J. Catal.*, 2017, **38**, 726–735.

60 K. Searles, K. W. Chan, J. A. Mendes Burak, D. Zemlyanov, O. Safonova and C. Copéret, *J. Am. Chem. Soc.*, 2018, **140**, 11674–11679.

61 L. Xie, Y. Chai, L. Sun, W. Dai, G. Wu, N. Guan and L. Li, *J. Energy Chem.*, 2021, **57**, 92–98.

62 Y. Wang, Z. P. Hu, W. Tian, L. Gao, Z. Wang and Z. Y. Yuan, *Catal. Sci. Technol.*, 2019, **9**, 6993–7002.

63 L. Rochlitz, K. Searles, J. Alfke, D. Zemlyanov, O. V. Safonova and C. Copéret, *Chem. Sci.*, 2020, **11**, 1549–1555.

64 Y. Nakaya, J. Hirayama, S. Yamazoe, K. Shimizu and S. Furukawa, *Nat. Commun.*, 2020, **11**, 2838.

65 S. Zha, G. Sun, T. Wu, J. Zhao, Z. J. Zhao and J. Gong, *Chem. Sci.*, 2018, **9**, 3925–3931.

66 S. Takamoto, C. Shinagawa, D. Motoki, K. Nakago, W. Li, I. Kurata, T. Watanabe, Y. Yayama, H. Iriguchi, Y. Asano, T. Onodera, T. Ishii, T. Kudo, H. Ono, R. Sawada, R. Ishitani, M. Ong, T. Yamaguchi, T. Kataoka, A. Hayashi, N. Charoenphakdee and T. Ibuka, *Nat. Commun.*, 2022, **13**, 2991.

67 A. Nakata, D. R. Bowler and T. Miyazaki, *Phys. Chem. Chem. Phys.*, 2015, **17**, 31427–31433.

68 C. Romero-Muñiz, A. Nakata, P. Pou, D. R. Bowler, T. Miyazaki and R. Pérez, *J. Phys. Condens. Matter*, 2018, **30**, 505901.

69 Y. Nanba and M. Koyama, *Phys. Chem. Chem. Phys.*, 2022, **24**, 15452–15461.

70 G. V. Huerta, Y. Nanba, I. Kurata, K. Nakago, S. Takamoto, C. Shinagawa and M. Koyama, *arXiv*, , DOI:10.1039/D2CP01848A.

Chapter 6

General Conclusions

6. General Conclusions

In this thesis, a series of innovative alloy-based catalysts were synthesized and tested for the dehydrogenation of methylcyclohexane and propane. The developed catalysts functioned as remarkably efficient catalysts. In addition, detailed characterization, kinetic studies, and theoretical calculations revealed the origin of excellent catalytic performance in atomic-scale.

Chapter 2 concludes that the $Pt_3(Fe_{0.75}Zn_{0.25})$ pseudo-binary alloy supported on silica acted as a highly active, selective, and stable catalyst for the dehydrogenation of methylcyclohexane. The substitution of part of Fe by Zn forms the $Pt_3(Fe_{0.75}Zn_{0.25})$ pseudo-binary alloy structure, which exhibits a three times higher TOF than that of Pt/SiO_2, excellent toluene selectivity (>99%, methane: <500 ppm), and long-term durability (>50 h). Fe has a unique capability to facilitate the hydrogenation of coke precursor to methane. Zn makes Pt electron-rich and further dilutes Pt_3 hollow sites, which strongly accelerates toluene desorption owing to the ligand and ensemble effects, respectively. The synergy of enhanced decoking capability and toluene desorption serves an outstanding catalytic performance. Therefore, the catalyst design based on the pseudo-binary alloy structure allows to construct multifunctional active sites that are highly efficient for methylcyclohexane dehydrogenation.

Chapter 3 concludes that the surface decoration of PtGa intermetallics using Pb as a modifier served a highly stable active site for propane dehydrogenation. PtGa has four different surface terminations, denoted as Pt_3, Ga_3, Pt_1, and Ga_1 at the most stable (111) plane. Although both Pt_3 and Pt_1 sites are active for C–H scissions of propane, Pt_3 sites also catalyze the overdehydrogenation of propylene and subsequent C–C scissions, while the Pt_1 sites can selectively generate propylene. The Pt_3 ensembles were successfully blocked by Pb deposition, while the Pt_1 sites remained. The developed $PtGa–Pb/SiO_2$ catalyst exhibited high propylene selectivity (99.6% propylene selectivity) without deactivation for 96 h at 600°C in the presence of co-feed H_2 (τ = 1159 h). DFT calculations revealed that Pt_1 sites well catalyze the first and second C–H activation, while effectively inhibits the third one, which minimizes the side reactions to coke and drastically improves the selectivity and stability.

Chapter 4 concludes that doubly-decorated PtGa by Ca and Pb worked as a highly stable propane dehydrogenation. Pb was deposited on the Pt_3 sites of the PtGa nanoparticles, whereas Ca was placed around the nanoparticles to impart them with an electron-enriched Pt_1 site. The effects of these modifications were synergistic and remarkably improved the catalytic stability in propane dehydrogenation. $PtGa–Ca–Pb/SiO_2$ exhibited an outstandingly high catalytic stability, even at 600°C (τ = 3067 h), and almost no deactivation of the catalyst was observed for up to one month for the first time.

Chapter 5 concludes that the Pt_1 sites in high-entropy intermetallics functioned as ultrastable active sites for propane dehydrogenation. Pt–Pt ensembles, which cause side reactions, are entirely diluted by the component inert metals in PtGe-type high-entropy intermetallics. The resultant $(PtCoCu)(GeGeSn)/Ca–SiO_2$ catalyst exhibited an outstandingly high catalytic stability, even at 600°C (τ = 4146 h), and almost no deactivation of the catalyst was observed two months for the first time. Detailed experimental studies and theoretical calculations demonstrated that the combination of the site-isolation and entropy effects upon multi-metallization of PtGe drastically enhanced the desorption of propylene and the thermal stability, eventually suppressing the side reactions even at high reaction temperatures.

In summary, this thesis not only demonstrates outstanding catalytic performance, but also opens a new paradigm for the catalyst design concept. I believe that this work would be a guideline for promoting the field of multimetallic alloy materials.

Acknowledgement

First of all, I would like to express my gratitude to my supervisor Prof. Shinya Furukawa. He not only guided my research, but also gave me many opportunities to develop my personality. Thanks to his guidance, I was able to motivate myself and continuously perform my research with high quality.

I would also like to appreciate the members of advisory committee for their suggestions and advice. I am truly grateful to all the staff and laboratory members in Shimizu lab for their kind help in the daily research.

Finally, I would like to acknowledge the Grant-in-Aid for JSPS Fellows (JSPS KAKENHI: 21J20594) for the financial support.

Yuki Nakaya

中谷　勇希